Thermal Optimisation of the Stator Vent Design for a Synchronous Generator



Kevin Bersch

Faculty of Engineering
University of Nottingham

Thesis submitted to the University of Nottingham for the degree of
Doctor of Philosophy

May 2019

Abstract

An appropriate cooling of electrical machines is essential for safe, reliable and efficient operation and to address the growing demand for highly power-dense machines. Conventional thermal design optimisation procedures have traditionally relied on simple analytical correlations, which are not well suited to investigate complex and novel designs. Computational Fluid Dynamics (CFD) enables a more accurate prediction of fluid flow and heat transfer. But to date, the high complexity of the geometry, mesh and solver setup have required the model setup to be updated manually when the machine design is changed.

Within this thesis, a novel methodology for the thermal optimisation of electrical machines is developed based on a 3-D Conjugate Heat Transfer CFD model of a synchronous generator. It enables the automated optimisation of multiple design parameters without requiring any additional user input after the initial model setup. The impact the design changes have on the electromagnetic performance was taken into account through analytical correlations developed from electromagnetic 2-D FEA. By implementing these correlations into the thermal optimisation procedure, an optimal machine design considering the thermal as well as the electromagnetic performance can be achieved.

The developed methodology was applied to improve the stator cooling of an air-cooled synchronous generator with a power rating of several hundred kVA used for continuous industrial power generation. Initially, a model of the current machine design was created to gain insight into its thermal performance. As the machine hot spot is located in the stator core windings, venting the stator was identified as a beneficial design change. Subsequently, five vent design parameters were optimised, reducing peak and average stator winding temperatures.

Based on the outcome of the design optimisation, a vented stator-casing arrangement was built and tested experimentally. In comparison to the original machine design, the peak stator winding temperature rise was reduced by 20.1 %, while the average stator winding temperature rise decreased by 12.3 %.

The investigated generator and the designed prototype were validated experimentally by torque, mass flow, rotor and stator winding temperature measurements. The temperature measurements were taken at various loads, including full load, while the machine was connected to the grid. This enabled an accurate prediction of the generator's thermal performance under normal operating conditions. Good agreement between CFD and experimental data was found, validating the design methodology.

Acknowledgements

I would like to thank my supervisors Dr. Carol Eastwick, Dr. Peter Connor and Dr. Michael Galea for their support during this project. Thanks for offering me the opportunity to do this PhD, and going out of your way to help me finish it.

Many thanks to all my colleagues who supported me during this project. Thanks to Colin Blackburn, John Hinchliffe and their teams for their technical support. Thanks to Chris Varley and Dan Fallows for their support with the setup and execution of my experiments and answering all my electrical questions. Thanks to Dr. Stefano Nuzzo for his contribution. Thanks to Cummins Generator Technologies for the prototype manufacture and the supply of measurement equipment.

I would like to thank all the friends I made during my time in Nottingham, who made my PhD an even more enjoyable experience. Thanks to PGSA and the nomads for all the megs and fun times on and off the football pitch. Thanks to the whole thermofluids office for the fun work environment and fika breaks. Thanks to Chris Varley for teaching me how many beers I could safely drink on a week night. Thanks to Patrick Bointon for his tough love training methods, and his friendship in general.

Ganz besonders möchte ich meinen Eltern, Großeltern und meiner Schwester für ihre Unterstützung in allen Lebenslagen danken. Ohne euch wäre das alles nicht möglich gewesen.

Finally, thanks to Orla, for everything.

Publications

Some of the findings presented in this thesis have been published previously by the author of this thesis in the following documents:

- K Bersch, P H Connor, C N Eastwick, M Galea and R Rolston. CFD optimisation of the thermal design for a vented electrical machine. *Proceedings – 2017 IEEE Workshop on Electrical Machines Design, Control and Diagnosis (WEMDCD 2017)*, pp. 39-44, Nottingham, UK. 2017.
- K Bersch, P H Connor, C N Eastwick and M Galea. A CFD and experimental investigation into a non-intrusive method for measuring cooling air mass flow rate through a synchronous generator. *The Journal of Engineering*, 2019.
- K Bersch, S Nuzzo, P H Connor, C N Eastwick, M Galea, R Rolston, and G Vakil. Combined Thermofluid and Electromagnetic Optimisation of Stator Vent Cooling. *Proceedings - 2018 23rd International Conference on Electrical Machines (ICEM 2018)*, Alexandroupoli, Greece. 2018.

Table of contents

List of figures **xv**

List of tables **xxiii**

Nomenclature **xxv**

1 Introduction **1**

1.1 Background 1

1.2 Aim and Objectives 3

1.2.1 Aim 3

1.2.2 Objectives 4

1.3 Machine under investigation 4

1.4 Thesis structure 6

2 Literature Review **9**

2.1 Losses and Efficiency 10

2.1.1 Copper losses 10

2.1.2 Iron losses 11

2.1.3 Mechanical losses 11

2.1.4 Stray losses 12

2.2 Computational Modelling Techniques 12

2.2.1 Lumped Parameter Thermal Networks 12
2.2.2 Finite Element Analysis 13
2.2.3 Computational Fluid Dynamics 13
2.2.4 Multi-Physics Modelling 15
2.2.5 Design Optimisation 16
2.3 Correlations based on simple Geometries 17
2.4 Experimental Investigations 21
2.5 Stator Vents 23
2.6 Summary and Conclusions 26

3 CFD Modelling of Electrical Machines 29
3.1 General CFD Workflow 29
3.2 Geometry Creation 32
3.2.1 Periodicity 32
3.2.2 Geometry Simplifications 35
3.2.3 Geometry Division 36
3.3 Meshing 36
3.3.1 Cell types and mesh quality 37
3.3.2 Conformal/Non-conformal Interfaces 39
3.3.3 Mesh Independence 40
3.3.4 Boundary Condition Definition 42
3.4 Solver Setup 43
3.4.1 Governing equations of fluid flow 43
3.4.2 Compressibility 43
3.4.3 Turbulence Modelling 44
3.4.4 Rotation Modelling 45
3.4.5 Heat Loss Implementation 48

3.4.6 Anisotropic Conductivity 49
3.5 Solution Methods and Controls 49
3.6 Post-processing 51
3.7 Novel Methodologies Developed 51
3.7.1 Automated Interface Creation 51
3.7.2 Anisotropic Conductivity Modelling in Endwindings 52
3.7.3 Temperature Dependent Heat Generation 57

4 Experimental Test Facility 61
4.1 Lab and Test Rig Setup 61
4.2 Mass Flow Measurements 63
4.2.1 Plenum and Inlet duct Design 65
4.3 Torque Measurements 69
4.4 Thermal Measurements 70
4.4.1 Stator Measurements 71
4.4.2 Rotor Measurements 72
4.4.3 Air Temperature Measurements 74
4.4.4 Test Procedure 74
4.5 Loss Measurements 75

5 Experimental Validation and Analysis of the Benchmark CFD Model 77
5.1 Mass Flow Results 77
5.2 Torque Results 81
5.3 Thermal Results 83
5.3.1 Stator Results 85
5.3.2 Rotor Results 95
5.4 Conclusions 97

6 Stator Vent Design Methodology and Results 99

6.1 Methodology Development on Simplified Geometry 100

6.2 Implementation of Variable Loss Distribution 111

6.3 Vented Prototype Design Methodology 115

6.4 Optimisation Design Parameters 121

6.4.1 Vent Location 121

6.4.2 Vent Width 124

6.4.3 Baffle Height 126

6.5 Optimisation Results 131

7 Experimental Validation of the Vented Prototype CFD Model 137

7.1 Baffle Design 137

7.2 Mass Flow Results 139

7.3 Torque Results 142

7.4 Thermal Results 145

7.4.1 Impact of the Rotation Modelling Approach 146

7.4.2 Stator Results 152

7.4.3 Rotor Results 161

7.5 Conclusions 163

8 Conclusions and Outlook 165

8.1 Project Summary and Conclusions 166

8.2 Novelty in this thesis 167

8.2.1 Parametric CFD Design Optimisation 167

8.2.2 CFD Methodology Developments 168

8.2.3 CFD Investigations 169

8.2.4 Experimental Investigations 171

8.3 Future Work 171

References 173

Appendix A Computational Fluid Dynamics Theory 181

A.1 Governing equations of fluid flow 181

A.2 Discretisation 182

A.3 RANS Turbulence Modelling 183

Appendix B Fluent Scripts and User Defined Functions 185

B.1 Automatic creation of periodic boundaries 185

B.2 Automatic creation of periodic repeats 186

B.3 Anisotropic Conductivity Modelling in Endwindings 188

B.4 Temperature dependent heat generation 191

List of figures

1.1 Schematic of the investigated generator showing the inlet (yellow) and outlet (red) locations 5

1.2 180° schematic of the investigated machine; only solid parts shown; casing not displayed 5

1.3 Project overview 8

2.1 Taylor vortices for co-rotating cylinders [48] 19

2.2 Schematic of rotor investigated by Fénot *et al.* [53] 20

2.3 Stator and attached traverse for stator vent outflow measurements [11] . . . 22

2.4 Modification of stator bars by Küng *et al.* to reduce stator vent pressure loss [62] 24

2.5 Wall heat flux on the (a) slot trailing (b) slot bottom (c) slot leading side [63]; High heat flux on the leading side caused by impingement of rotating fluid shown in red 26

3.1 Workflow of CFD investigations 30

3.2 Comparison of inlet locations on real machine and CFD model 34

3.3 Volume division required to achieve a high quality mesh in the airgap and implement rotation; rotating parts (blue), stationary parts (red) 36

3.4 Benchmark Machine mesh showing areas meshed with hex and tet cells and non-conformal interfaces (in red); side view 38

3.5 Benchmark Machine mesh showing areas meshed with hex and tet cells; axial slice through centre of core 39

3.6 Comparison of conformal and non-conformal mesh interfaces 39
3.7 Division of the boundary layer in the near-wall region in semi-logarithmic scale [69] 42
3.8 Separation of benchmark machine geometry into rotating (grey) and stationary (purple) domain 46
3.9 Temperature rise contours in the axial centre of a vent of the Vented Prototype; Temperature rise normalised according to equation 5.4 47
3.10 Orientation of the rotor and stator windings in the global coordinate system 53
3.11 Rotor and Stator Endwindings of the Benchmark Machine 54
3.12 Influence of the loss implementation approach on stator winding temperature rise of the BM CFD model; Temperature rise normalised according to equation 5.4 59

4.1 Test laboratory overview 62
4.2 Test rig schematic 62
4.3 Schematic of the mass flow measurement system 64
4.4 Plywood plenum designed for mass flow measurements 64
4.5 CFD geometry used to determine the optimal plenum and duct dimensions . 66
4.6 CFD prediction of static pressure drop introduced by plenum and duct at 1500 RPM 66
4.7 Correlation between duct diameter and mass flow rate predicted by CFD for a constant plenum size; Mass flow rate normalised according to equation 4.2 68
4.8 Measured torque during the first two hours of operation; Torque normalised according to equation 5.3 70
4.9 Location of the RTDs (in red) distributed over the stator core windings . . . 71
4.10 Schematic showing RTD location in the stator slots 72
4.11 Locations of the RTDs (marked in red) distributed over the rotor core windings and endwindings; location mirrored at other machine end 73

5.1 Overview of conducted experimental tests 77

5.2 Experimentally measured mass flow rates through the Benchmark Machine at various rotational speeds; Mass flow rate normalised according to equation 5.1 78

5.3 Comparison of CFD and experimentally measured mass flow rate through the machine at various rotational speeds; Mass flow rate normalised according to equation 5.1 80

5.4 Pressure fluctuation with time during a Sliding Mesh simulation with a 1° time step 81

5.5 Comparison of CFD and experimentally measured windage and friction torque of the benchmark machine at various rotational speeds; Torque normalised according to equation 5.3 82

5.6 Core length schematic 84

5.7 Experimentally measured stator winding temperature rise in the core at full load and 0.8 power factor; NDE at the left; Temperature rise normalised according to equation 5.4 85

5.8 Temperature rise contours of the Benchmark Machine CFD MRF model; Temperature rise normalised according to equation 5.4 87

5.9 Comparison between CFD MRF and experimentally measured stator winding temperature rise in the core at full load and 0.8 power factor; NDE at the left; Temperature rise normalised according to equation 5.4 88

5.10 Influence of the magnitude of anisotropic stator winding conductivity in radial and tangential direction on stator winding temperature rise; Temperature rise normalised according to equation 5.4 90

5.11 Influence of the magnitude of anisotropic stator iron conductivity in axial direction on winding temperature rise; Temperature rise difference taken in relation to temperature rise of isotropic case according to equation 5.8 . . . 91

5.12 Stator endwindings of Benchmark Machine 92

5.13 CFD MRF temperature rise variation within a single slot at an axial location of 0.7 l_n; Temperature rise normalised according to equation 5.4 93

5.14 Comparison between CFD MRF (lines) and experimentally measured (bars) stator winding temperature rise at full load and 0.8 PF; Temperature rise normalised according to equation 5.4 94

5.15 Comparison between CFD MRF and experimentally measured rotor winding temperature rise at full load and 0.8 power factor; NDE at the left; Temperature rise normalised according to equation 5.4 96

5.16 CFD MRF temperature rise variation within the rotor coils at an axial location of 0.74 l_n; Temperature rise normalised according to equation 5.4 97

6.1 Schematic of the simplified model 101

6.2 Axial view of the simplified model core geometry 102

6.3 Maximum stator winding temperature of configurations simulated during the Design Optimisation in chronological order; Temperature normalised according to equation 6.1; Normalised core length displayed next to data points 104

6.4 Relationship between maximum stator winding temperature and vent position; Temperature normalised according to equation 6.1 105

6.5 Temperature contours of non-vented case (top) and vented case (bottom) with optimal vent position; Temperature normalised according to equation 6.1 106

6.6 Comparison of peak and average rotor and stator winding temperatures depending on vent location; Temperature normalised according to equation 6.1 107

6.7 Velocity contours in the axial centre of the vent; Velocity normalised according to equation 6.4 108

6.8 Close-up of velocity vectors in the axial centre of the vent around the two windings marked in figure 6.7; Velocity normalised according to equation 6.4 109

6.9 Distribution of total mass flow through the vent between the channels; Channels are numbered from the left to the right as shown in figure 6.7 (counter-rotation) 110

6.10 Variation of static pressure in the airgap with angular location in the axial centre of the vent; 0° corresponds to the centre of channel 1 110

6.11 Correlation between rotor copper loss (top), rotor iron loss (middle), stator iron loss (bottom) and combined vent width; A loss value of 1 corresponds to the respective loss of the non-vented Benchmark Machine 114

6.12 Workflow during the design optimisation procedure 116

6.13 Geometry of the vented model used for the design of the vented prototype; Only solids shown for greater clarity 116

6.14 Model schematic showing the optimised input parameters (in red) 117

6.15 Workflow of the Adaptive Single-Objective algorithm [71] 120

6.16 Static pressure profile along the core length in the stator-casing duct and airgap 122

6.17 Relationship between vent mass flow rate and vent location for a case with a single vent and a constant vent width; Mass flow rate normalised according to equation 5.1 122

6.18 Relationship between peak stator winding temperature rise difference and vent location for a case with a single vent and a constant vent width; Temperature rise difference normalised according to equation 6.9 123

6.19 Relationship between vent mass flow rate and vent width for a case with a single vent and a constant vent location; Mass flow rate normalised according to equation 5.1 125

6.20 Relationship between peak rotor and stator temperature rise difference and vent width for a case with a single vent and a constant vent location; Temperature rise difference normalised according to equation 6.9 125

6.21 Comparison of pressure distribution between stator-casing duct and airgap with (top) and without (bottom) a baffle 127

6.22 Relationship between mass flow rate through the vents and baffle length; Mass flow rate normalised according to equation 5.1 127

6.23 Static pressure in the stator-casing duct and airgap with and without a baffle 128

6.24 Relationship between total mass flow rate and baffle length; Mass flow rate normalised according to equation 5.1 129

6.25 Relationship between peak & average stator winding temperature rise difference and baffle height; Temperature rise difference normalised according to equation 6.9 130

6.26 Temperature rise contour comparison between Benchmark Machine (top) and Vented Prototype (DP 5) (bottom); Temperature rise normalised according to equation 5.4 133

6.27 Comparison of stator winding temperature rise in the core between Benchmark Machine, DP 2 & DP 5; NDE at the left; Temperature rise normalised according to equation 5.4 134

7.1 Baffle 3-D printed from Polycarbonate 138

7.2 Experimentally measured mass flow rates through the Vented Protoype with and without grilles at various rotational speeds; Mass flow rate normalised according to equation 5.1 139

7.3 Comparison of experimentally measured mass flow rates without grilles through the Benchmark Machine and Vented Protoype at various rotational speeds; Mass flow rate normalised according to equation 5.1 140

7.4 Comparison of CFD and experimentally measured mass flow rate through the Vented Prototype at various rotational speeds; Mass flow rate normalised according to equation 5.1 142

7.5 Comparison of experimentally measured windage and friction torque between the Benchmark Machine and the Vented Prototype at various rotational speeds; Torque normalised according to equation 5.3 143

7.6 Comparison of CFD windage and friction torque between the Benchmark Machine and the Vented Prototype at various rotational speeds; Torque normalised according to equation 5.3 144

7.7 Comparison of CFD and experimentally measured windage and friction torque of the Vented Prototype at various rotational speeds; Torque normalised according to equation 5.3 145

7.8 Temperature contour comparison between MRF and SM simulations with various solid time step sizes conducted on a sub model 147

7.9 Convergence of rotor and stator winding temperature rises during the CHT SM simulation of the Vented Prototype; Temperature rise normalised according to equation 5.4 148

7.10 Comparison of MRF and SM temperature rise contours at an axial location of $0.70\,l_n$; Temperature rise normalised according to equation 5.4 150

7.11 Comparison of stator winding temperature rise variation between slots between the MRF and SM approach; Temperature rise normalised according to equation 5.4 151

7.12 Comparison of experimentally measured stator winding temperature rise in the core at full load and 0.8 power factor between the BM and VP; NDE at the left; Temperature rise normalised according to equation 5.4 152

7.13 Comparison of heat flux from stator core windings to stator iron and vents between Benchmark Machine and Vented Prototype; Radially inwards view 154

7.14 Comparison between Vented Prototype CFD MRF and experimentally measured stator winding temperature rise in the core at full load and 0.8 power factor; NDE at the left; Temperature rise normalised according to equation 5.4 155

7.15 Comparison of CFD MRF stator winding temperature rise in the core at full load and 0.8 PF between BM and VP under consideration of the reduced copper losses; NDE at the left; Temperature rise normalised according to equation 5.4 156

7.16 Influence of anisotropic stator iron conductivity in axial direction on peak stator winding temperature rise difference; Comparison between machines with no, one and two stator vents; Temperature rise difference taken in relation to temperature rise of isotropic case according to equation 5.8 . . . 158

7.17 Comparison between CFD MRF (lines) and experimentally measured (bars) VP stator winding temperature rise at full load and 0.8 PF; Temperature rise normalised according to equation 5.4 159

7.18 Comparison between experimentally measured stator winding temperature rise of the Benchmark Machine and Vented Prototype at full load and 0.8 PF; Temperature rise normalised according to equation 5.4 160

7.19 Comparison of experimentally measured rotor winding temperature rise in the core at full load and 0.8 power factor between BM and VP; NDE at the left; Endwindings included; Temperature rise normalised according to equation 5.4 162

7.20 Comparison between VP CFD MRF and experimentally measured rotor winding temperature rise at full load and 0.8 power factor; NDE at the left; Temperature rise normalised according to equation 5.4 163

List of tables

2.1 Results of mesh sensitivity study in [65] 25

3.1 Heat loss distribution in the Benchmark Machine at 0.8 PF; Copper and mechanical losses determined experimentally; Iron losses determined by FEA; Exciter and Stray losses taken from manufacturer data sheet 48

4.1 Comparison of various plenum and duct configurations 67

5.1 Comparison of CFD MRF and experimentally measured stator endwinding temperature rise; Temperature rise normalised according to equation 5.4 . . 95

6.1 Design optimisation parameter range; Vent location and width normalised according to equation 5.5; Baffle length normalised according to equation 6.7 118

6.2 Normalised mass flow rates and normalised stator winding temperature rise differences in the benchmark and vented machines with and without a baffle 131

6.3 Domain Reduction 131

6.4 Most promising design points identified during the optimisation procedure; Manufactured DP marked in green; All properties normalised 132

7.1 Comparison of MRF and SM simulations results; All properties normalised 151

7.2 Comparison of VP CFD MRF & experimentally measured stator endwinding temperature rise; Temperature rise normalised according to equation 5.4 . . 161

8.1 Agreement between Benchmark Machine CFD and experimental results . . 166

8.2 Agreement between Vented Prototype CFD and experimental results 167

Nomenclature

Abbreviations

AC	Alternating Current
ASO	Adaptive Single-Objective
BM	Benchmark Machine
BS	British Standard
CAD	Computer Aided Design
CAE	Computer Aided Engineering
CFD	Computational Fluid Dynamics
CGT	Cummins Generator Technologies
CHT	Conjugate Heat Transfer
DC	Direct Current
DE	Drive End
DNS	Direct Numerical Simulation
DoE	Design of Experiment
DP	Design Point
EM	Electromagnetic
EW	EndWinding

FEA Finite Element Analysis

FEM Finite Element Method

FVM Finite Volume Method

hex hexahedral

HPC High Performance Computing

HTC Heat Transfer Coefficient

IP Interpolar

IR Infrared

LES Large Eddy Simulation

LPTN Lumped Parameter Thermal Network

MISQP Mixed-Integer Sequential Quadratic Programming

MRF Multiple Reference Frame

NDE Non Drive End

NEMA National Electrical Manufacturers Association

OLS Ordinary Least Square

OSF Optimal Space-Filling

PF Power Factor

PIV Particle Image Velocimetry

RANS Reynolds-averaged Navier Stokes

RPM Revolutions Per Minute

RTD Resistance Temperature Detector

SIMPLE Semi-Implicit Method for Pressure-Linked Equations

SM Sliding Mesh

SST Shear Stress Transport

TEFC Totally Enclosed Fan Cooled

tet tetrahedral

UDF User Defined Function

UoN University of Nottingham

VP Vented Prototype

VPI Vacuum Pressure Impregnation

Geometric Symbols

D	Diameter	m
d_B	Bearing diameter	m
D_h	Hydraulic diameter	m
e	Annular gap	m
L	Characteristic length	m
L	Total core length	m
l	Core length	m
R	Radius	m
r_B	Radial baffle height	m
r_b	Bending radius	m
r_{SC}	Radial stator-casing duct height	m
s	Axial gap	m
t	Material thickness	m

Indices

a axial

c	critical
i	inner
o	outer
ref	reference

Non-dimensional Numbers

$\dot{m}_n$	Non-dimensionalised mass flow rate	$\dot{m}_n = \frac{\dot{m}}{\dot{m}_{ref}}$
$\dot{m}_{n,plenum}$	Non-dimensionalised plenum mass flow rate	$\dot{m}_n = \frac{\dot{m}}{\dot{m}_u}$
b_n	Non-dimensionalised baffle length	$b_n = \frac{r_B}{r_{SC}}$
C_m	Torque Coefficient	$C_m = \frac{2M}{\rho\omega^2 R^5}$
k_{ar}	Thermal conductivity anisotropy ratio	$\frac{k_{ax}}{k_{rad\tan}}$
l_n	Non-dimensionalised core length	$l_n = \frac{l}{L}$
M_n	Non-dimensionalised torque	$M_n = \frac{M_{windage}}{M_{ref}}$
Ma	Mach number	$Ma = \frac{v_{fluid}}{v_{sound}}$
Nu	Nusselt number	$Nu = \frac{hL}{k}$
Pr	Prandtl number	$Pr = \frac{\mu}{\alpha}$
Re	Reynolds number	$Re = \frac{\rho v L}{\mu}$
Re_a	Axial Reynolds number	$Re_a = \frac{\rho v_a L}{\mu}$
Re_r	Rotational Reynolds number	$Re_r = \frac{\rho\omega R^2}{\mu}$
Re_{eff}	Effective Reynolds number	$Re_{eff} = \frac{\sqrt{v_a^2 + C(\omega R)^2}e}{\nu}$
T_n	Non-dimensionalised temperature rise	$T_n = \frac{T - T_{in}}{T_{ref} - T_{in}}$
$T_{n,cfd}$	Non-dimensionalised CFD temperature	$T_{n,cfd} = \frac{T}{T_{max,B}}$
Ta	Taylor number	$Ta = \frac{4\omega^2 L^4}{\nu^2}$
y^+	Non-dimensional wall distance	$y^+ = \frac{u_T y}{\nu}$

Physics Symbols

$\alpha\varepsilon$	Compound coefficient of conical inlet duct	-
α	Thermal diffusivity	$\mathrm{m^2\,s^{-1}}$
$\dot{m}$	Mass flow rate	$\mathrm{kg\,s^{-1}}$
$\dot{m}_u$	Unrestricted mass flow rate	$\mathrm{kg\,s^{-1}}$
$\dot{m}_{ref}$	Reference mass flow rate	$\mathrm{kg\,s^{-1}}$
ε	Turbulence kinetic energy dissipation rate	$\mathrm{m^2\,s^{-3}}$
μ	Dynamic viscosity	$\mathrm{kg\,m^{-1}\,s^{-1}}$
μ_B	Bearing friction coefficient	-
ν	Kinematic viscosity	$\mathrm{m^2\,s^{-1}}$
ω	Rotational speed	$\mathrm{rad\,s^{-1}}$
ω	Specific turbulence kinetic energy dissipation rate	$\mathrm{s^{-1}}$
ρ	Density	$\mathrm{kg\,m^{-3}}$
τ_w	Wall shear stress	$\mathrm{N\,m^{-2}}$
$\vec{v}$	Velocity vector	$\mathrm{m\,s^{-1}}$
a, b, C, m, n, K_h, K_e	Generic constants	-
F_r	Radial bearing load	N
h	Heat transfer coefficient	$h = \frac{q}{T_{wall} - T_{ref}}$
I	Current	A
i	Internal energy	$\mathrm{J\,kg^{-1}}$
k	Thermal conductivity	$\mathrm{W\,m^{-1}\,K^{-1}}$
k	Turbulence kinetic energy	$\mathrm{m^2\,s^{-2}}$
k_{ax}	Axial thermal conductivity	$\mathrm{W\,m^{-1}\,K^{-1}}$

k_h	Thermal conductivity in wire orientation	$\mathrm{W\,m^{-1}\,K^{-1}}$
k_l	Thermal conductivity perpendicular to wire orientation	$\mathrm{W\,m^{-1}\,K^{-1}}$
k_{rad}	Radial thermal conductivity	$\mathrm{W\,m^{-1}\,K^{-1}}$
k_{tan}	Tangential thermal conductivity	$\mathrm{W\,m^{-1}\,K^{-1}}$
M	Torque	Nm
M_B	Bearing friction torque	Nm
M_{ref}	Reference torque	Nm
$M_{windage}$	Windage torque	Nm
p	Pressure	Pa
P_{copper}	Copper losses	W
P_e	Eddy current losses	W
P_h	Hysteresis losses	W
q	Heat flux	$\mathrm{W\,m^{-2}}$
R^2	Coefficient of determination	-
T	Temperature	K
t	Time	s
$T_{air,in}$	CFD Air Inlet Temperature	K
T_{in}	Averaged inlet temperature	K
$T_{max,B}$	Peak Benchmark CFD Winding Temperature	K
T_{ref}	Reference temperature	K
T_{wall}	Wall Temperature	K
u, v, w	Velocity components in x, y, z-direction	$\mathrm{m\,s^{-1}}$
u_T	Friction velocity	$\mathrm{m\,s^{-1}}$

V	Voltage	V
v	Velocity	$\mathrm{m\,s^{-1}}$

Chapter 1

Introduction

1.1 Background

In 2016, over 96 % of the net electricity generated in the EU was produced by electrical generators [1]. 48.7 % of the net EU electricity was produced by generators driven through the combustion of fuels such as coal, oil and natural gas [1] in large power plants. As burning fossil fuels emits carbon dioxide (CO_2), a main contributor to climate change, highly efficient generators are crucial to reduce the ecological impact of electricity production. An additional upside of improving generator efficiency are decreased costs of electricity generation resulting in direct savings for industry and individuals. While large machines are used predominantly in power plants, small electrical machines are used in a wide variety of applications. Motor-driven systems use 65-70 % of all electricity consumed in industry in the EU [2], meaning there is huge potential for electricity savings by improving electrical motor efficiency.

The energy generation sector currently undergoes a major step change. Driven by the requirement to reduce CO_2 emissions, the proportion of electricity generated by renewable energy sources such as wind, hydro and solar power, has increased substantially in recent years. The net electricity generated from renewable sources in the EU increased from 13.6 % to 25.5% from 2006 to 2016. In 2018, the EU established a new renewable energy target of 32 % for 2030 [3] and many member states have set themselves more ambitious national targets. Except for photovoltaic cells, renewable energy sources still require generators to produce electricity, emphasising the importance of highly efficient generators.

The requirement to reduce CO_2 emissions also motivated a step change in the automotive industry, causing car manufacturers to invest into the electrification of cars. The United Kingdom set a target of every car and van being a zero emission vehicle by 2050 in 2015 and announced in 2017 that new conventional petrol and diesel cars will not be sold anymore by 2040 [4]. To meet such ambitious targets, highly power dense, robust and efficient electrical motors are required. The development of machines with a higher power density is currently limited, because excess heat cannot be removed efficiently. As thermal analysis did not have as much attention as the electromagnetic (EM) design of small and medium sized machines in the past [5], there is a great demand for research in this area.

One way to improve the efficiency of electrical machines is by improving their cooling. In most machines, the majority of losses occur in the windings. As the winding resistance, and hence the copper losses occuring within the windings, increases with temperature, improving the thermal management of an electrical machine increases its efficiency. Improving the thermal management also extends the machine lifetime. Windings are covered in electrically insulating resin and varnish layers, whose rate of ageing is directly related to its temperature. As a a rule of thumb, a 10° C decrease in peak temperature will double the machine lifetime [6].

The interdependency of thermal and electromagnetic performance makes an optimal design of electrical machines challenging. Design features, which are beneficial from a thermal perspective, are often disadvantageous for the EM performance and vice versa. To achieve an holistically optimal design, it is important to consider them both simultaneously, and as early in the design process as possible.

Depending on the machine application, different cooling fluids are employed. If a high power density is required, liquid cooling using water or oil is generally used due to their higher heat capacity in comparison to gases. Evaporative or jet cooling can be implemented, improving the heat extraction even further. While these methods perform well from a thermal point of view, they are complex to design, expensive to manufacture and operate, and often less robust. If power density is not a priority, air is most commonly utilised as a cooling fluid.

In larger, air-cooled machines, it is common to add radial vent airgaps between the stator laminations to pass cooling air between the stator-casing cooling channel and the airgap. This brings the convective cooling air closer to the heat sources. Designing the placement, sizing and number of these vents is a highly complex and inter-disciplinary engineering problem, as a different split of air flow through the machine can cause a change in both the temperature and loss distribution.

1.2 Aim and Objectives

1.2.1 Aim

Within this project, the growing demand for holistic design approaches of electrical machines is addressed. Focussing on improving the thermal design, a new methodology for the simultaneous optimisation of multiple design parameters is developed. This methodology can be implemented in the early machine design stage allowing right-first-time design. Despite the focus on the thermal performance, the impact the design changes have on the electromagnetic performance is taken into account and fed back to the thermal optimisation process. This approach allows for an optimal design considering the thermal as well as the electromagnetic performance.

The methodology is developed by adding multiple radial stator vents to an air-cooled synchronous generator and optimising five vent design parameters. As the machine's peak temperature is located in the stator windings, improving the stator cooling increases the machine lifetime and efficiency. Alternatively, the power output can be increased for a given temperature limit, boosting the machine power density.

The air flow and heat transfer in the machine core is highly complex and changes considerably depending on the vent locations, widths and other vent design parameters. Therefore accurate numerical modelling techniques are required to predict it correctly. To date, Computational Fluid Dynamics (CFD) is the only modelling approach capable of solving turbulent fluid flow, convective and conductive heat transfer simultaneously. Hence, it was utilised for the modelling in this thesis. The novelty in this thesis lies in the development of an automated optimisation procedure considering convective and conductive heat transfer, as well as electromagnetic effects, on the overall machine performance.

The developed computational modelling approach is applied in conjunction with experimental validation to reduce the peak and average stator winding temperatures of the investigated generator.

1.2.2 Objectives

The objectives identified for this thesis are:

1. Creation of a Conjugate Heat Transfer (CHT) CFD model of the current machine design.
2. Experimental validation of the CFD model created in objective 1.
3. Creation of a fully parametric CHT CFD model including multiple radial stator vents based on the validated model created in objective 1. The model must be capable of investigating different machine configurations automatically without requiring additional user input after the initial setup and consider the change in electromagnetic loss distribution resulting from venting the stator.
4. Optimisation of multiple vent design parameters with the aim of minimising the peak stator winding temperature.
5. Experimental validation of the optimal configuration determined in objective 4.

1.3 Machine under investigation

The investigated machine is a 4-pole, air-cooled, synchronous generator with a power rating of several hundred kVA used for continuous industrial power generation (view figures 1.1 and 1.2). It is manufactured by Cummins Generator Technologies (CGT).

As typical for synchronous generators, three-phase armature windings are located in the stator [6]. The rotor is equipped with a single-phase field winding. Supplying a direct current to the rotor windings and rotating the rotor at synchronous speed (1500 RPM for a 4-pole rotor), produces a rotating magnetic field, which induces a voltage in the stator windings. The rotor current is supplied by brushless excitation using an exciter. The exciter is an outer pole synchronous generator whose field windings are located in the stator. Rotation induces a 3-phase AC current in the exciter rotor, which is converted to DC current by a rectifier mounted on the shaft. The DC current is supplied to the main rotor, producing the magnetic field.

Cooling air enters the machine through two inlets located on the Non-Drive-End (NDE) of the machine and exits through four outlets located on the Drive-End (DE) as shown in figure 1.1. Air is driven through the machine by a centrifugal fan located on the generator DE. Figure 1.2 shows a schematic of the investigated machine with all the major parts being

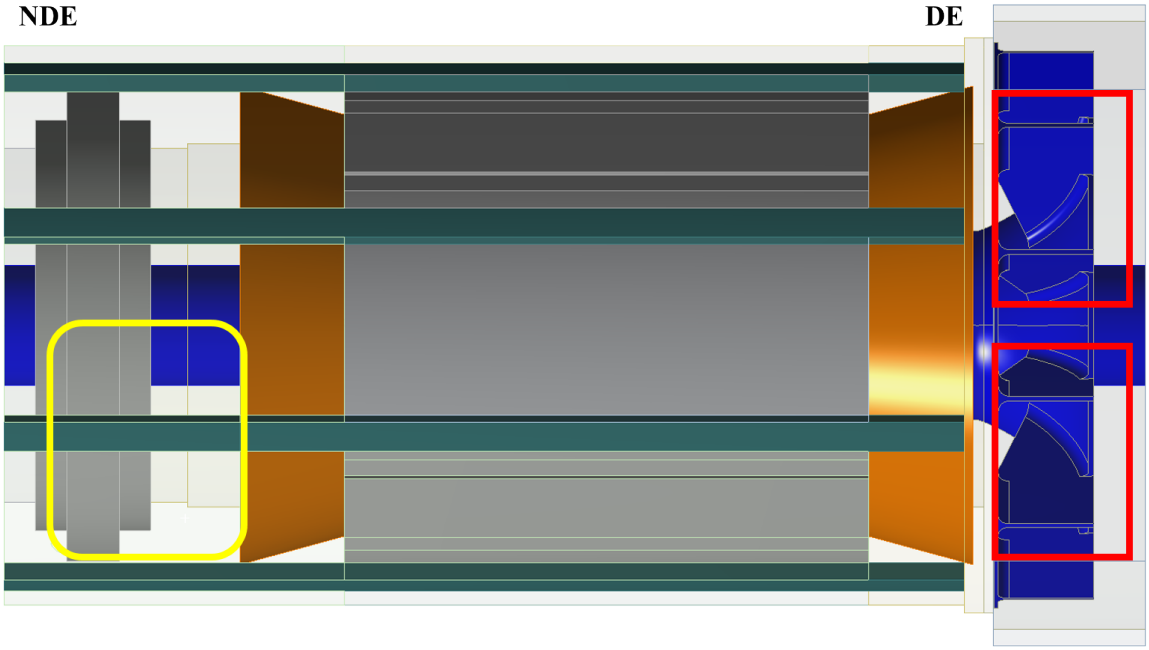


Fig. 1.1 Schematic of the investigated generator showing the inlet (yellow) and outlet (red) locations

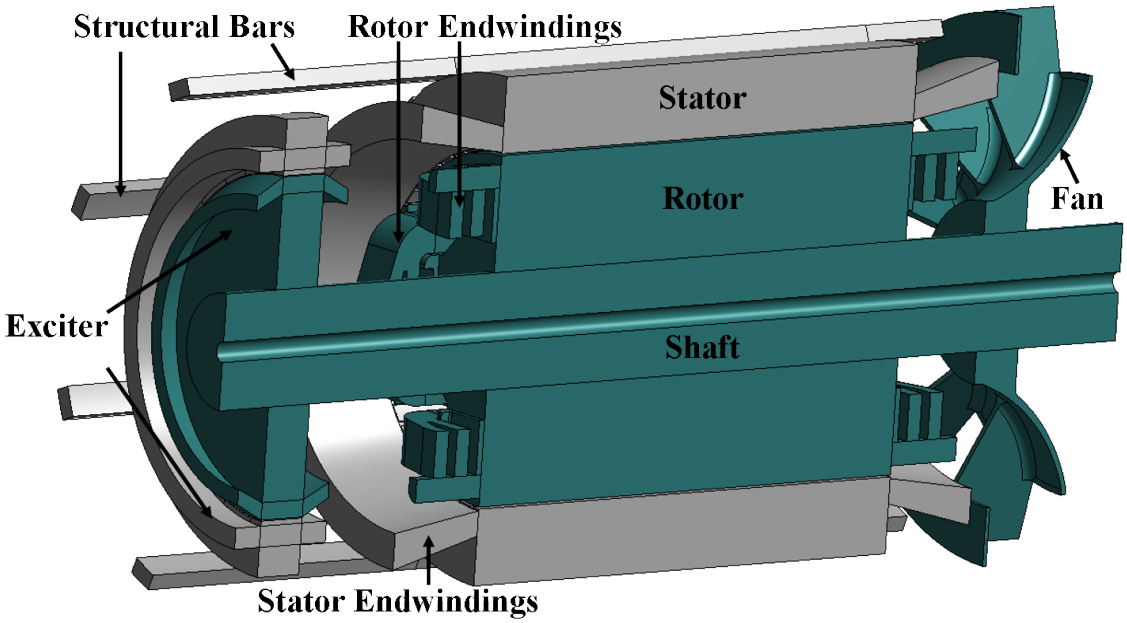


Fig. 1.2 180° schematic of the investigated machine; only solid parts shown; casing not displayed

labelled. For better visibility, only 180° of the machine geometry is shown and the casing is not displayed.

The rating of the electrical insulation system according to the National Electrical Manufacturers Association (NEMA) is class H, allowing for a peak temperature of 180 °C based upon a reference ambient temperature of 40 °C [7].

The standard configuration of the investigated machine is referred to as the "Benchmark Machine" (BM) throughout this thesis. Local temperatures, windage, efficiency, etc. vary between various machines of the same type due to manufacturing uncertainties. Hence the term Benchmark Machine refers to the specific machine that was investigated in the University of Nottingham (UoN) test facility by the author of this thesis. The newly designed, vented machine is referred to as the "Vented Prototype" (VP). Due to the same manufacturing uncertainties, this term refers to the specific Vented Prototype machine investigated in the UoN test facilities.

1.4 Thesis structure

This thesis is structured as follows:

- Chapter 1 introduces the project and the investigated machine.
- Chapter 2 reviews the literature concerned with the thermal management of electrical machines, focussing on CFD investigations and experimental testing techniques. Special attention is paid to multi-physics modelling approaches, thermal optimisation procedures and work related to stator vents.
- Chapter 3 gives a general introduction into CFD and its utilisation for the thermal analysis of electrical machines. The state-of-the-art CFD methodology applied and the novel methodologies developed within this project are presented.
- Chapter 4 describes the experimental test facility and the setup of the test rig used for validation. Its design, the used equipment and the conducted tests are described in detail.
- Chapter 5 covers the experimental validation of the Benchmark Machine. CFD and experimental test results are presented, analysed and compared to each other and the reasons for differences between computational and experimental results are discussed.
- Chapter 6 presents the novel methodology for the simultaneous optimisation of multiple design parameters developed within this project. It discusses the setup and results of

the optimisation procedure as well as the influence of the optimised design parameters on the thermal and electromagnetic performance of the machine.

- Chapter 7 discusses the experimental validation of the Vented Prototype. CFD and experimental test results of the Vented Prototype are presented, analysed and compared to each other and the reasons for differences between computational and experimental results are discussed. The experimental results of the Vented Prototype are compared to the results of the Benchmark Machine, highlighting the improved thermal performance.
- Chapter 8 presents the drawn conclusions and identifies future work building on this thesis.

Figure 1.3 summarises the work conducted in this project in chronological order from top to bottom.

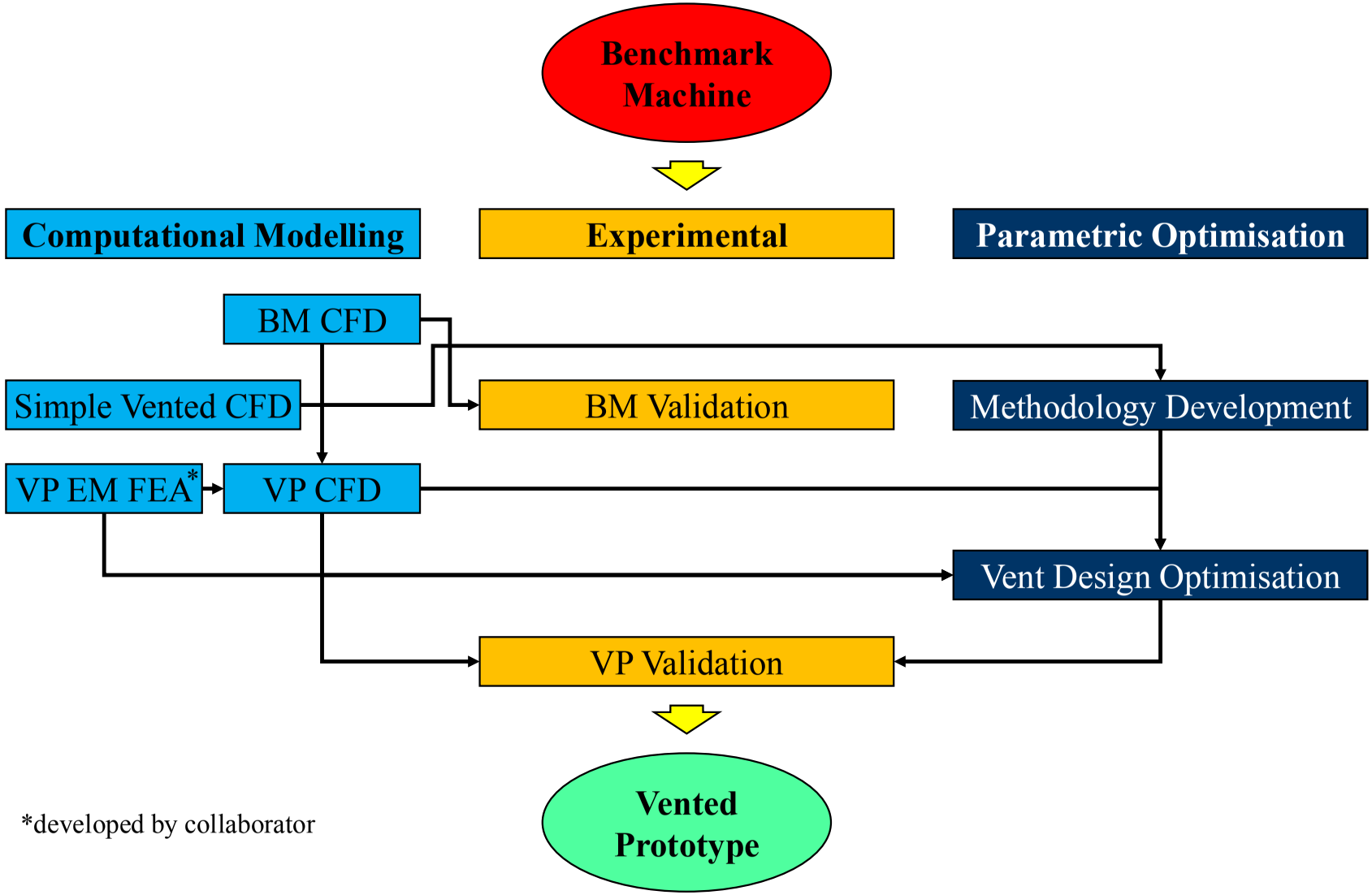


Fig. 1.3 Project overview

Chapter 2

Literature Review

To ensure a safe and efficient operation of electrical machines it is essential to cool them appropriately. The maximum temperature of an electrical machine is determined by the class of the insulation material [7], which typically degrade above a temperature of 130-180° C. A 10° C rise in temperature will half the machine lifetime [6]. Furthermore, the resistance of the windings and thus the induced copper losses increase with rising temperature. A temperature rise of 50° C above ambient increases the resistance by 20 % [6]. A well designed ventilation system can improve efficiency, power density and reliability, hence reducing operating costs as well as the ecological impact.

Traditionally, designers of electrical machines focussed on improving the electromagnetic properties while neglecting the thermal design of said machines [5]. In recent years however, the increasing demand for smaller and more efficient machines has led to a requirement for more accurate consideration of their thermal aspects and hence an increase in research in this area. A number of thermal modelling techniques with different levels of accuracy and computational demand have been developed and validated with experimental studies, ranging from analytical approaches [8, 9] to Finite Element Analysis [10] and Computational Fluid Dynamics [11–14].

This literature review focusses on the research that has been carried out in the area of thermal design of electrical machines using CFD and its experimental validation. Special attention is paid to work relating to stator vents.

2.1 Losses and Efficiency

The purpose of electrical machines is the conversion of mechanical energy to electrical energy (generators) or vice versa (motors). Whilst the conversion efficiency is generally high ($\geq 90\,\%$), there are various loss mechanisms which cannot be avoided completely.

2.1.1 Copper losses

Copper losses, also known as Joule losses or "I^2R" losses, are the main loss contributor in most electrical machines. They are caused by Joule heating, which occurs when current flows through a conductor. They can be calculated from the current flowing through a conductor I and the conductor resistance R according to the following equation [6]:

$$P_{copper} = I^2 R \tag{2.1}$$

Copper losses occur in the stator and rotor windings and are temperature dependent, as the copper winding resistance R_{copper} increases with temperature. In the temperature range occuring in the investigated machine the resistance increases linearly with temperature according to equation 2.2 [15]:

$$R_{copper} = R_0(1 + \alpha_0(T_{copper} - T_0)) \tag{2.2}$$

with T_{copper} being the winding temperature, R_0 the winding resistance at temperature T_0 and α_0 the winding temperature coefficient of resistance at T_0. For pure copper at $20\,^{\circ}\mathrm{C}$, α_0 amounts to $0.393\,\%\,^{\circ}\mathrm{C}^{-1}$. Thus, the copper losses increase by approximately $4\,\%$ for a $10\,^{\circ}\mathrm{C}$ increase in temperature. As the copper losses are often the biggest loss contributor and their location makes heat removal difficult, machine hot spots can often be found in the windings and appropriate winding cooling is essential. In the Benchmark Machine, the stator copper losses amount to $37.6\,\%$ of the total losses at full load and 0.8 power factor, while the rotor copper losses make up $23.3\,\%$.

2.1.2 Iron losses

Iron losses occur in the rotor and stator laminations. According to Steinmetz [16, 17], the iron losses can be divided into two separate loss mechanims: Hysteresis and eddy current losses. Hysteresis losses (P_h) occur when a magnetic material is excited by a varying magnetic field and can be calculated from the excitation field frequency f and the maximum flux density B_m according to equation 2.3 [6]:

$$P_h = K_h f B_m^n \tag{2.3}$$

with K_h and n being material dependent constants. The alternating magnetic field induces an electromagnetic force in the core iron, which produces a current flowing through the iron core. This current is subject to Joule heating, producing a loss component which is known as the eddy current P_e loss and can be calculated according to equation 2.4 [6]:

$$P_e = K_e f^2 B_m^2 t^2 \tag{2.4}$$

with t being the material thickness and K_e a material dependent constant. The eddy current losses increase with the square of the material thickness. To reduce them, rotor and stator cores are usually built from steel laminations separated by thin insulating resin layers. Hysteresis and eddy current losses are converted into heat in the rotor and stator laminations. In the Benchmark Machine, the combined rotor and stator iron losses amount to 19.9 % of the total losses. It is not possible to experimentally measure the iron losses separately in the rotor and stator, hence electromagnetic Finite Element Analysis (FEA) is required to determine the iron loss split.

2.1.3 Mechanical losses

Mechanical losses are caused by two mechanisms. The first is the resistance of the surrounding air to rotating components within the machine, also known as windage. It is caused by viscous effects and pressure acting on the rotating parts. In the investigated machine, the majority of the windage losses are caused by pressure effects in the fan (view section 5.2), which do not contribute to heat generation within the machine. The second mechanical loss is caused by friction in the bearings. The friction and windage losses amount to 6.7, % of the total losses in the Benchmark Machine.

2.1.4 Stray losses

Additional losses, which cannot be attributed to any of the above loss mechanisms, are designated as stray losses. According to B.S. EN 60034-2-1:2014, they are defined as the difference between the mechanical input power and the sum of friction, windage and copper losses determined from a short-circuit test [18]. They amount to 10.1 % of the total losses in the Benchmark Machine.

2.2 Computational Modelling Techniques

The computational modelling techniques most commonly used for the thermal analysis of electrical machines are presented in this section.

2.2.1 Lumped Parameter Thermal Networks

Lumped Parameter Thermal Network (LPTN) modelling is an analytical lumped circuit approach analogous to electrical network modelling. Heat transfer within an electrical machine is calculated by dividing it into components of similar temperatures and defining thermal resistances considering convection, conduction and radiation for every node [5]. It is the most established thermal computational modelling technique and has widely been used for the analysis of electrical machines [5, 8, 9, 19–21]. LPTN can be coupled with Lumped Parameter Flow Network analysis to calculate convective heat transfer coefficients (HTC) based on empirical correlations. Flow Networks use empirical, dimensionless formulations to determine pressure drop and local flow velocities [22].

The biggest advantages of this modelling approach are fast computation times and the relatively simple model setup. LPTN modelling allows for many different configurations being simulated in a short time frame, which is particularly valuable during the early design stages. However, it requires accurate predictions of local heat transfer coefficients to achieve realistic results. Whilst a multitude of validated correlations exists for simple geometries, they have to be determined from experiments or simulations using numerical modelling techniques for complex geometries. In [9, 23, 24], Computational Fluid Dynamics (CFD) is used to calibrate the LPTN models. In [25], experimental testing is used for the calibration instead. Additionally, many of the complex thermal phenomena cannot be predicted by

a purely analytical approach and require user experience to calibrate the model correctly [5, 26].

Motor-CAD is the most commonly used commercial LPTN software for the analysis of electrical machines [27]. It requires the user to choose from a variety of frequently used geometries and materials using a graphical interface. Thermal resistances and the overall thermal performance are then calculated automatically using analytical correlations [22].

2.2.2 Finite Element Analysis

Finite Element Analysis (FEA) is a numerical modelling approach that is widely used for the electromagnetic analysis of electrical machines. It can also be used to model the conductive heat transfer through solid parts. Many FEA-packages for EM analysis offer the user the possibility to perform a thermal analysis as well. FEA is commonly used to determine conductive heat transfer in complex geometries inside an electrical machine that cannot be modelled adequately by a lumped parameter approach [5].

Equivalent to Thermal Network modelling, FE modelling requires accurate local heat transfer coefficients as input parameters, as it is not capable of determining the convective surface heat transfer. In [10], a 5 kW permanent magnet servo motor is investigated via transient thermal FEA. CFD was used to calculate the convective HTC. A similiar approach was taken in [28], where CFD was used to calculate the flow field around a 200 kW asynchronous motor. The local velocities were subsequently used as input parameters for a coupled thermal and electromagnetic FEA.

While FEA enables accurate conduction modelling in complex geometries, it is not well suited to predict heat transfer in machines in which the cooling is dominated by convective heat transfer. This is particularly true for novel and complex cooling designs, for which convective HTC cannot be determined easily from literature.

2.2.3 Computational Fluid Dynamics

CFD is the most holistic modelling approach for the thermal analysis of electrical machines. A physical domain is divided into a number of control volumes and the governing equations of fluid flow and energy are integrated over all cells. The integral equations are converted into a system of algebraic equations by discretisation and solved using an iterative method [29]. Flow velocities, pressure, temperature and many more fluid properties are determined

in every cell allowing an accurate prediction of local convective heat transfer even in complex geometries. Conduction through solid parts can be solved simultaneously in a Conjugate Heat Transfer (CHT) model.

The wealth of information that can be extracted from a CFD model comes at a price though. CFD is a computationally expensive technique requiring simulation times several magnitudes higher than those required for analytical models such as LTPN. Furthermore, the meshing and model setup require a considerable amount of time and user experience [5, 29]. A significant challenge lies in creating a mesh that is sufficiently refined to capture the physical behaviour correctly, while keeping the cell count to a manageable size. Identifying and removing geometrical features that have a negligible influence on the thermal performance (e.g. bolts and minor fillets) is an important step to reduce the model size.

Due to the high computational cost, the use of CFD for the thermal analysis of electrical machines was not practicable until about 25 years ago. Some of the earliest investigations using CFD in this area were carried out at the University of Nottingham. Pickering *et al.* [30] modelled the end region of a totally enclosed fan cooled (TEFC) induction motor to ascertain the usefulness of CFD as a design tool. Their results were validated with detailed flow velocity and heat transfer measurements. Whilst they found good agreement overall, heat transfer coefficients were underpredicted by up to 30 %. The use of the Multiple Reference Frame (MRF) method, which time-averages the emerging unsteady flow, was identified as the main reason causing the difference. Shanel [11] confirmed this assumption and observed HTC to be up to 20 % lower using the MRF method in comparison to the transient Sliding Mesh (SM) approach.

As many electrical machines are rotationally periodic, it is common to model only a periodical sector to decrease the computational effort [11, 30, 31]. Furthermore, it is often necessary to focus on a sub-geometry of particular interest (e.g. endwindings, airgap) instead of modelling the whole machine to afford a sufficient local resolution [12, 32]. The validity of a submodel is dependent on accurate boundary conditions, which can be difficult to determine due to the complicated flow field occuring in electrical machines. In 2014, Connor [13] proved the feasibility of modelling a complete machine using a 360° CFD Conjugate Heat Transfer model. The machine investigated in his work is similar to the generator under investigation in this thesis.

The choice of an appropriate turbulence model is an important aspect of any CFD simulation. The standard k-ε model is most commonly used for radial flux machines [11–14, 30, 32], due to its robustness and the possibility to use wall functions instead of having to resolve the

boundary layer for all walls. Whilst it is generally considered not to be accurate in strongly rotating flows, Pickering [33] found it to give almost identical results to the RNG k-ε and k-ω model while converging twice respectively five times as fast. Howey [34] compared the stator Nusselt number of an axial flux machine using the standard k-ε, SST and baseline Reynolds Stress Model and found the results to be independent of the chosen turbulence model as well. Shanel [11] observed the average rotor HTC using the standard k-ε model to be 30 % higher in comparison to the Reynolds Stress and RNG k-ε Model. He decided to use the standard k-ε model anyway as it showed the best convergence and balanced the HTC underprediction resulting from using the MRF method.

La Rocca [35] used a combination of analytical and numerical modelling techniques to analyse the heat transfer and optimise the cooling design of a liquid cooled high speed aero-engine starter/generator with a nominal power rating of 45 kW and a maximum speed of 32000 RPM. LPTN were created in MotorCAD to investigate the thermal behaviour of initial machine designs. Conjugate Heat Transfer CFD models were used to predict the airflow and thermal performance in critical areas, such as the end regions, the axial ducts and the airgap. Additionally, the CFD models were used to adjust the LPTN and improve their accuracy. The heat transfer in the bearing chambers was investigated via LPTN developed in Simulink.

Using CFD for the thermal optimisation of electrical machines has become more and more popular in recent years due to the demand for an accurate prediction of the thermal performance and advancements in computing power. The CFD modelling undertaken in this project is based on the previous work identified in this section and section 2.5.

2.2.4 Multi-Physics Modelling

Due to to the strong interdependence of electromagnetic and thermal performance in electrical machines it is desirable to model them simultaneously. Most multi-physics models to date use LPTN for the thermal analysis. The electromagnetic performance is often determined using a lumped parameter approach as well [20, 21, 25], though some authors prefer to use the more accurate 2-D FEM [36]. The models are coupled by using the temperatures calculated in the thermal model as an input for the electromagnetic model, which calculates the temperature dependent heat losses to be fed back to the thermal model. This process is repeated until convergence is reached. As the time constant of the thermal model is much larger than the electromagnetic time constant, computation time can be reduced by updating the EM model only if the change in resistivity resulting from a temperature change is significant [36].

The use of CFD for multi-physics analysis is not as common due to its high computational costs and issues with coupling it to an electromagnetic solver. Slupik *et al.* [14] used ANSYS Fluent, a commercial CFD solver, for the thermal analysis of a small 240 W DC motor. The copper and iron losses were calculated using SPEED, an analytical electromagnetical modelling software. No details are given on how the two models were coupled. Deeb [10] used ANSYS Maxwell for 2D and 3D electromagnetic FEA and the transient thermal solver within ANSYS Workbench for the thermal analysis of a 5 kW permanent magnet servo motor. ANSYS CFX was used to determine the convective HTC required as input parameters for the thermal FEA. Multiple cooling channel dimensions were optimised using a Goal Driven Optimization. Zhang *et al.* [28] used CFD to calculate the flow field around a 200 kW asynchronous motor. The local velocities were used as input parameters for a coupled thermal and electromagnetic 3D-FEA. The CFD model was highly simplified for computational reasons, e.g. the motor endwindings were not modelled.

2.2.5 Design Optimisation

Automated optimisation procedures are commonly used to optimise the electromagnetic design of electrical machines using 2-D FEA [37–39]. The high robustness of the automatic mesh generator and short computation times enable the investigation of many different designs. [40] reviews recent developments and future trends in the area of electrical machine design optimisation.

A " Special Section on Optimization of Electric Machine Designs" has recently been published in the IEEE Transactions of Industrial Electronics [41, 42]. It consists of 44 papers illustrating the current state of the art, latest advances and future trends of using optimisation procedures for the design of electrical machines.

For the thermal modelling, especially in multi-physics optimisations, LPTN are typically used due to their low computational cost, such as in [43]. But the use of thermal FEA has become more common lately. In [44], a thermal 2-D FE model is used to model conduction in a TEFC machine and optimise its fin design. The convective boundary conditions were determined by analytical equations. 10 configurations were investigated using a simplified 3-D CHT CFD model afterwards. The fan was not modelled and the volumetric air flow rate at the inlet was kept constant for all cases. Temperatures were found to be underpredicted using the 2-D FE model, but the temperature trend was consistent between the two modelling approaches.

In [45], the electromagnetic and thermal design of an asynchronous induction machine is optimised with the aim of minimising magnetic current, rotor and stator temperatures. 2-D EM FEA is used to calculate the magnetising current and power losses. The calculated power losses are implemented into a thermal 3-D FE model, which predicts the temperature distribution inside the machine. The convective heat transfer coefficients required for the thermal model were calculated using an analytical flow network.

2.3 Correlations based on simple Geometries

Convective heat transfer coefficients are often calculated using correlations based on simple geometries such as concentric rotating cylinders as they are widely available and well validated. These correlations are also useful to get an idea of the expected magnitude of various parameters and, depending on the geometric similarity, for a first validation of CFD models. When using these correlations, care must be taken that they are applicable to the case in question. Non-dimensional parameters for fluid flow (e.g. Reynolds number), heat transfer (e.g. Nusselt number) and geometry (e.g. gap ratio) must match the range the correlations were derived from. The non-dimensional numbers used for correlations are defined and explained in this section.

The Reynolds number is the ratio between inertial and viscous forces within a fluid. It is named after Osbourne Reynolds [46], who discovered that the characteristics of the flow of water through a circular pipe depend on the flow rate. It is defined as:

$$Re = \frac{\rho v L}{\mu} \tag{2.5}$$

with ρ being the fluid density, μ the kinematic viscosity, v the characteristic velocity and L the characteristic length. The definition of v and L depends on the flow application. For example, for flow through a circular pipe, L is the pipe diameter and v is defined as the mean flow velocity in the pipe. Definitions for various applications used in this thesis can be found in the nomenclature. There are three distinct flow regions, which can be characterised as follows:

- **Laminar:** Laminar flow is steady with no mixing between adjacent fluid layers.
- **Transition:** In the transitional region, turbulent flow characteristics start to appear locally.

- **Fully turbulent:** Fully turbulent flow is characterised by velocity and pressure oscillations and the emergence of vortices, resulting in good mixing of the fluid.

The Nusselt number is the ratio of convective heat transfer resulting from the fluid motion, to conductive heat transfer, which can be observed if the fluid is stagnant. It is defined as:

$$Nu = \frac{hL}{k} \tag{2.6}$$

with h being the convective heat transfer coefficient, L the characteristic length and k the thermal conductivity of the fluid.

Couette [47] investigated concentric rotating cylinders and observed that the torque required to rotate the inner cylinder (with the outer cylinder being stationary) rises linearly with the rotation speed ω until it reaches a critical rotation speed ω_c. From this point on the torque increases faster than before. Taylor [48] showed that the torque increase is caused by a change in flow behaviour. For $\omega < \omega_c$, the flow is laminar. For $\omega > \omega_c$, instabilities called Taylor vortices appear (view figure 2.1). In addition to the rotational speed, the appearance of Taylor vortices depends on geometrical features and fluid viscosity, which led to the definition of the non-dimensional Taylor number Ta. For concentric cylinders it is defined as:

$$Ta = \frac{4\omega R_i (R_o - R_i)^3}{\nu^2} \tag{2.7}$$

with R_i being the radius of the inner cylinder, R_o the radius of the outer cylinder and ν the kinematic viscosity.

Daily and Nece [49, 50] investigated a smooth disk rotating inside a cylindrical chamber filled with water and identified four different flow regimes: Laminar flow with merged boundary layers, laminar flow with separate boundary layers, turbulent flow with merged and turbulent flow with separate boundary layers. They defined a torque coefficient

$$C_m = \frac{2M}{\rho \omega^2 R^5} \tag{2.8}$$

with M being the torque on both faces of the disk and found C_m to be a function of rotating Reynolds number Re_r, axial gap width s and the surface roughness. They determined correlations for each of the flow regimes. For smooth cylinders and turbulent flow with merged boundary layers, as it appears in the airgap of most electrical machines, they proposed

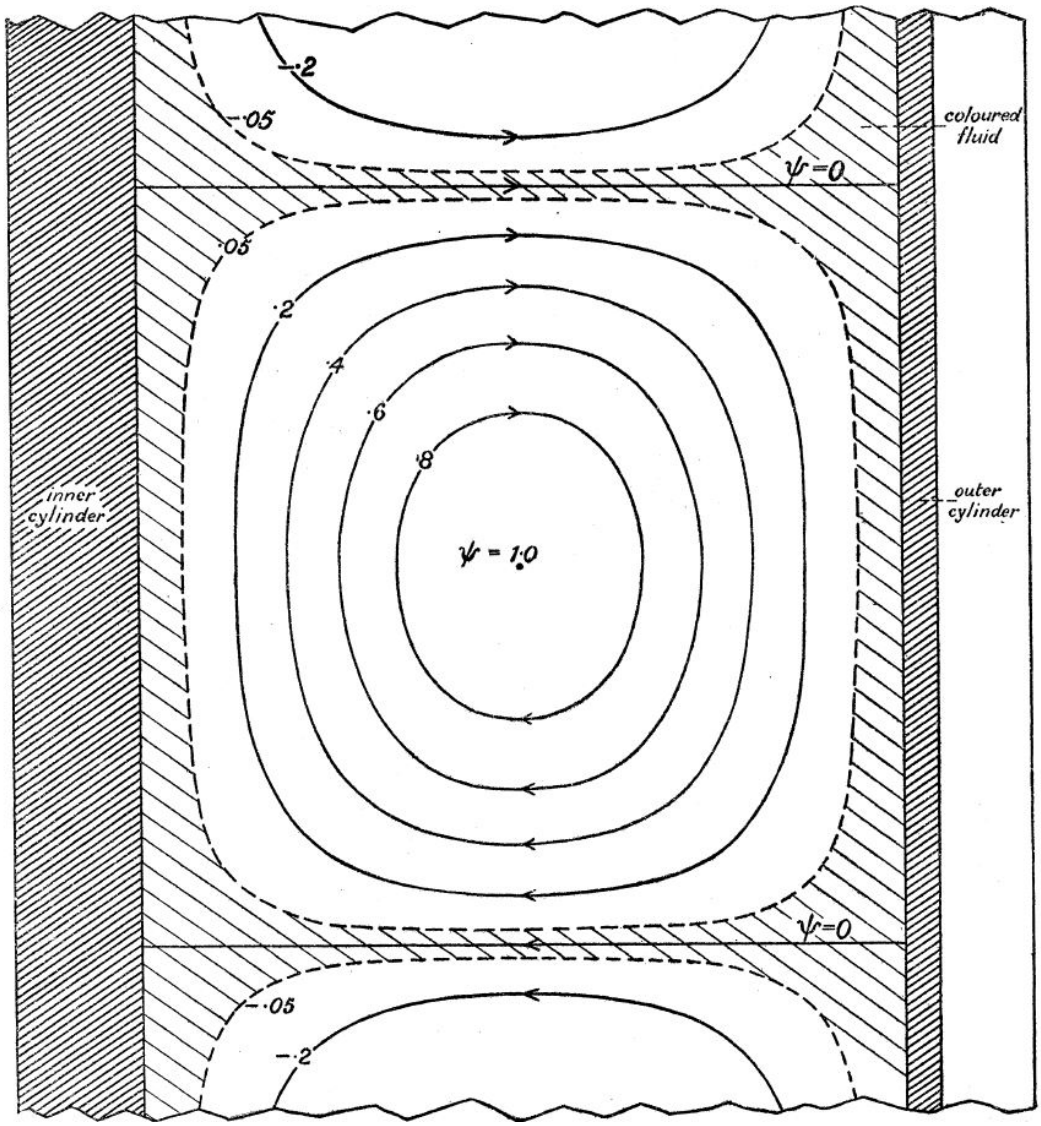


Fig. 2.1 Taylor vortices for co-rotating cylinders [48]

the following correlation:

$$C_m = \frac{0.080}{(s/R)^{\frac{1}{6}} Re_r^{\frac{1}{4}}} \tag{2.9}$$

Several authors (e.g. [51, 52]) measured the heat transfer in the annular gap between a rotating inner and a stationary outer cylinder without superimposed axial flow and found correlations between Nusselt number and Taylor number of the form

$$Nu = C \cdot Ta^n \qquad C, n = const \tag{2.10}$$

for Taylor vortex and turbulent flow ($Ta > Ta_c$).

Fénot *et al.* [53] investigated the local convective heat transfer of a 4-pole cylinder rotating inside of a smooth stator (view figure 2.2) over a range of axial and rotational Reynolds numbers. Geometry and Reynolds numbers are similar to the ones examined in this project. The rotor and stator surfaces were electrically heated through thin copper foils linked to a DC supply. Rotor and stator surface temperatures were measured using infrared (IR) thermography through four IR windows that were drilled into the stator. The heat transfer coefficients were defined using the average air temperature in the rotor-stator gap as a reference temperature. The local rotor and stator Nusselt numbers were found to decrease with the axial length until they reach a constant value at an axial length Y to hydraulic diameter D_h ratio of $\frac{Y}{D_h} = 25$. Rotor heat transfer was highest at the slot leading side, followed by the trailing side and lowest at the pole surface. Heat transfer increases with axial as well as rotational Reynolds number. They proposed correlations of the form of

$$\overline{Nu} = C \cdot Re_{eff}^{n} (\frac{Y}{D_h})^{m} \tag{2.11}$$

for all rotor and stator surfaces with R_{eff} being the effective Reynolds number and C, n, m being constants.

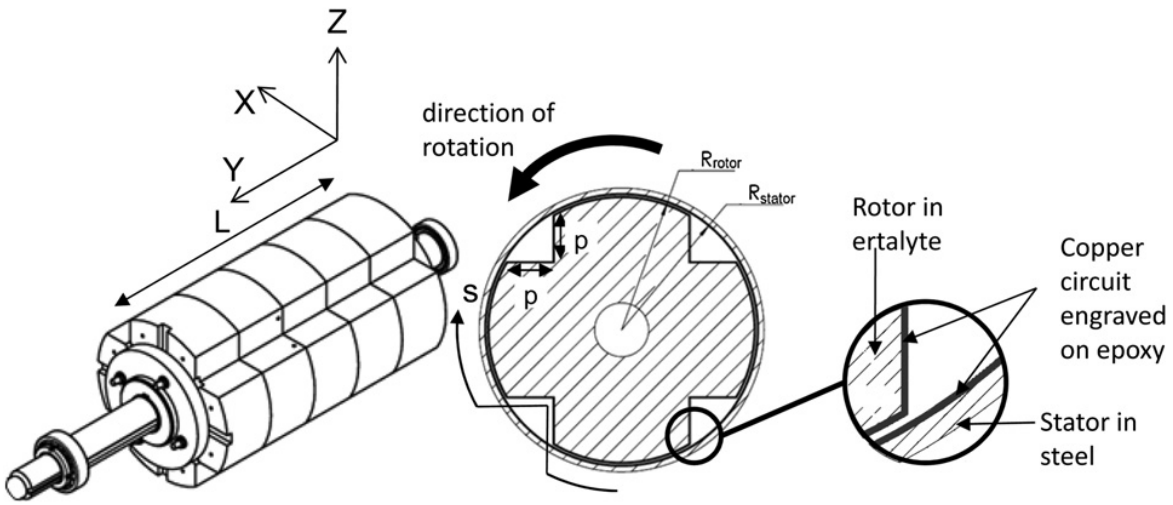


Fig. 2.2 Schematic of rotor investigated by Fénot *et al.* [53]

Fénot *et al.* [54] reviewed the research on flow and heat transfer in concentric rotating cylinders. The majority of research focussed on the simple case of a smooth cylindrical gap without throughflow (Taylor-Couette flow) and there is good agreement between different authors for this case. If axial throughflow is added (Taylour-Couette-Poiseuille flow) authors

arrive at contradicting conclusions, however. Fénot concludes that this is caused by the increase of influential parameters and identifies differing input conditions for the axial flow as the most likely cause for disparity. The disagreement in results is even more distinguished when slots are added to the rotor and/or stator as this results in an even larger number of influential parameters. This highlights the difficulty of choosing correct convective heat transfer coefficients for lumped parameter thermal modelling and the requirement to use numerical modelling techniques to determine them accurately.

2.4 Experimental Investigations

Experimental studies focussing on the thermal aspects of electrical machines have been conducted for more than 90 years. Some of the earliest studies have been carried out by Fechheimer [55, 56], who investigated the ventilation of large turbo alternators. Extensive measurements of volume flow and pressure were carried out using a model created of hardwood and steel. [55] focussed on the distribution of volume flow in axial and circumferential direction. In [56], structural independent variables were identified and their influence on the measured flow properties determined. Volume flows were measured using rotating vane anemometers. Pressures were determined by manometers. Heating caused by electromagnetic losses was not considered.

Taking measurements inside an electrical machine is a challenging task due to the difficulty of accessing zones of interest. Therefore, it is common practice to perform measurements on representative models instead of real machines [11, 32, 34, 55–58]. If the measurements are conducted for CFD validation, performing them on an experimental model can improve the consistency between numerical and experimental data. Features of a real machine that are ignored for the CFD model can be neglected in the experimental setup as well.

Due to the limited access to the inside of a generator, especially into tight spaces such as the airgap, holistic measurements are widely used for the CFD airflow validation. Commonly utilised measurements are the inlet mass flow or velocity [11, 13, 57, 58], outlet pressure [11, 13, 57, 59] and windage torque [11–13]. The most common technique for the thermal validation is the use of heat flux sensors and surface temperature measurements through thermocouples [11–13, 59]. As local bulk air temperatures are difficult to obtain many authors prefer to use the inlet air temperature as a reference temperature for the calculation of heat transfer coefficients instead [11, 13, 58, 59].

Two examples of experimental investigations are presented that are similar to the one undertaken in this project. Shanel [11] built a model of a 1 MVA 4-pole synchronous generator out of wood and aluminium filled resin coating. Instead of supplying cooling air via the shaft-mounted fans, an external fan was used to decouple the air mass flow from the rotational speed. The inlet mass flow was determined by pressure tappings on the conical inlet of the inlet duct. The stator was vented, and stator vent outlet velocities were measured with Pitot tubes attached to a traverse as shown in figure 2.3. The rotor losses were partly considered by implementing electrical heater pads at different locations on one pole. Stator losses were not considered. Surface heat fluxes and temperatures were measured using calibrated heat flux gauges. The reference air temperature for the calculation of HTC was measured by thermocouples. The measurement uncertainty of above mentioned values was determined to be up to 6 %.

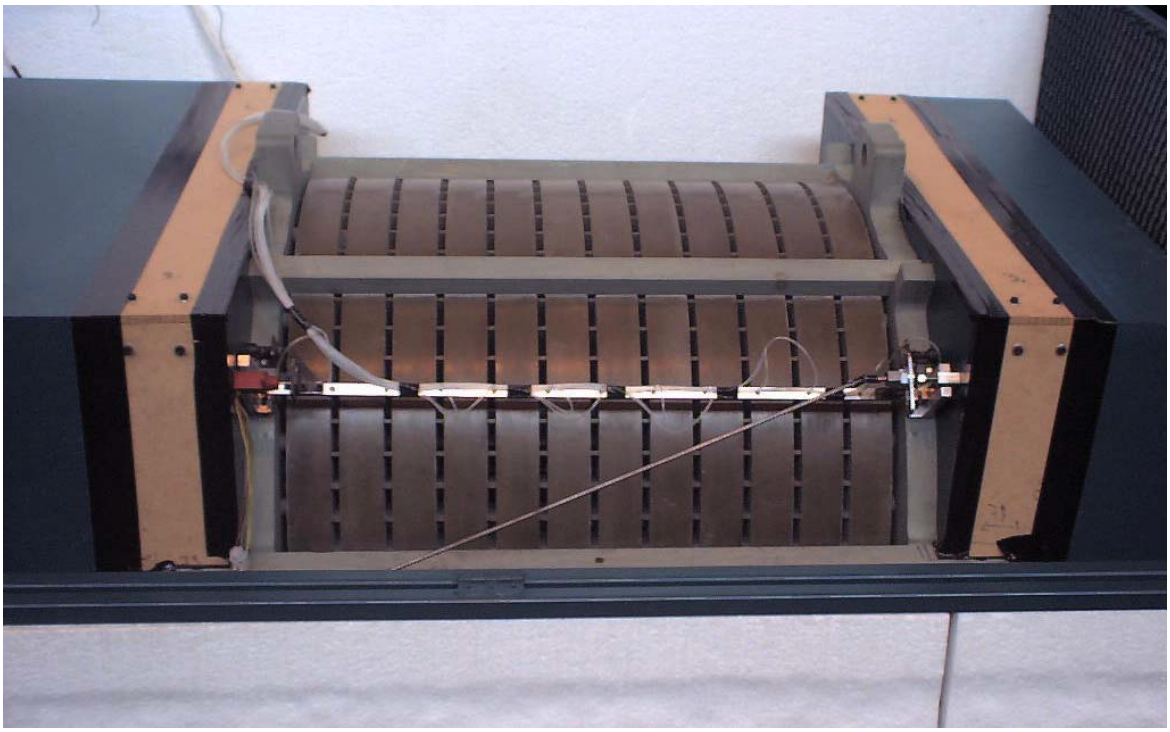


Fig. 2.3 Stator and attached traverse for stator vent outflow measurements [11]

Connor [13] used a similar approach as Shanel, but performed the measurements on a synchronous generator in the sub-250 kVA range instead of a model. Windage losses were determined using a torque transducer mounted axially between the drive motor and the investigated generator. As the bearing friction losses are included in this measurement, they had to be estimated and deducted. The generator was run at no-load to remove uncertainty

regarding windage due to power generation. Heat generation was incorporated by heating the stator windings with a DC supply. The uncertainty of the measured heat transfer coefficients was determined to be 20-30 %.

Jamshidi *et al.* [57] used an interesting and novel approach for their experimental measurements to overcome the problem of limited access to the machine core. Manufacturing transparent models allows the usage of modern measurement techniques such as Particle Image Velomicetry (PIV), which enable velocity measurements in tight spaces with limited accessibility. Jamshidi created a half-scale model of a hydrogenerator made from plexi-glass using a rapid prototyping method to allow optical experimental access. This enabled the use of PIV to take velocity measurements inside the stator vents. In addition to the PIV measurements, a 5-hole probe was used to measure the fan inlet velocity. The total pressure at the stator vent outlets was measured using a total pressure probe rake. The experiments were performed without heating the rotor or stator.

2.5 Stator Vents

Research focussing on stator vents in electrical machines has exclusively been carried out for machines with a power rating above the machine that is analysed in this project. It has traditionally not been considered beneficial to use stator vents in the sub-MW range. The design of these larger machines differs from the design of the investigated generator, but some of the findings are applicable nevertheless.

The entry to the stator vents was determined as the main reason for the pressure drop across a vented electrical machine by several authors [11, 60, 61]. Carew [60] determined the entry loss to be in the order of 50-70 % of the total pressure loss across a vent in salient pole machines. Other notable contributions to the total pressure loss of a machine are the interpolar entrance losses and the expansion losses inside the vent between the teeth and back iron region. Skin friction losses in the interpolar spaces only play a minor part. Carew proposed correlations for all the above mentioned losses and calculated the static pressure in the interpolar spaces and vent volume flows for a 1900 kVA machine. The results showed reasonable agreement with experimental measurements. No details were given on how the measurements were taken.

The aforementioned pressure loss caused by the sudden expansion of the vent between the teeth and back iron has been noticed by other authors as well [62, 63]. Küng *et al.* [62]

proposed to add diffuser wedges to the stator bars (view figure 2.4) to allow a smooth deceleration of the air passing through the vent, hence reducing the pressure loss. CFD calculations were performed to improve the cooling performance of self-ventilated induction motors in the 2-15 MW range. Additional modifications to improve the cooling performance were smoothing the inlet to the rotor axial bores, smoothing the cross-sectional shape of the rotor bars and reducing the inner radius of the stator gap supports. These modifications improved the coolant mass flow by 10 % and decreased the stator winding temperature by the same amount.

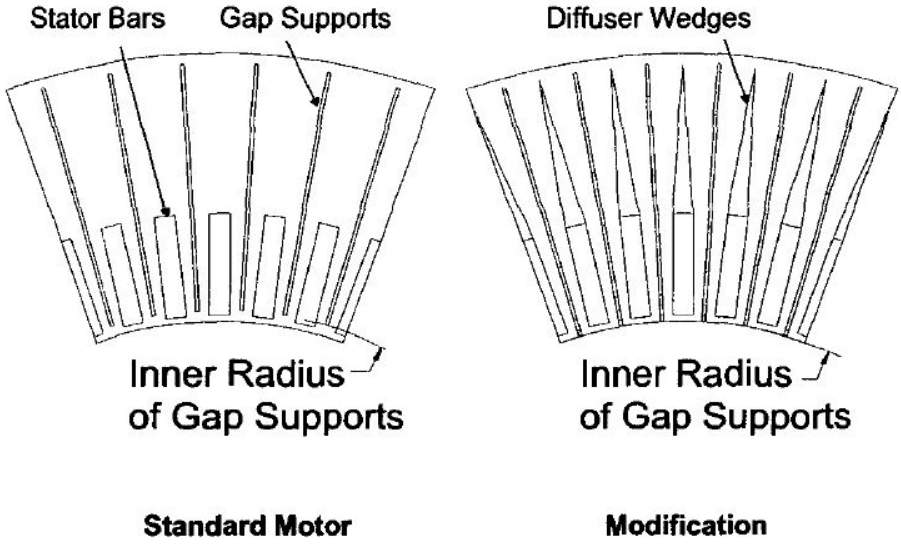


Fig. 2.4 Modification of stator bars by Küng *et al.* to reduce stator vent pressure loss [62]

Some work has focussed on stator vents in large hydrogenerators using CFD validated by experimental measurements [57, 61, 63, 64]. Hydrogenerators are low speed machines with large diameters [57]. They feature a short core length in relation to the diameter and a vertical axis of rotation. Altea and Yanagihara [61] modelled a single stator duct using ANSYS CFX and validated their results by comparing the pressure drop coefficient to experimental data published in previous work. As boundary conditions, radial and tangential velocities obtained from experiments were used at the inlet and a uniform pressure was specified at the outlet located 5 duct lengths downstream. Heating was not considered. They performed a grid independence study and estimated the uncertainty due to discretisation errors. The numerical results showed a maximum difference of 2 % from the experiment for the higher values of typical duct Reynolds numbers. For lower Re the difference reached up to 10 %. They concluded that the higher discrepancy at low Re is caused by the unsteadiness of the

inlet velocity over time due to the low rotational speed. The assumed homogeneity of the inlet velocities might be another aspect causing the difference.

Connor [65] performed a mesh sensitivity study using a Conjugate Heat Transfer CFD model of a synchronous generator containing multiple stator and rotor vents. Only the core region of the machine was modelled and the geometry was considered to be 45° periodic. Vent spacers were modelled as thin surfaces. The investigated geometry is typical for a synchronous generator in the MW-range. The influence of the airgap radial cell count, stator vent axial cell count, stator vent entry region radial cell count and rotor vent axial cell count on vent mass flow rates, heat transfer coefficients, local velocities and windage were investigated. Vent mass flow rates and velocities were found to vary by up to 55 %. Vent heat tranfer coefficients were found to vary by up to 128 %. The total windage varied by up to 7.5 %. Table 2.1 shows the investigated range of parameters and cell count required for mesh independence.

Table 2.1 Results of mesh sensitivity study in [65]

Cell Count	**Investigated Range**	**Mesh Independency**
Airgap radial	4-30	20
Stator vent axial	2-20	15
Stator vent entry region radial	2-20	15
Rotor vent axial	2-20	10

The axial stator vent cell count was found to be more influential further down the axial core length, as the flow profile is more developed at this point and affected more by rotational flow, and in regions where both stator and rotor vents are located. Local velocities in the stator vents were found to peak approximately 80 % along their axial width. For less than 15 axial cells across the vent, this behaviour is not captured correctly. Locations in the airgap which had interaction with both rotor and stator vents incorrectly predicted axial flow reversal for less than 15 radial cells across the airgap.

One of the few investigations taking heating into account was conducted by Schrittwieser *et al.* [63]. One pole of a large hydrogenerator was modelled using constant temperature wall boundary conditions. The average stator vent HTC was found to be independent of the near wall resolution for the k-ε turbulence model, while the SST model showed a variation of 10 %. Furthermore, the heat transfer on the slot leading side was noticed to be 33 % higher than on the trailing side (view figure 2.5). This is caused by the majority of the flow entering the vent from the airgap attaching to the leading side of the slot. The CFD results were not validated experimentally, however, as measurements in the stator ducts were considered to be unfeasible because the flow field and heat transfer would be affected by the measurement

devices in the stator duct channels. In addition, the small channel height of a few millimetres prevents a reliable installation of the measurement sensors.

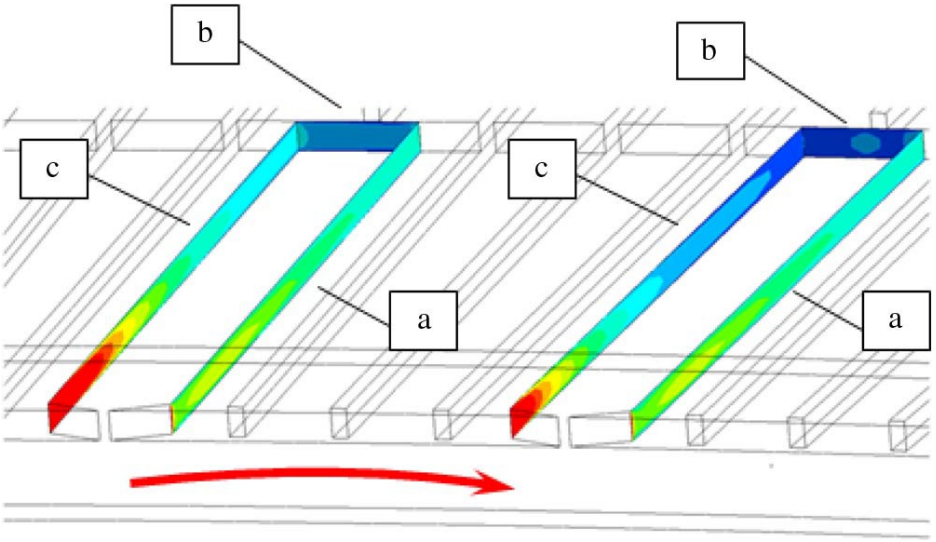


Fig. 2.5 Wall heat flux on the (a) slot trailing (b) slot bottom (c) slot leading side [63]; High heat flux on the leading side caused by impingement of rotating fluid shown in red

Fechheimer [56] observed large oscillations of the static pressure in stator vents caused by the rotor pole passing the vent entry and smaller ones by the pole passing from tooth to slot. This indicates that a steady state simulation would not be sufficient to capture the complex flow developing inside the vents correctly.

Summarising it can be said that while there has been research on stator venting in the past, it focussed exclusively on large machines. Furthermore, CFD as well as experimental investigations were mostly performed isothermally without considering the heat losses generated inside the machine. If heat losses were taken into account, they were modelled by using constant temperature wall boundary conditions.

2.6 Summary and Conclusions

Ever growing demands on power density and machine efficiency have resulted in an increased focus on thermal considerations for the design of electrical machines in recent years. Due to the strong interdependence of electromagnetic and thermal performance in electrical machines, it is desirable to model them simultaneously to achieve a better machine design.

Whilst analytical LPTN models are quick to solve, they rely on correlations developed on simple and well understood geometries and require calibration to predict the thermal performance of an electrical machine accurately. Hence, they are not well suited to predict the performance of complex or novel cooling arrangements for which no correlations exist. FEA is well suited to modelling conductive heat transfer in complex geometries that cannot be modelled adequately by an analytical approach, but requires an accurate prediction of convective heat transfer coefficients to achieve accurate results.

CFD is the only modelling approach capable of predicting turbulent flow, convective and conductive heat transfer simultaneously. Whilst CFD enables an accurate prediction of the conjugate thermal performance, its usage is limited by its high computational cost, as well as the considerable amount of time and user experience required to set up the model correctly [5, 29]. This limits its utilisation in the early design stage, where it is often necessary to analyse a large variety of different configurations.

Accurate thermal and electromagnetic modelling is critical for the design of highly efficient and power dense machine. Up to date, most multi-physics models and thermal design optimisation procedures use either LPTN or FEA for the thermal analysis, relying on CFD or experimental tests to determine the convective HTC required as input parameters. In many cases, the CFD models used for calibration are simplified by neglecting to model certain parts of the machine, such as the fan or endwindings, whose impact on the thermal performance can be critical. As LPTN and FE models are often calibrated through the use of CFD, the next logical step is to develop a CFD based methodology which allows for an automated optimisation of design parameters.

This thesis addresses the growing demand for holistic design approaches by developing a holistic, CFD based methodology, which allows for an automated optimisation of multiple design parameters without requiring additional user input after the initial model setup (view section 1.2). The impact the design changes have on the electromagnetic performance are considered by implementing analytical correlations developed from electromagnetic FEA. The feasibility of this novel approach is demonstrated by optimising the stator vent design of an industrial synchronous generator.

Chapter 3

CFD Modelling of Electrical Machines

At the beginning of this chapter, a general introduction into CFD and its utilisation for the thermal analysis of electrical machines is given. The workflow required to achieve meaningful simulation results is explained. The simplifications, setup and solver settings of the models solved within this project are explained.

3.1 General CFD Workflow

CFD is used to investigate different physical phenomena in a variety of fields. Fluid flow, heat transfer, combustion, chemical reactions and many other phenomena can be simulated. While the model complexity, equations solved and solution strategy can vary substantially depending on the application, the workflow for a succesful CFD investigation generally consists of the five steps shown in figure 3.1. Despite the general validity of the shown workflow, explanations and examples in this chapter will focus on aspects relevant to the modelling of electrical machines.

The first step of every CFD investigation is the creation of the geometry to be analysed. Most commercial CFD software packages include geometry creation packages, e.g. DesignModeler in the ANSYS software package. It is also possible to directly import Computer Aided Design (CAD) geometries. They often require a cleanup before they can be used however, as CAD software is not designed to create geometries well suited to CFD analyses. If the geometry is highly complex, cleaning up the CAD geometry can require more effort than creating a new geometry from scratch in a software package designed for CFD geometry creation. A further advantage of creating the geometry within the CFD software package is the

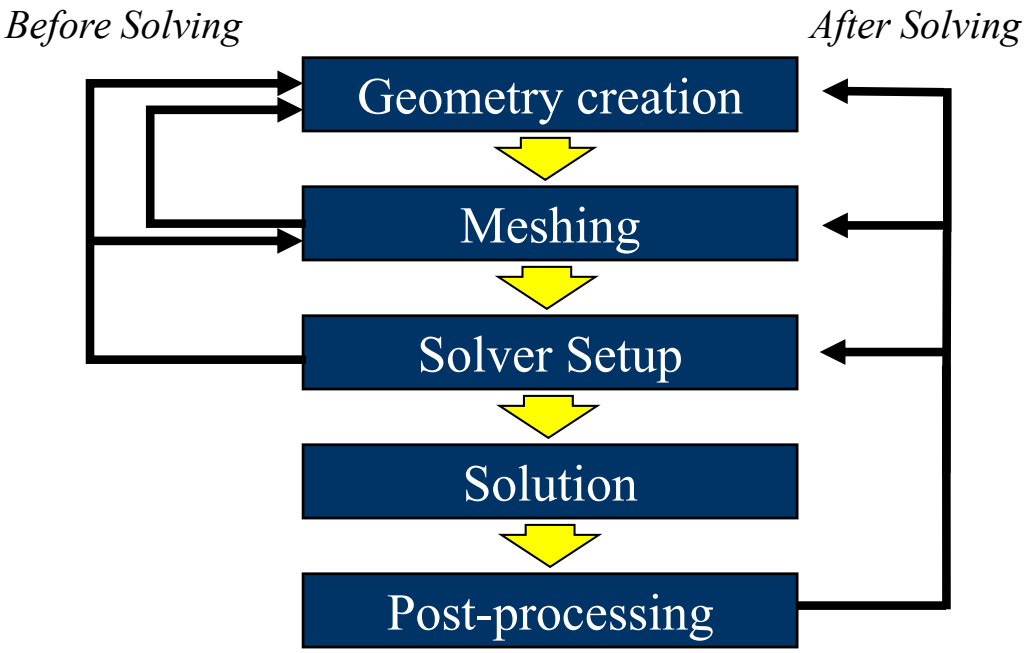


Fig. 3.1 Workflow of CFD investigations

increased model robustness if the design is changed or various design parameters are to be investigated. Therefore, the geometry within this project was created from scratch in ANSYS DesignModeler.

Mesh creation is usually the most time consuming process of the CFD workflow for electrical machine analysis, due to the high complexity of the geometry, air flow and heat transfer. Multiple parallel flow paths with different magnitudes of size need to be represented appropriately. The thermal conductivity of different components can vary by more than a factor of 1000. Creating a mesh which is sufficiently fine to capture the air flow and heat transfer correctly, while keeping the mesh to a size which can be solved by desktop PCs within a reasonable time frame is a challenging task. Multiple iterations between the geometry, meshing and solving stage are usually required to achieve this.

After the mesh has been generated, the solver needs to be set up according to the aim of the conducted investigation. Some of the typically required settings are:

- The equations to be solved must be selected and appropriate boundary conditions defined.
- Appropriate settings, such as material, source terms, rotation, etc. must be assigned to the different volumes.

- Non-conformal interfaces need to be defined between adjacent volumes having meshes that do not share common nodes.
- The solution methods and discretisation must be chosen.
- The initial conditions must be specified.
- Solution monitors, convergence settings and the maximum number of iterations or time steps must be selected.
- Additional zones, surfaces or lines must be created for solution monitoring and post-processing purposes.

Depending on the model complexity, solving a CFD model can be very time-consuming. Run times of multiple hours or days are not uncommon for steady-state simulations of electrical machines. Transient simulations can require days to weeks to converge. During the solution process, residuals and user-defined monitors, which have been defined during the solver setup stage, can be used to judge if the solution has converged. If the level of convergence is not satisfactory or the solution diverges, solver settings, the mesh and/or the geometry need to be amended.

Identifying and extracting data of interest after the simulation has completed can be time consuming due to the wealth of information resulting from CFD simulations. The effort required during the post-processing stage can be minimised by planning ahead and defining zones and properties of interest during one of the previous stages. Findings during the post-processing stage often expose weaknesses in the model and require the user to go back to one of the previous stages to correct them.

It is important to note that CFD investigations are an iterative process. While the initial order of steps taken is depicted by the yellow arrows in figure 3.1, it is usually required to go back to one of the earlier steps later on, as indicated by the black arrows. For example, the user might notice during meshing that the geometry is not sliced sufficiently to create a high quality mesh, so the geometry needs to be modified. Or post-processing shows that the mesh is not fine enough in a certain region to capture the flow behaviour correctly, so the mesh needs to be amended. User experience can help with minimising the amount of iterations required, but they can never be eliminated completely for complex simulations. Its iterative nature makes CFD investigations even more time consuming. Whenever an earlier step is changed, all subsequent steps need to be updated.

The modelling in this thesis was exclusively carried out within the Computer Aided Engineering (CAE) software ANSYS Workbench. Initially, version 16.2 was used. Approximately one year into the project ANSYS was updated to version 17.2 which was used for the majority of

the work. Towards the end of the project, version 18.2 was used for some models containing a high number of non-conformal interfaces and surfaces created within ANSYS Fluent as it proved to be more reliable for these features.

The advantage of using one software suite for all parts of the CFD workflow is the increased model robustness when it comes to machine design changes. As one of the major aims of this project was the creation of a fully automatic optimisation procedure, which does not require any additional user input after the initial model setup, maintaining a good model robustness throughout all steps of the investigation process is essential. The following software packages have been used for the various steps:

- Geometry creation: ANSYS DesignModeler [66]
- Mesh creation: ANSYS Meshing [67]
- Solver setup & solution: ANSYS Fluent [68, 69]
- Post-processing: ANSYS Fluent, ANSYS CFD-Post [70], Python 2.7, Microsoft Excel
- Optimisation procedure: ANSYS DesignXplorer [71]

3.2 Geometry Creation

For every model, simplifications must be made in comparison to the real geometry. Some characteristics, such as the random wire distribution in the stator slots, are unknown and assumptions must be made to represent them as realistically as possible. Features which require a large amount of cells to model correctly, but have a negligible influence on the flow solution (e.g. nuts and bolts), need to be identified and excluded from the model. Investigations using submodels can be useful to determine the influence that specific simplifications have on the model solution. Care must be taken to assure that the applied simplifications do not invalidate the simulation results.

All model geometries within this thesis were created in ANSYS DesignModeler based on the CAD drawings from the machine manufacturer and measurements taken from the benchmark machine.

3.2.1 Periodicity

If the investigated geometry is rotationally or translationally periodic, it is possible to reduce the model size by only modelling one periodic sector. Geometries that are not entirely periodic can often be simplified in a way that makes it possible to represent them using

a periodic sector. Some features of the generator investigated within this thesis are not periodic. But as a full 360° model was computationally too expensive, two simplifications have been made to the machine geometry to make all features rotationally periodic. This made it possible to represent the machine using a 180° model.

Firstly, the 13 blade fan driving the airflow through the machine has been replaced by a 12 blade fan. The validity of this simplification was investigated using submodels comparing the performance of a:

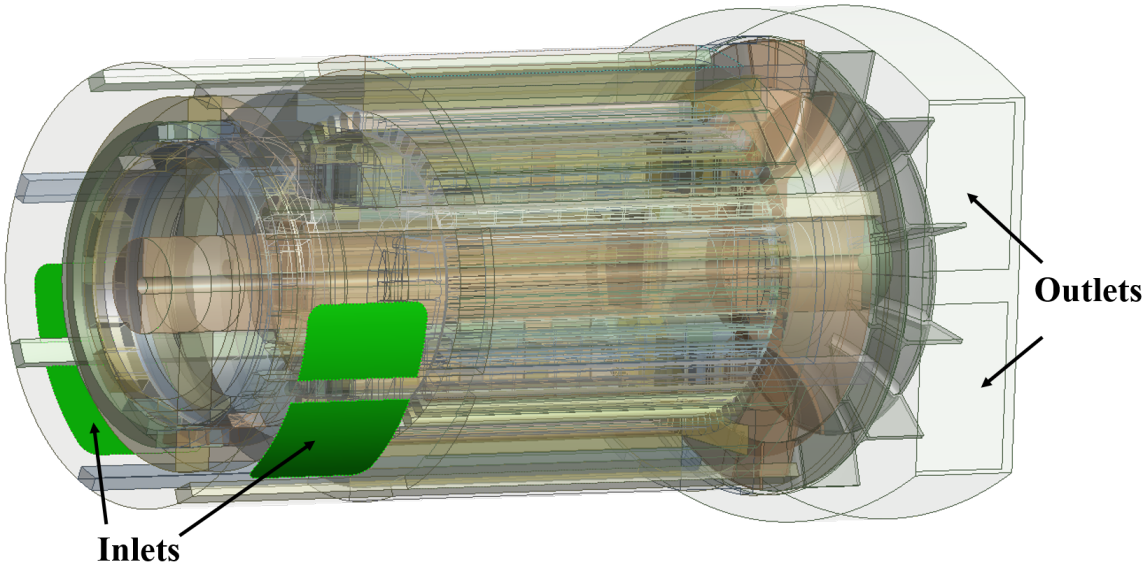
- 360° 13 blade fan
- 360° 12 blade fan
- Periodic 180° 6 blade fan (12 blades in 360°)
- Periodic 90° 3 blade fan (12 blades in 360°)

The submodels consisted of a simplified machine casing, the rotor, stator, stator endwindings and the fan. The core was included to ensure realistic inflow conditions into the fan, but the core length was reduced to 25 % of its actual size to reduce the cell count. The casing was surrounded by a cylindrical domain whose walls were 6 times the casing diameter away from the fan outlet to ensure realistic outflow conditions.

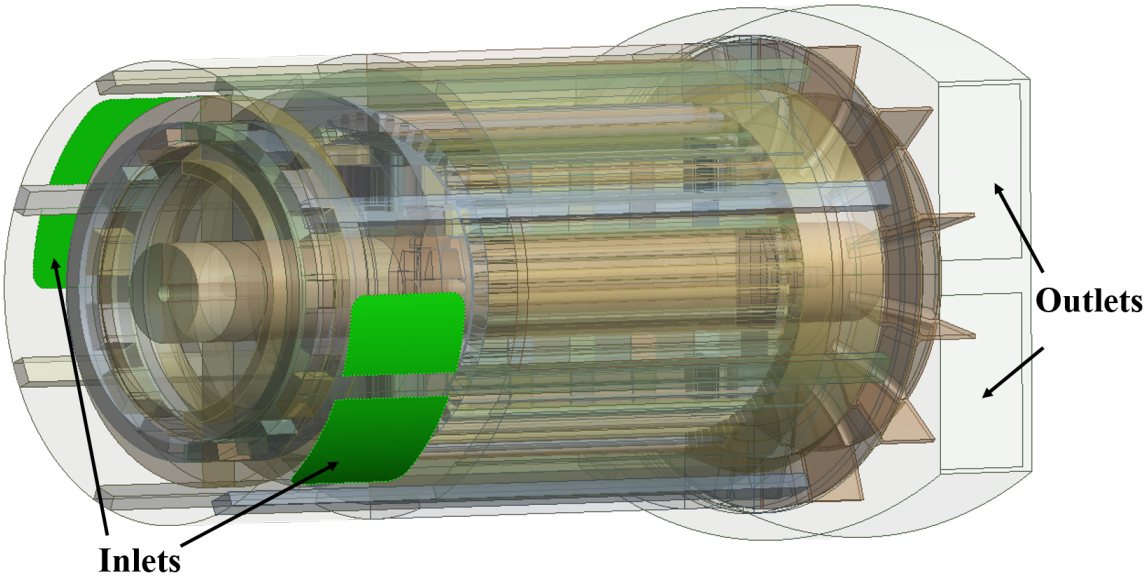
There was no noticeable difference in performance between the different 12 blade fan models. The total flow rate, the flow split between the stator-casing gap and the core region, and the fan torque was identical. Furthermore, the difference in total flow rate and flow split between the 12 blade fan and the 13 blade fan models was negligible. The 13 blade fan produced 4 % more torque than the 12 blade fan. This was considered an acceptable simplification.

Secondly, the location of one of the inlets was moved circumferentially. In the real machine, the inlets are symmetric around a vertical plane going through the central axis of rotation (view figure 3.2a). By modelling the generator with a rotational periodicity of 180°, one of the inlets had to be moved to the location shown in figure 3.2b instead.

Moving the inlet location changes the flow distribution in the gap between the stator and the casing. The stator-casing gap is divided into 8 sections by 8 structural bars which fix the generator in place inside the casing. The flow rate between the different sections varies from 11.6 % to 14.2 % (values taken from 180° model) of the total stator-casing duct flow rate depending on their position relative to the inlets. This is in agreement with the findings of Connor [13], who investigated a machine with a similar topology. The change in flow distribution between the stator-casing gap sections was considered an acceptable error. As the stator back iron is sufficiently far away from the machine hot spot in the stator windings, the impact on the thermal performance of the model in critical locations is negligible.



(a) Inlet locations on real machine



(b) Inlet locations on modelled machine

Fig. 3.2 Comparison of inlet locations on real machine and CFD model

3.2.2 Geometry Simplifications

In addition to the modifications described in the previous section, the following simplifications have been made to the model geometry due to their negligible impact on the airflow and thermal performance of the generator:

- All nuts and bolts were removed and the surfaces they were attached to were patched.
- Welds were not modelled.
- The stator skew was not considered as early CFD investigations showed its influence on the airflow and thermal performance to be negligible.
- Stator laminations, and the varnish separating adjacent laminations, were not modelled. The stator was modelled as a solid part instead. A CFD sensitivity study showed that the influence of the axial thermal conductivity of the stator iron on the thermal performance is negligible (view sections 5.3.1 and 7.4.2).
- The machine shaft was only modelled inside the casing.
- The bearings supporting the rotor were not modelled. The bearing torque was calculated according to equation 4.4 instead.
- The generator feet and terminal box were not modelled.
- The generator casing was modelled as a thin surface. Implementing the wall thickness by using the thin-wall thermal resistance feature within ANSYS Fluent showed that the casing thickness did not have any measurable influence on the thermal performance, as the majority of the heat is removed by convection through the outlets.
- The lab infrastructure and drive motor were not modelled. The generator was surrounded by a cylindrical air domain with an axial length of 5x the core length and a diameter of 8x the stator outer diameter bounded by a constant pressure outlet to allow air flow into the domain. Increasing the domain size further, or replacing the pressure outlet with a wall, did not have any impact on the results, confirming the appropriate sizing of the domain.
- Due to the considerable cell count required to model airgaps in electrical machines, the exciter (view section 1.3) airgap was replaced by copper instead. The heat generated in the exciter is small in comparison to the main rotor/stator core, resulting in low exciter temperatures. As the exciter axial length is only 10 % of the main core length and approximately 90 % of the total machine torque is produced by the fan (view section 5.2), the resulting reduction in total windage is negligible. The exciter is located outside of the main air flow path between the machine inlets and outlets.

Therefore only a the small amount of air passes through the exciter airgap and the change in inflow conditions into the core by not considering it is negligible.

- The grilles covering the inlets and outlets were not modelled since they would require a very fine mesh around them. However, their influence on the machine performance is significant as they reduce the total flow rate through the Benchmark Machine by 6.4 % at synchronous speed (view section 5.1). To enable consistent validation, the grilles were removed during the experimental tests.
- Rotor and stator windings consist of copper wires, insulation material, resin and slot liners. As the cell count required to model them all separately would be excessive, they were modelled as an equivalent lumped anisotropic material instead (view section 3.4.6).

3.2.3 Geometry Division

Another important aspect that needs to be considered during the geometry creation is the division of the whole geometry into separate volumes. This is an important step for several reasons. First of all, volumes requiring different settings at the solver stage need to be separated. Common settings requiring division of cell zones are different materials, source terms or rotation settings. Secondly, division is important to achieve a high quality mesh, particularly if a swept mesh is required (view section 3.3). Figure 3.3 shows the volume division required to achieve a high quality mesh in the airgap and to implement rotation correctly.

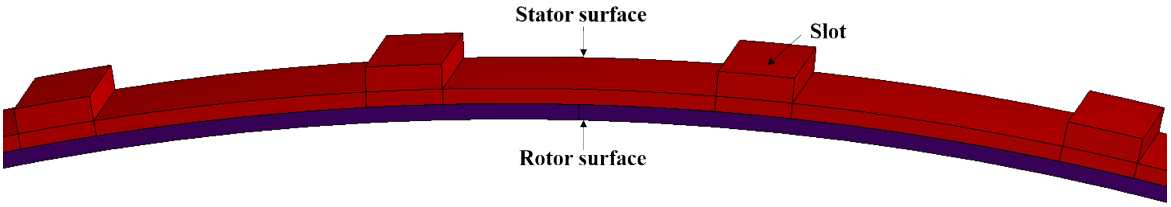


Fig. 3.3 Volume division required to achieve a high quality mesh in the airgap and implement rotation; rotating parts (blue), stationary parts (red)

3.3 Meshing

After the geometry has been created, it needs to be divided into a number of control volumes in which the governing equations of fluid flow and energy are solved. Creating a mesh

which is sufficiently fine to capture the airflow and heat transfer correctly while keeping the mesh to a size which can be solved within a reasonable time frame is a challenging task, due to the complexity of the geometry, air flow and heat transfer in electrical machines. As a result, meshing is usually the most time consuming process of electrical machine CFD investigations.

All meshes within this thesis were created in ANSYS Meshing.

3.3.1 Cell types and mesh quality

There are two main types of cell shapes used for CFD meshes: Tetrahedral (tet) and hexahedral (hex) cells. As the name implies, tet cells are tetrahedrons in shape, while hex cells are hexahedrons. A combination of both cell types has been used to create the high quality mesh required to model airflow and heat transfer within the investigated generator. ANSYS Fluent also supports the generation of polyhedral cells, which are polyhedrons with more than six faces. But they have not been utilised within this project and will therefore not be discussed.

One way to judge the quality of a mesh is by using metrics such as skewness and aspect ratio. Cell skewness is a measure of how far the shape of a cell differs from the ideal cell shape, which is defined as equilateral for triangles and equiangular for rectangles. Skewness can vary from 0-1 with 0 being ideal and 1 a completely degenerate cell. The cell aspect ratio is defined as the ratio of the longest side to the shortest side of a cell, with 1 being the aspect ratio of an ideal cell. High aspect ratios of ≥ 20 are usually only acceptable in areas where there is no flow transverse to the long side of the cell, such as in boundary layers. Highly skewed cells and cells with high aspect ratios (if the flow is not one-dimensional) cause interpolation errors and need to be avoided, particularly in regions with complex, 3-dimensional flow. A complete definition of skewness, aspect ratio and many other mesh quality metrics can be found in [67].

The use of hexahedral cells is advantageous when the modelled geometry is simple or well structured. Hex cells are particularly well suited to fill volumes with a constant cross-section that require a constant mesh size across the cross-section. Hex cells have a few advantages over tet cells. They can be aligned with the flow direction, minimising the error introduced by numerical diffusion resulting from the discretisation of the set of differential equations. It is possible to achieve higher aspect ratios in comparison to tet cells without deforming the cell excessively. Generally, a well defined hex mesh requires fewer cells than a tet mesh to model the flow to the same level of accuracy, thus reducing the computational expense

and improving convergence. Considerably more time needs to be spent at the geometry and meshing stage for complex geometries though, as hex meshes can only be used for volumes with a constant cross-section.

Tet cells are better suited to modelling complex geometries, particularly if the mesh needs to be refined locally and grow out from there in multiple directions. A good example for that are the machine inlets and outlets, which require a fine mesh that can grow out quickly into the surroundings. While they are computationally less efficient than hex cells, tet cells are required to mesh the most complex shapes in electrical machines appropriately. The choice of cell type needs to be carefully considered by the user for each part of the geometry to achieve a high quality mesh. In figures 3.4 and 3.5, which show the mesh of the benchmark machine model, the areas which were meshed by each cell type can be seen.

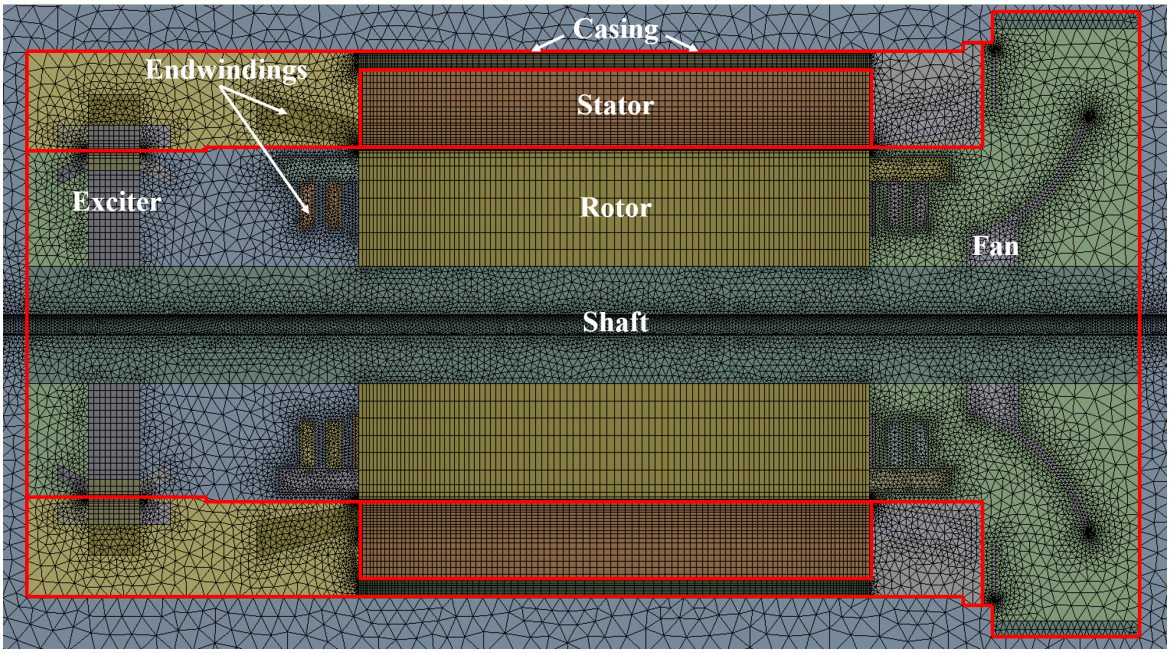


Fig. 3.4 Benchmark Machine mesh showing areas meshed with hex and tet cells and non-conformal interfaces (in red); side view

Except for the shaft, the mesh of the core region contains exclusively hex cells. The constant cross-section of all core parts along the rotation axis makes the geometry well suited to apply a hex mesh. As the flow through the core is highly complex and critical for the thermal performance, a very fine mesh is required which could not be achieved with a reasonable cell count using tet cells. Additionally, tet cells are not well suited for filling narrow gaps like the airgap and vents and in boundary regions.

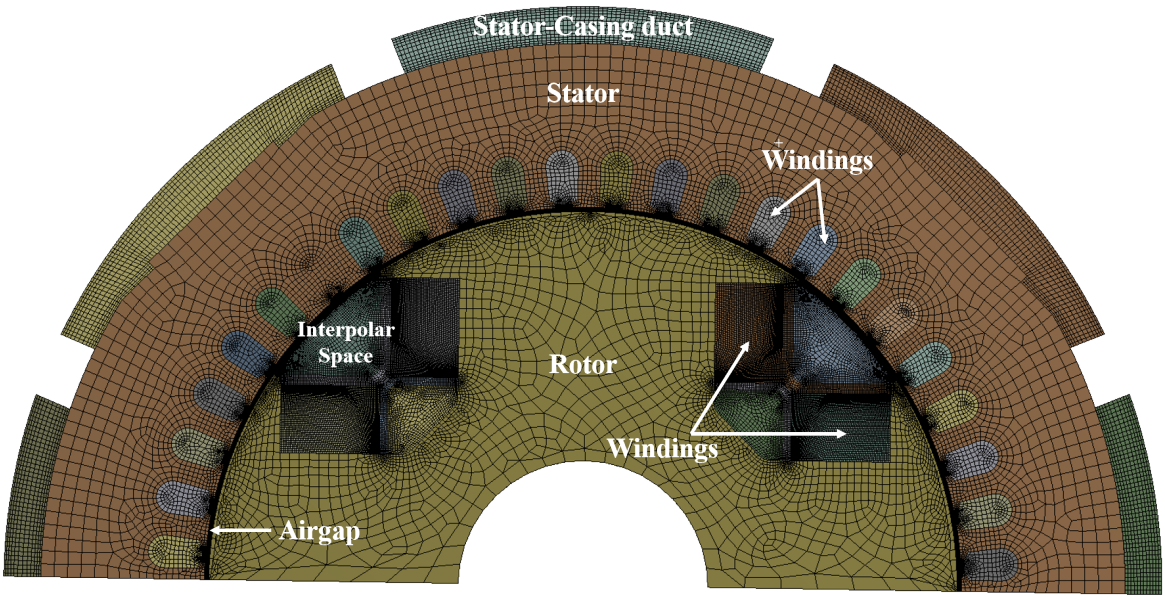
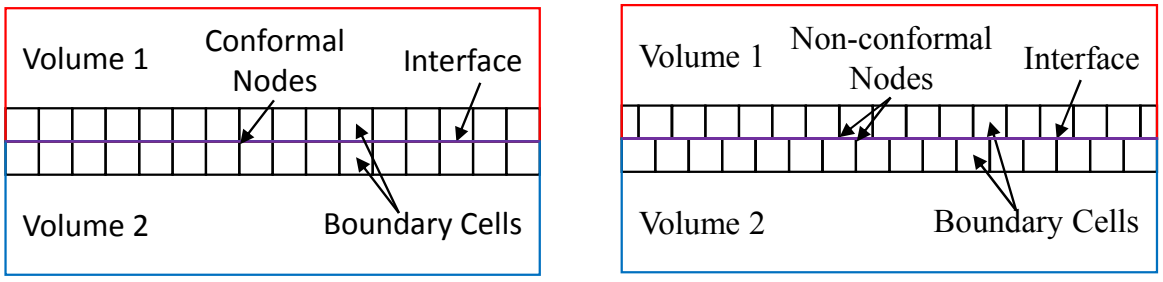


Fig. 3.5 Benchmark Machine mesh showing areas meshed with hex and tet cells; axial slice through centre of core

3.3.2 Conformal/Non-conformal Interfaces

The mesh needs to be connected between separate volumes to ensure fluid flow and heat transfer are solved correctly. Two different methods exist to achieve this. If the nodes on the coincident surfaces are in the same location (view figure 3.6a), the mesh interface between the volumes is called conformal. If the nodes are not in the same location (view figure 3.6b), the mesh interface is referred to as non-conformal.



(a) Conformal mesh interface

(b) Non-conformal mesh interface

Fig. 3.6 Comparison of conformal and non-conformal mesh interfaces

Non-conformal interfaces require interpolation to transmit data between the coincident surfaces. To keep the error introduced by interpolation to a minimum, non-conformal interfaces should not be located in regions with high gradients of the solution variables (pressure,

velocity, temperature, turbulence). As the interpolation is necessary for every iteration, a high number of non-conformal interfaces can increase the solving time in comparison to a model which mostly consists of conformal interfaces. Non-conformal interfaces also require additional input by the user, as they need to be defined explicitly at the meshing and/or solving stage, while conformal interfaces are created automatically by the software.

One of the benefits of using non-conformal interfaces is the possibility to have different cell sizings on adjacent bodies. For example, the mesh in the airgap requires a finer resolution in the axial direction than the solid rotor and stator parts. Non-conformal interfaces can thus reduce the total cell count. They are also beneficial if two surfaces with different mesh requirements need to be connected, such as between the airgap and the inlet/outlet regions. Growing tet cells from the high aspect ratio hex cells in the airgap would result in highly skewed cells. Furthermore, non-conformal interfaces are required for transient simulations, which include relative movement between different parts of the mesh, such as the sliding mesh simulations explained in section 3.4.4.

Figure 3.4 shows where the non-conformal interface are situated in the model of the benchmark machine. Additional non-conformal interfaces, which can not be seen in figure 3.4, are located between the airgap/IP space and the core inlet/outlet regions. Except for additional non-conformal interfaces at the vent entries and exits, which do not exist in the Benchmark Machine, the interface locations for the Vented Prototype model are exactly the same.

3.3.3 Mesh Independence

It is important to confirm that the calculated solution is mesh independent. This means that the solution does not change with a further refinement of the mesh. Mesh independence studies can often be conducted on submodels to reduce computation time. In areas with a highly structured hex mesh, such as the airgap, it is often easiest to increase the cell count in one direction until mesh independence is reached. Tet cell sizes are usually refined by defining a maximum cell size at important surfaces and a growth rate, which controls how quickly the cells grow from the surface up to the maximum allowed value. Mesh independence can be reached by varying these sizings. Large growth rates, and abrupt changes in cell size, introduce numerical errors. The growth rate within this thesis is kept below 1.2, meaning that the maximum possible size difference between two adjacent cells is 20 %. A maximum growth rate of 1.2 is generally considered appropriate for CFD investigations of electrical machines [68].

It is not feasible to check mesh independence for every single sizing. Thus the non-dimensional wall distance y^+ has been used as a metric to control the mesh refinement at wall boundaries for which no in-depth sensitivity studies were concluded. y^+ is the non-dimensional distance of a cell next to a wall boundary and is defined as:

$$y^+ = \frac{u_T y}{\nu} \tag{3.1}$$

with y being the distance to the nearest wall, ν the local kinematic fluid viscosity and u_T the friction velocity at the nearest wall defined as

$$u_T = \sqrt{\frac{\tau_w}{\rho}} \tag{3.2}$$

depending on the wall shear friction τ_w and fluid density ρ. It has been shown experimentally that the fluid boundary layer consists of three zones (view figure 3.7):

- The viscous sublayer: $y^+ \leq 5$
- The buffer layer or blending region: $5 \leq y^+ \leq 30-60$
- The fully turbulent or log-law region: $30-60 \leq y^+ \leq 200-300$

In the viscous sublayer, the flow is dominated by viscous effects. In the outer layer, known as the fully turbulent or log-law region, fluid flow and heat transfer are dominated by turbulent effects. Between these two regions a buffer layer, in which both effects are equally important, is situated. Figure 3.7 shows the relationship between non-dimensionalised fluid velocity and the non-dimensional wall distance in the near-wall region.

If the flow near the walls is particularly important, such as in the airgap or vents where the boundary layers of opposite walls merge, the viscous sublayer needs to be resolved, ideally with a y^+ value of around 1 and 10-20 cells over the boundary layer [67]. It would be computationally too expensive to do this for all walls, however. Fortunately, the flow in the fully turbulent region can be approximated by logarithmic correlations, such as the ones published by Launder and Spalding in [72] which was utilised in this thesis. If the Enhanced Wall Treatment feature in Fluent is activated, the solver uses a blending function depending on the non-dimensional wall distance to take the viscous and turbulent effects into account appropriately [69].

During the mesh generation, care was taken to avoid y^+ values in the buffer layer as the model accuracy is at its worst in this region [73]. For a similar reason, $y+$ values beyond the extent of the fully turbulent region were avoided, as the logarithmic wall function correlations

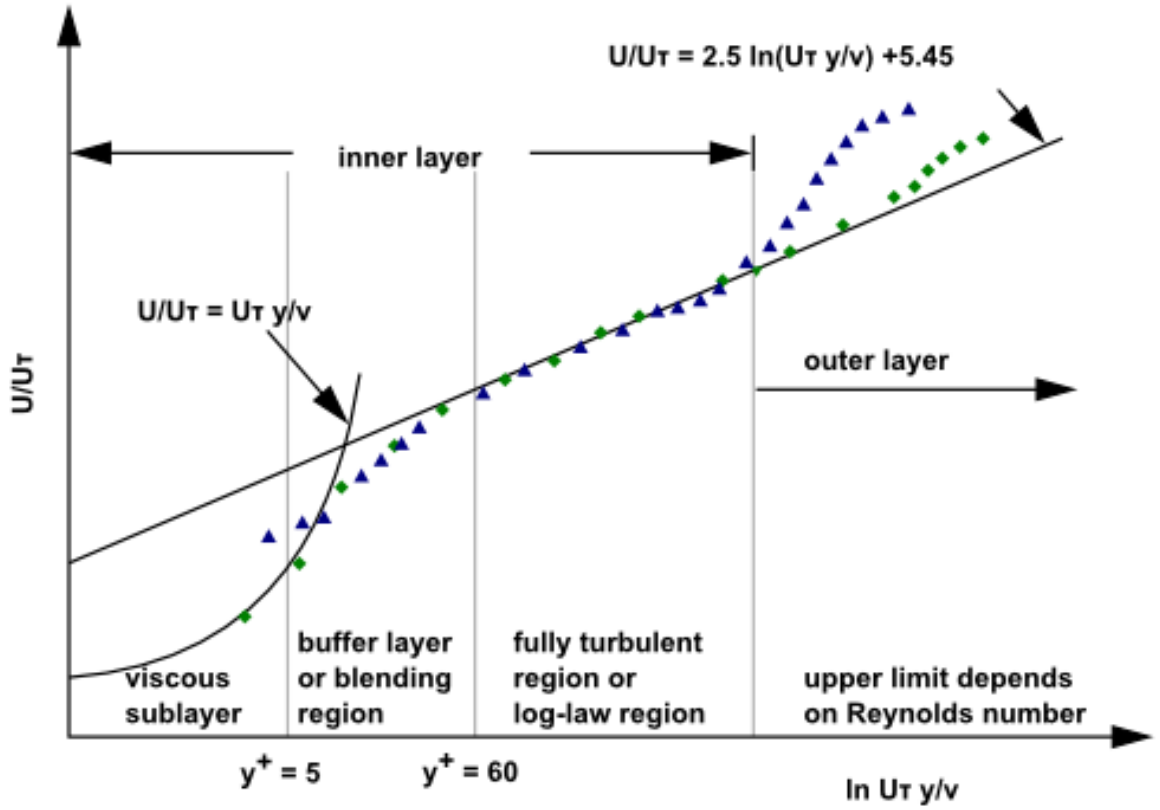


Fig. 3.7 Division of the boundary layer in the near-wall region in semi-logarithmic scale [69]

are invalid there. More information about the treatment of near-wall cells can be found in section 3.4.3.

3.3.4 Boundary Condition Definition

To facilitate the definition of boundary conditions during the solver setup, surfaces can be selected and grouped together during the meshing stage. By naming them according to the conventions defined in the ANSYS Meshing manual [67], the correct boundary conditions for walls, inlets, outlets, interfaces, interior surfaces, etc. will automatically be applied when the mesh is imported into ANSYS Fluent. ANSYS Meshing automatically creates non-conformal interfaces between non-conformal volumes when started, but the automatic interface creation was found to be problematic for complex models and therefore turned off. The non-conformal interfaces were coupled manually at the meshing stage instead. This results in them automatically being coupled in ANSYS Fluent when the mesh is loaded, reducing the effort at the solver setup stage. This is only possible for normal interfaces

however. Periodic Boundaries (required for simulating periodic geometries), Periodic Repeats (required for sliding mesh simulations of periodic geometries) and Coupled Walls (required to model heat transfer at non-conformal wall interfaces correctly) need to be defined manually at the solver setup stage.

3.4 Solver Setup

After the mesh has been created, the solver needs to be set up appropriately for the investigation in question. The physical phenomena to be solved must be selected, boundary conditions defined, the solution methods, discretisation and settings chosen and convergence monitors and settings defined. Additionally, zones and properties of interest should be defined at this point to facilitate post-processing.

ANSYS Fluent is the solver used for all CFD investigations within this thesis.

3.4.1 Governing equations of fluid flow

As the airflow and local temperatures are of interest within this project, the following conservation laws of physics, also called the governing equations of fluid flow [29], need to be considered:

- Conservation of mass
- Conservation of momentum
- Conservation of energy

More detail on the governing equations and their discretisation can be found in appendix A.

3.4.2 Compressibility

Fluid compressibility is the relative volume change of a fluid caused by a change in pressure. As a result, the fluid density depends on the pressure. While all fluids are compressible in reality, the change of fluid density with pressure and the impact it has on the flow is negligible in flows with low velocities (incompressible flows). To determine if a flow is incompressible, the Mach number Ma is used, which is a non-dimensional metric expressing the fluid velocity

v_{fluid} relative to the velocity of sound in that fluid v_{sound}:

$$Ma = \frac{v_{fluid}}{v_{sound}} \tag{3.3}$$

Compressibility is important for transonic ($Ma \sim 1$), and supersonic/hypersonic ($Ma > 1$) flows. As the maximum Mach number within the investigated machine amounts to 0.18 (calculated based on CFD results), and is therefore well below the range compressibility needs to be considered (typically $Ma \geq 0.3$), the flow was modelled as incompressible.

3.4.3 Turbulence Modelling

Turbulence is the random and chaotic variation of velocity and pressure with time, which occurs if the Reynolds number of a flow exceeds the critical Reynolds number. While laminar flow can be described adequately using the equations presented in section 3.4.1 and appendix A.1, additional equations are required to model turbulent flows. Three major turbulence modelling approaches exist:

- Reynolds-averaged Navier Stokes (RANS)
- Large Eddy Simulation (LES)
- Direct Numerical Simulation (DNS)

LES and DNS are computationally too expensive to be considered for the analysis of complex electrical machine geometries, hence RANS modelling has been chosen for this investigation. The theoretical background of the RANS modelling approach can be found in A.3.

Within this project, the standard k-ε model has been utilised, as it showed the best convergence behaviour and agreement with experimental results for the investigated machine. It has been used and validated for radial flux machines by a variety of researchers [11–14, 30, 32] in the past. The standard k-ε model was chosen initially as it showed the best convergence in initial investigations using submodels. The appropriateness of the choice was confirmed by validating the final models of the Benchmark Machine and Vented Prototype experimentally (view chapters 5 and 7).

The standard and the realizable k-ε model produced almost identical results. Maximum and average winding temperatures varied by less than 1° C, the total windage torque varied by 0.5 % and the total mass flow rate through the machine by 1.4 %. The residuals were of the same magnitude, with the continuity residual being around $2e^{-4}$, momentum and turbulence residuals around $1e^{-5}$ and the energy residual around $1e^{-6}$.

The k-ω standard and the k-ω SST model did not converge well, with residuals being two magnitudes higher in comparison to the k-ε standard model. Flow properties, such as mass flow rates, torque and local pressures never converged suitably, still fluctuating considerably after a high number of iterations. This suggests that neither model is well suited to model the airflow through an electrical machine. While the standard k-ω model is well suited to internal flows and can be superior to the k-ε models in near-wall regions, it is sensitive to free-stream and inlet boundary conditions. This sensitivity is less distinct for the k-ω SST model, as it utilises the k-ε equations in free stream regions. The k-ω equations are only applied near walls. Between these two regions, the different equations need to be blended together, making this model unsuited for geometries with complex flow in the blending regions. This is the case in electrical machines, due to the many different surfaces constraining the flow inside the machine.

Flow near the walls has been modelled by utilising the Enhanced Wall Treatment option, which uses a blending function depending on the non-dimensional wall distance $y+$ to take the viscous and turbulent effects into account appropriately (view section 3.3.3). It is required to model the flow in narrow spaces with merged boundary layers, such as the airgap and vents, correctly. The turbulent wall functions described in section 3.3.3 are not applicable in these regions.

3.4.4 Rotation Modelling

Fluent offers two different approaches to model rotation within electrical machines in 3-D: The Multiple Reference Frame (MRF) and the Sliding Mesh (SM) approach [68]. While the flow inside a generator is inherently transient, the MRF approach allows the case to be simulated as steady-state with respect to the moving frame. The moving parts are frozen in a specific location and the flow field developing in that position can be observed [68]. While less accurate than the fully transient SM approach, it is usually used for the analysis of electrical machines [11–13, 30], due to the much lower computational effort required. Both approaches require the geometry to be separated into a moving and a stationary domain as shown in figure 3.8.

For the majority of the models solved within this thesis, rotation is modelled using the Multiple Reference Frame (MRF) technique. Design Optimisation procedures on complex models cannot be conducted with a transient approach within a reasonable time frame. The model used for the final design optimisation required approximately 14 hours to solve

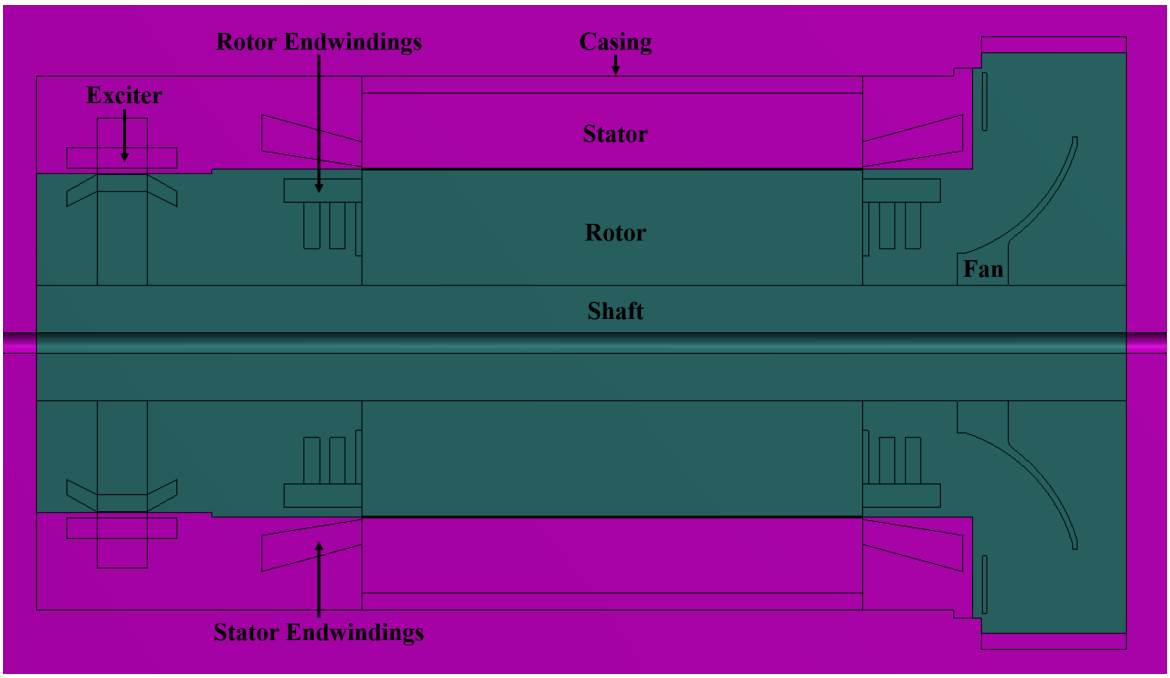


Fig. 3.8 Separation of benchmark machine geometry into rotating (grey) and stationary (purple) domain

each design point using the MRF approach, while running a fully transient SM simulation with a time step of 2° took around 2 (fluid flow only) to 5 (CHT) weeks per design point. Transient simulations have been studied in detail, however, to determine the influence using a steady-state approach has on the simulation results (view chapters 5 and 7).

While the thermal performance of an electrical machine can be predicted using the MRF approach, it is important to be aware of the introduced simplifications and their consequences. As the flow is solved steadily in one specific rotor position, the resulting flow varies circumferentially depending on the relative position of the rotor to the stator. Figure 3.9, showing the temperature rise above ambient in the axial centre of a vent of the Vented Prototype, illustrates this phenomenon. The temperature rise has been normalised by dividing it through the experimentally measured peak stator winding temperature rise above ambient at full load and 0.8 PF (view section 5.3). The stator slots above the IP spaces are cooler in comparison to the ones above the pole centres, as they are in direct contact with more cooling fluid. In reality, the temperatures do not vary circumferentially as the rotor moves relative to the stator. It is therefore essential to average properties of interest circumferentially to get meaningful results using the MRF approach.

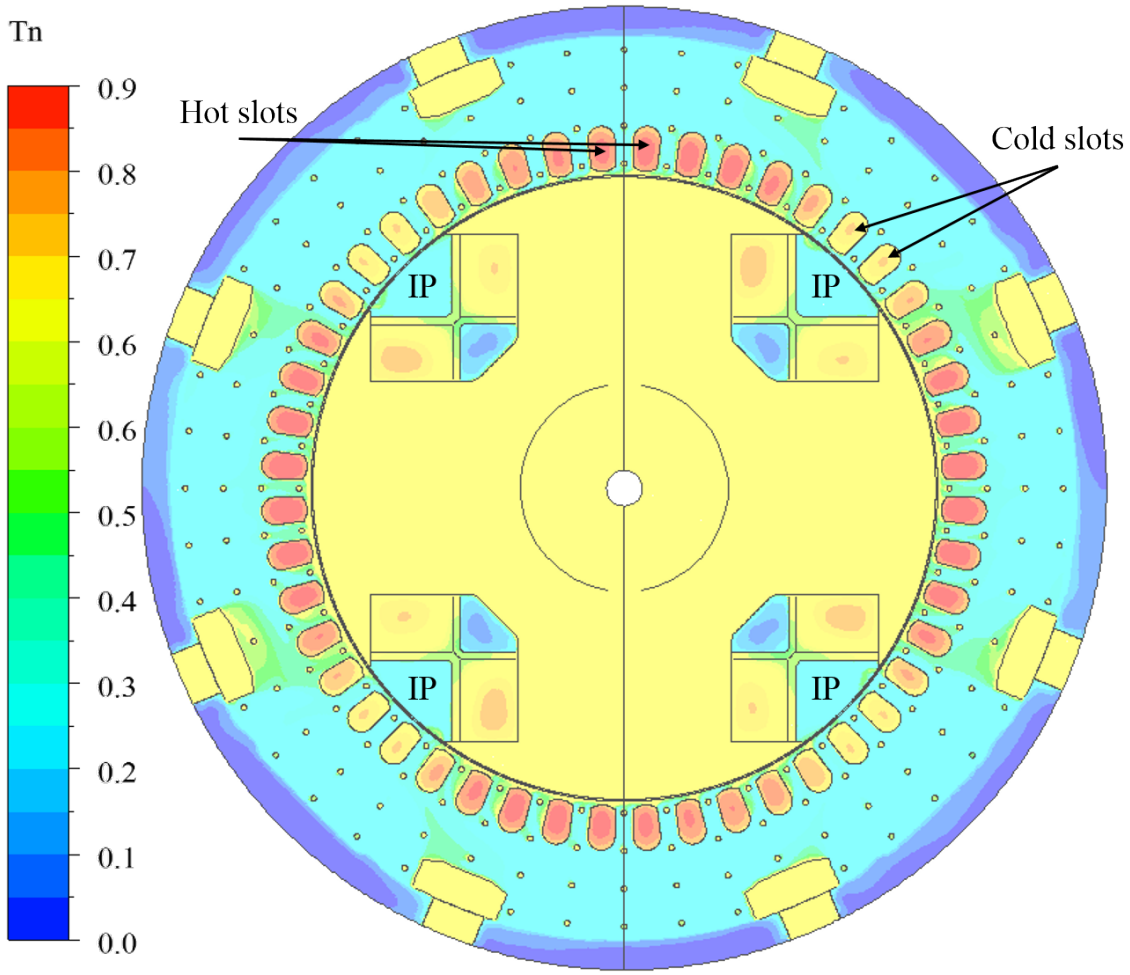


Fig. 3.9 Temperature rise contours in the axial centre of a vent of the Vented Prototype; Temperature rise normalised according to equation 5.4

A major problem of using the SM approach for modelling Conjugate Heat Transfer (CHT) is the substantial difference in time scale between the fluid flow and the thermal solution in the solid components. Selecting an appropriate time step is essential to achieve accurate results. Small time steps of around 1 °/revolution (1.11×10^{-4} s) are required to model the fluid flow correctly, and the flow solution takes around three 360° revolutions to show converged, periodic behaviour. But the investigated machine takes 3-4 hours to reach steady thermal temperatures at full load, hence ~100 million time steps would be required for the thermal solution to converge, which would take several years on a desktop PC. This made the SM approach unfeasible to apply for CHT simulations initially. In ANSYS Fluent v18.0, a new feature was introduced making it possible to choose different time step sizes for the fluid

and solid parts of the domain. This enabled the investigation of the influence the rotation modelling approaches have on the thermal solution presented in chapter 7.4.1.

The SM approach is also more sensitive to the choice of initial conditions. For complex models, it is required to solve the case using the MRF approach first and use the MRF solution for initialisation of the SM case to avoid divergence [68]. Further differences between the two rotation modelling approaches are analysed in detail in chapters 5 and 7, where the results of the CFD investigations and their experimental validation are discussed.

3.4.5 Heat Loss Implementation

To predict machine temperatures, the losses generated within the machine (view section 2.1) need to be implemented into the model. This was achieved by using the volumetric heat generation feature within Fluent. A constant heat generation rate has been assigned to every loss creating solid part. Table 3.1 shows the loss distribution at full load and 0.8 power factor (PF) within the Benchmark Machine and the parts they have been assigned to.

Table 3.1 Heat loss distribution in the Benchmark Machine at 0.8 PF; Copper and mechanical losses determined experimentally; Iron losses determined by FEA; Exciter and Stray losses taken from manufacturer data sheet

Loss Type	Allocated Parts	Total losses
Stator copper	Stator Windings	37.6 %
Rotor copper	Rotor Windings	23.3 %
Stator Iron	Stator Laminations	18.4 %
Rotor Iron	Rotor Laminations	1.6 %
Exciter	All Exciter Parts	2.3 %
Mechanical	-	6.7 %
Stray	Stator, Rotor, Exciter Stator, Exciter Rotor	10.1 %

The winding copper losses in particular vary with temperature. Using User Defined Functions (UDF), it is possible to implement temperature dependent losses and vary the heat generated within parts locally. However, the influence of implementing a heat generation based on local cell temperatures on the investigated generator is negligible in comparison to basing it on the average winding temperature and keeping it constant (view section 3.7.3).

The rotor copper, rotor iron and stator iron losses of the Vented Prototype depend on the combined vent width. As active core material is removed, more current needs to be supplied to the rotor windings to achieve the same power output as the Benchmark Machine. 2-D

electromagnetic FEA has been used to develop correlations between these losses and the combined vent width. These correlations were then implemented into the vent optimisation procedure. The EM FEA was conducted by Nuzzo and not the author of this thesis. More details of the EM investigations can be found in [37, 74, 75] and section 6.2.

3.4.6 Anisotropic Conductivity

As windings are a combination of copper wires, resin and insulation material, the winding thermal conductivity perpendicular to the copper wire direction is considerably lower compared to the conductivity in wire direction. The thermal conductivity in the wire direction was assumed to be that of pure copper with a conductivity of $400\,\mathrm{W\,m^{-1}\,K^{-1}}$. The resin thermal conductivity was given by the manufacturer as $0.2\,\mathrm{W\,m^{-1}\,K^{-1}}$. As the resin and copper wire enamel layer conductivity are of a similar magnitude, they were assumed to be equal. The radial and tangential wire thermal conductivity were calculated according to the Hashin and Shtrikman approximation [76] from the thermal conductivity of copper k_c and resin k_{res}:

$$k_{rad/tan} = k_{res}\frac{(1+v_c)k_c + (1-v_c)k_{res}}{(1-v_c)k_c + (1+v_c)k_{res}} \tag{3.4}$$

with v_c being the slot fill factor, defined as the ratio of copper volume to total slot volume. This approach has been used and validated by other researchers in the past [77, 78]. The change in copper wire orientation when the windings leave the core has been considered by varying the thermal conductivities using custom UDFs which have been created and implemented by the author (view section 3.7.2).

The thermal conductivity of the stator windings perpendicular to the wire orientation calculated according to equation 3.4 amounts to $0.43\,\mathrm{W\,m^{-1}\,K^{-1}}$. As the rotor winding fill factor is higher, the thermal conductivity perpendicular to the wire orientation is higher in comparison to the stator windings. It was calculated to be $1.45\,\mathrm{W\,m^{-1}\,K^{-1}}$

3.5 Solution Methods and Controls

The Semi-Implicit Method for Pressure-Linked Equations (SIMPLE) algorithm is used to couple pressure and velocity. No convergence issues were found regarding the continuity, momentum and turbulence equations, hence Fluent's default under-relaxation factors have been used for the solution.

Using highly anisotropic conductivities in the windings lead to divergence of the energy equation. This issue was previously identified by Connor [13] and he proposed solver settings enabling convergence. Some of the settings proposed in [13] were adopted to enable convergence:

- Enabled explicit relaxation of the energy equation
- Disabled secondary gradient of temperature
- Changed energy equation multigrid cycle to W-cycle and enabled BCGSTAB stabilisation method

The energy equation under relaxation factor was kept at its default value of 1. It was not necessary to switch to the coupled solver to reach convergence as proposed by Connor [13].

Besides the residuals, which are monitored by default, additional monitors were created to judge convergence. Mass flow rates, torque, pressure and temperatures were monitored in multiple locations. The residual convergence criteria were turned off, as the residuals converged faster than some of the critical fluid flow properties. The solution was considered to be converged when the residuals and monitored properties were steady. The fan blade torque, monitored by defining a moment coefficient (C_m) monitor at the blade surfaces, was usually the last property to converge. Using the Standard Initialization in Fluent, approximately 5000 iterations were required until the solution was fully converged.

While the final simulation results are independent of the initial guess (unless it causes divergence), using solution data from previously solved cases as an initial guess can reduce the number of iterations required to reach convergence considerably. If the mesh is the same as in the previous case, as it was the case when the influence of rotation speed on mass flow rate and torque was investigated, the previous results can be directly imported. If the mesh has changed, the results of the previous case need to be exported as an interpolation file. This file can be read into the new case and the old solution data is interpolated. If the geometry has changed, new regions are filled with the default value defined in Fluent. This initialisation method was used during the final design optimisation, requiring approximately 1000 iterations to reach a converged solution.

The energy equation converges much faster (20-50 iterations) than the equations governing fluid flow ($\geq$ 1000 iterations). As air is considered to be incompressible, there is no correlation between temperatures and fluid properties. The fluid viscosity is assumed to be constant, which is a reasonable assumption for air in the occurring temperature range. Hence, solving the fluid flow only first, and only turning on the energy equation at the end, saves simulation

time. Calculation Activities and Case Modifications were used to turn the energy equation on automatically during the solution process.

3.6 Post-processing

Most of the post-processing was done within ANSYS Fluent using volume, surface and line plots and reports. Scripts written in the programming language Scheme facilitated the data analysis within Fluent. ANSYS CFD-Post was used to create contour and vector plots comparing data between different cases. Python 2.7 and Microsoft Excel were used for the creation of scatter plots and data analysis involving more advanced post-processing activities, such as circumferential data averaging and interpolation.

One of the challenges related to data analysis is the slow speed of data-processing caused by the mesh size. Loading a single case from a Solid State Drive takes approximately 5 minutes. Some of the more complex data extraction and averaging activities can take several minutes. To reduce the time spent post-processing, important parameters should be defined before the start of the simulation, so they are automatically calculated, displayed and exported at the end.

3.7 Novel Methodologies Developed

Several novel methodologies have been developed during this project to model and optimise the investigated machine appropriately, as well as to facilitate the model setup and post-processing. They are presented in this chapter.

3.7.1 Automated Interface Creation

One of the reasons limiting the use of CFD investigations for the thermal analysis of electrical machines is the high amount of manual user input required to set up the simulations. One time consuming process, which needs to be done before the start of any simulation, is the definition and creation of interfaces. ANSYS Meshing automatically creates and couples interfaces when two non-conformal bodies share one surface. While this works reasonably well for simple models, the automatic interface creation fails for complex models containing multiple non-conformal interfaces as required for the modelling of electrical machines. In

ANSYS Fluent v18.0, automatic interface coupling within Fluent was introduced, which enables coupled walls to be created between fluid and solid zones. Periodic Boundaries and Periodic Repeats still need to be defined manually. But tests using Fluent v18.2 showed that the automatic coupling fails for complex models, equivalent to the automatic interface creation in ANSYS Meshing, even if the interfaces to be coupled are defined manually in ANSYS Meshing. Hence this feature was not used.

The easiest and fastest way to couple non-conformal interfaces manually is to define and couple them in ANSYS Meshing, which results in them automatically being created when Fluent is started. This approach only works for normal interfaces, however. Coupled Walls, Periodic Boundaries and Periodic Repeats still need to be defined manually in Fluent. The creation of Periodic Boundaries and Periodic Repeats is particularly time consuming, as they can only be coupled one by one.

To reduce the amount of time spent on repetitive work, several functions were created in Scheme, the programming language which can be used for automation within Fluent. These functions enabled the automatic creation of Periodic Boundaries, Periodic Repeats and Coupled Walls based on manually created interfaces in Meshing. These functions considerably reduced the time to set up a model in Fluent. Further details on Scheme and how to use it for automation within Fluent can be found in [68] and [79].

The source code of the developed scripts can be found in appendix B.1 and B.2.

3.7.2 Anisotropic Conductivity Modelling in Endwindings

As windings consist of copper wires, resin and insulation material, their thermal conductivity perpendicular to the copper wire direction is considerably lower compared to the conductivity in the wire direction. To consider this effect, the windings were modelled as a bulk material with an anisotropic conductivity as explained in section 3.4.6. This is easy to implement in the core windings, where the wire orientation does not change and is aligned with the axis of revolution (z-axis), by using the orthotropic conductivity option. It requires the definition of thermal conductivity in the direction of three orthogonal axes. A constant conductivity of $k_h = 400\,\mathrm{W\,m^{-1}\,K^{-1}}$ was defined in the z-direction, $k_{l,stat} = 0.43\,\mathrm{W\,m^{-1}\,K^{-1}}$ in the x and y-direction for the stator windings and $k_{l,rot} = 1.45\,\mathrm{W\,m^{-1}\,K^{-1}}$ in the x and y-direction for the rotor windings. Figure 3.10 shows the orientation of the rotor and stator windings in the global coordinate system.

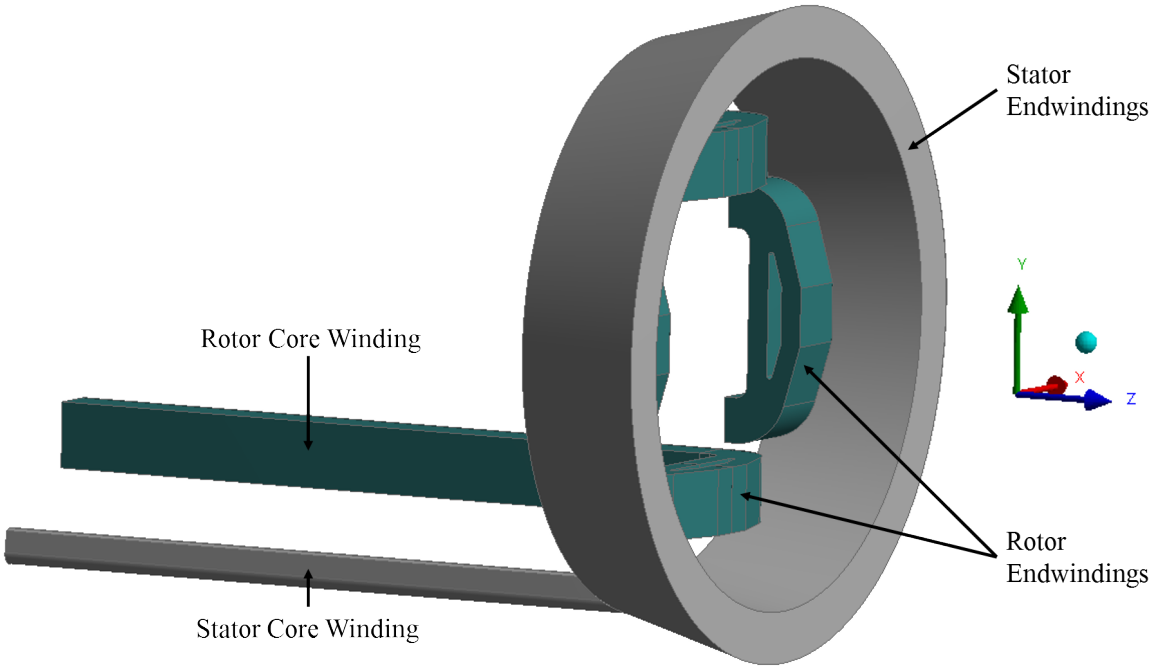
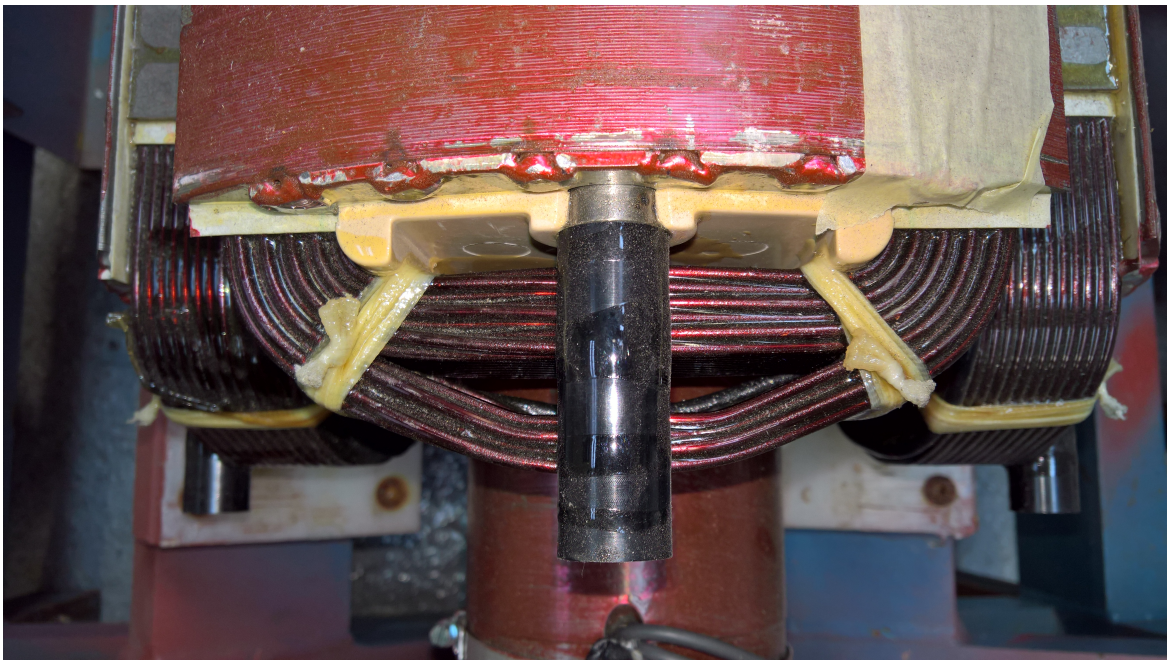


Fig. 3.10 Orientation of the rotor and stator windings in the global coordinate system

But in the endwinding region, the wire orientation changes as shown in figure 3.11. Methodologies have been developed in the past to model the change in wire orientation in the endwindings. Connor [13] split the rotor endwindings into straight and circular sections, used the orthotropic option for the straight sections and the cylindrical orthotropic option for the circular sections. The cylindrical orthotropic option enables the definition of anisotropic conductivity based on a cylindrical coordinate system, which is well suited to circular geometries. The downside of this modelling approach is the high manual user input required. Connor had to split the rotor windings into 18 different sections at the geometry stage and custom materials with different anisotropic conductivity axes had to be defined and assigned within Fluent.

The stator endwindings were modelled by dividing them into an inner section, where the wire orientation was assumed to be coincident with the axis of rotation, and an outer section, where the wire orientation was assumed to be circumferential around the axis of rotation and the cylindrical orthotropic option was used. The sudden change in dominant thermal conductivity direction from axial to circumferential created non-physical hotspots between the inner and outer endwinding sections, which were removed by creating copper bridges between them. To remove the high manual effort and improve the model accuracy, Connor identified the use of User Defined Functions (UDF) within Fluent to represent the change in



(a) Rotor Endwindings



(b) Stator Endwindings

Fig. 3.11 Rotor and Stator Endwindings of the Benchmark Machine

wire direction as future work. The novel endwinding modelling approach developed within this project is based on this idea.

UDFs make it possible to vary the magnitude of thermal conductivity in any direction instead of using a constant value for the orthotropic and cylindrical orthotropic modelling approaches. For the stator endwindings, a custom material with cylindrical orthotropic conductivity around the z-axis was defined and the axial, radial and circumferential conductivity values were defined dependent on the cell axial location. As the endwindings extend straight out of the slots before they start to bend (view figure 3.11b), the axial conductivity k_{ax}, the radial conductivity k_{rad} and the tangential conductivity k_{tan} for the first 20 % of the total axial endwinding length were defined according to the following equations:

$$k_{ax} = k_h \tag{3.5}$$

$$k_{rad} = k_{l,stat} \tag{3.6}$$

$$k_{tan} = k_{l,stat} \tag{3.7}$$

From here on, the windings start to bend towards the circumferential direction. A gradual change of thermal conductivity was implemented by assuming a bending radius r_b of 50 % of the total axial endwinding length and implementing a linear relationship between the conductivity components and the axial distance z according to the following equations:

$$k_{ax} = (1 - \frac{z}{r_b})k_h + \frac{z}{r_b}k_{l,stat} \tag{3.8}$$

$$k_{rad} = (1 - \frac{z}{r_b})k_{l,stat} + \frac{z}{r_b}k_h \tag{3.9}$$

$$k_{tan} = (1 - \frac{z}{r_b})k_{l,stat} + \frac{z}{r_b}k_h \tag{3.10}$$

The bending radius was based on measurements on the Benchmark Machine endwindings in multiple locations. For the final 30 % of the axial extension of the endwindings, the windings were assumed to revolve around the axis of rotation and the conductivity components were defined as:

$$k_{ax} = k_{l,stat} \tag{3.11}$$

$$k_{rad} = k_{l,stat} \tag{3.12}$$

$$k_{tan} = k_h \tag{3.13}$$

The gradual change in thermal conductivity from high to low for the axial component and vice versa for the radial and tangential components introduced by equations 3.8-3.10 increases the model robustness and avoids the creation of non-physical hot spots Connor identified without having to implement copper bridges.

To model the rotor endwindings, a custom material with orthotropic conductivity was created. Equivalent to the stator, the rotor endwindings extend in the axial direction initially after leaving the core. Hence the conductivity components for the initial 14 % of the total axial endwinding length were defined as:

$$k_x = k_{l,rot} \tag{3.14}$$

$$k_y = k_{l,rot} \tag{3.15}$$

$$k_z = k_h \tag{3.16}$$

Figures 3.10 and 3.11a show how the rotor endwindings bend from the z- towards the x- and y-direction (depending on the endwinding orientation) afterwards. In the bending region, the conductivity components are calculated depending on their z-coordinate and the coordinate of the axis the windings are bending towards. For the endwindings bending towards the x-direction, the conductivity components in the bending region are calculated according to the following equations:

$$k_x = \sqrt{(\frac{x}{r_{ew}}k_l)^2 + (\frac{z}{r_{ew}}k_h)^2} \tag{3.17}$$

$$k_y = k_{l,rot} \tag{3.18}$$

$$k_z = \sqrt{(\frac{x}{r_{ew}}k_h)^2 + (\frac{z}{r_{ew}}k_l)^2} \tag{3.19}$$

with $r_{ew} = \sqrt{z^2 + x^2}$. To calculate the components for the endwindings bending towards the y-direction, x and y must be exchanged in equations 3.17-3.19. After the bending region, the following equations are applied for an endwinding bending towards the x-direction:

$$k_x = k_h \tag{3.20}$$

$$k_y = k_{l,rot} \tag{3.21}$$

$$k_z = k_{l,rot} \tag{3.22}$$

Again, to calculate the components for the endwindings bending towards the y-direction, x and y must be exchanged in equations 3.20-3.22. While the outer endwinding bundle has a small section after the bending area in which the wires do not run perfectly parallel to the x- respectively y-axis, the angle between wires and axis is so small it can be considered negligible.

The gradual change in thermal conductivity in the rotor endwindings via UDFs improves the model robustness and reduces the manual effort required for the endwinding modelling, as it is not necessary to split the endwindings into several volumes and only one custom material needs to be created.

The developed approach for the modelling of anisotropic conductivity in the endwindings can be utilised for any endwinding shape and enables an accurate prediction of the local anisotropic conductivity components depending on the wire orientation. Additionally, it improves the model robustness due to the gradual change in the dominant direction of thermal conductivity.

The source code of the developed scripts can be found in appendix B.3.

3.7.3 Temperature Dependent Heat Generation

The copper losses in the rotor and stator windings can be calculated by determining the rotor/stator current I from electromagnetic FEA or experiments and measuring the rotor/stator winding resistance R at a known temperature T_0. The copper losses can then be calculated according to equation 2.1, which is repeated below:

$$P_{copper} = I^2 R$$

The rotor and stator copper losses are temperature dependent (view section 2.1.1), as the resistance of copper increases linearly with temperature according to equation 2.2 [15], which is repeated below:

$$R_{copper} = R_0(1 + \alpha_0(T_{copper} - T_0))$$

with T_{copper} being the winding temperature, R_0 the winding resistance at temperature T_0 and α_0 the winding temperature coefficient of resistance at T_0.

In ANSYS Fluent, heat losses are usually implemented into Conjugate Heat Transfer simulations by using the volumetric heat generation feature. The losses have to be defined as a

heat generation per volume ($\mathrm{W\,m^{-3}}$) and are evenly distributed over a part (e.g. the stator windings) by adding a source term to the energy equation in every cell. The best way to implement the copper losses accurately using the volumetric heat generation feature is to:

- Measure the rotor and stator resistance at a known temperature
- Run the machine under load and measure the steady-state rotor and stator currents and temperatures
- Calculate the average rotor and stator winding temperatures
- Calculate the hot rotor and stator resistances according to equation 2.2
- Calculate the rotor and stator copper losses according to equation 2.1
- Divide the copper losses by the rotor/stator winding volume according to Fluent and implement the result as a volumetric heat generation into the respective windings

While this approach is well suited for validation purposes, the main disadvantage for utilising it during the machine design stage is that the average winding temperatures are not known. They have to be estimated initially and subsequently adjusted based on the results of the CFD simulations as the copper losses depend on them, resulting in a time consuming iterative process. Additionally, the volumetric heat generation approach assumes a constant heat generation all over the windings. In reality, the local losses vary depending on the local temperatures, which can vary considerably within the windings.

To address the shortcomings of the traditional heat loss implementation, UDFs were developed for the rotor and stator windings. For every cell the local resistance is calculated using equation 2.2 based on the local cell temperature. The local heat generation is subsequently calculated based on the calculated resistance and the currents calculated via FEA using equation 2.1 and returned to the solver. Fluent automatically divides the returned value by the cell volume and implements the resulting source term into the enerqy equation for every cell.

The difference in simulation results using the new, temperature dependent loss calculation in comparison to using a constant volumetric heat generation is small for the Benchmark Machine. This was determined by running a simulation using the variable temperature approach based on experimental data and extracting the calculated copper losses. These values were then used as an input for a simulation using a constant volumetric heat generation for the rotor and stator windings. Figure 3.12 shows a comparison of the stator winding temperature rise calculated using the different approaches. The temperature rise was extracted from the geometric centre of the slots, averaged over all slots and normalised according to equation 5.4. The core length was non-dimensionalised according to equation 5.5.

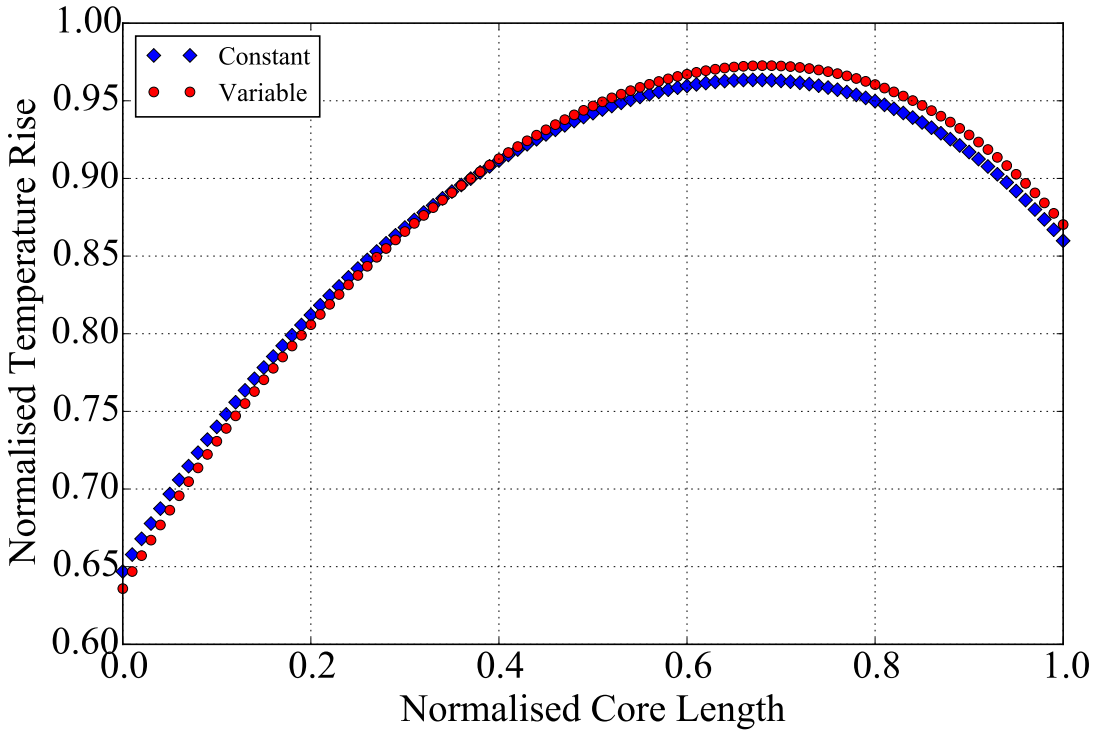


Fig. 3.12 Influence of the loss implementation approach on stator winding temperature rise of the BM CFD model; Temperature rise normalised according to equation 5.4

The stator winding temperature rise is almost identical for the two approaches. The peak temperature rise of the variable temperature approach is 0.9 % higher. The difference in average temperature rise is only 0.3 %. Towards the core ends, the temperature rise of the variable approach drop slightly below the temperature rise of the constant approach. This behaviour is expected, as more heat is generated in the hot spot approximately 70 % along the core length, and less heat towards the core ends in comparison to the constant approach. The difference in winding temperature rise between the two loss implementation approaches was even less distinct in the rotor windings.

The small difference between the modelling approaches for this particular machine is presumably caused by the high conductivity of the windings in wire orientation and the fact, that some of the heat generated within the core is conducted towards the endwindings and extracted from there. It is important to note that the difference between the two approaches might be considerably bigger for different machine types.

The developed approach for the implementation of temperature dependent copper losses is an important step towards improving multi-physics simulations, particularly if the software used for the EM simulations is not part of the ANSYS Workbench software package. It is only required to know the current and resistance at one temperature to calculate localised, temperature dependent losses. Even though the complexity of the energy equation increases, due to the interdependence of loss generation and local temperatures, no convergence issues were noted using the developed approach. It enables a more accurate implementation of the heat generated within the windings, resulting in a more accurate prediction of the local winding temperatures. Additionally, it is not required to iteratively adjust the copper losses during the machine design stage any more, reducing manual user input and computation time.

The source code of the developed script can be found in appendix B.4.

Chapter 4

Experimental Test Facility

A number of experimental tests were carried out to validate CFD results and gain an increased insight into the performance of the investigated machine. This chapter gives an overview of the setup of the laboratory and test rig and describes the conducted tests and the equipment used in detail. The test procedures, including post-processing of the collected data, are presented. The uncertainty associated with the test setup and measurement equipment is determined.

Mass flow rate and torque measurements were taken to validate the airflow modelling. Temperature measurements in the rotor and stator were used to validate the thermal performance of the Conjugate Heat Transfer model and quantify the benefit of the implemented design changes.

4.1 Lab and Test Rig Setup

Figure 4.1 shows an overview of the laboratory where the experimental testing described in this thesis was performed. The test rig area and the terminal box of the investigated generator can be seen at the bottom left. To ensure safe operation, the yellow door allowing access to the test rig area cannot be opened while the rig is powered.

The rig is controlled through a computer located in the control area on the right of the lab. Next to the control area, 6x3 m double doors open to the outside. During the tests these doors were opened to provide ventilation to cool the lab as a considerable amount of heat is generated while the machines are in operation, particularly at full load.



Fig. 4.1 Test laboratory overview

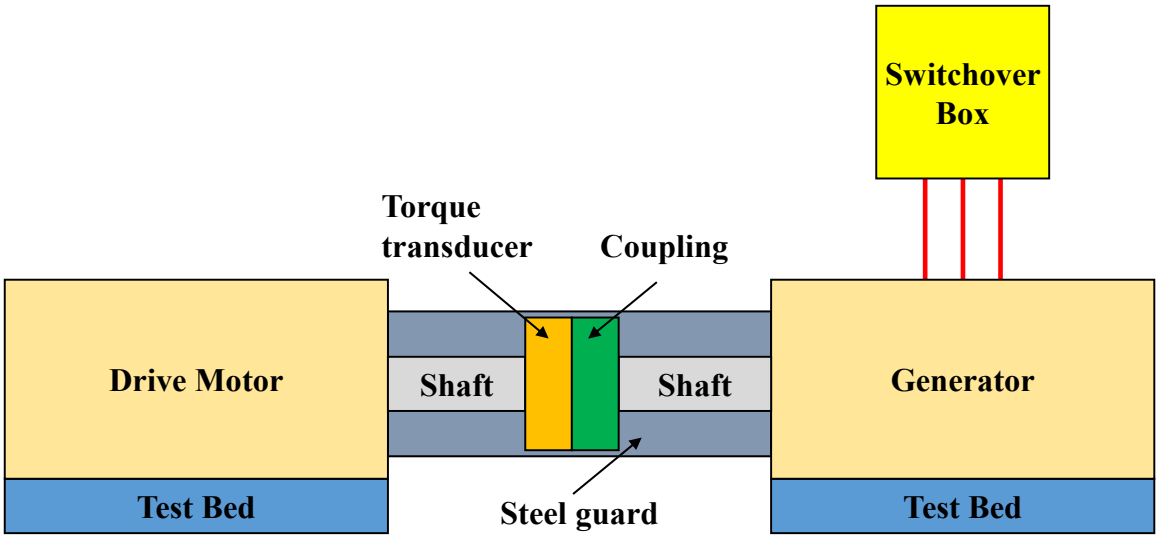


Fig. 4.2 Test rig schematic

A schematic of the test rig can be seen in figure 4.2. The investigated generator is located on the right. It is driven by an electric 860 kW motor. The coupling between the two machines is covered by a steel guard as an additional safety measure. A HBM T12 torque transducer is located between the drive motor and the coupling. It is used to control the test rig operation and measure the torque data collected during this project (view section 4.3). To enable power generation, the generator terminals are connected to a switchover box by the red wires on the right. Depending on the test requirements, the generator can be connected to either a 200 kW load bank located in the adjacent room or the electrical grid. This makes it possible to test the machine under a variety of different conditions such as load, power factor, etc.

A Vacon NX AC drive is used to control the drive motor. It is connected to a PC in the rig control area which uses the software Texcel, supplied by the motor manufacturer Froude Hofmann, to manually operate and monitor the rig. Data such as speed, torque, voltage, etc. can be monitored during operation and logged for later analysis.

4.2 Mass Flow Measurements

As the investigated machine is cooled by air being driven through its core, the total air mass flow rate through the machine is an important parameter determining the cooling performance. Additionally, flow rate measurements of the machine at different speeds up to its synchronous speed of 1500 RPM (at 50 Hz grid frequency) are used for CFD validation purposes.

Two inlets are located at the bottom side of the generator Non Drive End (NDE). Air is sucked through the machine by a centrifugal fan located at the Drive End (DE) and blown into the surroundings through four outlets (view figure 1.1). Local flow velocities vary substantially over the inlets and outlets making it difficult to determine an accurate velocity profile to calculate the flow rate through the machine. Covering the inlets or outlets with a duct would make it possible to calculate the flow rate. The inflow and outflow would be affected considerably, however, introducing measurement uncertainty and decreasing the validity of the results compared to normal machine operation.

To determine the machine flow rate, while minimising the change in inflow conditions, it was decided to build an airtight box, or plenum, around the machine inlets (view figures 4.3 and 4.4). The plenum walls were placed sufficiently far away from the inlets to not affect the inflow into the machine. The only opening was connected to a conical inlet duct manufactured according to B.S.848 [80]. Four pressure tappings are located equidistant circumferentially

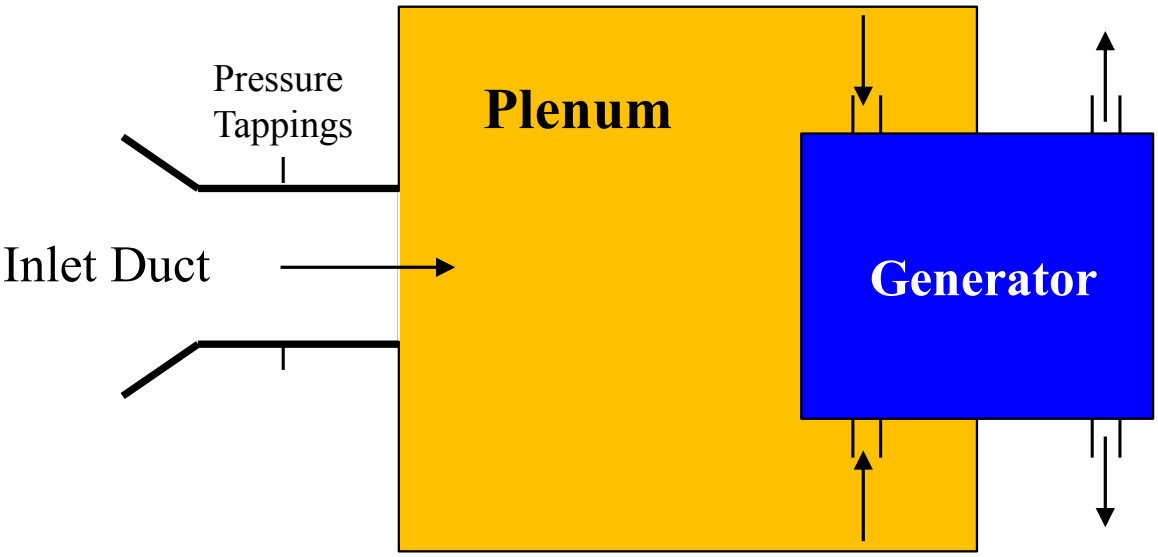


Fig. 4.3 Schematic of the mass flow measurement system



(a) View from inlet end (b) View from outlet end

Fig. 4.4 Plywood plenum designed for mass flow measurements

downstream of the inlet and connected together with plastic tubing. A Sensocon A1 Digital Differential Pressure Gauge is used to measure the averaged pressure drop over the four tappings. The mass flow rate $\dot{m}$ can be calculated from the pressure drop Δp using the following correlation provided in [80]:

$$\dot{m} = \alpha\varepsilon\pi\frac{d^2}{4}\sqrt{2\rho_u\Delta p} \tag{4.1}$$

The compound coefficient $\alpha\varepsilon$ is dependent on the duct Reynolds number and amounts to 0.94 for this application. ρ_u is the air density upstream of the conical inlet and has been determined by measuring the air temperature close to the inlet with a PT100 Resistance Temperature Detector (RTD). This approach to determine the flow rate has been used succesfully by other authors in the past [81].

The pressure gauge used for the pressure measurements has a measurement range of 0-60 Pa with a 1 % full scale accuracy. Measurements were logged using the integrated 4-20 mA output, which was connected to a DataTaker DT80 Datalogger.

Mass flow measurements were taken at 150 RPM intervals from 450-1500 RPM for the Benchmark Machine, and ranging from 150-1500 RPM for the Vented Prototype. The pressure measurements were logged with a frequency of 5 Hz and averaged over a timeframe of at least one minute. While the flow rate changes almost instantaneously with the change of rotational speed, the machine was run at each speed for at least one minute before averaging the data.

4.2.1 Plenum and Inlet duct Design

Determining the plenum dimensions was supported by initial CFD simulations. The performance of a 180° airflow model (view figure 4.5) inside the plenum was compared to one placed in an empty room.

Special attention was paid to the pressure drop added by the plenum and inlet duct, and the resulting changes in mass flow rate and inflow conditions into the machine. The findings of this investigation have previously been published in [82] by the author of this thesis.

The flow rate through the machine is dependent on the pressure drop the fan needs to overcome. As the duct and plenum reduce the air pressure at the generator inlet, the CFD results can be used to predict the reduction in mass flow rate when compared to unrestricted

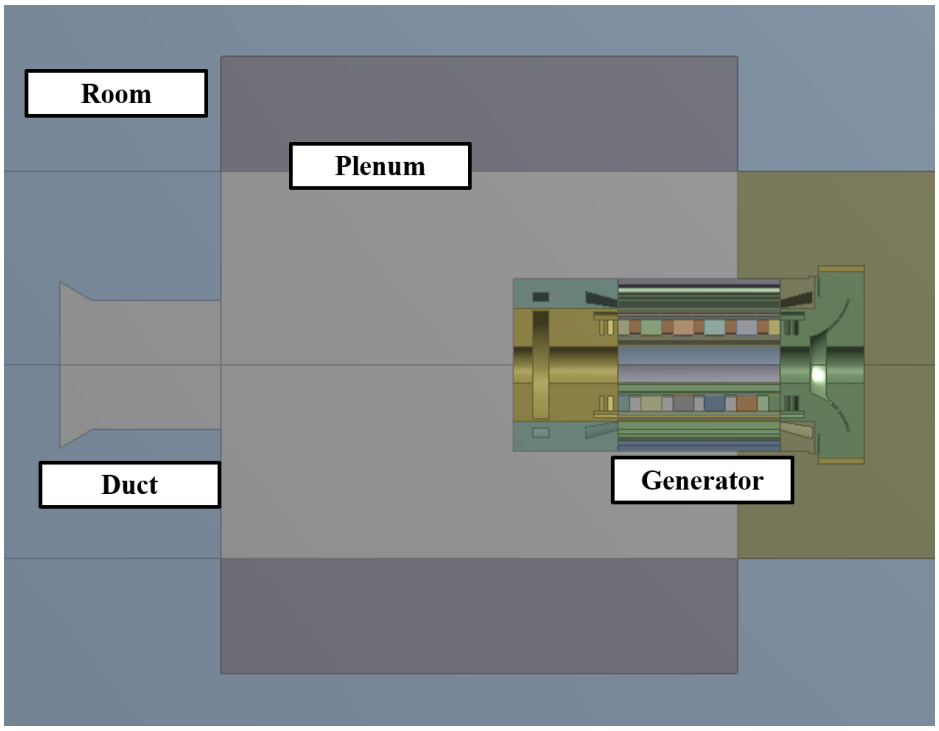


Fig. 4.5 CFD geometry used to determine the optimal plenum and duct dimensions

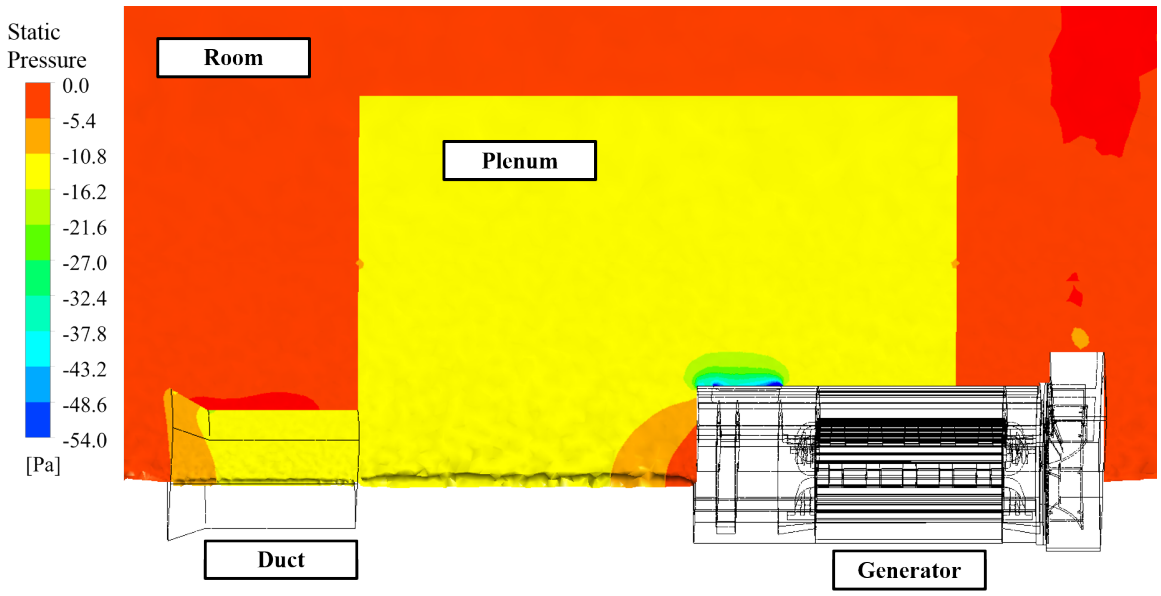


Fig. 4.6 CFD prediction of static pressure drop introduced by plenum and duct at 1500 RPM

operation. In figure 4.6, the static pressure drop introduced by the measurement system can clearly be seen.

The pressure drop is caused by the following factors:

Contraction/Expansion at the duct inlet/outlet
The contraction at the duct inlet and the sudden expansion at the outlet cause energy to be dissipated resulting in an irreversible pressure drop.

Friction and turbulent energy dissipation
Kinetic energy is converted to heat due to internal fluid friction, wall friction and turbulent dissipation resulting in an irreversible pressure drop.

Conversion of static pressure to kinetic energy in the duct
The increase in flow velocity in the duct causes the static pressure to drop resulting in a reversible pressure drop. Most of the kinetic energy cannot be recovered in this configuration however, as the majority of the flow impinges onto the generator back plate after exiting the duct. Placing a flow deflector between duct and generator would decrease the pressure drop, but was considered unnecessary for this application, as the change in flow rate of the optimal system configuration is small enough to be considered negligible

Initially, a model without the plenum system was solved to provide baseline data against which the influence of the measurement system was compared. Table 4.1 gives an overview over various simulated duct and plenum configurations and the influence they have on key parameters of interest, such as the change in mass flow rate and the measurement uncertainty.

Table 4.1 Comparison of various plenum and duct configurations

Duct (mm)	Plenum dimensions (m)	Added pressure drop (Pa)	Change in flow rate	Measurement uncertainty
200	1x1x1	148	-19.9%	0.2%
300	1x1x1	51	-6.2%	0.9%
100	1.9x1.5x1.6	337	-69.4%	0.1%
150	1.9x1.5x1.6	247	-40.3%	0.1%
200	1.9x1.5x1.6	148	-18.7%	0.2%
250	1.9x1.5x1.6	81	-9.5%	0.5%
300	1.9x1.5x1.6	47	-5.7%	0.9%
400	1.9x1.5x1.6	16	-2.2%	2.6%
500	1.9x1.5x1.6	8	-1.1%	6.2%

The added pressure drop at the machine inlet increases with decreasing duct diameter and plenum dimensions, reducing the flow rate. The duct diameter impacts the flow rate

substantially. Figure 4.7 shows how the flow rate through the generator changes with the duct diameter for a constant plenum size of 1.9 m x 1.5 m x 1.6 m. The mass flow rate has been normalised according to the following equation:

$$\dot{m}_{n,plenum} = \frac{\dot{m}}{\dot{m}_u} \tag{4.2}$$

with $\dot{m}$ being the mass flow rate for the specific duct diameter and $\dot{m}_u$ the flow rate for the unrestricted case.

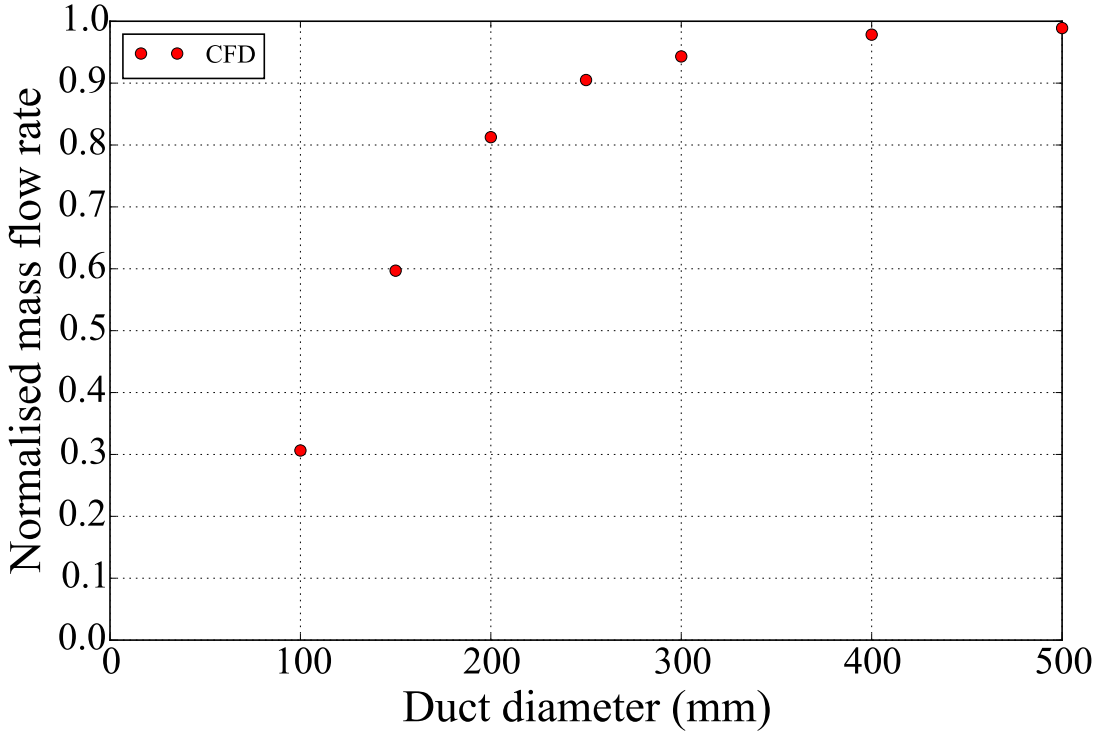


Fig. 4.7 Correlation between duct diameter and mass flow rate predicted by CFD for a constant plenum size; Mass flow rate normalised according to equation 4.2

The duct diameter determines the magnitude of the static pressure measured in the duct pressure tappings. Rearranging equation 4.2 shows that the pressure drop, which is used to calculate the mass flow rate, is inversely proportional to the fourth power of the duct diameter. As the measurement uncertainty of the used pressure gauge is constant over the full pressure range, the mass flow rate measurement uncertainty $\pm\dot{m}$ increases with the duct diameter as following:

$$\pm\dot{m} \sim d_d^4 \tag{4.3}$$

As a result of the CFD investigations, it was decided to use a 400 mm duct. It enables a reasonable measurement uncertainty for 30-100 % synchronous speed while decreasing the flow rate by only 2.2 %. The dimensions of the manufactured plenum were chosen as 2.44 m x 2.00 m x 2.00 m, utilising all the available space around the test rig (view figure 4.4).

4.3 Torque Measurements

Torque measurements at a variety of rotational speeds were taken for validation purposes and compared to the windage calculated by CFD. To avoid uncertainty with dividing the measured torque into electromagnetic torque and torque produced by friction and windage, all torque measurements were carried out at no load. The rotor was disconnected electrically from the exciter in order to minimise the torque created by residual magnetism.

A HBM T12 Torque Transducer, located between the drive motor and the coupling, was used to determine the torque. It can measure torque from 0-10 kNm with a 0.03 % full scale accuracy. The collected data was measured with a sampling rate of 300 Hz and logged via a HBM QuantumX MX460B pulse and frequency measurement module connected to the torque transducer.

During the first two hours of operation, the torque decreases steadily, as shown in figure 4.8. This is mainly caused by the warming up of the grease in the bearings, decreasing its viscosity and thus reducing friction. Therefore all torque tests have been performed after warming up the machine for at least two hours.

Torque measurements were taken at 150 RPM intervals from 150-1500 RPM. After the initial warmup period, the rig was stopped and the torque transducer zeroed. The speed was then increased (initially to 1500 RPM) and kept constant for 20 minutes. This procedure was repeated for the subsequent measurements with decreased speed. A slight drop in torque was observed over the first few minutes after every speed change. Therefore the torque data was averaged over the steady value recorded over the last 10 minutes of each operating point.

The measured torque includes the friction generated in the bearings. As this is not considered in the CFD model, it needs to be estimated and subtracted from the experimental torque to make the data comparable. The actual bearing friction is complex to calculate and is influenced by a variety of factors, such as the type of bearing, the bearing age, the bearing arrangement, etc. As a lot of the influencing factors were unknown, a simple analytical approach was chosen to estimate the bearing friction torque T_B from the bearing friction

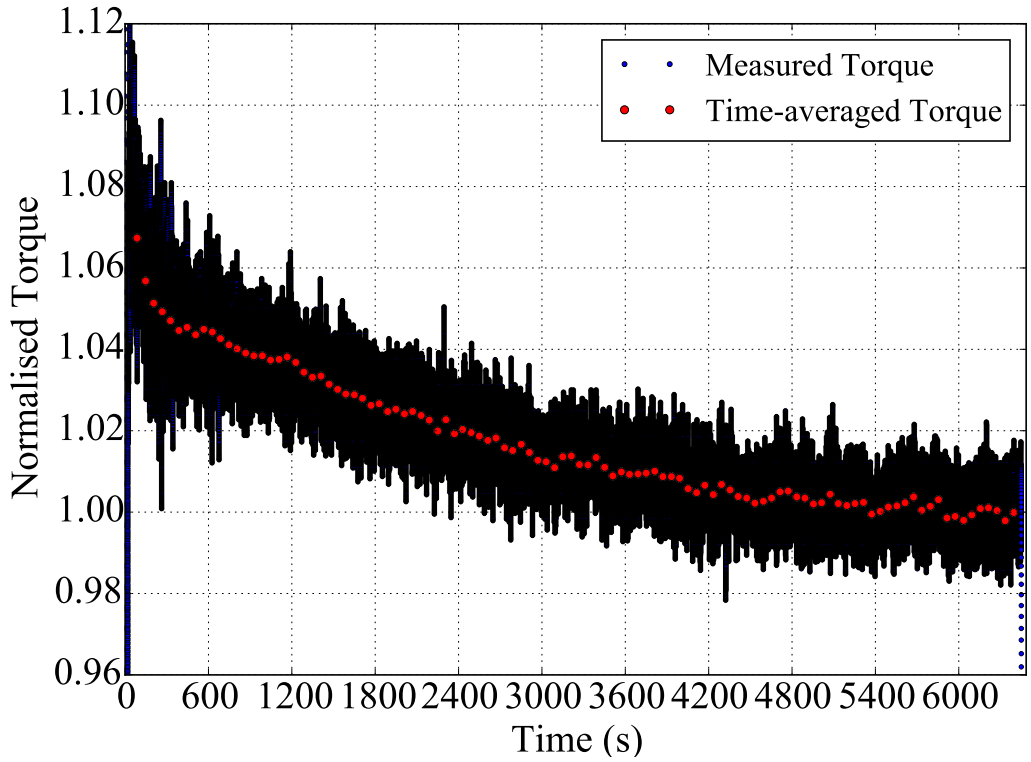


Fig. 4.8 Measured torque during the first two hours of operation; Torque normalised according to equation 5.3

coefficient μ_B, the radial bearing load F_r and the bearing bore diameter d_B according to the following equation [6]:

$$T_B = 0.5\mu_B F_r d_B \tag{4.4}$$

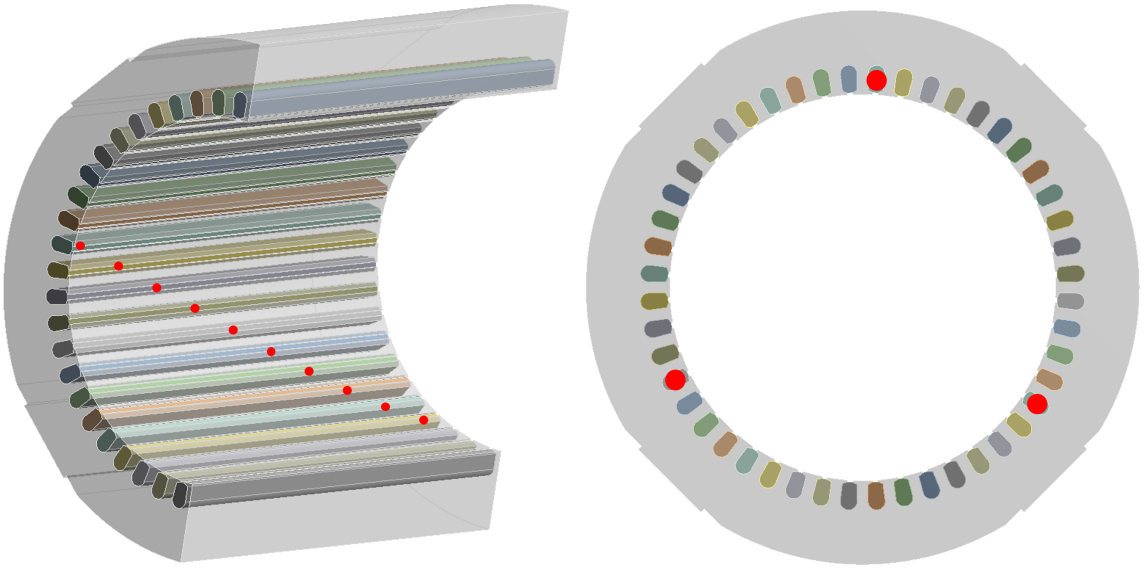
4.4 Thermal Measurements

During the generator manufacture, PT100 Class B RTDs were built into the rotor and stator windings in various locations (view sections 4.4.1 and 4.4.2) . Their uncertainty is $\pm 0.4\,^{\circ}\mathrm{C}$ at room temperature and $\pm 1.2\,^{\circ}\mathrm{C}$ at the rated winding temperature of $180\,^{\circ}\mathrm{C}$. As the majority of the losses are generated in the windings, the hot spots are to be expected there. The temperature measurements were used for the thermal validation of the Conjugate Heat Transfer CFD model as well as to gain a better understanding of the thermal behaviour of the machine under normal operating conditions. As a result of the thermal measurements (in

conjunction with the CFD modelling), the Benchmark Machine hot spot was identified and targeted to be cooled more efficiently through the addition of radial stator vents.

4.4.1 Stator Measurements

33 RTDs were located in the stator core windings. 30 RTDs were distributed equidistantly over 10 axial locations as shown in figure 4.9a. RTDs in adjacent axial locations are placed one slot apart. These RTDs were placed in the middle of the slot next to the slot separator as shown in figure 4.10. The 3 sensors in the same axial location were placed 120° apart as shown in figure 4.9b. 45 % along the core length (measured from the NDE), 3 additional RTDs were placed in the bottom, centre and top of the same slot to gain a better understanding of the temperature variation over the slot height.



(a) Axial distribution (b) Distribution of RTDs in the same axial location

Fig. 4.9 Location of the RTDs (in red) distributed over the stator core windings

12 RTDs were distributed circumferentially over the stator endwindings next to the phase separators, 6 on each end of the machine. 4 additional RTDs were used to measure the air temperature close to the entrance and exit of the stator-casing duct and airgap.

To minimise the impact of RTDs on the thermal performance of the machine, thin film RTDs were used in the core windings. Bead RTDs were chosen for the sensors in the endwindings and air. The stator temperatures were logged every 10 seconds with a DataTaker DT80 Datalogger, making it possible to monitor temperatures in real time as well as store them

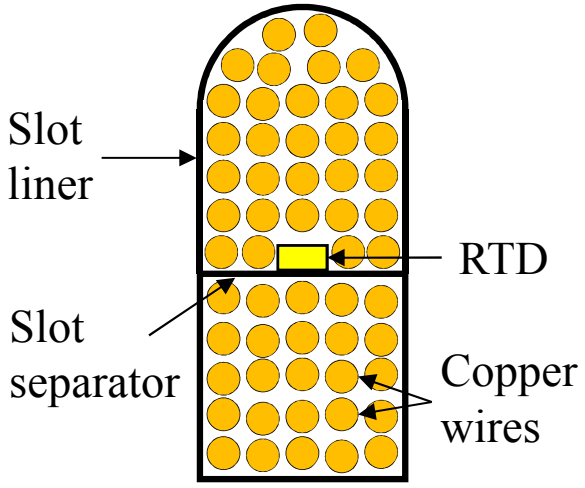


Fig. 4.10 Schematic showing RTD location in the stator slots

for postprocessing. In initial tests, electromagnetic interference issues were observed for approximately half of the core RTDs, measuring sudden, unphysical jumps in temperature when the machine load was increased to full load. This issue was resolved by increasing the RTD excitation current coming from the datalogger from 200 μA to 2.5 mA.

Placing RTDs in the stator core windings is a tricky process fraught with uncertainty. The RTD location is limited to the upper half of the slot above the slot separator shown in figure 4.10. But the exact axial, radial and circumferential position of the sensors can change when the machine is wound and the measured temperature depends on the exact location. It is not possible to determine the exact sensor position except for cutting up the stator, thus destroying the machine.

Additionally, manufacturing uncertainties can cause temperature variations between slots (view sections 5.3.1 and 7.4.2). The RTDs and connection cables are fragile and can easily be damaged during manufacture and transportation. Fortunately, only one of the stator RTDs embedded in the Benchmark Machine, and none of the RTDs embedded in the Vented Prototype, had been damaged during manufacturing.

4.4.2 Rotor Measurements

20 bead RTDs were placed in the rotor windings, 12 of them located in the core and distributed equidistantly over 6 axial locations. These RTDs were placed in the centre of the trailing edge windings of two adjacent rotor poles. The other sensors were located on the surface

of the endwindings of the same poles as used for the core RTDs in the locations shown in figure 4.11.

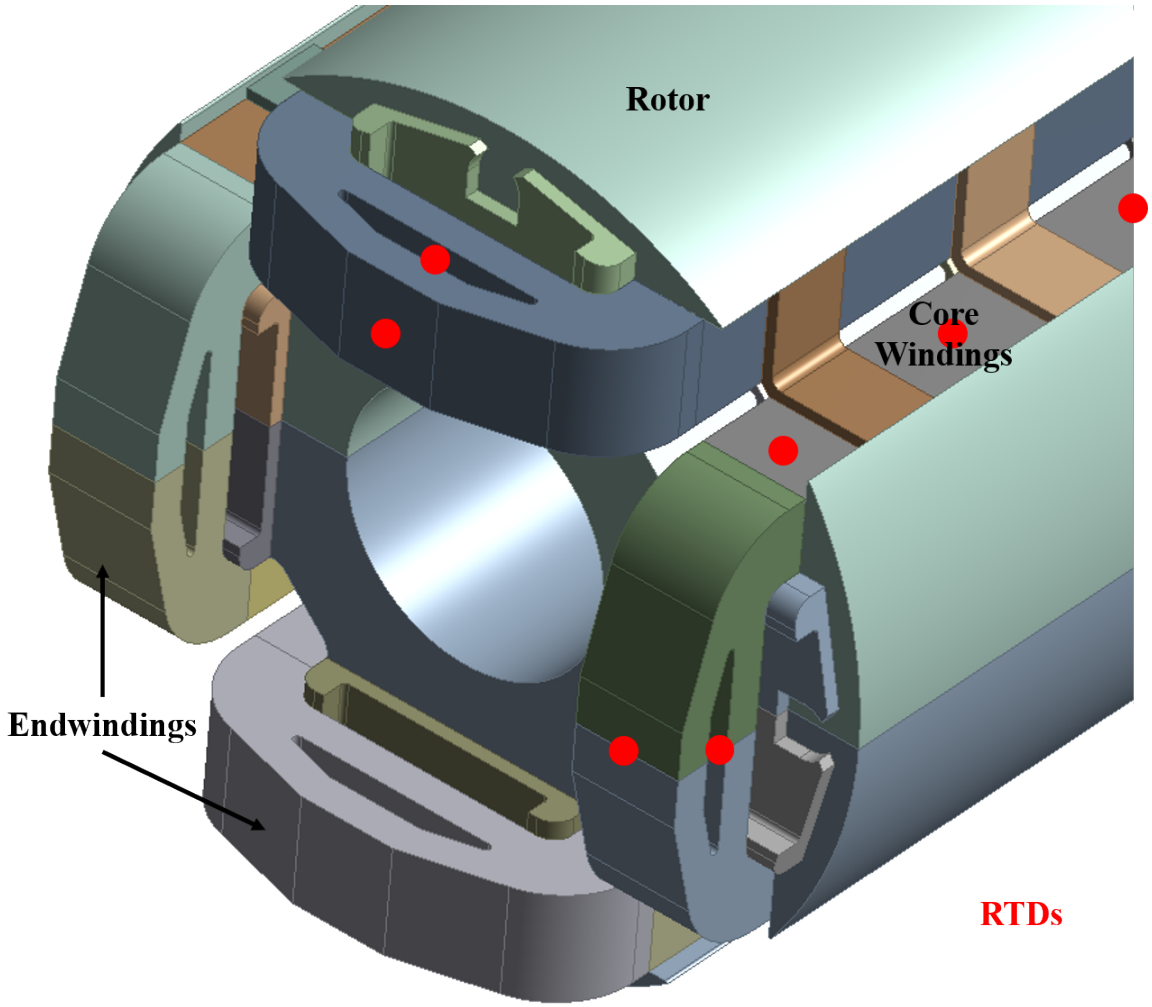


Fig. 4.11 Locations of the RTDs (marked in red) distributed over the rotor core windings and endwindings; location mirrored at other machine end

Logging the measured temperatures from the rotor RTDs during machine operation is more complicated than for the stator. They cannot just be connected to a stationary datalogger as they are rotating. Two different rotor datalogging systems have been used during this project:

Yoyo Ring

Five YL-T12 TempLog dataloggers, each capable of logging two RTDs, were placed in a housing designed by Cummins Generator Technologies (CGT). It is bolted to the Non Drive End of the shaft, outside of the generator casing. The rotor RTD cables leave the machine at

the NDE through two holes drilled into the shaft and can thus be connected to the datalogging system. This system has a few disadvantages, however:

- It is only possible to log 10 of the 20 rotor RTDs simultaneously.
- Rotor temperatures cannot be monitored in real time.
- The heat generated in the generator core caused the batteries powering the dataloggers to fail repeatedly.

Real Time Telemetry Ring

Due to the inability to monitor rotor temperatures in real time and the recurrent failures of the previously described system, a different rotor telemetry system was developed by CGT. It can be bolted to the shaft NDE as well and is capable of logging up to 32 RTDs simultaneously. Additionally, the rotor current and voltage can be measured. A key advantage of this system is that the logged data can be sent to a computer during operation using a wifi transmitter, enabling real time monitoring. For the rotor RTDs, the same measurements uncertainties as associated with the stator RTDs are relevant (view section 4.4.1). Of the 20 rotor RTDs two were found to be faulty after manufacturing.

4.4.3 Air Temperature Measurements

The temperature of the air flowing into the machine determines the heat that can be removed from the machine core by convection. Therefore additional RTDs were placed in the surrounding air. The temperatures at each inlet and outlet as well as in the centre of the lab were monitored. As the lab facility is not actively cooled through air-conditioning, the collected data had to be made independent of the environment temperature, which varied depending on the day and time the measurements were taken. To achieve this, the temperatures over both inlets were averaged and subtracted from all temperature measurements.

4.4.4 Test Procedure

Thermal tests were performed at various loads, ranging from 25 %-100 % full load and 0.8-1 power factor. To start the test, the generator speed was increased to 1500 RPM at no load. It was then synchronised with the grid and the load was increased to the test load. Due to the size of the machine and the low thermal conductivity of some parts, it takes several hours for the generator to heat up and all temperatures to become steady. Temperatures were considered to be steady if the change in temperature of every RTD was below 1 °C/hour for

at least one hour of operation. It takes approximately 4 hours to reach steady state conditions from no load to full load. Subsequent steady-state times after load changes were found to be shorter and dependent on the load.

4.5 Loss Measurements

In addition to the loss data supplied by the machine manufacturer for the Benchmark Machine, measurements were taken in the University's test facility. The loss data for the Vented Prototype was measured exclusively at the University. The separate losses described in section 2.1 were determined according to BS EN 60034-2-1:2014 section 7.1.3 (Method 2-1-2B) [18].

A Newtons4th PPA2530 power analyser was used to measure the stator current, voltage, power factor and output power. It can measure voltages up to 3000 V_{pk} with the following accuracy:

$$\pm V = 0.0004 V_{meas} + 1.201\,V + 0.04 f \tag{4.5}$$

with V_{meas} being the measured voltage and f the frequency in Hertz. Currents up to 300 A_{pk} can be measured with the following accuracy:

$$\pm A = 0.0004 I_{meas} + 0.1201\,A + 0.04 f \tag{4.6}$$

with I_{meas} being the measured current. The stator copper losses were determined from the 3-phase averaged stator current I_{stat} and the stator resistance at thermal steady state R_{stat}:

$$P_{copper,stat} = I_{stat}^2 R_{stat} \tag{4.7}$$

The stator resistance was calculated by measuring stator resistances at various temperatures and developing a linear correlation between the average stator winding temperature and the stator resistance.

The rotor voltage and current were measured using the real time telemetry ring described in section 4.4.2. The rotor copper losses were determined by measuring the rotor voltage V_{rot} and current I_{rot} when the machine had reached thermal steady state conditions according to equation 4.8:

$$P_{copper,rot} = V_{rot} I_{rot} \tag{4.8}$$

By taking these measurements at various temperatures, and plotting them against the average rotor winding temperature, a linear relationship between average rotor winding temperature and rotor resistance was developed which was implemented into the CFD models.

The friction and windage losses were determined by running the machine at synchronous speed and no load with the rotor field disconnected from the exciter, as described in section 4.3. The windage and friction losses can be calculated from the measured torque T_{noload} and the rotational speed ω in $\mathrm{rad\,s^{-1}}$ according to the following equation:

$$P_{w+f} = \omega T_{noload} \tag{4.9}$$

The iron losses were determined by running the machine at synchronous speed and no load with the rotor field connected to the exciter. The iron losses are calculated from the measured torque $T_{noload,mag}$, the rotational speed ω, the windage and friction losses P_{w+f} and the excitation current I_{exc} and voltage V_{exc} according to the following equation:

$$P_{iron} = \omega T_{noload,mag} - P_{w+f} - V_{exc} I_{exc} \tag{4.10}$$

These are the combined rotor and stator iron losses. The distribution of the total iron losses between the rotor and stator, which is required for the CFD simulations, was determined by 2-D electromagnetic FEA conducted by Nuzzo. Details of the setup and results of the FE models can be found in [37, 74, 75]. While the iron losses are traditionally measured at no load, they increase under load. Hence, the iron loss measurements were only used for the validation of the FE models and not as an input for the CFD simulations.

The iron loss of the Benchmark Machine was determined based on measurements taken by Nuzzo [37]. All other experiments were conducted by the author of this thesis.

Chapter 5

Experimental Validation and Analysis of the Benchmark CFD Model

In this chapter, the CFD and experimental test results of the Benchmark Machine are presented, analysed, compared and discussed. Figure 5.1 gives an overview of the conducted experimental tests.

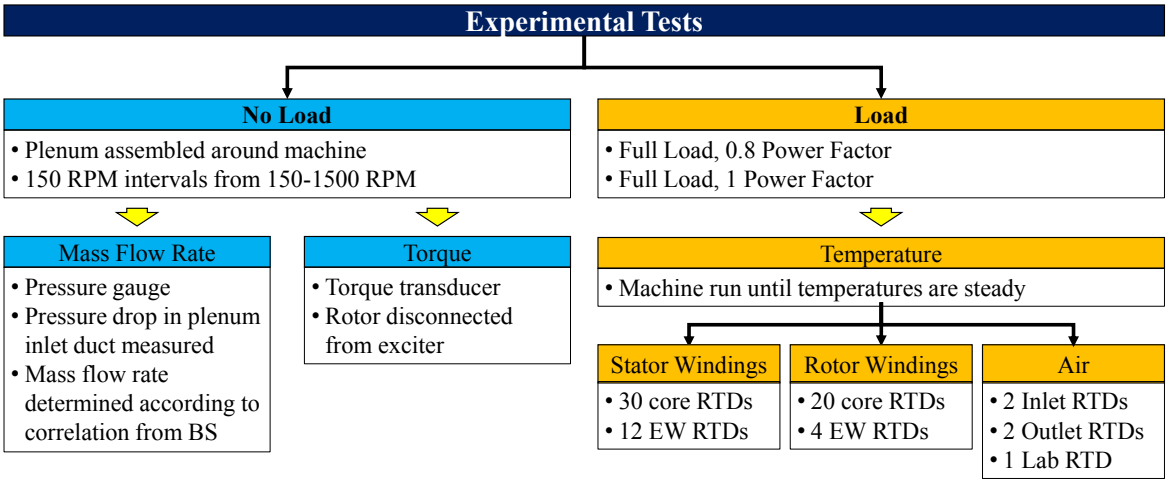


Fig. 5.1 Overview of conducted experimental tests

5.1 Mass Flow Results

The mass flow rate was measured experimentally using the plenum system described in section 4.2. Measurements were taken at 150 RPM intervals in a rotational speed range from

450-1500 RPM. Figure 5.2 shows the relationship between total mass flow rate through the machine and the rotational speed with and without grilles covering the inlets and outlets. The mass flow rate was non-dimensionalised according to the following equation:

$$\dot{m}_n = \frac{\dot{m}}{\dot{m}_{ref}} \tag{5.1}$$

with $\dot{m}$ being the measured mass flow rate and $\dot{m}_{ref}$ the reference mass flow rate, defined as the experimentally measured flow rate of the Benchmark Machine at synchronous speed without grilles covering the inlets and outlets.

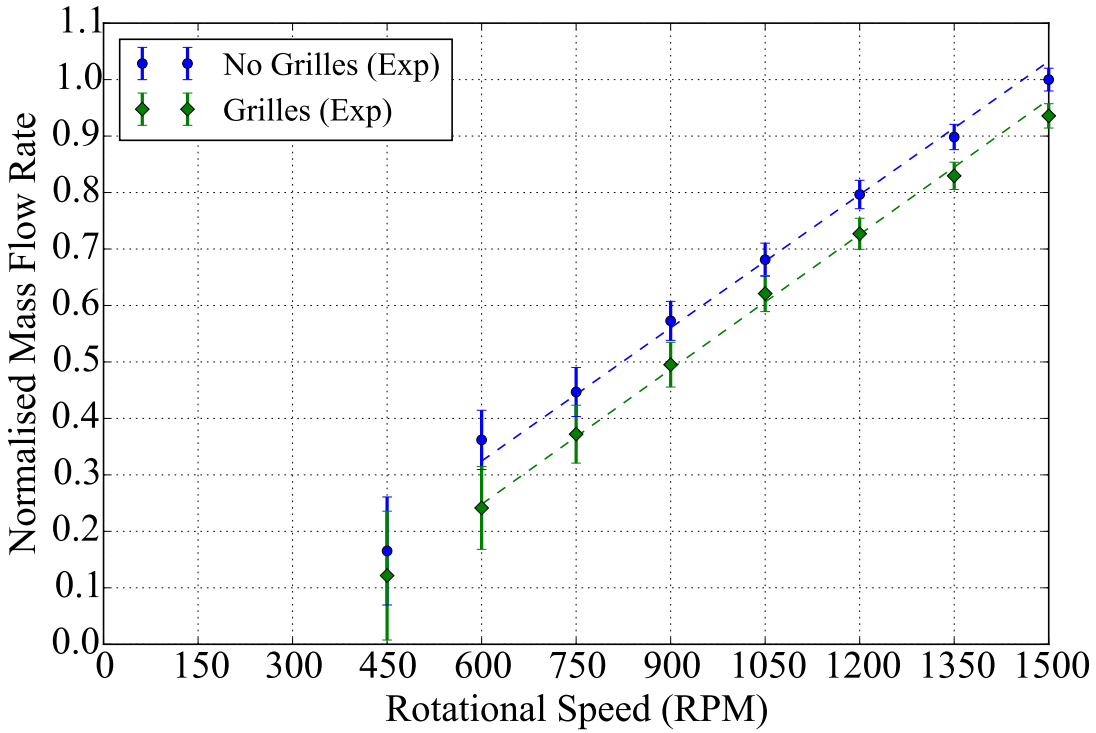


Fig. 5.2 Experimentally measured mass flow rates through the Benchmark Machine at various rotational speeds; Mass flow rate normalised according to equation 5.1

In normal operation, the machine inlets and outlets are covered with grilles for health and safety reasons. Modelling the flow through the grilles correctly requires a very fine mesh in this region and would therefore be computationally expensive. For that reason, the grilles were not considered in the CFD model and removed from the machines during all experimental tests for validation purposes. As the grilles restrict the air flowing in and out of

the machine, the total flow rate through the machine is higher without them. The difference amounts to 6.4 % at synchronous speed (1500 RPM).

Figure 5.2 clearly shows that a linear relationship exists between the mass flow rate and the rotational speed for 600-1500 RPM. The trendlines in figure 5.2 were calculated using the Ordinary Least Square (OLS) method. They show a good fit to the experimental data with R^2 values of 0.998 with and 0.991 without the grilles. The linear trend cannot be observed at lower rotational speeds. This is most likely caused by the fan stalling and the increasing measurement uncertainty. The mass flow rates are calculated according to equation 4.1 from the pressure drop measured at the inlet duct. As the measurement uncertainty of the used pressure gauge is constant at 1 % full scale and the pressure drop decreases with the flow rate, the measurement uncertainty is higher at low flow rates, as indicated by the error bars in figure 5.2.

The CFD model used for the determination of the mass flow rate through the machine was set up as described in chapter 3. To reduce computation time, the energy equation was turned off and only the fluid flow equations were solved. As air is modelled as incompressible with a constant viscosity, the fluid temperature does not influence the flow solution. The mass flow rate was monitored at the machine inlet, which was defined as a separate surface during the meshing stage. As a 180° periodic model was utilised, the monitored flow rate $\dot{m}_{cfd}$ had to be multiplied by 2. Additionally, it had to be adjusted for the difference in density between CFD (ρ_{cfd}) and experimental data (ρ_{exp}) for validation according to the following equation:

$$\dot{m} = 2\dot{m}_{cfd}\frac{\rho_{exp}}{\rho_{cfd}} \tag{5.2}$$

Figure 5.3 compares CFD and experimental mass flow rates at different speeds. The flow rates have been normalised according to equation 5.1. Only the experimental flow rates without the grilles are shown, as the grilles were not considered for the CFD model. Two different approaches were used to model rotation: Multiple Reference Frame, a steady state approach, and Sliding Mesh, a transient approach. More details on the rotation modelling approaches can be found in section 3.4.4. The MRF model was run for rotational speeds ranging from 150-1500 RPM at 150 RPM intervals. The SM model was only run at 1500 RPM due to its high computational expense.

Equivalent to the experimental data, the CFD MRF results show a linear correlation between rotational speed and mass flow rate for 600-1500 RPM, predicting the mass flow rate trend correctly. The computed mass flow rates are slightly lower in comparison to the experimental

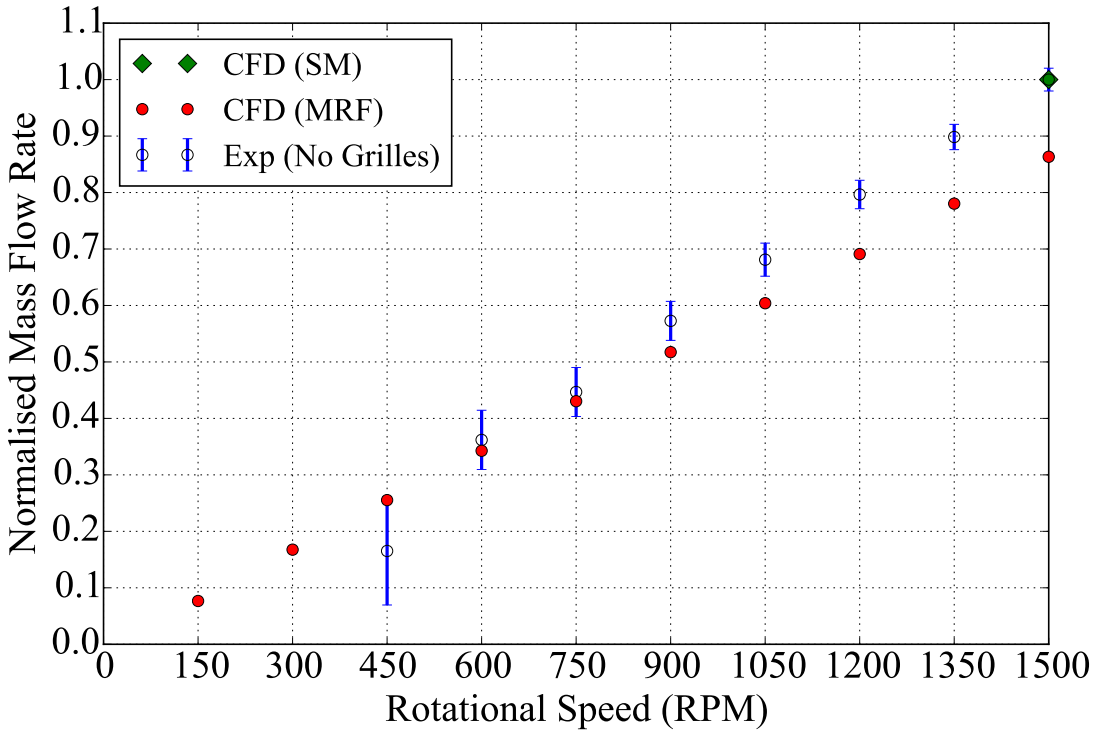
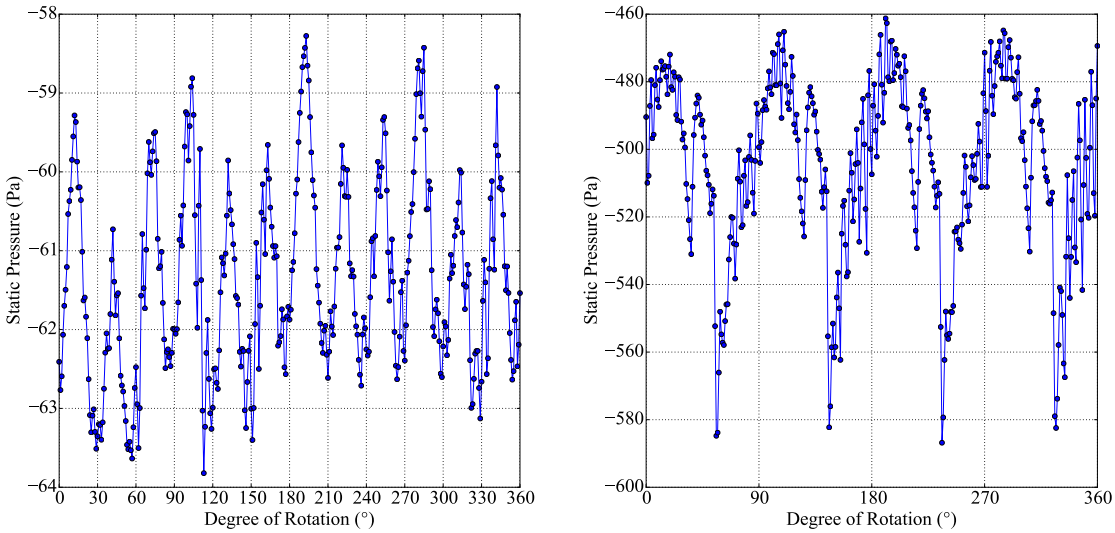


Fig. 5.3 Comparison of CFD and experimentally measured mass flow rate through the machine at various rotational speeds; Mass flow rate normalised according to equation 5.1

data with a 13.7 % difference at synchronous speed. The results of the SM simulation makes it clear that the difference between computational and experimental data is caused by the rotation modelling approach. The flow rate predicted using the SM approach is almost identical to the measured flow rate, differing by only 0.003 %. However, it is currently not feasible to investigate electrical machines in detail using the SM approach with a desktop PC (view section 3.4.4).

The reason for the lower flow rates predicted by the MRF approach is that the pumping effect occurring between the salient rotor and stator, as well as the fan blades and the fan housing, cannot be predicted correctly using a steady state approach. A transient simulation is required to model pressure fluctuations with time and the influence they have on the total flow rate correctly. Figure 5.4 illustrates the pressure fluctuation over time caused by the interaction of rotating and stationary parts during a Sliding Mesh simulation with a 1° time step.

On the left of figure 5.4, the area-weighted averaged static pressure at the machine inlet is shown. The pressure fluctuates with a 30° periodicity, which is caused by the interaction



(a) Average inlet pressure

(b) Local airgap pressure

Fig. 5.4 Pressure fluctuation with time during a Sliding Mesh simulation with a 1° time step

of the 12-blade fan with the fan housing. The difference between minimum and maximum pressure is 9 % of the average inlet pressure. On the right side of figure 5.4, the local pressure in the airgap at the axial core centre can be seen. The passing of the salient 4-pole rotor causes the pressure to oscillate with a 90° frequency. The magnitude of the pressure oscillation is high, amounting to 24.9 % of the average local pressure. This effect cannot be captured using the steady-state MRF approach, which explains why the flow rate is underpredicted in comparison to the SM simulation and experimental results.

The mass flow split between the stator-casing duct and the core region is independent of the rotation modelling approach. According to CFD results, 65 % of the total mass flow rate pass through the stator-casing duct, while the remaining 35 % pass through the airgap and interpolar space.

5.2 Torque Results

The torque measurements were taken as described in section 4.3 at 150 RPM intervals from 150-1500 RPM. Figure 5.5 shows the relationship between the measured windage and friction

torque and the rotational speed. The torque has been non-dimensionalised according to the following equation:

$$M_n = \frac{M_{windage}}{M_{ref}} \tag{5.3}$$

with $M_{windage}$ being the difference of measured torque M and the bearing torque M_B calculated according to equation 4.4. M_{ref}, the reference torque, is defined as $M_{windage}$ at synchronous speed. The CFD torque was determined from the same simulations described in the previous section 5.1. It was calculated by exporting the moments of all rotating surfaces about the axis of rotation and multiplying them by 2, as a 180° periodic model was utilised.

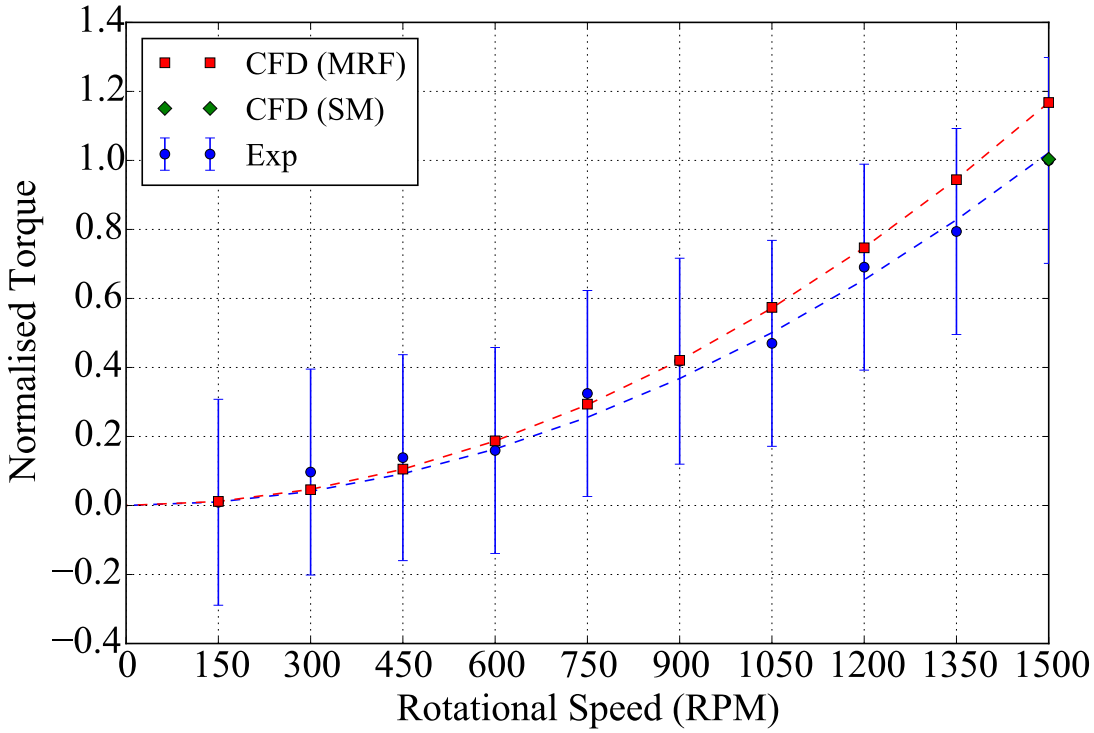


Fig. 5.5 Comparison of CFD and experimentally measured windage and friction torque of the benchmark machine at various rotational speeds; Torque normalised according to equation 5.3

Figure 5.5 shows good agreement between CFD and experimental results. The maximum difference between CFD MRF and experimental data amounts to 16.8 % at synchronous speed. Using the SM approach, the difference between CFD and experimental data is 0.3 %. A square relationship between rotational speed and windage and friction torque can be observed, which is predicted correctly by the CFD simulations. The trendlines were

calculated using the OLS method assuming a y-intercept of 0. They show an excellent fit to the data points with a R^2 value of 0.983 for the experimental and 1.000 for the CFD MRF data.

As the utilised torque transducer is used for measuring torque and controlling the rig at full load, its relative accuracy at no load is relatively poor with a measurement uncertainty of $\pm 14.9\,\%$ at synchronous speed. As the agreement between CFD and experimental data was good, it was not deemed necessary to design a test rig with an improved measurement uncertainty. It is also important to keep in mind that a simple analytical correlation has been used for the calculation of the bearing losses, adding some additional measurement uncertainty which could not be quantified within this project. An accurate determination of the bearing losses would require disassembling the machine completely and measuring the torque of the bare shaft.

According to the CFD results, the majority of the torque is produced by the fan: The MRF approach attributes 90.4 % of the total torque (excluding the bearing torque) to the fan. The SM approach predicts 87.0 % of the total torque (excluding the bearing torque) to be produced by the fan.

5.3 Thermal Results

For the thermal validation, the machine was run at various power factors and loads. This chapter focusses on the thermal results for full load and a power factor of 0.8, as this is the operating point the machine is designed for. Temperatures were measured in multiple locations in the stator and rotor windings as described in section 4.4. To enable a comparison to CFD temperatures and make test data taken on different days directly comparable, the temperatures at both inlets were averaged and subtracted from the winding temperatures. The resulting temperature rise was non-dimensionalised according to the following equation:

$$T_n = \frac{T - T_{in}}{T_{ref} - T_{in}} \tag{5.4}$$

with T being the measured temperature, T_{in} the averaged inlet temperature and T_{ref} the reference temperature, defined as the peak stator winding temperature at full load and 0.8 PF. The core length l was non-dimensionalised by dividing it through the total core length L

according to the following equation:

$$l_n = \frac{l}{L} \tag{5.5}$$

The NDE of the core is defined as the axial position corresponding to zero l_n and the core DE is defined as a core length of one l_n as shown in figure 5.6. This convention follows the air flow direction through the machine.

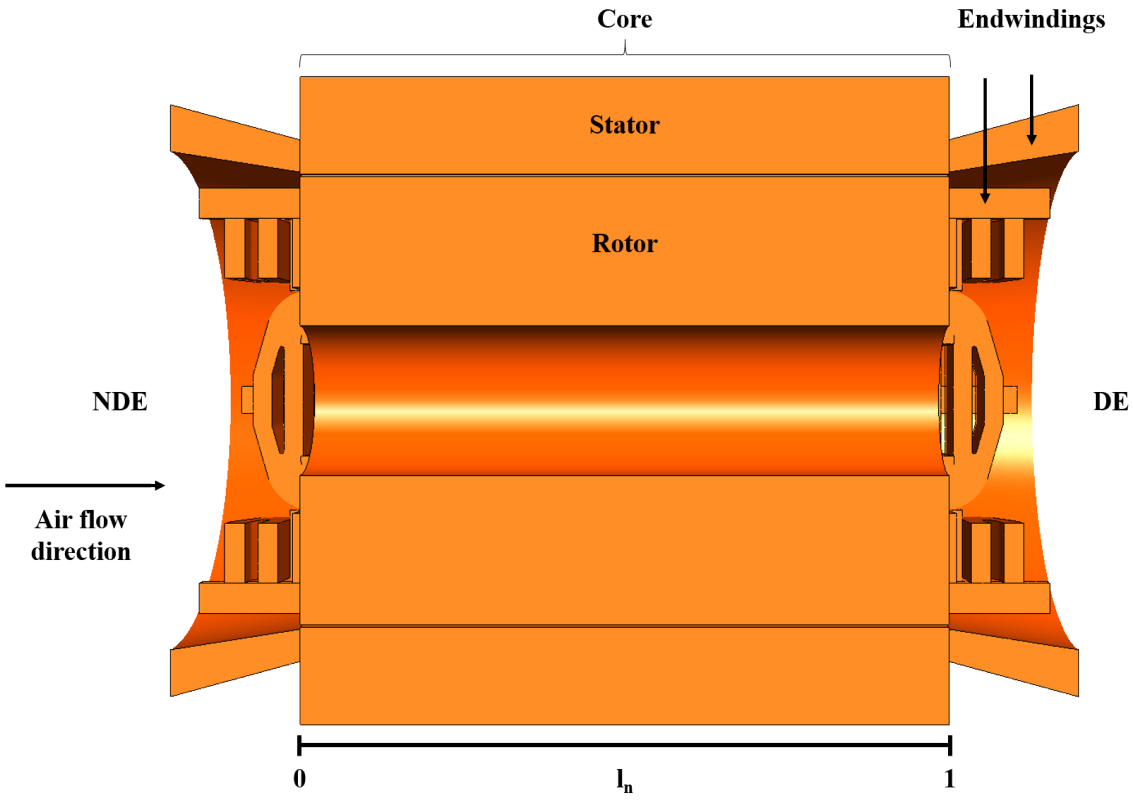


Fig. 5.6 Core length schematic

The stator copper losses implemented into the CFD model were calculated according to equation 4.7 based on the experimentally measured 3-phase averaged stator current and the resistance calculated based on the measured average stator winding temperature. The rotor copper losses were calculated according to equation 4.8 based on the experimentally measured rotor current and voltage. The exciter losses were assumed to be 10 % of the rotor copper losses. The rotor and stator iron losses were implemented based on Nuzzo's [37] electromagnetic FEA results. The stray losses were taken from the manufacturer's data sheet and distributed over the main rotor and stator iron and the exciter rotor and stator iron based on volume.

5.3.1 Stator Results

The experimentally measured stator winding temperature rise in the core at full load and a power factor of 0.8, displayed in figure 5.7, shows a considerable variation between RTDs in the same axial location with a maximum variation of 17.3 % at 0.65 l_n. RTDs in the same axial location (locations 1-3) are situated 120° apart as explained in section 4.4.1.

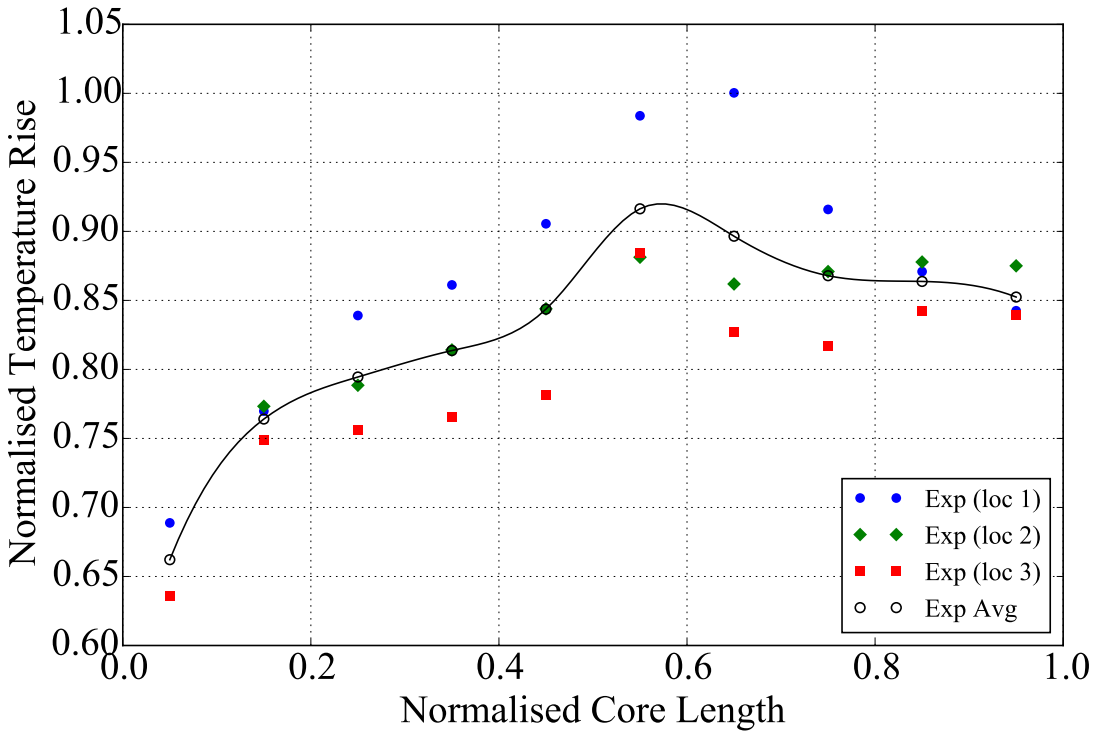


Fig. 5.7 Experimentally measured stator winding temperature rise in the core at full load and 0.8 power factor; NDE at the left; Temperature rise normalised according to equation 5.4

The temperature variation is partly caused by the uncertainty related to the axial, radial and circumferential position of the RTDs within the slots. The RTDs are inserted during the winding process and can move within the slot while the machine is being wound. The only way to determine the actual position of the RTDs after the winding process is to cut the stator open and measure it, thus destroying the machine. This introduces a measure of uncertainty as the winding temperature depends on the exact location of the RTD.

Another reason for the temperature variation are manufacturing uncertainties. The stator windings are insulated electrically by impregnating them with resin during a Vacuum Pressure

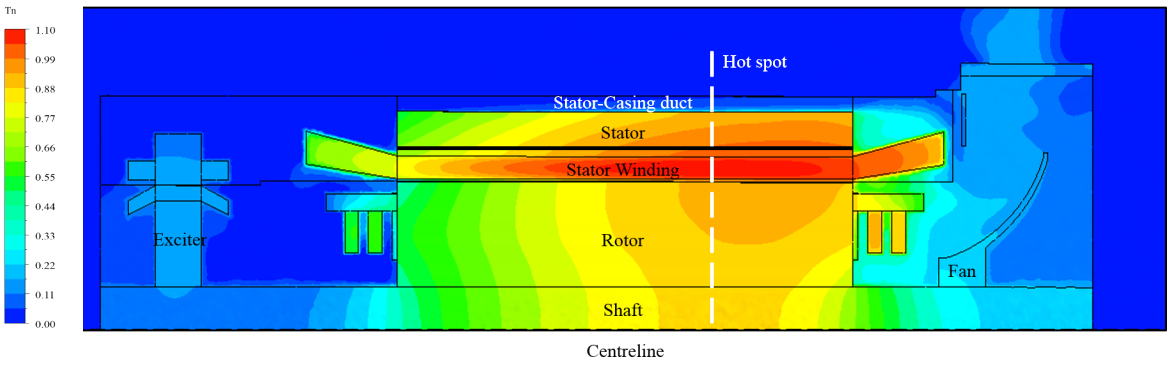
Impregnation (VPI) process. It is well known that not all air cavities will be filled during this process [83]. Variations in insulation quality are therefore expected between different slots, which cause variations in thermal conductivity and thus temperature (view figure 5.10). As the stator is randomly wound, the difference in exact wire location in the slots will amplify the effect.

Another factor to consider is the current imbalance between the three phases. The imbalance depends on the grid demand. The test corresponding to figure 5.7 showed a 6.2 % difference in current between the minimum and maximum phase current. No correlation could be found between the variation in phase current and temperature however, implying that this factor is negligible in comparison to the other ones discussed.

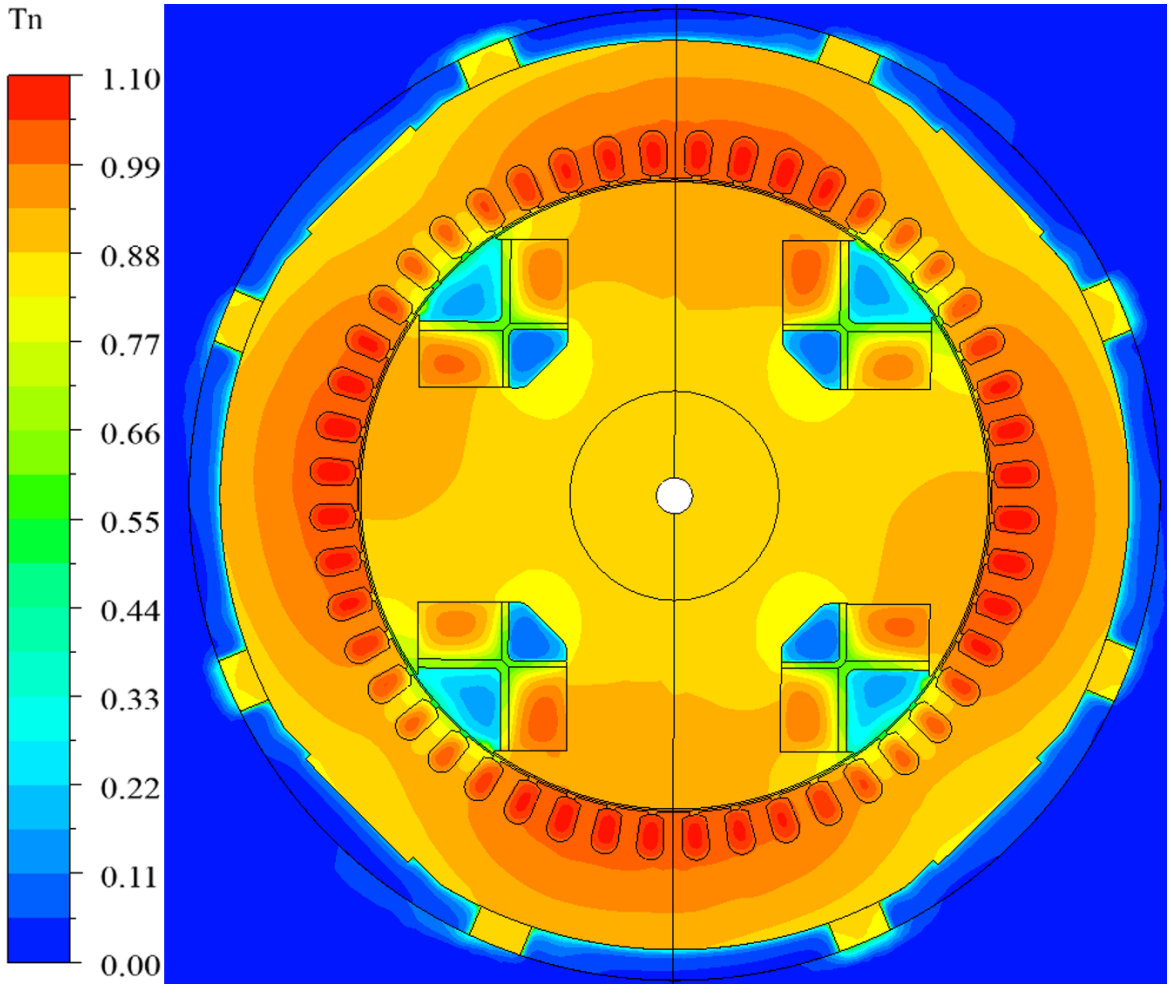
The left side of figure 5.7 corresponds to the core end on the Non-Drive End of the generator. The stator winding temperature rise steadily increases from $0.66\,\mathrm{T_n}$ there until its peak, located at $0.55\,\mathrm{l_n}$ for the 3-slot average and at $0.65\,\mathrm{l_n}$ for the single slot maximum. From there on the temperature rise decreases towards the Drive End of the core, with the 3-slot average temperature rise being $0.85\,\mathrm{T_n}$ at the DE. The temperature rise profile can be explained by the cooling arrangement. The NDE, facing the inlets drawing cold air into the machine, is cooled best. While the air flows along the core it extracts the heat generated within the generator, hence warming up. The heat $\dot{Q}$ that can be extracted from the core decreases with increasing air temperature T_{air} according to equation 5.6:

$$\dot{Q} = hA(T - T_{air}) \tag{5.6}$$

with h being the heat transfer coefficient and A the total surface area. Therefore, the stator winding temperature rise increases until the peak approximately two thirds along the core length. Even though the air temperature continues to increase from there on, the winding temperature rise declines as the stator endwindings are cooled better than the core windings and that effect propagates towards the centre. Only 35 % of the air entering the generator flows through the rotor-stator gap. The remaining 65 % passes through the stator-casing duct and gets heated up less in comparison to the air passing through the airgap and interpolar space (view figure 5.8), because of the bigger distance to the main loss generating parts of the machine and the lower flow velocity, which results in lower HTCs. As the endwindings are directly cooled by all the air entering the machine and their surface area is substantially larger in comparison to the core windings, their cooling is superior. The higher temperature rise at the Drive End in comparison to the Non-Drive End can be attributed to the higher temperature of the cooling air, which cumulatively heats up while it flows through the machine core.



(a) Side view



(b) Axial view at 0.69 l_n (location of the stator winding hot spot); Geometry mirrored vertically

Fig. 5.8 Temperature rise contours of the Benchmark Machine CFD MRF model; Temperature rise normalised according to equation 5.4

Figure 5.9 shows a comparison between the CFD MRF and the experimentally measured stator winding temperature rise at full load and a power factor of 0.8. The CFD temperature rise was taken in the geometric centre of the slot and averaged over all slots to make up for the circumferential temperature variation resulting from the MRF rotation modelling approach (view section 3.4.4, figure 3.9 and figure 5.8b).

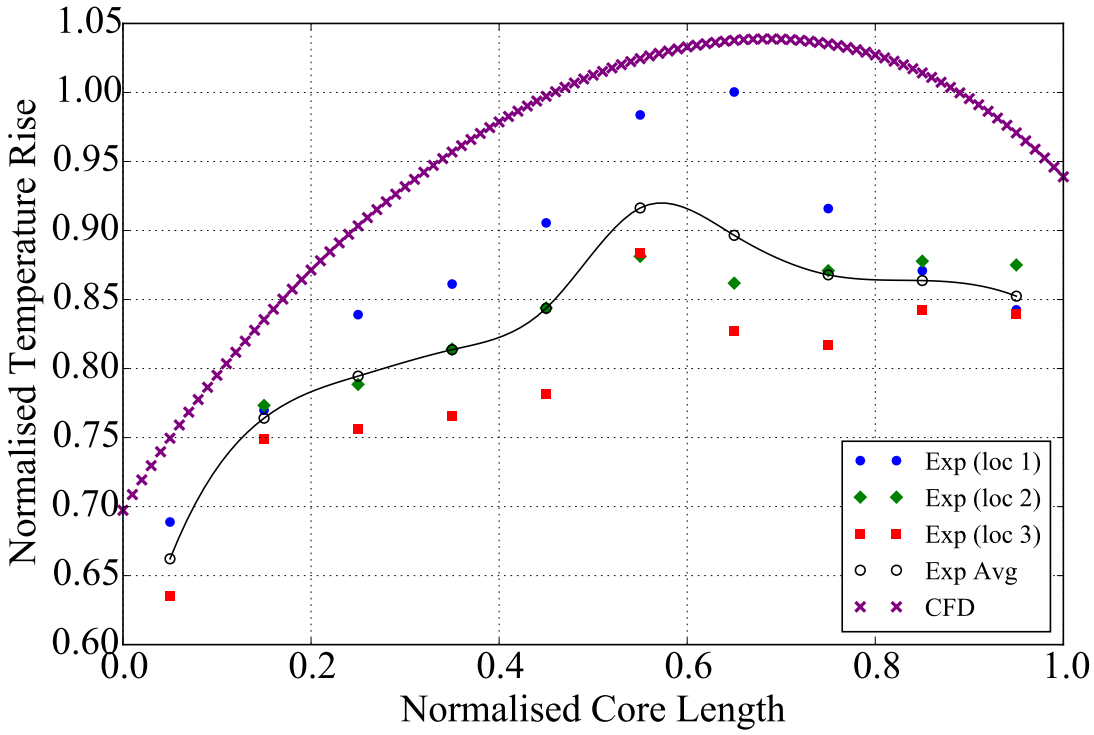


Fig. 5.9 Comparison between CFD MRF and experimentally measured stator winding temperature rise in the core at full load and 0.8 power factor; NDE at the left; Temperature rise normalised according to equation 5.4

The stator winding temperature rise profile along the axial core length is predicted well by the CFD model. The temperature rise increases from 0.70 T_n at the NDE until it reaches its peak value of 1.04 T_n at 0.69 l_n. From there on it declines to 0.94 T_n at the DE.

In comparison to the experimental data, the CFD temperature rise is higher. The average stator core winding CFD temperature rise exceeds the 3-phase averaged experimental stator core winding temperature rise by 12 %. The peak temperature rise difference between CFD and single phase experimental data is 4.0 %. While the agreement between computational and experimental data is good, several reasons causing the differences are discussed hereafter.

There is a negative correlation between the total mass flow rate through the machine and the stator winding temperature rise. As discussed in section 5.1, the MRF approach underpredicts the total flow rate through the machine by 13.7 %. This causes the CFD stator winding temperature rise to be overpredicted. To quantify this effect, the vented model was solved using the SM approach and a 5 minute time step for the solid parts and compared to the MRF results. Due to the very high computational expense of running a transient CHT simulation, this investigation has not been conducted for the Benchmark Machine. The SM average stator winding temperature rise was found to be 0.085 T_n lower in comparison to the MRF approach. While the exact difference between SM and MRF for the benchmark model will be different from this value, it is expected to of a similar magnitude. An in depth comparison between MRF and SM Conjugate Heat Transfer results can be found in section 7.4.

The stator windings were modelled as a single material with an anisotropic thermal conductivity. The thermal conductivity in the copper wire direction was assumed to be that of pure copper (400 $\mathrm{W\,m^{-1}\,K^{-1}}$). The conductivity in radial and tangential direction was calculated to be 0.43 $\mathrm{W\,m^{-1}\,K^{-1}}$ according to equation 3.4. The magnitude of the conductivity in radial and tangential direction has a big influence on the winding temperatures. This was investigated by solving the benchmark CFD model with different anisotropic stator winding conductivities. Figure 5.10 shows how a variation of the radial and tangential thermal conductivity influences the stator winding temperature rise.

With decreasing thermal conductivity, even small changes in anisotropic conductivity have a noticeable influence on the predicted stator winding temperatures. A reduction in thermal conductivity from 5 $\mathrm{W\,m^{-1}\,K^{-1}}$ to 1 $\mathrm{W\,m^{-1}\,K^{-1}}$ increases the peak stator winding temperature rise by 5.6 %. A further reduction to 0.5 $\mathrm{W\,m^{-1}\,K^{-1}}$ adds an additional 5.5 %. The anisotropic thermal conductivity of the stator windings was calculated to be 0.43 $\mathrm{W\,m^{-1}\,K^{-1}}$ according to equation 3.4. Thus, the predicted temperature rise is sensitive to the correct choice of anisotropic conductivity, which can only be estimated. Additionally, the assumption of the windings being a single material is a simplification introducing further uncertainty.

The stator is manufactured by coating the laminations with a thin sheet of insulating resin and pressing them into a stack. The thermal conductivity of the insulating resin is lower in comparison to that of the electrical steel the laminations are made of, reducing the axial conductivity of the stator stack. The axial conductivity is reduced further by the contact resistances between adjacent stator laminations. As the reduction in axial conductivity is highly dependent on the manufacturing method and hard to quantify, a sensitivity study investigating the influence of the axial stator iron conductivity on the stator and rotor winding

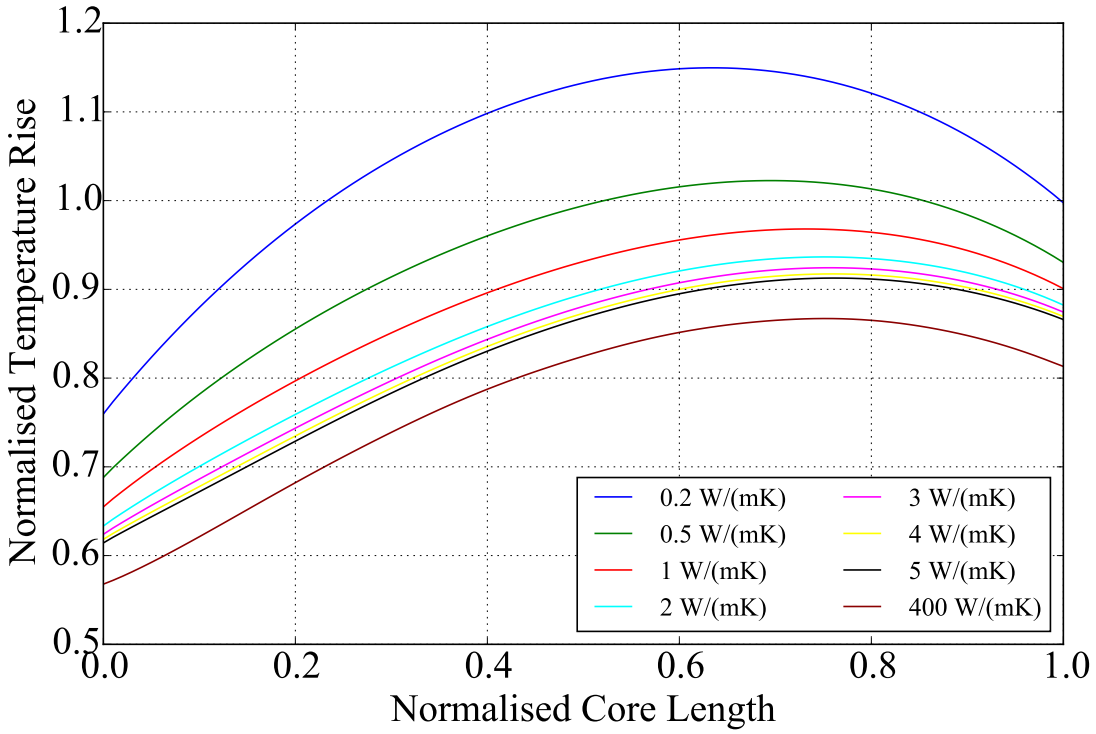


Fig. 5.10 Influence of the magnitude of anisotropic stator winding conductivity in radial and tangential direction on stator winding temperature rise; Temperature rise normalised according to equation 5.4

temperature rises has been carried out. Figure 5.11 shows how a variation of the thermal stator iron conductivity in axial direction influences the peak and average rotor and stator winding temperature rises.

The thermal conductivity in the radial (k_{rad}) and tangential (k_{tan}) direction was kept constant and assumed to be equivalent to the thermal conductivity of the lamination material. The anisotropy ratio is defined as the ratio between axial (k_{ax}) and radial/tangential thermal conductivity according to the following equation:

$$k_{ar} = \frac{k_{ax}}{k_{rad/tan}} \tag{5.7}$$

The temperature difference ΔT is defined as the temperature difference in comparison to the isotropic case ($k_{ar} = 1$) according to the following equation:

$$\Delta T = T(k_{ar}) - T(k_{ar=1}) \tag{5.8}$$

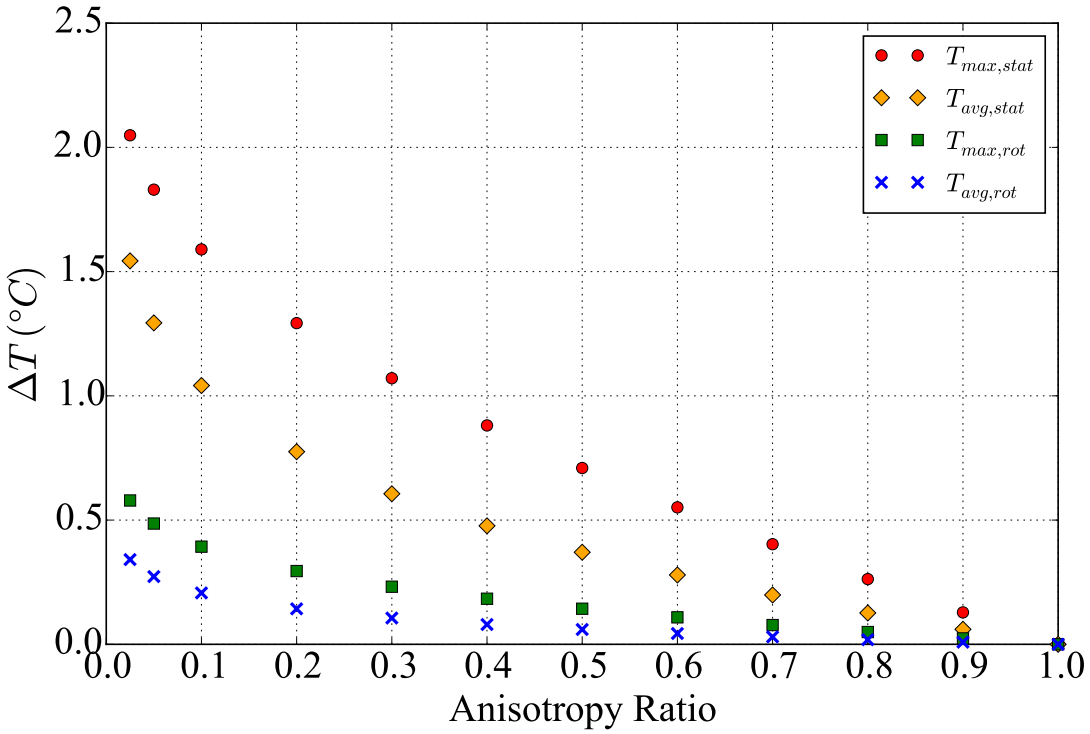


Fig. 5.11 Influence of the magnitude of anisotropic stator iron conductivity in axial direction on winding temperature rise; Temperature rise difference taken in relation to temperature rise of isotropic case according to equation 5.8

The sensitivity study was carried out for a anisotropy ratio range of 0.025-1. Figure 5.11 shows that the peak and average rotor and stator winding temperatures increase with decreasing axial stator iron conductivity. The impact on the rotor winding temperature rise is marginal. The maximum increase in peak rotor winding temperature rise is 0.6 °C at an anisotropy ratio of 0.025, while the average rotor winding temperature rise increases by 0.3 °C. The impact on the stator winding temperature rise is more noticeable. The maximum increase in peak stator winding temperature rise is 2.0 °C at an anisotropy ratio of 0.025, while the average stator winding temperature rise increases by 1.5 °C.

Based on empirical data, the machine manufacturer estimated the axial stator iron anisotropy ratio to be 0.15. For this case, the assumption of an isotropic stator iron material underpredicts the stator winding temperature rise by 1.4 °C (peak) and 0.9 °C (average). This was considered a negligible error and it was decided to model the stator iron as an isotropic material with a thermal conductivity equivalent to that of the stator lamination material.

The stator endwindings were modelled as toroids with a smooth surface. While the endwinding shape is toroidal, their surface is not smooth in reality. This can be seen in figure 5.12, which shows the inside of the stator endwindings of the Benchmark Machine.



Fig. 5.12 Stator endwindings of Benchmark Machine

As the windings exit the core, they bend in the circumferential direction and create an uneven, rough surface together with the slot liners, phase separators and resin. The surface roughness increases the heat transfer from the endwindings in comparison to a smooth surface according to equation 5.6, as the endwinding surface area is increased. Additionally, more turbulence is induced when air flows over a rough surface, increasing the heat transfer even further. As the core windings of the investigated machine are hotter than the endwindings, some of the heat generated inside them follows the main conduction path to the endwindings where it is dissipated into the cooling air. Hence, underpredicting the endwinding heat transfer results in an overprediction of the stator core windings, as well as the endwindings.

The fact that modelling the stator endwindings as smooth toroids underpredicts the heat transfer has already been observed by other authors. Connor [13] proposed to account for the reduced heat transfer of the simplified endwinding shape by reducing the heat input into the endwindings. La Rocca [84] proposed to improve the geometric shape of the endwindings by extruding each winding individually as it exits the slot, turning it into an elliptical shape and adding a cylindrical and conical filler. The new approach was tested on a small TEFC machine, where the endwinding heat transfer has a high impact on the

total thermal performance. It was found to increase the endwinding heat transfer by 62 % in comparison to the simplified toroidal approach. As the stator endwinding temperatures are not critical within the investigated machine and the cooling design improvements focus on reducing the machine hot spot in the stator core windings, the error introduced by the simplified endwinding modelling approach was considered acceptable.

Another factor causing the difference between CFD and experimental results is the uncertainty regarding the exact position of the RTDs within the slot. Figure 5.13 shows the temperature rise variation within a single slot at an axial position of 0.7 l_n. The CFD temperature rise was extracted from the geometric centre of the slot, marked in black in figure 5.13, which is very close to the winding hot spot. As the temperature rise varies by 17 % over the slot and the exact position of RTDs within the slot is unknown, the experimental results are expected to deviate towards the lower end.

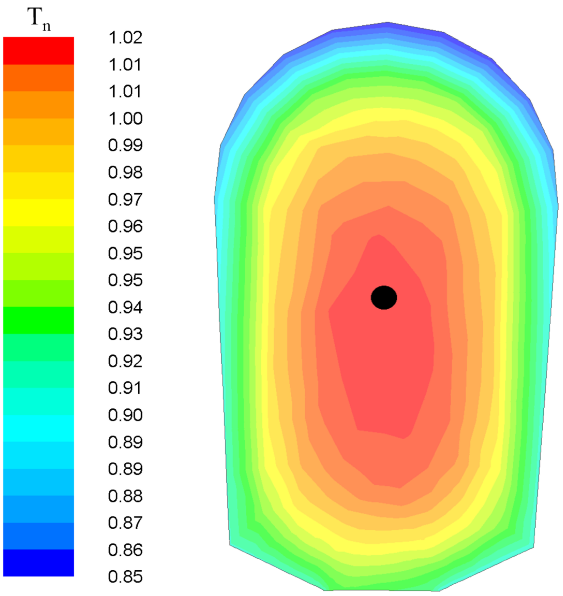
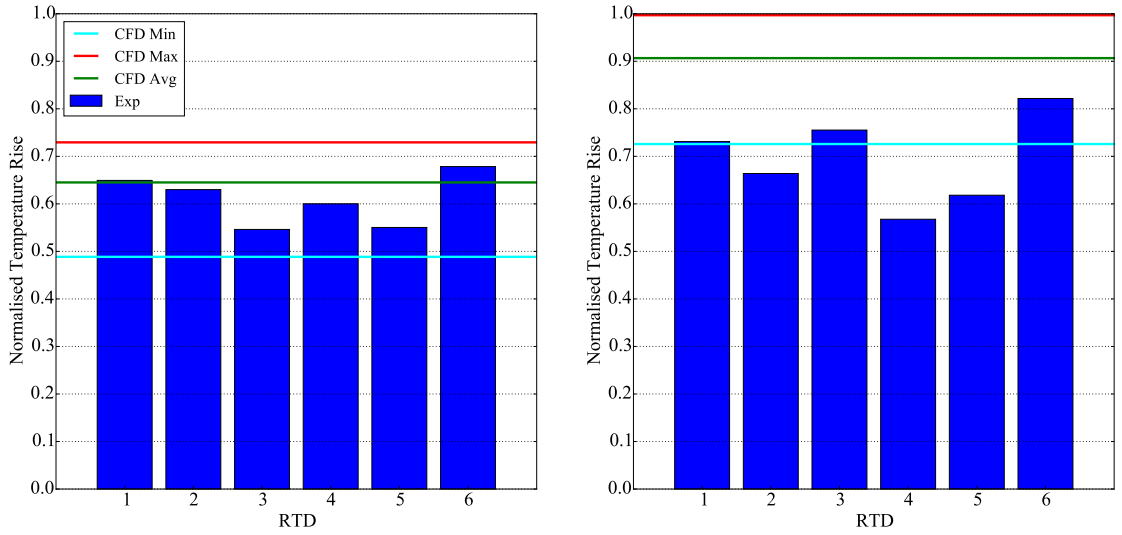


Fig. 5.13 CFD MRF temperature rise variation within a single slot at an axial location of 0.7 l_n; Temperature rise normalised according to equation 5.4

Experimentally validating the stator endwinding temperature rises proved to be difficult. 6 RTDs were distributed over the endwindings on each side during manufacturing, but the exact location of the RTDs within the endwindings was unknown. The local temperature rise within the stator endwindings varies considerably depending on their location. Figure 5.14 shows the experimentally measured temperature rise in the NDE (left) and DE (right) stator endwindings, represented by the blue bars. They are compared to the simulation results,

with the minimum CFD temperature rise represented by the light blue lines, the maximum temperature rise by the red lines and the average temperature rise by the green lines.



(a) Non-Drive End

(b) Drive End

Fig. 5.14 Comparison between CFD MRF (lines) and experimentally measured (bars) stator winding temperature rise at full load and 0.8 PF; Temperature rise normalised according to equation 5.4

The experimentally measured temperature rises at the NDE range from 0.546 to 0.678 T_n, varying by 0.132 T_n. They show good agreement with the simulation results, staying within the range predicted by the CFD model. The agreement regarding the average temperature rise is good. The average CFD endwinding temperature rise exceeds the experimentally measured average temperature rise only by 3.6 %.

The experimentally measured temperature rises at the DE range from 0.568 to 0.822 T_n varying by 0.254 T_n. The agreement between CFD and experimental data is worse in comparison to the NDE, with the simulated temperature rise being overpredicted. Only three of the six RTDs measured temperature rises within the predicted range and the difference in average temperature rise is 21.4 %. One reason for the difference between CFD and experimental results is the underpredicted endwinding heat transfer resulting from the simplified endwinding modelling approach discussed previously. Another reason is the higher complexity of the flow field around the DE endwindings. While the NDE is directly cooled by the air entering through the inlets with a known temperature, the DE endwindings are cooled by a mix of air exiting the stator-casing duct as well as the airgap and interpolar space. The flow around the DE endwindings is more restricted due to their proximity to the machine casing and the fan.

This explains the worse agreement of CFD and experimental data on the Drive End. Table 5.1 summarises the thermal validation of the stator endwindings.

Table 5.1 Comparison of CFD MRF and experimentally measured stator endwinding temperature rise; Temperature rise normalised according to equation 5.4

	NDE		DE	
	CFD (T_n)	**Experimental (T_n)**	**CFD (T_n)**	**Experimental (T_n)**
Min	0.489	0.546	0.726	0.568
Max	0.729	0.679	0.997	0.822
Spread	0.241	0.133	0.271	0.254
Average	0.645	0.609	0.907	0.693

5.3.2 Rotor Results

Figure 5.15 shows a comparison between the CFD and experimentally measured rotor winding temperature rise for full load and a power factor of 0.8. The CFD temperature rise was taken in the geometric centre of the winding and averaged over all windings. The rotor endwindings are displayed in the regions of -0.2-0 l_n and 1-1.2 l_n.

Similar to the stator windings, temperature rises in the same axial location vary. The variation is less distinguished in comparison to the stator windings, however, with a maximum difference of 7.6 % at 0.4 l_n. The rotor windings are form-wound, while the stator windings are randomly distributed, making the rotor windings' thermal behaviour more predictable. The fill factor and insulation quality is superior, removing a cause for uncertainty in the winding temperature measurements.

The experimental rotor winding temperature rise increases steadily from the beginning until the end of the core, approximately following a linear trend. The peak temperature rise is 1.012 T_n at 1.0 l_n, slightly exceeding the peak stator winding temperature rise. The rotor endwindings are cooler than the core windings, with the outer winding layer being cooler than the inner one (view figure 4.11 for the location of the EW RTDs). Equivalent to the stator, the rotor endwindings are hotter at the Drive End as the cooling air heats up while it flows through the generator core and stator-casing duct.

CFD and experimental data show good agreement with the CFD temperature rises being between the values measured at the two poles equipped with RTDs for the majority of the core length. The average CFD rotor winding temperature rise is 3.6 % below the experimentally measured value. The main difference between simulation and experimental results is that

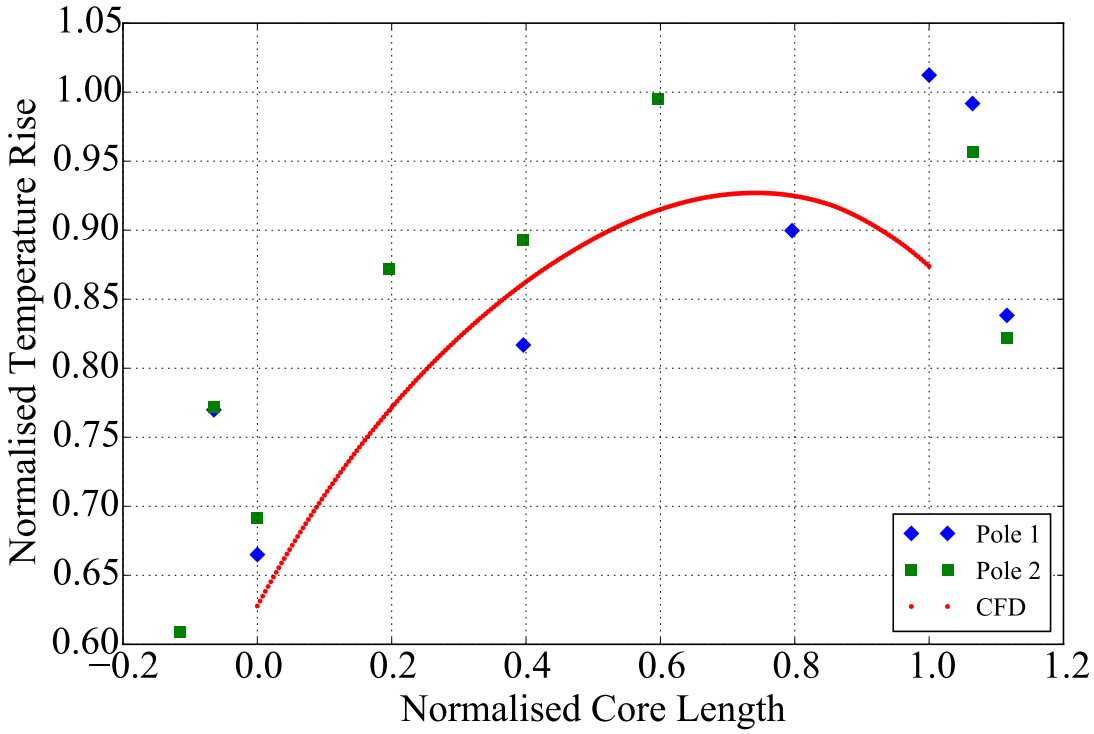


Fig. 5.15 Comparison between CFD MRF and experimentally measured rotor winding temperature rise at full load and 0.8 power factor; NDE at the left; Temperature rise normalised according to equation 5.4

the CFD model predicts the rotor winding temperature rise to peak at 0.74 l_n, while the peak experimental temperature rise is located at 1.0 l_n.

Figure 5.16 shows the temperature rise variation within the rotor coils at the axial hot spot location of 0.74 l_n. The location the RTDs are placed in, and the CFD temperature rise was extracted from, is marked in black.

It is obvious that the temperature rise within the rotor windings varies considerably with the radial and circumferential position. The difference between the peak temperature rise, close to the winding centre, and the minimum temperature rise, on the inside of the interpolar space, amounts to 43 %. This means that even small misplacements of the RTDs during the insertion process can result in large discrepancies between simulation and experimental results. There is also a difference in temperature rise between the leading and the trailing winding. The peak temperature rise of the trailing winding is 3.8 % above the leading winding according to the CFD results. The difference in average winding temperature rise is almost the same at

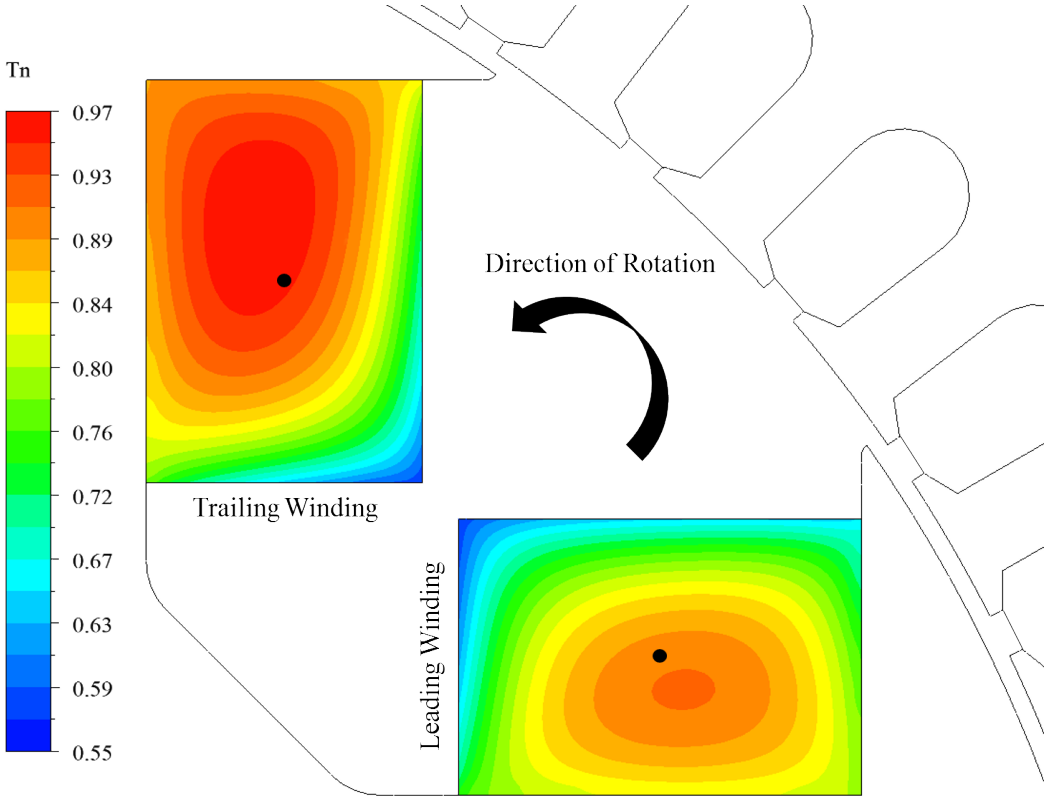


Fig. 5.16 CFD MRF temperature rise variation within the rotor coils at an axial location of 0.74 l_n; Temperature rise normalised according to equation 5.4

3.7 %. As the RTDs are all located in the trailing windings, but the CFD temperature rises have been averaged over all windings, the CFD temperature rises are expected to be slightly underpredicted.

5.4 Conclusions

This chapter presented the experimental validation of the Benchmark Machine CFD model. The model shows good agreement with the experimental results regarding the measured air flow and thermal properties. Based on the validated model, the CFD model used for the design optimisation of the Vented Prototype, which will be presented in the following chapter, was developed.

Chapter 6

Stator Vent Design Methodology and Results

CFD is the most accurate modelling approach for the thermal analysis of electrical machines. To date, it is the only modelling approach capable of solving fluid flow, convective and conductive heat transfer simultaneously. Whilst CFD enables an accurate prediction of the conjugate thermal performance, its usage is limited by its high computational cost, as well as the considerable amount of time and user experience required to set up the model correctly [5, 29].

In the early design stage it is often necessary to analyse a variety of different configurations. Traditionally, every step of the CFD workflow described in section 3.1 needs to be repeated manually for every configuration, as geometry, mesh, and solver setup are highly interdependent. This limits the use of CFD to the investigation of only the most promising designs. Fast analytical modelling techniques such as LPTN are often used to narrow down the choice of designs initially. But unless simple and well understood geometries are investigated, LPTN models require calibration for every design change, making them unsuited for the analysis of novel and complex geometries.

As analytical models are often calibrated through the use of CFD [9, 23, 24], the next logical step is to develop a CFD methodology which allows for an automated optimisation of design parameters without requiring additional user input after the initial model setup. Considering that the time-frame for the design, manufacture and testing of a prototype is usually in the range of months to years, machine designers should not be discouraged by the long time it takes for CFD simulations to solve. By using a more accurate modelling approach, the total

length of the design process will most likely be shortened, as less prototype iterations need to be manufactured to create a machine that fits the design criteria.

This chapter presents the methodology development, model setup and results of the novel optimisation methodology developed within this thesis. ANSYS Fluent is the solver used for all CFD investigations.

6.1 Methodology Development on Simplified Geometry

To prove the feasibility of the novel approach for the parametric design optimisation of complex 3-D CFD electrical machine models, a model of a simplified generator was created initially with the aim of minimising the peak stator temperature by varying the axial location of a single stator vent. By generating a single parameterised case, and automating the optimisation, the simulations were run independently after the initial setup, hence, reducing both computational and user time. The setup and results of this feasibility study were published previously in [85] by the author of this thesis and will be discussed in this chapter.

The simplified model geometry has been created based on the geometry of the Benchmark Machine. Fluid as well as solid zones were considered. The vent width was chosen to be 2.5 % of the core length. To reduce the computational effort the machine was assumed to be rotationally periodic. Hence, only one 90° pole sector was modelled. Furthermore, only the core of the machine without rotor or stator endwindings was represented. The fan and exciter were neglected. The casing, shaft and surrounding fluid were extended 2.5 core lengths upstream and 5 core lengths downstream of the core. To facilitate meshing of the vent region, the vent gap supports were neglected. Figure 6.1 shows a side view schematic of the created geometry. An axial view of the core geometry can be seen in figure 6.2.

The creation of geometry and mesh, as well as the subsequent simulation and the optimisation process, all took place within ANSYS Workbench 17.2. Using one software package for the complete workflow facilitates the creation of input and output parameters of interest and their interdependencies. Additionally, it enables the creation of a model robust enough to handle the automatic updates during the optimisation process. Substantial effort has been put into the creation of a fully parametric geometry and mesh. Whilst creating a parametric model adds time to the initial model setup, the total investigation time is reduced. The mesh has been created based on the methodologies developed and validated in [13, 65, 81]. Meshing of the stator vent and airgap were particularly challenging. They require special attention, due

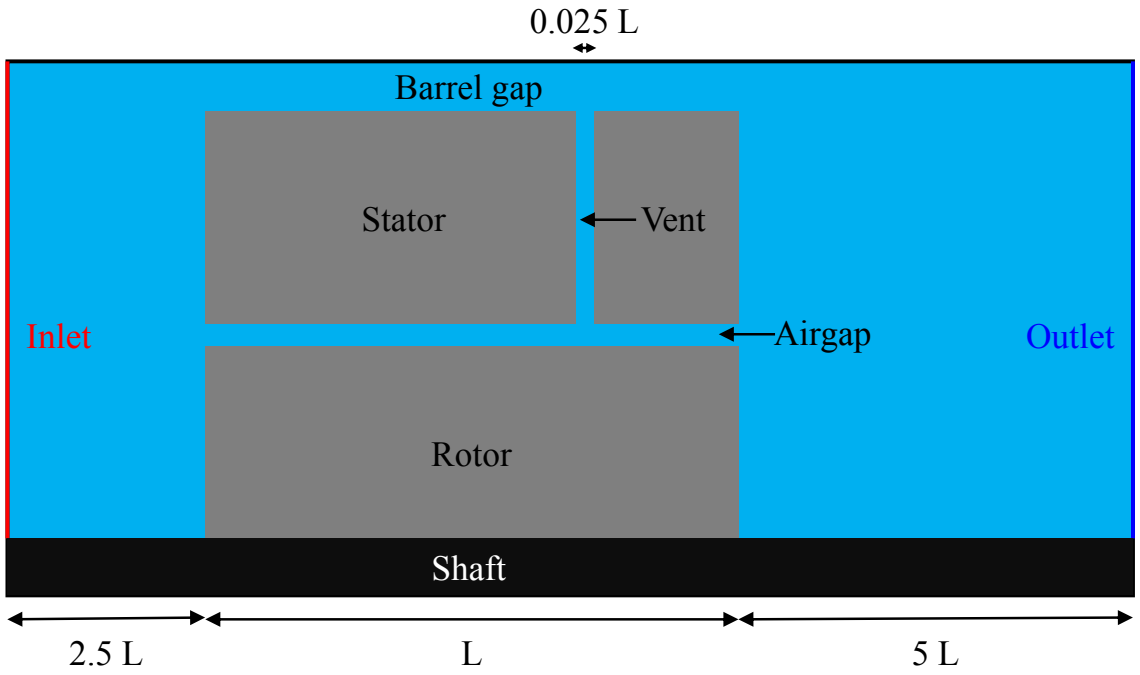


Fig. 6.1 Schematic of the simplified model

to their high influence on the flow solution [65]. The main challenge to overcome during the methodology development was to create a model robust enough to handle the fully automatic update of the mesh and solver following the variation of design parameters at the geometry stage.

Air enters the computational domain through a velocity inlet at a temperature of 300 K. The outlet is defined as a constant pressure boundary. Both are normal to the machine axis of rotation (view figure 6.1). They are placed far enough away from the zone of interest to not interfere with the flow solution. Conduction in all solids is assumed to be isotropic. The heat generated inside the machine (mostly through copper and iron losses) has been taken into account by adding volumetric heat generation to all loss generating solid parts. The loss distribution is based on the findings in [13] and assumed to be constant for all investigated cases. The change in loss distribution as a result of venting the stator (view section 6.2) was not considered.

The standard k-ε model with Enhanced Wall Treatment was chosen for the turbulence modelling. Pressure and velocity were coupled by the SIMPLE algorithm. The spatial discretisation of all variables was second order accurate. Rotation was modelled using the Multiple Reference Frame (MRF) technique. To avoid divergence during the first iterations,

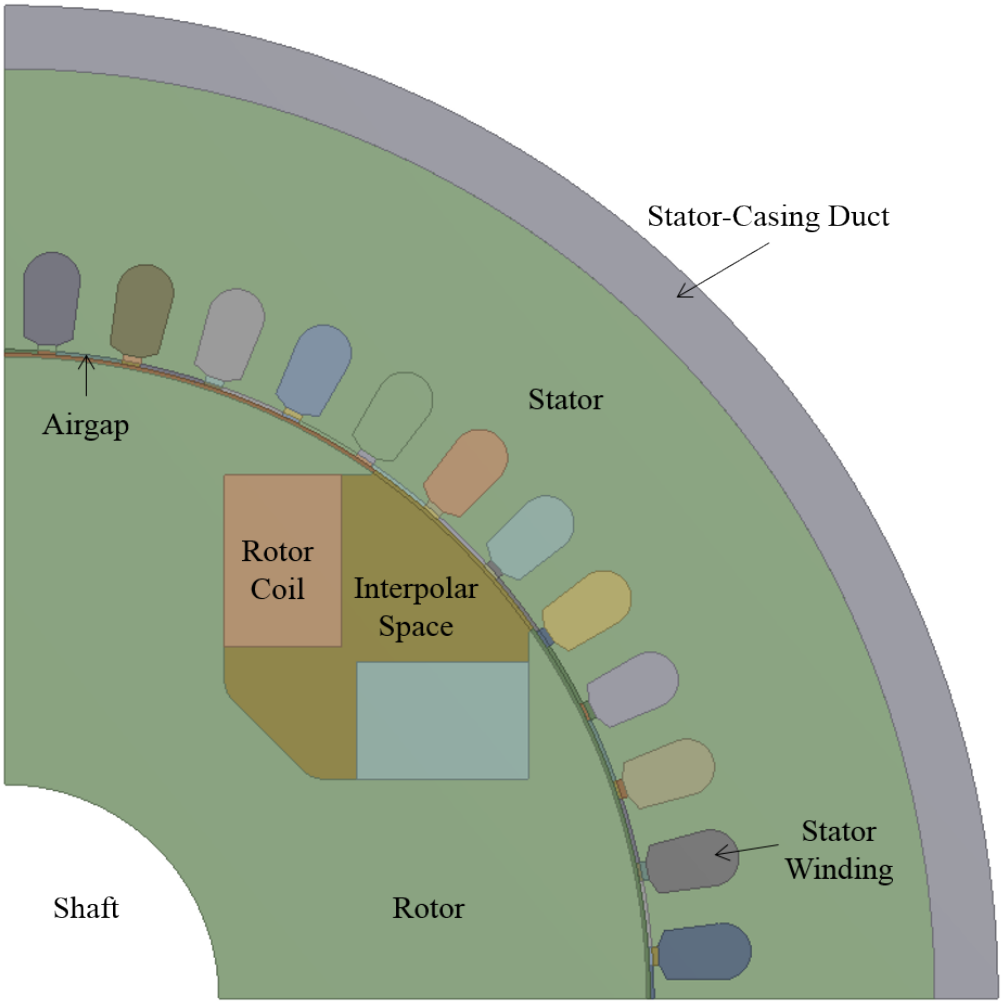


Fig. 6.2 Axial view of the simplified model core geometry

the energy equation was turned off initially. This also reduces the computation time, as the flow field requires more iterations to converge than the temperature distribution.

Convergence was monitored using residuals and variables of interest such as moment coefficients, vent mass flow, winding temperatures etc. The first design point was initialised using the results of a fully converged non-vented case. Each subsequent design point was initialised from the previous solution to decrease the number of iterations required, reducing the total investigation time. Early investigations showed that convergence was reached after solving the airflow only for 500 iterations followed by solving the full Conjugate Heat Transfer model for another 500 iterations. This resulted in a computation time of 4:30 hours per design point (DP) on a desktop PC featuring a 3.5 GHz Intel Xeon Hexa-Core CPU and 64 GB RAM. The mesh size was 9.2 million cells.

The optimisation aim was to locate the vent's axial position minimising the peak stator winding temperature. Thus, the axial distance between the vent and the core upstream face was defined as an input parameter at the geometry stage. The maximum temperature in the stator solids was defined as an output parameter in Fluent and set as the optimisation objective. Additional input parameters needed to be defined to enable the fully automatic creation of geometry and mesh regardless of the vent position after the initial model setup. Further output parameters helped to monitor other variables of interest, such as the average stator winding temperature and the mass flow rate through the vent.

The minimum and maximum vent position was limited to be 0.1 core lengths away from the core ends to avoid meshing problems. The simulation results confirmed that this is a reasonable limitation of the domain which does not influence the optimisation results (view figure 6.4).

Since only one variable input parameter exists, it was decided to perform a Direct Optimisation. During a Direct Optimisation, the impact of the variation of the selected input parameters is investigated by directly solving the specified CFD simulation. The Adaptive Single-Objective method is the optimisation algorithm chosen for this investigation. It creates a Response Surface from a small number of initial design points. Additional DP are selected based on gradient and used for refinement of the response surface as well as reduction of the search domain until the convergence criteria are met. [71] provides an overview and in-depth explanation of the optimisation algorithms available in ANSYS Workbench.

To quantify the benefit of adding a vent into the stator, a model without any vents was solved initially. The maximum winding temperature of this model is defined as the benchmark temperature $T_{max,B}$. All temperatures in section 6.1 are normalised as:

$$T_{n,cfd} = \frac{T}{T_{max,B}} \tag{6.1}$$

with T being the winding temperature of the vented cases. Stator temperatures are related to the peak stator temperature, while rotor temperatures are related to the peak rotor temperature. The vent position is normalised by dividing it to the total core length according to equation 5.5.

The optimisation procedure converged after 19 evaluations of different vent positions, taking approximately 3 and a half days in total to solve. The peak stator winding temperature for the optimal vented machine is 9.0 % below the temperature of the non-vented case. The average stator winding temperature decreased by 9.4 % for this configuration. Figure 6.3 shows the maximum stator winding temperature for each tested design point chronologically over the

course of the design optimisation. Figure 6.4 shows the relationship between maximum stator winding temperature and vent position.

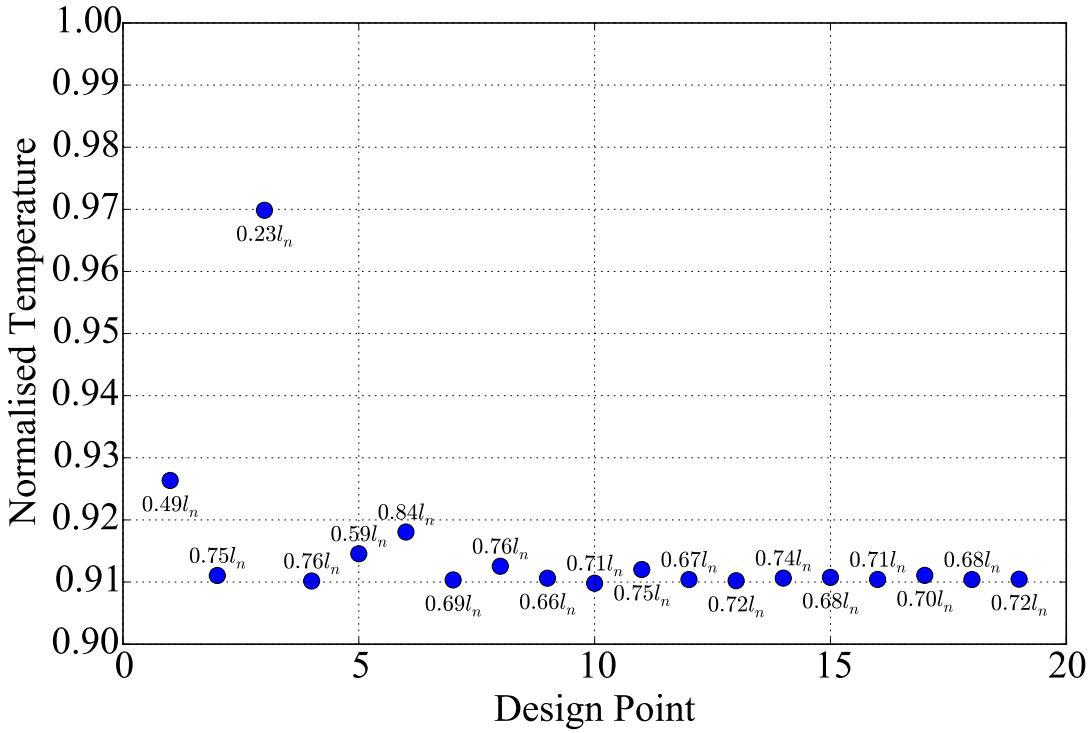


Fig. 6.3 Maximum stator winding temperature of configurations simulated during the Design Optimisation in chronological order; Temperature normalised according to equation 6.1; Normalised core length displayed next to data points

The original response surface is built from the first three design points which are distributed evenly over the domain. Each additional design point is used to either refine the response surface or reduce the domain. Whilst it takes 19 evaluations for convergence to be reached, the temperature difference between the optimal design point found on the initial response surface (DP 4) and the global optimum (DP 10) is negligible.

As the optimisation algorithm quickly identifies the approximate optimal region, some design points have been added manually to better visualise the influence of vent position on stator temperature across the total search domain. The addition of DP also validates that the found optimum is indeed the global optimum and not just a local one.

For $0.65 \leq l_{vent} \leq 0.75$, the variation in peak stator temperature is negligible ($\leq$0.2 K). This is most likely the reason why the optimisation algorithm quickly identifies the approximate

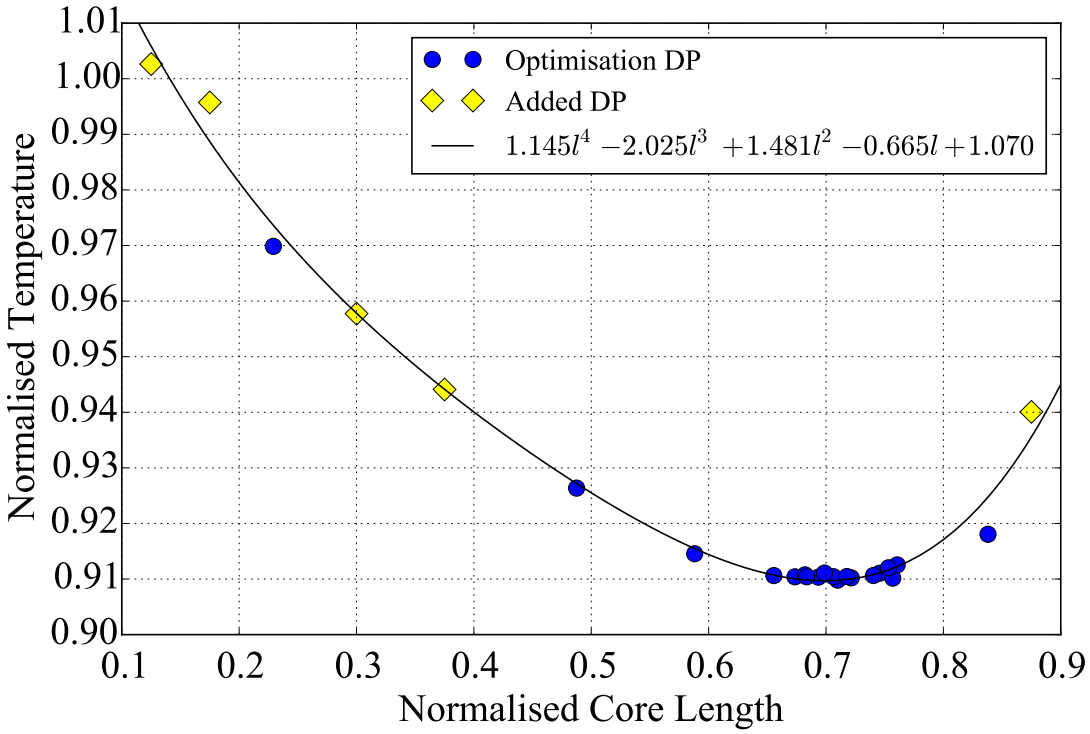


Fig. 6.4 Relationship between maximum stator winding temperature and vent position; Temperature normalised according to equation 6.1

optimal vent location but requires 15 additional evaluations to reach convergence. After the evaluation of the initial response surface (DP 1-3) and its optimum (DP 4), the algorithm evaluates one configuration on either side of this region (DP 5 at $l_{vent} = 0.59$ and DP 6 at $l_{vent} = 0.84$) and determines them to be worse. Outside of the region mentioned above, the temperature quickly increases towards the core ends and even surpasses the temperature of the non-vented case if the vent is positioned close to the inlet. This temperature increase above the non-vented case is caused by the diversion of airflow from the airgap and inter-polar space, as a result of the early vent positioning. At the same time, the vent cools a part of the stator that is far away from the hot spot and already sufficiently cooled. This demonstrates the sensitivity of such a complex flow system with parallel flow paths and hence, the requirement for CFD modelling. The correlation between temperature and core length can be described by a 4th order polynomial with the following equation:

$$T_{n,cfd} = 1.145l^4 - 2.025l^3 + 1.481l^2 - 0.665l + 1.070 \tag{6.2}$$

The polynomial was fitted to the data using the Ordinary Least Square method. It provides a good fit to the simulation results with a R^2-value of 0.99.

In figure 6.5, the temperature contours in the core are compared between the non-vented case and the case with an optimally placed vent. The view is equivalent to the view in figure 6.1. Temperatures are non-dimensionalised by dividing them through the peak rotor temperature of the benchmark case.

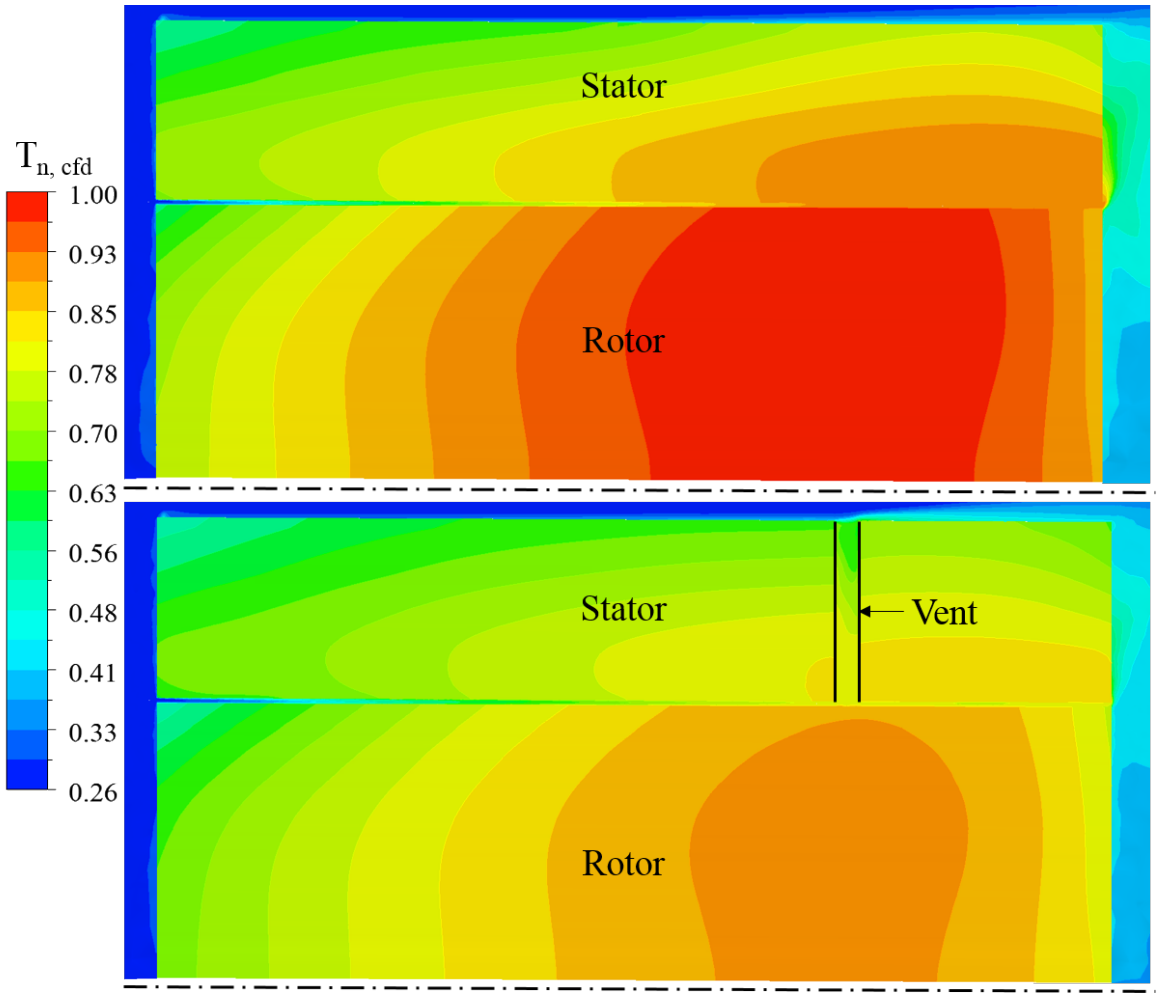


Fig. 6.5 Temperature contours of non-vented case (top) and vented case (bottom) with optimal vent position; Temperature normalised according to equation 6.1

The stator hot spot of the non-vented case is placed in the back third of the windings. The temperature of the air passing through airgap and IP space has increased too much by this point for it to provide sufficient cooling to the windings. By venting the stator in this area the

winding surface area in contact with the cooling air, and hence the convective heat transfer, increase as:

$$\dot{Q}_{conv} = hAdT \tag{6.3}$$

with $\dot{Q}_{conv}$ being the heat removed through convection, h the local heat transfer coefficient, A the surface area and dT the temperature difference between surface and free stream. It can be seen in figure 6.5 that the machine hot spot is actually located in the rotor windings. Interestingly, venting the stator decreases the peak rotor temperature as well in this case. The vent position optimising the cooling of the rotor hot spot is located in the same region as for the stator.

Figure 6.6 compares the peak and average rotor and stator winding temperatures depending on the vent location. While the stator average and rotor temperatures have not been considered for this optimisation, it is possible to target several objectives simultaneously and assign them weights depending on their importance [71]. This is particularly useful for the simultaneous optimisation of contradicting objectives.

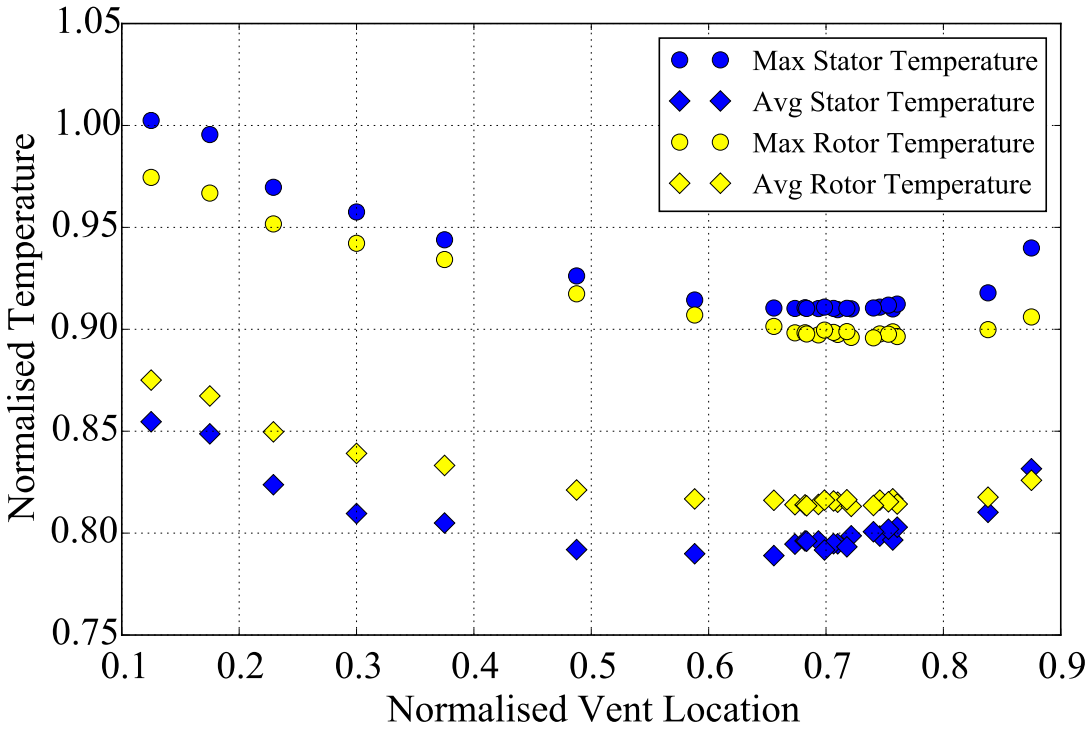


Fig. 6.6 Comparison of peak and average rotor and stator winding temperatures depending on vent location; Temperature normalised according to equation 6.1

As the airflow through the vent is of high importance for the thermal performance of the machine, it is considered in detail in the following section. Velocities are normalised according to equation 6.4, where v is the local velocity and v_{tip} is defined as the rotor tip velocity.

$$v_n = \frac{v}{v_{tip}} \tag{6.4}$$

The static pressure is presented as shown in equation 6.5, where p is the local pressure and $p_{vent,out}$ the average pressure at the junction of vent and stator-casing duct.

$$p_n = p - p_{vent,out} \tag{6.5}$$

The flow through the vent is driven by the pressure difference between the airgap and IP space and the stator-casing duct. As the pressure is higher in the centre of the machine, air flows radially outwards through the vent. Figure 6.7 shows the velocity contours in the axial centre of the vent. Figure 6.8 is a close-up of the velocity vectors around the two windings marked with a black circle in figure 6.7 in the same plane.

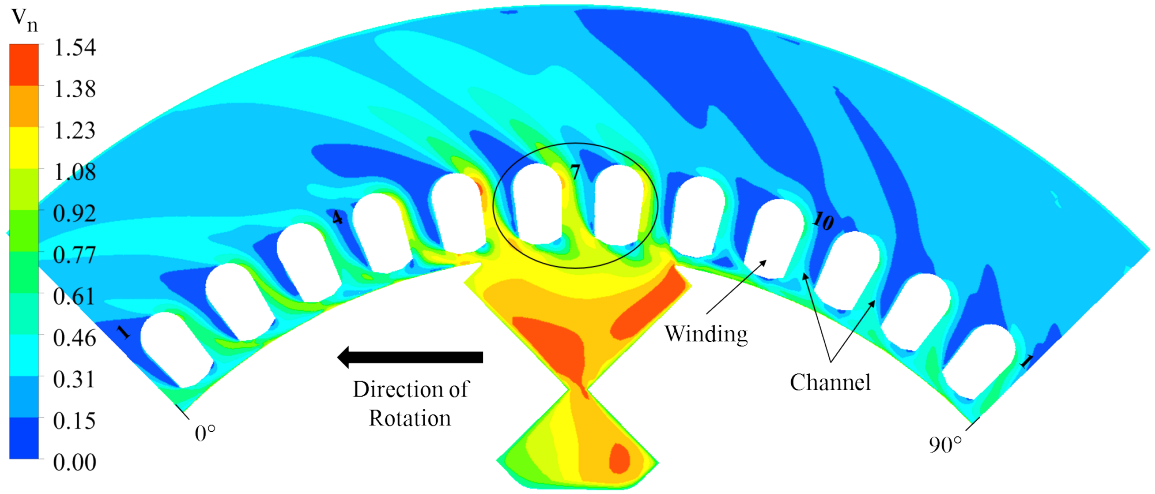


Fig. 6.7 Velocity contours in the axial centre of the vent; Velocity normalised according to equation 6.4

When the air passes through the channel between two windings, the local velocity is higher at the side of the windings facing the direction of rotation. The flow attaches to the curvature of the windings due to the drastic change in dominant flow direction from circumferential in the airgap and IP space to radial in the vent. This observation is in agreement with the results in [63].

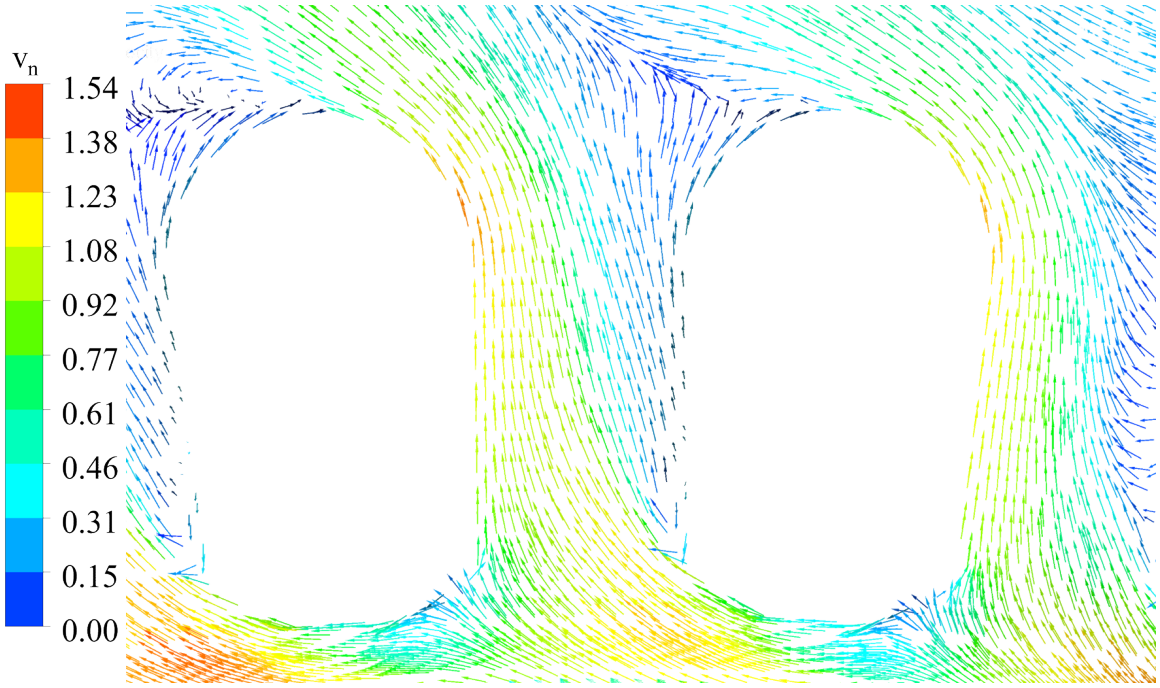


Fig. 6.8 Close-up of velocity vectors in the axial centre of the vent around the two windings marked in figure 6.7; Velocity normalised according to equation 6.4

On top of the mass flow distribution imbalance inside each channel, the flow is distributed unevenly between the various channels (view figure 6.9). The channel mass flow rate depends on its position relative to the rotor. The channels directly fed by the inter-polar space (6-8) show the highest flow rate with a proportion of 12-14 % of the total mass flow through the vent passing through each. In comparison, the minimum flow rate through the channel trailing the IP space (9) only amounts to 4.4 %. From there on it increases steadily against the direction of rotation until it reaches a value of 8.6 % in channel 3.

The variation in channel mass flow is driven by the pressure distribution in the airgap (view figure 6.10). The variation in pressure corresponds to the mass flow distribution observed in figure 6.9. As the pressure in the stator-casing duct is almost uniform around the circumference, the pressure wave created by the rotor poles determines the flow distribution. The local pressure oscillations apparent in figure 6.10 are caused by the windings restricting the flow entering the vent (view figure 6.8).

The conducted investigation on a simplified geometry presented in this section proves the feasibility of using complex 3-D Conjugate Heat Transfer CFD models for the optimisation of electrical machine parameters. No additional user input is required beyond the initial setup of the model by creating a parametric geometry, mesh and solver setup and using the

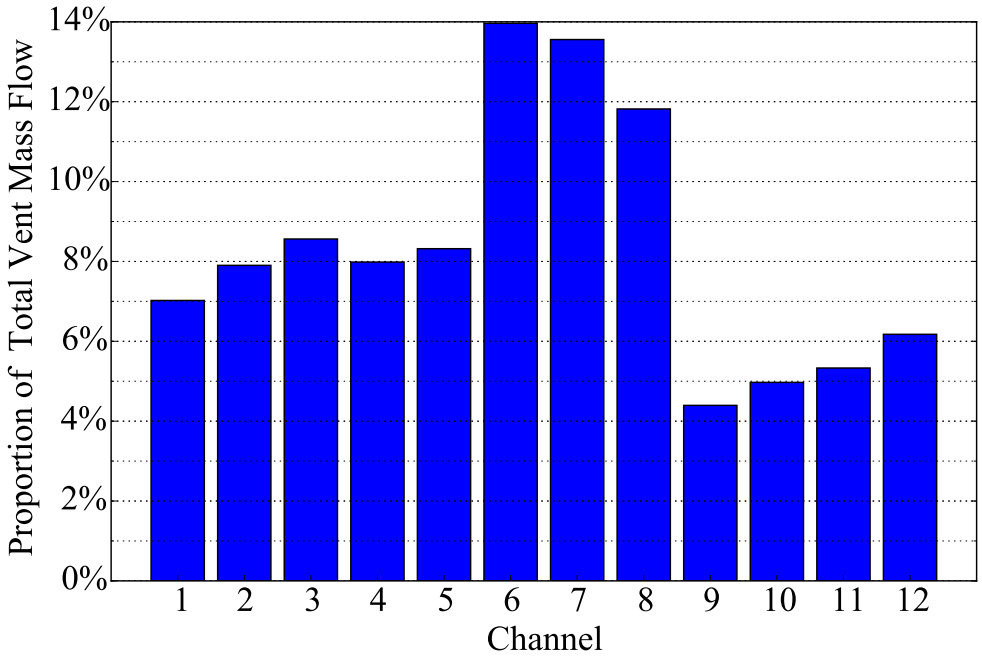


Fig. 6.9 Distribution of total mass flow through the vent between the channels; Channels are numbered from the left to the right as shown in figure 6.7 (counter-rotation)

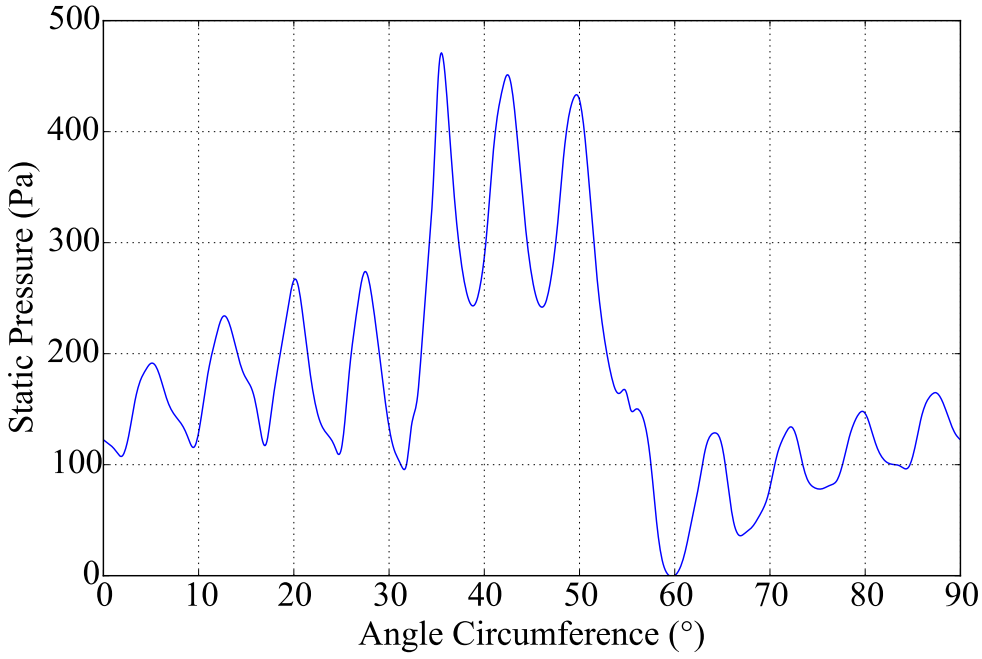


Fig. 6.10 Variation of static pressure in the airgap with angular location in the axial centre of the vent; 0° corresponds to the centre of channel 1

Design Optimisation feature (DesignXplorer) integrated into ANSYS Workbench to control the optimisation routine. Whilst a simplified geometry was used, and the results are not transferable to the real machine, it gave valuable insight into how to create a robust model in ANSYS Workbench. The created model can handle the automatic updates of geometry, mesh and solver setup required during the optimisation procedure. Furthermore, it confirmed that venting the stator can reduce peak and average stator winding temperatures for a machine of the size investigated in this project. It also proved that analytical correlations can be created based on the simulation results, which can be used as an input into other models investigating different characteristics of the machine performance.

6.2 Implementation of Variable Loss Distribution

In addition to the thermal implications, venting the stator influences the electromagnetic performance of the machine. The change in EM performance needs to be considered during the design optimisation procedure to predict the thermal performance correctly and choose the optimal design. From a thermal point of view, the change in loss distribution is the most important change in EM performance. This chapter focusses on the calculation of the new loss distribution and how the variation of losses with the combined vent width was implemented into the optimisation procedure. The EM FE investigations were conducted by Nuzzo [37, 75]. Although not directly conducted by the author of this thesis, the EM FE investigations are discussed in this chapter, as correlations were developed based on them and implemented into the optimisation procedure. The setup and validation of the Benchmark Machine FE model have previously been published by Nuzzo in [37]. The setup and findings of the vented FE model have previously been published by Nuzzo and the author of this thesis in [75].

Venting the stator removes active core lamination material, which needs to be compensated for to keep the output power constant. One option is to extend the core length by the thickness of the removed laminations. Due to the constraints related to the actual dimensions of the casing enclosing the whole generating set, this is not always possible. Extending the core length also requires additional changes during the manufacturing process, such as extending the length of the rotor core and the stator and rotor windings, increasing the material mass and cost. Another alternative is to keep the stack length the same and let the voltage regulation system compensate for the reduced magnetic flux by increasing the DC current through the

rotor field windings to keep the output power the same. This approach was chosen for the design of the Vented Prototype to minimise the impact on the manufacturing process.

Increasing the field current results in higher rotor copper losses according to equation 2.1. At the same time, the stator and rotor iron losses decrease due to the reduction in active material and the decreased flux density across the vents. To determine correlations between the different loss contributors and the combined vent width, Nuzzo conducted EM FE investigations for various combined vent widths ranging from 0-0.08 l_n. A brief overview of the setup and results of the FEA will be given in this chapter. More details about the EM FEA and its experimental validation can be found in [37] and [75].

Initially, a 2-D FE model of the Benchmark Machine was created in Infolytica MagNet. 3-D features, such as the endwindings, were taken into account via lumped resistances, which were calculated from the experimentally measured resistances of the rotor and stator windings. The iron loss calculation is based on the Steinmetz equations. As the classical Steinmetz model can lead to inaccurate results when high flux density harmonics are present, it was extended to all harmonics according to the procedure detailed in [37]. The model was validated experimentally by measuring the rotor and stator copper losses at various loads and power factors, as well as measuring the iron losses at no-load.

The validated FE model of the Benchmark Machine was then modified to predict the performance of the vented machine. Despite radial vents being inherently a 3-D feature, they can be implemented in 2-D models using an equivalent length to take the core removal into account. The flux density of the generator is more or less constant over the solid parts of the stator core, but changes in the direction of the shaft at the radial stator vents, decreasing and increasing gradually over the axial length of the vent. To take this field edge effect into account, the equivalent axial length L_{eq} can be calculated according to equation 6.6 by applying the classical Carter factor k_C [6]:

$$L_{eq} = L - k_c \sum_i w_{v,i} \tag{6.6}$$

with L being the total core length and $w_{v,i}$ the width of vent i.

Using the newly developed model, 7 combined vent widths equidistantly distributed over a range of 0.02-0.08 l_n were simulated under full load conditions with a power factor of 0.8. In order to achieve the same airgap flux density as the Benchmark Machine, the field current was increased to compensate for the presence of the radial vents, ensuring the same output power for all configurations. Figure 6.11 shows the relationships between rotor copper, rotor iron,

stator iron losses and combined vent width resulting from the FE analysis. The combined vent width has been normalised according to equation 5.5. The losses have been normalised by dividing them through the respective loss of the non-vented Benchmark Machine.

The rotor copper losses increase linearly with the combined vent width as a result of the increased rotor current. The trendline was fitted using the OLS method, showing an excellent fit to the data points with a R^2 value of 0.98. The iron losses decrease linearly with the combined vent width due to the reduction in overall core volume, which is directly proportional to the iron losses. The trend line was fitted using the OLS method ignoring the value for the non-vented case as it does not seem to follow the same linear trend observed for the vented machines. This is a reasonable assumption, as the developed correlations are only used for the simulation of vented machines. The trendlines show an excellent fit to the data points, with a R^2 value of 0.99 for the stator and 0.94 for the rotor.

As the stator current stays constant, the stator copper losses are independent of the combined vent width. It is important to note, that the temperature dependence of the losses, which is particularly important for the copper losses, has not been taken into account for the loss calculation presented in this chapter. It can be incorporated into the CFD simulations using the methodology presented in section 3.7.3.

To implement the developed correlations into the design optimisation procedure, they are assigned to the parameters defined in Fluent for the volumetric heat generation within the rotor and stator windings and iron core. The width of every vent was defined as a separate parameter during the geometry stage. Relationships between parameters in ANSYS can be created on the parameter tab in Workbench by selecting the dependent parameter and relating it to the parameters it depends on in the expression cell. More details on the setup of parameters can be found in [86] and section 6.3.

The presented methodology enables an automatic calculation of the change in loss distribution introduced by the design changes during the design optimisation procedure. Based on the simulation results of a validated 2-D FE model, analytical correlations were developed and implemented into the optimisation procedure. By considering the impact of venting the stator on the EM losses and incorporating them into the optimisation procedure, the model accuracy is improved, enabling a better machine design.

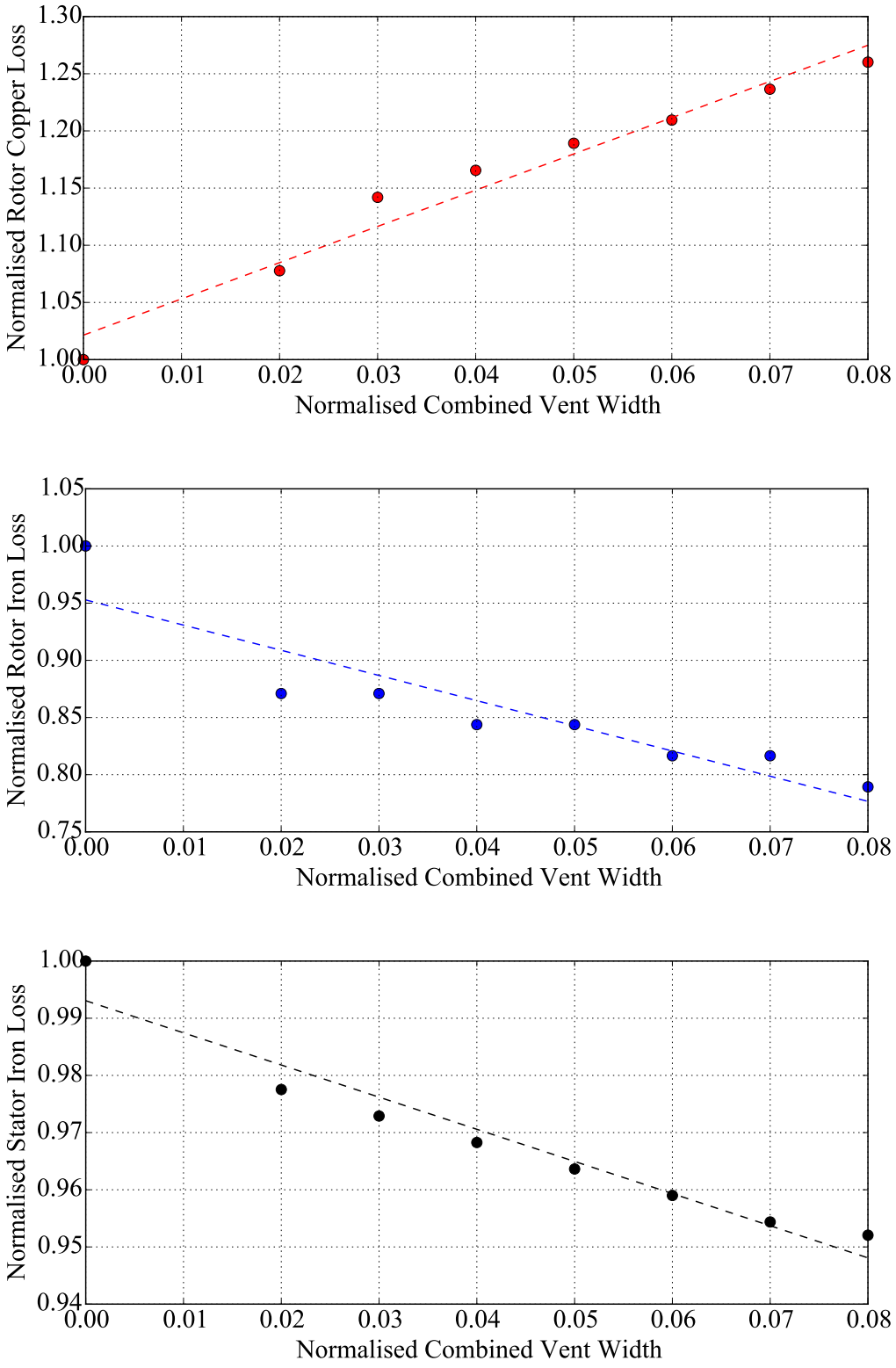


Fig. 6.11 Correlation between rotor copper loss (top), rotor iron loss (middle), stator iron loss (bottom) and combined vent width; A loss value of 1 corresponds to the respective loss of the non-vented Benchmark Machine

6.3 Vented Prototype Design Methodology

To determine the benefits the addition of radial stator vents has on the thermal performance of the investigated machine, the design optimisation methodology developed on a simplified geometry (view section 6.1), was applied to a substantially more complex and realistic vented model. This model was built based on the validated model of the Benchmark Machine (view chapters 3 and 5). The loss variation, dependent on the combined vent width, was implemented based on the correlations developed in section 6.2. The setup and results of this investigation have partly been published previously in [75] by the author of this thesis.

The model creation, solution and optimisation procedure all took place within ANSYS Workbench v17.2. The geometry and mesh were created using the DesignModeler and Meshing packages and subsequently solved with Fluent v17.2. The electromagnetic impact of the design changes was considered by defining the analytical correlations developed in section 6.2 as input parameters in Fluent. The optimisation procedure was executed using the DesignXplorer feature. Combining all steps of the solution and optimisation process in one software package facilitates the creation of a model robust enough to handle the automatic updates during the optimisation process. Figure 6.12 gives an overview of the steps taken during the design optimisation procedure.

Figure 6.13 shows the geometry of the vented model used for the design of the Vented Prototype. It was created by slicing the stator iron and windings, stator-casing duct and airgap of the Benchmark Machine geometry at the axial beginning and end of the vents. While it is possible to create the geometry by just slicing the stator iron, slicing the other zones is required to create the high quality mesh necessary to model the flow through the vents correctly.

The stator stack is manufactured by pressing the stator laminations axially. The vents are created by spot welding spacers to one lamination, keeping the laminations apart. The spacers were designed by the machine manufacturer. While they can have a substantial influence on the flow through the vent, redesigning the spacers was out of scope for this project due to the mechanical and manufacture considerations involved. Their approximate shape can be seen in figures 3.9 and 6.13.

The axial locations and widths of the vents were defined as parameters at the geometry stage. This enables them to be varied automatically by the optimisation algorithm. One of the biggest challenges was to create a high quality mesh for any design point. Parameter values

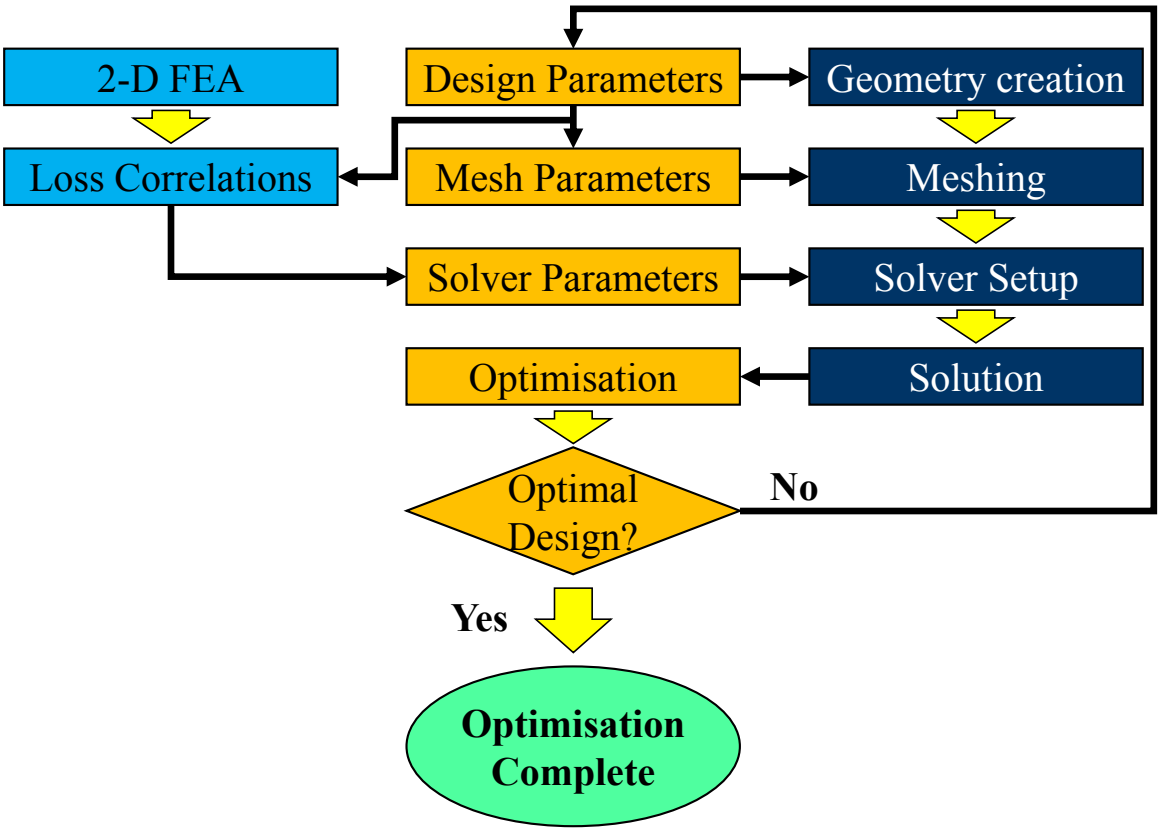


Fig. 6.12 Workflow during the design optimisation procedure

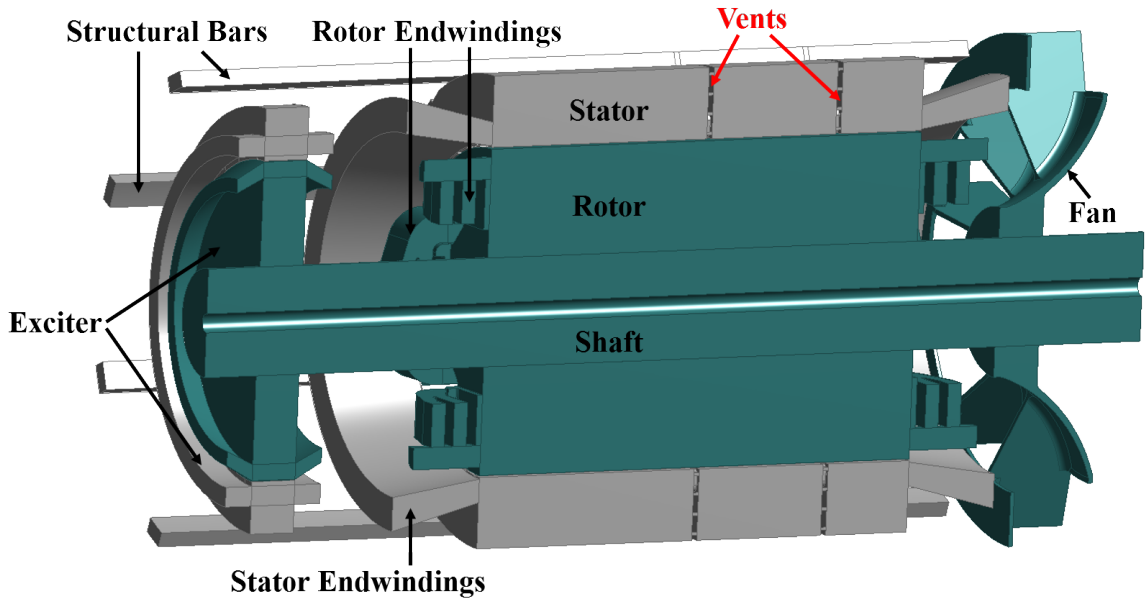


Fig. 6.13 Geometry of the vented model used for the design of the vented prototype; Only solids shown for greater clarity

close to the boundaries, such as vents close to the core ends or very thin/wide vents, can cause the meshing to fail or produce a poor quality mesh. Thus, multiple mesh controls were parameterised and related to the design parameters to be varied, enabling the creation of a high quality mesh for any configuration.

Early investigations showed that the addition of one vent would not be sufficient for the targeted decrease in stator winding temperature (view section 6.5). Therefore a second vent was added to the geometry. Varying the number of vents during the optimisation was not feasible due to the model complexity and requirement for a robust model with a high quality mesh. Any change in the number of volumes within the model caused the meshing to fail as some of the mesh controls became attached to the wrong surfaces or volumes. Adding a baffle to the stator-casing duct showed the potential to increase the flow rate through the vents and reduce the stator winding temperatures (view section 6.4.3). Locating the baffle at the rear axial surface of the first vent from the inflow direction (view figure 6.14), protruding radially inwards from the casing, was determined to be the best location to reduce the peak stator winding temperature during initial investigations. The radial height of this baffle was defined as an input parameter at the geometry stage. Whilst the axial baffle location could be varied, it was not possible to implement this into the optimisation procedure due to time constraints. The investigation time increases exponentially with the number of input parameters.

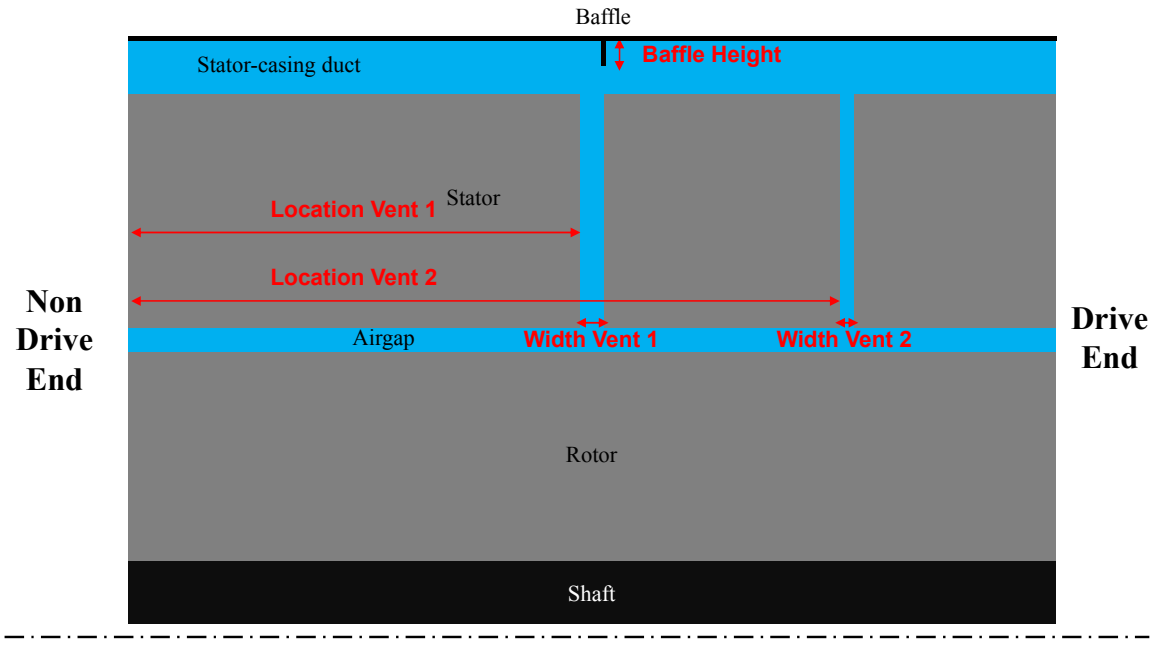


Fig. 6.14 Model schematic showing the optimised input parameters (in red)

Whilst it is theoretically possible to optimise a large number of input parameters simultaneously and consider multiple output parameters, the computational effort of CFD simulations limits the number of parameters to be varied in practice. In this case, it was feasible to optimise five input parameters simultaneously in the available timeframe. The machine hot spot in the investigated machine is located in the stator core windings. To increase machine lifetime, or increase the machine rating, minimising the peak stator temperature was set as the optimisation goal. The five parameters to be varied, marked in red in figure 6.14, were:

- Axial location of the vents (2 parameters, 1 per vent)
- Width of the vents (2 parameters, 1 per vent)
- Radial height of the baffle (1 parameter)

The vent widths were limited to 1-4 % of the total core length for manufacturing reasons (mechanical strength of the vent spacers). The axial locations and radial height of the baffle were restricted according to findings of preliminary investigations. Table 6.1 gives an overview of the parameter range of the design optimisation procedure. The vent location and vent width were non-dimensionalised according to equation 5.5. The baffle height b_n was non-dimensionalised by dividing its radial length r_B through the total radial length of the stator-casing duct r_{SC} according to the following equation:

$$b_n = \frac{r_B}{r_{SC}} \tag{6.7}$$

Table 6.1 Design optimisation parameter range; Vent location and width normalised according to equation 5.5; Baffle length normalised according to equation 6.7

	Lower Bound	**Upper Bound**
Location 1st Vent	$0.40\,l_n$	$0.60\,l_n$
Location 2nd Vent	$0.64\,l_n$	$0.88\,l_n$
Width 1st Vent	$0.01\,l_n$	$0.04\,l_n$
Width 2nd Vent	$0.01\,l_n$	$0.04\,l_n$
Baffle Length	$0.12\,b_n$	$0.88\,b_n$

All design points were initialised using the fully converged solution of one of the initially investigated cases. This reduced the number of iterations required to reach convergence. Only the air flow was solved for the first 900 iterations, as it requires more time to converge than the heat transfer. Air flow and heat transfer were solved simultaneously for the final 100 iterations. This solution strategy was shown to reduce the computation time by 39 % in comparison to solving all equations from the beginning and resulted in a computation

time of approximately 14 hours per design point (DP) on a desktop PC featuring a 3.5 GHz Intel Xeon Hexa-Core CPU and 64 GB RAM. The geometry was divided into 882 separate volumes to enable the creation of a high quality mesh. The mesh comprised tetrahedral and hexahedral cells with an average cell count of 33.3 million. 57 input parameters were defined to create a robust model, enabling the automatic creation and investigation of any design parameter configuration. 18 output parameters were defined to gain insight into the thermal performance of any investigated design.

The optimisation setup and methodology is based on the findings in [85]. The optimisation algorithm chosen for this investigation is the Adaptive Single-Objective (ASO) method. It combines the creation of Kriging Response Surfaces based on the Optimal Space-Filling (OSF) Design of Experiments (DoE) algorithm with the gradient-based Mixed-Integer Sequential Quadratic Programming (MISQP) optimisation algorithm, reducing the search domain until a converged solution is found. The workflow of the ASO method is shown in figure 6.15. The ASO method supports the optimisation of one objective and multiple constrains. It can be used for continuous and discrete parameters, but does not support the use of parameter relationships.

As shown in figure 6.15, the first step of the optimisation procedure is the application of the OSF algorithm to create the initial response surface. The minimum number of samples required for the response surface creation n_{OSF} depends on the number of input parameters n_{inp} according to the following equation:

$$n_{OSF} = \frac{(n_{inp}+1)(n_{inp}+2)}{2} \tag{6.8}$$

Increasing the number of samples does not necessarily improve the quality of the optimisation results, and significantly increases the number of evaluations and hence the computation time [71]. Thus the minimum number of 21 samples (based on 5 input parameters) was chosen for the response surface creation. Based on the results of the initial 21 design points, the first Kriging response surface is created and the MISQP algorithm is run on it with different starting points to find the best configurations (candidate points). If the Kriging error predictor of the identified configurations is sufficiently small, the optimisation domain is reduced around them. Otherwise, the candidate points are solved, added to the response surface and the MISQP algorithm is run on the new response surface. This process is repeated until the error predictor of the identified candidate points is acceptable.

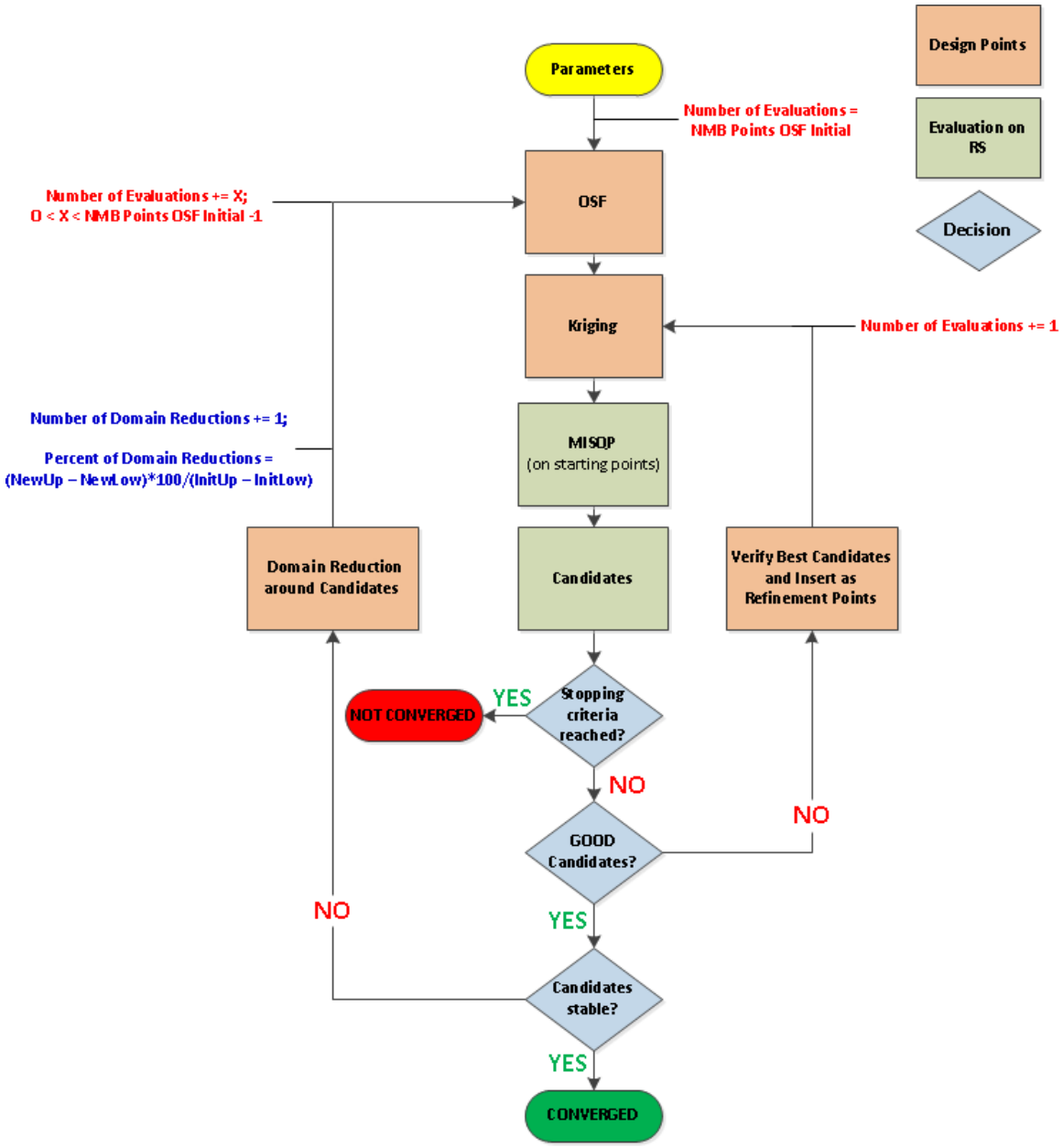


Fig. 6.15 Workflow of the Adaptive Single-Objective algorithm [71]

When the optimisation domain is reduced, the OSF algorithm is applied to create the samples for a new response surface in the reduced domain. Previously solved design points located in the new domain are kept, reducing the number of design points to be solved in comparison to the initial creation. The previously described workflow is then repeated until a converged solution is found, meaning all MISQP processes run on the response surface result in the

same candidate point regardless of their starting point. Further details about the optimisation setup and functionality of the algorithm can be found in [71] and [85].

Identifying candidate points on the response surface using the MISQP algorithm is fast with calculation times in the range of seconds. Solving the design points for the creation and refinement of the response surfaces on the other hand is slow, as it requires an update of geometry, mesh and CFD solution, which takes approximately 14 hours per design point.

6.4 Optimisation Design Parameters

In this chapter, the impact of the varied design parameters on the thermal performance of the generator is discussed.

6.4.1 Vent Location

The axial vent location has a high influence on the flow rate through the vent as well as the stator winding temperatures. To analyse its impact in detail, the location of a single vent with a constant vent width and no baffle was optimised with the aim of minimising the peak stator temperature.

It is interesting to note that air flows radially inwards through the vents. Typically, air flows outwards through radial stator vents, as the rotor pumps the air outwards. However, in the investigated machine the pressure in the stator-casing duct is higher than the pressure in the airgap for the majority of the core length. This can be seen in figure 6.16, showing the circumferentially averaged static pressure in the radial centre of the airgap and stator-casing duct for the Benchmark Machine.

The pressure in the airgap is above the pressure in the stator-casing duct as the air enters the core. But it quickly decreases towards the core end, while the stator-casing duct pressure only decreases marginally. Therefore, the airgap pressure drops below the stator-casing duct pressure approximately 25 % along the core length, resulting in a radially inward flow through the vents from this point on. Positioning a vent in the first quarter of the core is not beneficial for the thermal performance of the machine, as this part of the core is already cooled sufficiently. As the pressure difference between airgap and stator-casing duct increases with the core length, the mass flow rate through the vents increases with increasing axial vent location. This can be seen in figure 6.17, showing the correlation between vent mass flow

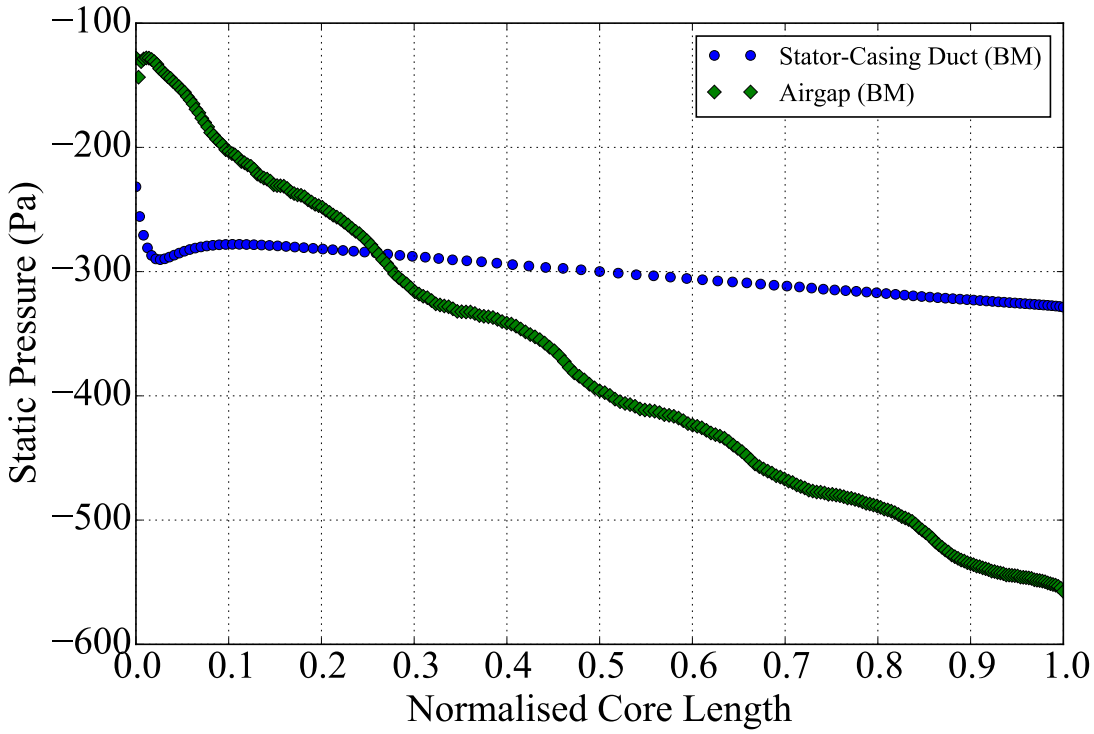


Fig. 6.16 Static pressure profile along the core length in the stator-casing duct and airgap

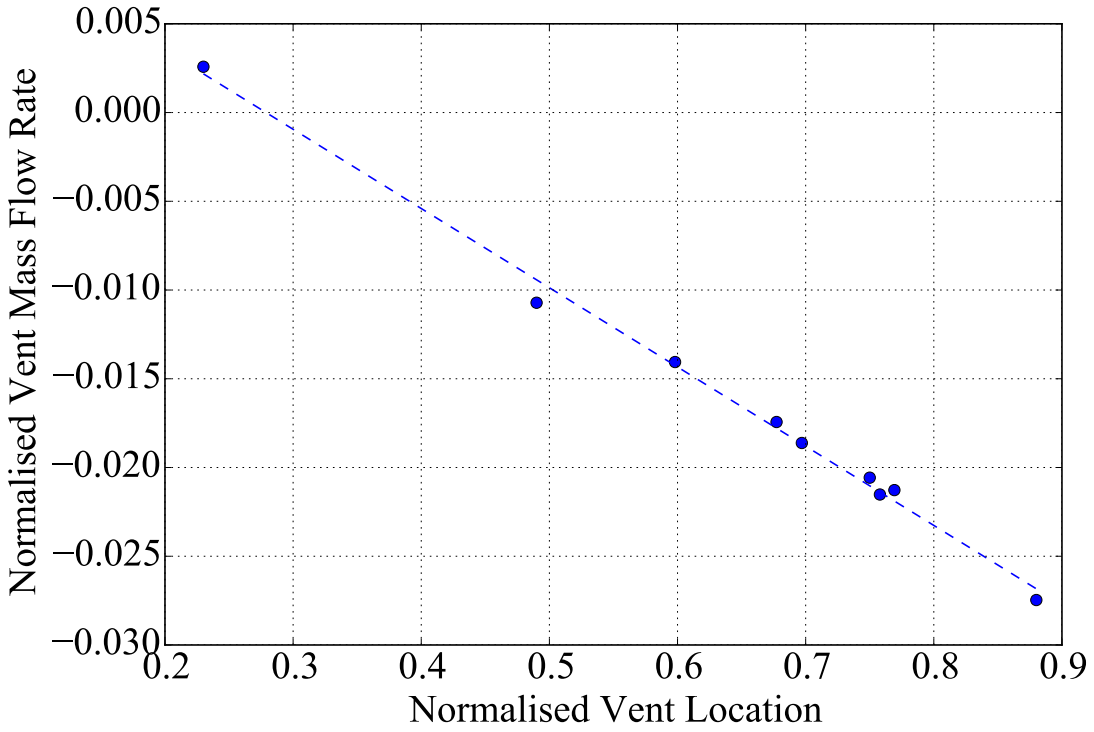


Fig. 6.17 Relationship between vent mass flow rate and vent location for a case with a single vent and a constant vent width; Mass flow rate normalised according to equation 5.1

rate and vent location for a machine with a single vent, no baffle and a constant vent width of $0.02\,l_n$. The vent mass flow rate has been non-dimensionalised according to equation 5.1.

As suggested by the pressure distribution between stator-casing duct and airgap, air flows radially outward through a vent located in the first quarter of the core length (positive flow rate). Because the pressure difference is small, the flow rate is low. After the first quarter, air flows radially inwards through the vent (negative flow rate) and the vent mass flow rate increases with increasing vent location. The correlation between vent mass flow rate and vent location is linear. The trendline in figure 6.17 is calculated using the OLS method and shows an excellent fit to the data points with a R^2 value of 0.995.

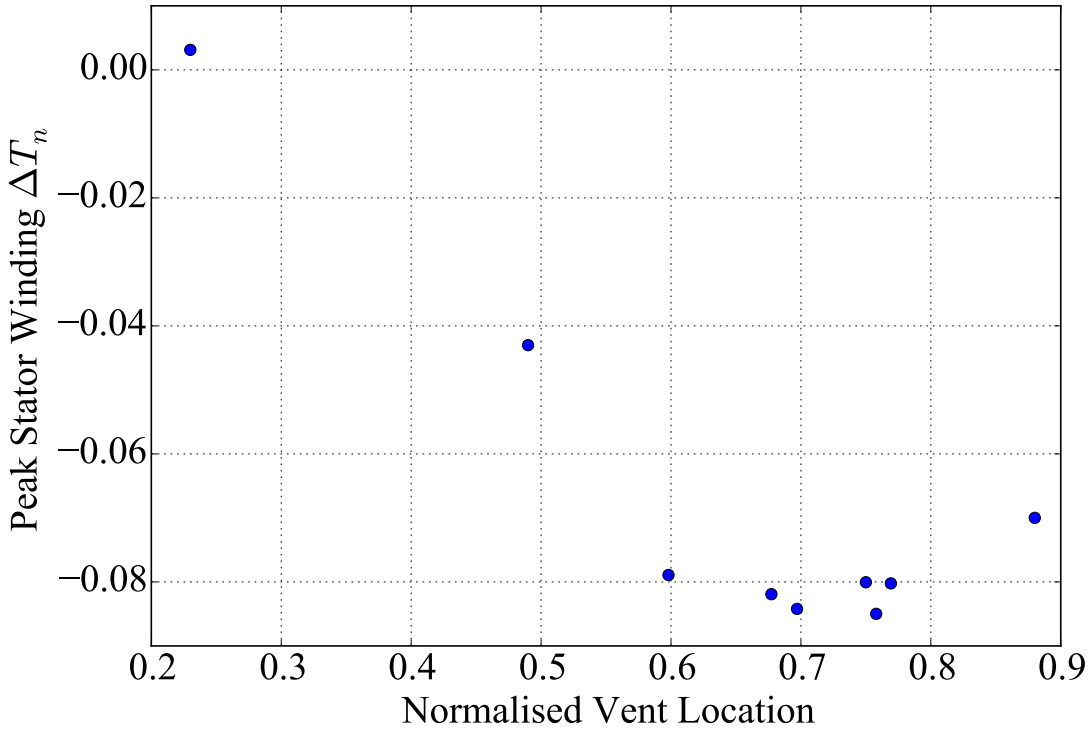


Fig. 6.18 Relationship between peak stator winding temperature rise difference and vent location for a case with a single vent and a constant vent width; Temperature rise difference normalised according to equation 6.9

The vent mass flow rate directly correlates with the heat that can be extracted from the stator, suggesting it would be best to locate the vent towards the end of the core, where the vent flow rate is highest. But the flow rate is not the only parameter influencing the stator cooling, targeting the winding hot spot with the vent is equally important. Figure 6.18 shows the relationship between the peak stator winding temperature rise difference and the vent location

for the design points simulated during the optimisation of a single vent with a constant vent width of $0.02\,l_n$ and no baffle. The temperature rise difference is taken in relation to the CFD peak stator winding temperature rise of the non-vented case $T_{max,B}$ and normalised by dividing it through the experimentally measured peak stator winding temperature rise of the Benchmark Machine at full load and 0.8 PF (view section 5.3). This results in the following equation for the normalised temperature rise difference ΔT_n:

$$\Delta T_n = \frac{T - T_{max,B}}{T_{ref} - T_{in}} \tag{6.9}$$

The optimal vent location is at an axial position of $0.76\,l_n$, close to the stator winding hot spot of the benchmark case. The peak stator winding temperature rise decreases by 8.5 % with the addition of a vent in comparison to the Benchmark Machine.

6.4.2 Vent Width

The vent width influences the flow rate through the vents and thus the cooling of the stator windings. As the rotor copper losses increase with the vent width, as discussed in chapter 6.2, the vent width also impacts the rotor winding temperatures. To analyse the impact of the vent width on various parameters, a sensitivity study was conducted for a machine with a single vent at a constant location of $0.76\,l_n$ and no baffle in the stator-casing duct. The loss distribution was incorporated based on the findings of chapter 6.2.

Figure 6.19 shows the relationship between vent mass flow rate and vent width for vent widths ranging from 0-0.05 l_n. The vent mass flow rate has been non-dimensionalised according to equation 5.1. The vent mass flow rate increases according to a square root relationship with the vent width. The trendline in figure 6.19 was calculated using the OLS method for a function of the type $y = \sqrt{ax}$ and shows an excellent fit to the data points with a R^2 value of 0.996. The vent width must be increased by a factor of 4 to double the vent flow rate, indicating that it would be more beneficial to manufacture two stator vents with the same width instead of doubling the vent width.

Figure 6.20, showing the relationship between peak rotor and stator winding temperature rise differences and vent width, confirms that assumption. The temperature rise differences are taken in relation to the peak rotor and stator winding temperature rises of the non-vented case and normalised according to equation 6.9.

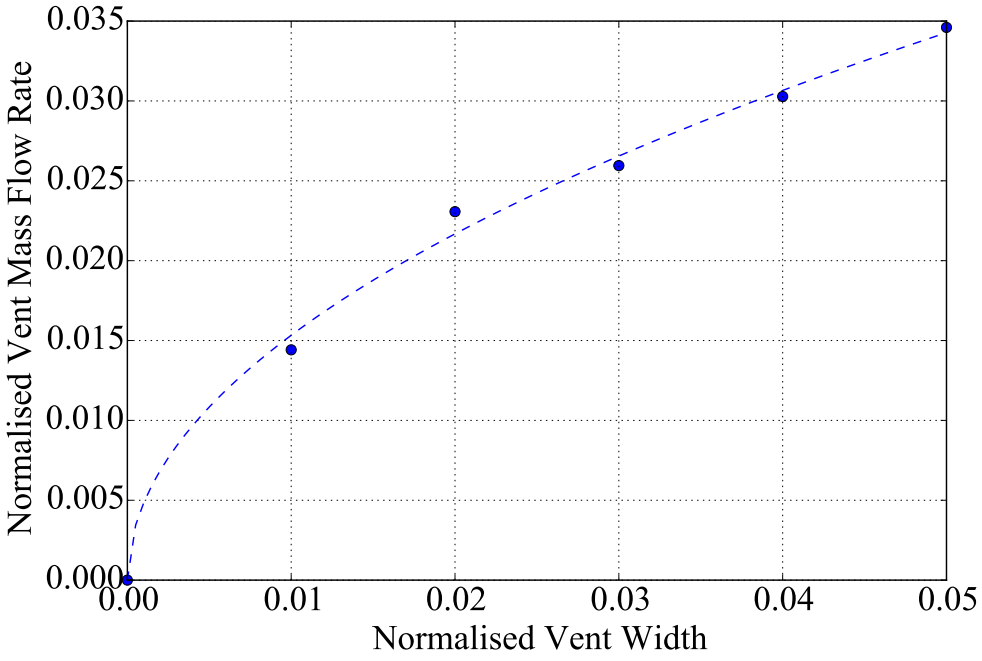


Fig. 6.19 Relationship between vent mass flow rate and vent width for a case with a single vent and a constant vent location; Mass flow rate normalised according to equation 5.1

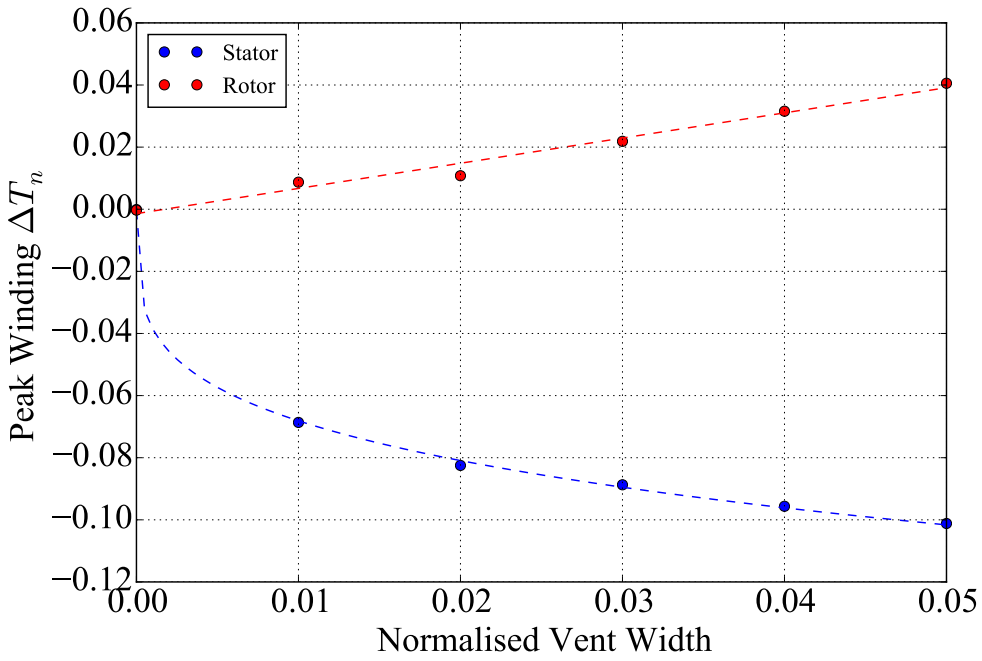


Fig. 6.20 Relationship between peak rotor and stator temperature rise difference and vent width for a case with a single vent and a constant vent location; Temperature rise difference normalised according to equation 6.9

The peak stator winding temperature rise decreases with an increasing vent width, following a 4^{th} root relationship. The rotor winding temperature rise increases linearly with an increasing vent width as a result of the increased rotor copper losses. The average rotor and stator winding temperature rise profiles are similar to the peak winding temperature profiles. Therefore, the addition of multiple thinner vents should be preferred over a single wide vent to maximise the stator winding cooling while limiting the rise in rotor winding temperatures.

The trendlines in figure 6.20 were calculated using the OLS method. For the rotor winding temperature rise, a linear relationship was assumed. The stator winding temperature rise profile was based on a function of the following type: $y = -\sqrt[4]{ax} + b$. They show an excellent fit to the data points with a R^2 value of 0.999 for the stator windings and 0.979 for the rotor windings.

6.4.3 Baffle Height

Locating a baffle in the stator-casing duct has the potential to reduce peak and average stator winding temperatures by influencing the mass flow and pressure distribution in the machine. Its axial position and radial height must be carefully chosen however, otherwise the baffle can have a negative impact on the thermal performance. Whilst the baffle improves the stator winding cooling, it reduces the stator back iron cooling. To investigate the impact of the baffle height on the thermal performance and find the optimal trade-off between increased stator winding and reduced stator back iron cooling, a sensitivity study varying the baffle height was conducted for a machine with two vents. The vents were located at $0.50\,\mathrm{l_n}$ and $0.8\,\mathrm{l_n}$ and were both $0.012\,\mathrm{l_n}$ wide.

Ideally, the axial baffle position would have been included in the optimisation procedure, but this was not feasible in the available time frame. Preliminary investigations showed that the best axial location for the baffle was immediately after the first vent (from the inflow direction), protruding radially inwards from the casing as shown in figure 6.14. The baffle reduces the air flow through the stator-casing duct, increasing the static pressure in front of the baffle in the stator-casing duct. This can be seen in figure 6.21, showing the pressure distribution in the stator-casing duct and airgap with and without a baffle.

As the pressure difference between the stator-casing duct and airgap determines the mass flow rate through the vents (view figures 6.16 and 6.17), the baffle can increase the vent flow rates. For the manufactured prototype with a baffle length of $0.41\,\mathrm{b_n}$, the flow rate through the first vent increases by 775 % in comparison to the design without the baffle. The flow rate

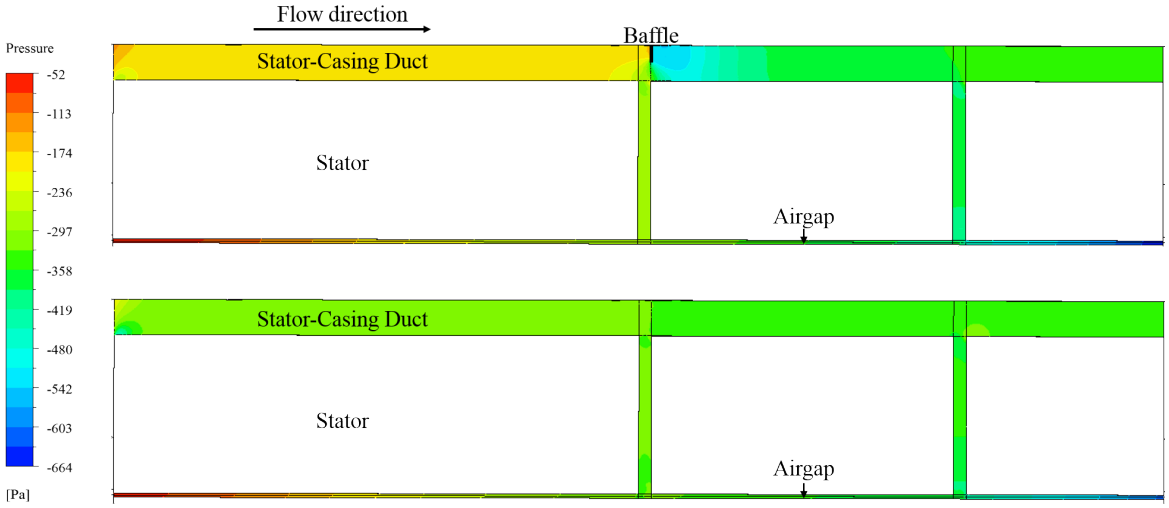


Fig. 6.21 Comparison of pressure distribution between stator-casing duct and airgap with (top) and without (bottom) a baffle

through the second vent increases by 17 %. The relationship between the flow rates through the 1st and 2nd vent and the baffle length is shown in figure 6.22.

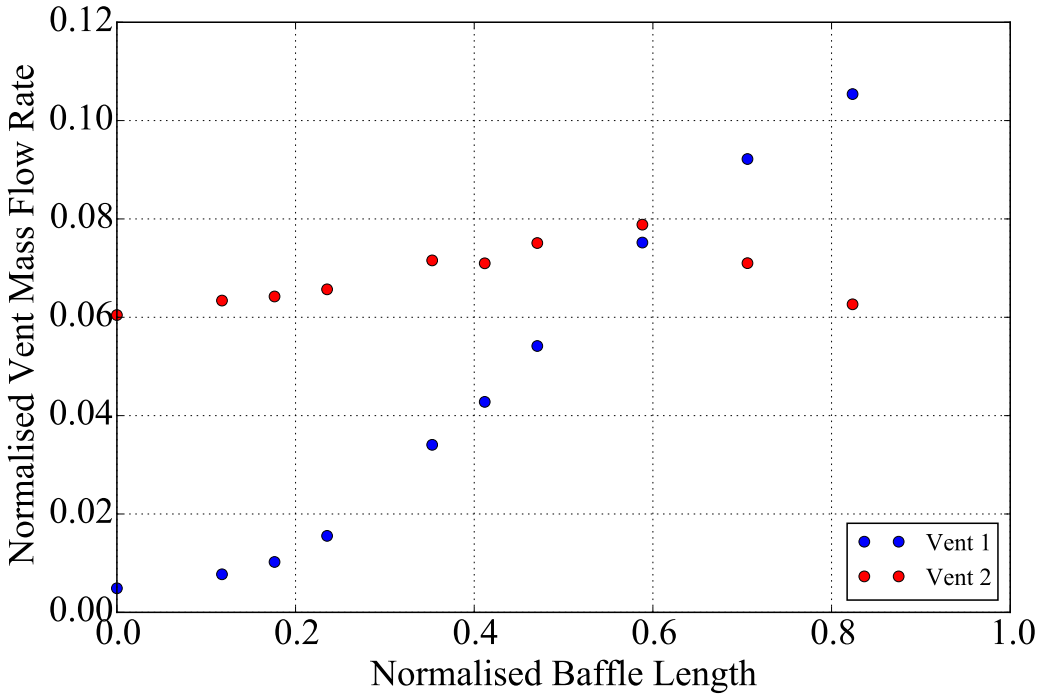


Fig. 6.22 Relationship between mass flow rate through the vents and baffle length; Mass flow rate normalised according to equation 5.1

The flow rate through the 1st vent increases significantly with the baffle length. For a baffle length of 0.25-0.8 b_n, the relationship between vent flow rate and baffle length is linear. The flow rate through the 2nd vent does not depend as much on the baffle length for the investigated baffle length range. It increases by 18 % up to a baffle length of 0.6 b_n. As more air flows through the first vent into the airgap, the static pressure in the airgap is reduced. The pressure in the stator-casing duct after the baffle recovers to approximately the same value as for the non-baffled case, increasing the pressure drop between stator-casing duct and airgap at the location of the second vent and hence increasing the vent flow rate. This can be seen in figure 6.23, showing the static pressure in the stator-casing duct and airgap with a baffle (0.41 b_n) and without a baffle. The pressures were taken in the radial centre of the stator-casing duct/airgap and averaged circumferentially.

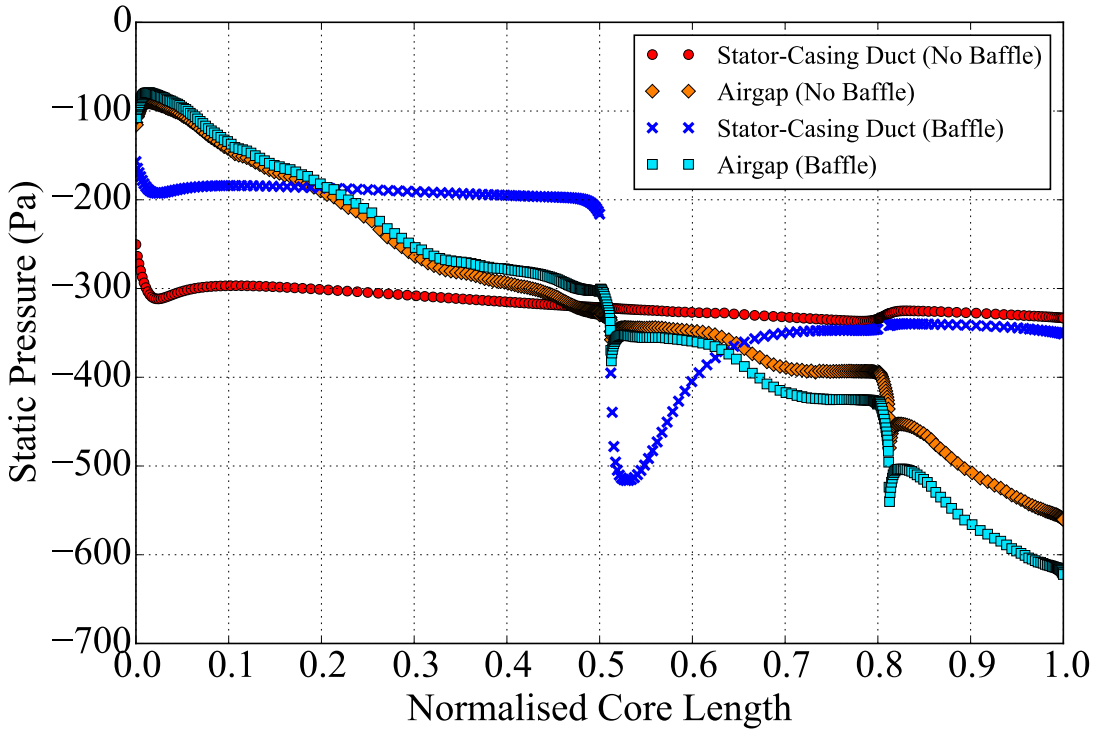


Fig. 6.23 Static pressure in the stator-casing duct and airgap with and without a baffle

From a baffle length of 0.6 b_n on, the flow rate through the stator-casing duct after the 1st vent is reduced so much that the 2nd vent cannot be fed sufficiently anymore by the fan. The flow rate through the 2nd vent decreases back to its original value around a baffle length of 0.85 b_n (view figure 6.22). A further increase in baffle length would reduce the flow rate until it reaches 0 when the stator-casing duct is fully blocked.

Without the addition of a baffle, the total mass flow rate through a vented machine stays almost the same (0.3 % reduction) in comparison to the non-vented machine. While an increased baffle length increases the vent flow rates, it reduces the total flow rate through the generator by increasing the flow resistance in the stator-casing duct. This can be seen in figure 6.24, showing the relationship between total mass flow rate through the machine and baffle length. For a baffle length of 0.25-0.8 b_n, the relationship between vent flow rate and baffle length is linear.

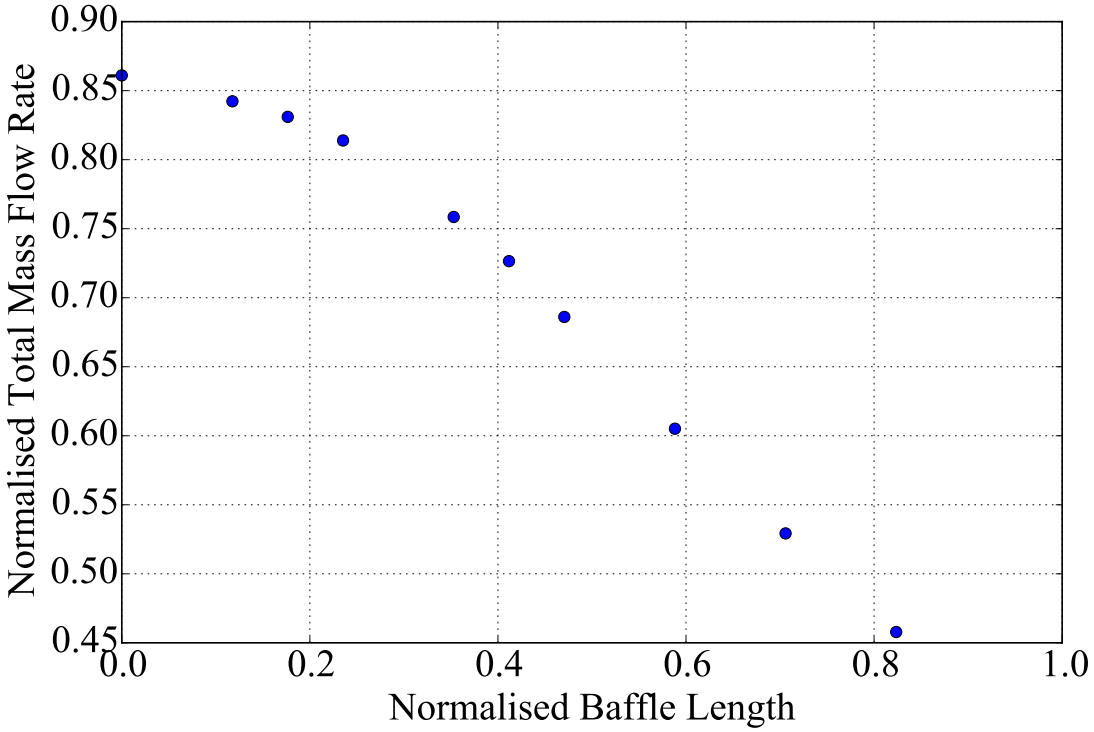


Fig. 6.24 Relationship between total mass flow rate and baffle length; Mass flow rate normalised according to equation 5.1

Interestingly, the baffle only influences the flow rate through the stator-casing duct. The mass flow rate into the core stays almost constant regardless of the baffle length. Hence, the reduction in total mass flow rate is equivalent to the reduction of mass flow rate through the stator-casing duct for the vented machine. The heat extracted from the stator back iron directly correlates with the mass flow rate through the stator-casing duct. To optimise the cooling performance, the flow rates through the vents (increasing with the baffle length) must be balanced with the flow rate through the stator-casing duct (decreasing with the baffle length).

Figure 6.25 shows how the peak and average stator winding temperature rise differences change with the baffle height. The temperature rise differences are taken in relation to the peak and average stator winding temperature rises of the non-vented case and non-dimensionalised according to equation 6.9. Figure 6.25 confirms that the chosen baffle size is optimal for the reduction of the peak stator winding temperature rise and close to the optimal length for a reduction in average stator winding temperature rise. The addition of the baffle reduces the peak stator winding temperature rise by 4.2 %, while reducing the average stator winding temperature rise by 2.0 % in comparison to a vented machine without a baffle. Placing multiple baffles in the stator-casing duct was not found to be beneficial for the thermal performance.

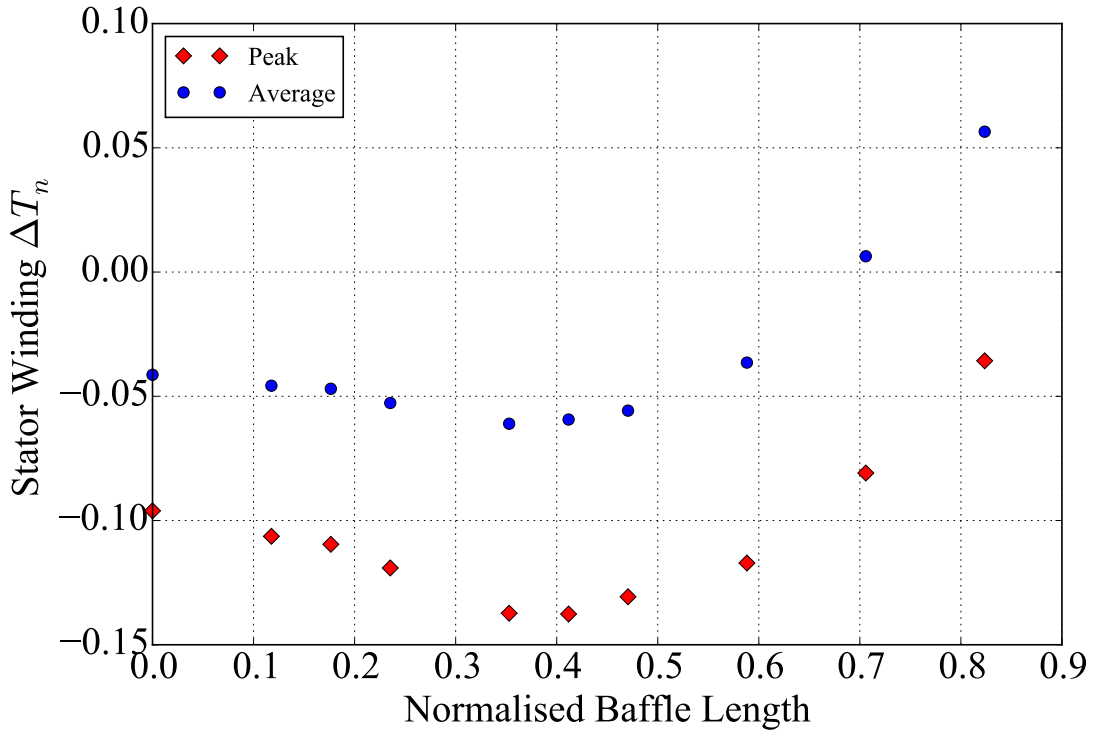


Fig. 6.25 Relationship between peak & average stator winding temperature rise difference and baffle height; Temperature rise difference normalised according to equation 6.9

Table 6.2 summarises the results of this section, comparing the mass flow distribution and stator winding temperature rise between the Benchmark Machine and the Vented Prototype with and without a baffle. Despite the reduction in total mass flow rate through the generator, adding a baffle to the stator-casing duct improves the stator cooling of the machine. The

reduced stator back iron cooling is more than compensated for by directly targeting the stator winding hot spot with more cooling air flowing through the vents.

Table 6.2 Normalised mass flow rates and normalised stator winding temperature rise differences in the benchmark and vented machines with and without a baffle

	Benchmark	**Vented (No Baffle)**	**Vented (Baffle)**
Mass Flow			
Total	0.863	0.861	0.726
Stator-Casing Duct In	0.563	0.581	0.447
Airgap In	0.300	0.280	0.279
Stator-Casing Duct Out	0.563	0.553	0.388
Airgap Out	0.300	0.308	0.339
Vent 1	-	0.002	0.021
Vent 2	-	0.030	0.035
Δ Temperature rise			
Peak Stator Winding	0.000	-0.096	-0.138
Average Stator Winding	0.000	-0.042	-0.059

6.5 Optimisation Results

In this section, the design optimisation procedure based on the methodology presented in section 6.3 and its results are discussed and compared to the CFD results of the Benchmark Machine.

After the solution of the first 21 design points and the creation of the response surface, one candidate point was solved and added to the initial response surface, as its error predictor was too high. In the following iteration, the error predictor of all candidate points was acceptable, resulting in a reduction of the optimisation domain. The range of two of the five input parameters was reduced: The location of the second vent (58 % reduction) and the baffle height (42 % reduction). Table 6.3 shows how the optimisation domain changed as a result of the domain reduction.

Table 6.3 Domain Reduction

	Initial Range	**Reduced Range**
Location 2nd Vent	**0.64** - 0.88	**0.78** - 0.88
Baffle Length	0.12 - **0.88**	0.12 - **0.56**

As 5 of the design points investigated so far were located in the reduced range, an additional 16 design points were created by the OSF algorithm for the creation of the new response surface.

To allow sufficient time for the prototype manufacture, the optimisation procedure had to be stopped manually after 14 days, before it reached convergence. At this point, 25 different stator ventilation configurations were evaluated and the parameter range narrowed down. The most promising designs at this point were identified and discussed with the machine manufacturer (DP 1-4). Their key parameters are shown in table 6.4. The temperature rise differences in table 6.4 are taken in relation to the Benchmark Machine CFD results and non-dimensionalised according to equation 6.9. The mass flow rates are non-dimensionalised according to equation 5.1. The negative mass flow rate through the vents indicates radially inwards flow.

Table 6.4 Most promising design points identified during the optimisation procedure; Manufactured DP marked in green; All properties normalised

	DP 1	DP 2	DP 3	DP 4	DP 5
Location 1st Vent	0.47	0.50	0.51	0.54	0.50
Location 2nd Vent	0.82	0.80	0.86	0.84	0.80
Width 1st Vent	0.019	0.020	0.038	0.021	0.012
Width 2nd Vent	0.011	0.012	0.021	0.029	0.012
Baffle Length	0.32	0.41	0.46	0.14	0.41
ΔT_{max} Stator Windings	-0.134	-0.150	-0.161	-0.125	-0.138
ΔT_{avg} Stator Windings	-0.064	-0.071	-0.087	-0.062	-0.059
ΔT_{max} Rotor Windings	0.033	0.019	0.038	0.053	0.013
ΔT_{avg} Rotor Windings	0.045	0.040	0.060	0.063	0.034
Total Mass Flow Rate	0.812	0.761	0.718	0.878	0.760
Mass Flow Rate 1st Vent	-0.021	-0.035	-0.059	-0.003	-0.022
Mass Flow Rate 2nd Vent	-0.033	-0.036	-0.060	-0.060	-0.037

As a result of the discussion with the machine manufacturer, DP 2 was identified as the most promising design. While DP 3 achieves a higher reduction in peak and average stator winding temperature rise, smaller vents are easier to manufacture and do not increase the rotor winding temperature rise as much. The design of DP 2 was slightly changed to facilitate manufacture by reducing the width of the 1st vent, making both vents equally wide, and changing their location by a few millimetres. The impact of the manufacture changes was investigated by running the CFD model with the new parameters (DP 5), confirming a substantial reduction in stator winding temperature rise would still be achieved despite the pragmatic design change.

Figure 6.26 shows a temperature rise contour plot of a circumferential plane slicing through the centre of a stator slot, comparing the Benchmark Machine to DP 5.

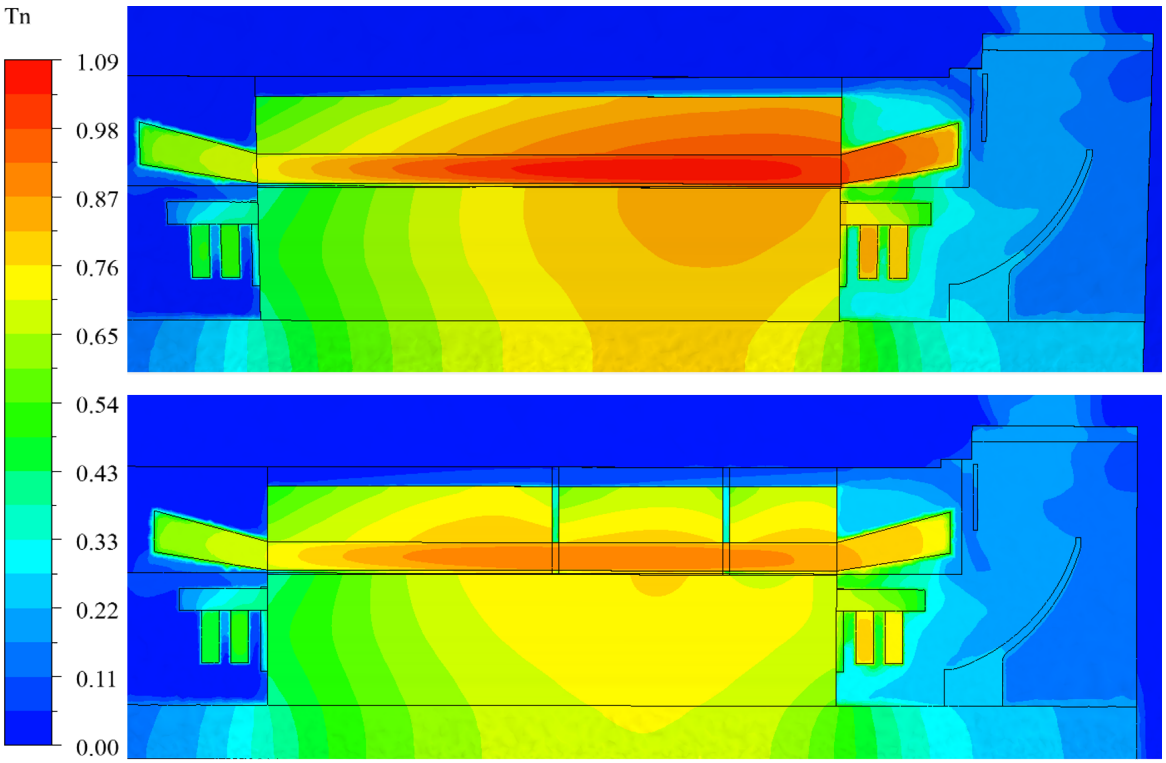


Fig. 6.26 Temperature rise contour comparison between Benchmark Machine (top) and Vented Prototype (DP 5) (bottom); Temperature rise normalised according to equation 5.4

In figure 6.27, the stator winding temperature rises of DP 2 and DP 5 are compared to the Benchmark Machine. The temperature rises were taken in the geometric centre of the slot and averaged over all slots. Figure 6.27 clearly shows the positive impact venting the stator has on the stator winding temperature rise, reducing the peak stator winding temperature rise by 15.0 % and the average stator winding temperature by 7.1 % for DP 2. Up to 0.15 l_n, the benchmark and vented machines show almost the same thermal behaviour. From there on, the temperature gradients of the vented machines decrease in comparison to the Benchmark Machine. A local temperature peak can be seen around 0.4 l_n. From here, the temperature rise decreases slightly until 0.5 l_n, the location of the first vent. The hot spot of the vented machines is located around 0.65 l_n.

The location of the two vents is evident by the two local minima at 0.5 l_n and 0.8 l_n. They are caused by the windings being directly cooled by the air flowing through the stator vents. By locating the vents on both sides of the Benchmark Machine hot spot, a fairly even temperature profile can be achieved. The stator winding temperature rise varies by less than 15 % in the

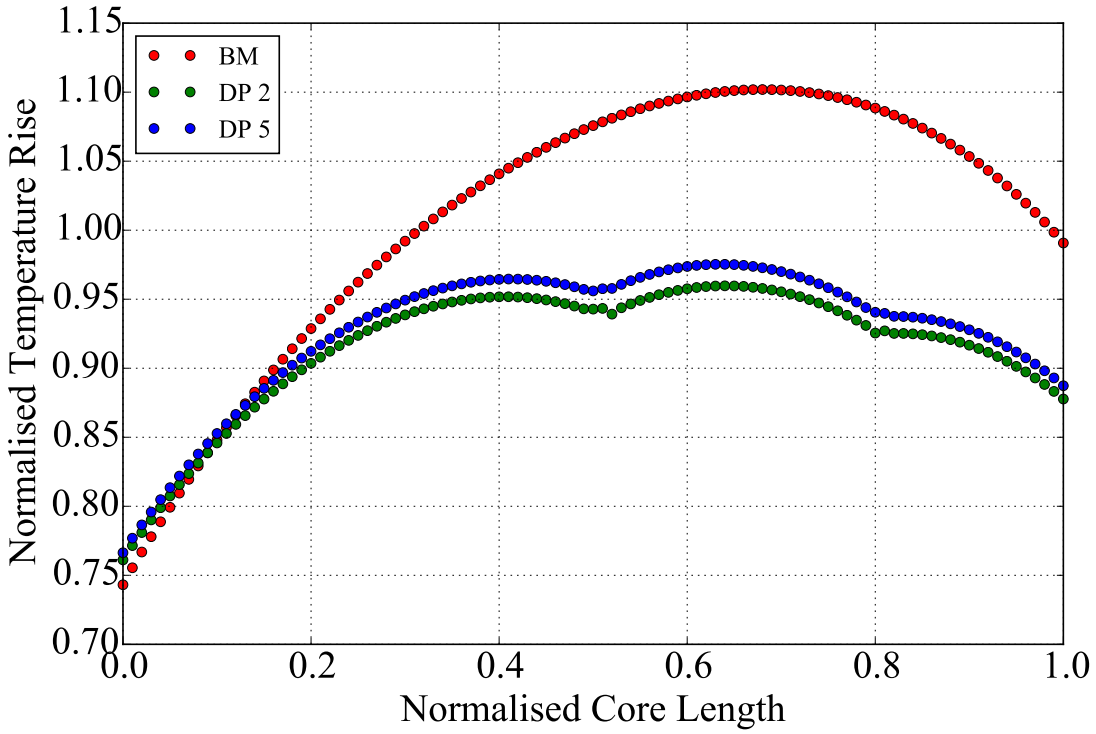


Fig. 6.27 Comparison of stator winding temperature rise in the core between Benchmark Machine, DP 2 & DP 5; NDE at the left; Temperature rise normalised according to equation 5.4

core for the vented machines, in comparison to 25 % for the Benchmark Machine, and is relatively constant for 0.3-0.8 l_n.

To keep the output power the same, the rotor current, and hence the rotor copper loss, is increased for the vented machines to compensate for the reduction in active material. This increases the rotor winding temperature rise. As the rotor copper loss increases linearly with the combined vent width (view section 6.2), the rotor temperature rise increases with the combined vent width (view table 6.4). The peak rotor winding temperature rise increases by 1.9 %, for DP 2, while the average rotor winding temperature rise increases by 4.0 %. Because the benchmark rotor winding temperature rise peaks in proximity to the stator winding temperature rise, the vents actually improve the rotor hot spot cooling. This was shown by running a simulation of the vented machine with the Benchmark Machine heat input. However, the improved rotor cooling is not sufficient to compensate for the increased rotor copper losses.

The temperature profile of DP 5 is very similar to DP 2. Due to the reduced width of the 1st vent, less air flows through the vent reducing the cooling performance. In comparison to DP 2, the peak and average stator winding temperature rises of DP 5 are increased by 1.2 %. The rotor peak and average temperature rises are 0.6 % lower because of the decrease in rotor current resulting from the reduced vent width.

As a result of the optimisation procedure and discussion with the machine manufacturer, the vented stator was built according to the specifications of DP 5 and subsequently tested to validate the design methodology (view chapter 7).

Chapter 7

Experimental Validation of the Vented Prototype CFD Model

In this chapter, the manufactured stator prototype and its baffle design are discussed. The CFD and experimental test results of the Vented Prototype are presented, analysed and compared to each other and the reasons for differences between computational and experimental results are discussed. The experimental results of the Vented Prototype are compared to the results of the Benchmark Machine, highlighting the improved stator cooling. For consistency, the same experiments as for the Benchmark Machine were performed on the Vented Prototype. Figure 5.1 gives an overview of the conducted experimental tests.

To enable a more consistent comparison between the Benchmark Machine and the Vented Prototype, the entire BM rotating assembly and the exciter stator were removed from the Benchmark Machine and inserted into the prototype stator for the experimental tests, eliminating rotor manufacturing uncertainty as an error source from the test results.

7.1 Baffle Design

The most economical way to manufacture the baffle and add it to the stator-casing duct would be to manufacture it out of a thin steel or aluminium sheet and spot weld it to the inside of the casing before the stator stack is pressed into the casing. But the creation of a flexible testing platform was prioritised over low manufacturing costs for this project. Therefore, it was decided to remove casing material at the axial location of the first vent after the stator stack was pressed into the casing and 3-D print baffles to be inserted into the casing cutouts.

Eight axial bars lending structural support to the stator-casing arrangement are located between the stator and casing (view figure 1.2). Therefore, 8 separate cutouts were made in the casing between these bars and 8 baffle pieces had to be manufactured. The baffles are in direct contact with the support bars, which touch the stator back iron, and thus get so hot under full load that conventional 3-D printing materials like Nylon are not suitable for the baffles. Two different temperature resistant materials were used for the manufacture of the baffles instead: Polycarbonate [87] and Copolyester [88]. Their suitability for this application has been determined by heating the baffles up to 120 °C in an oven for half an hour and testing if they deformed by applying pressure afterwards. No deformation was noted for either of the materials.

Figure 7.1 shows one of the baffles printed from polycarbonate. The inner cylindrical sector (2) is inserted into the casing cutout from the outside, with its walls to be coincident with the casing walls. The thin baffle (3) with a radial length of 0.41 b_n extends into the stator-casing duct, directing the flow into the first vent. The baffles are fixed in place by pressing the outer cylindrical sector (1) onto the casing and securing them with silicone sealant to assure an airtight fit.

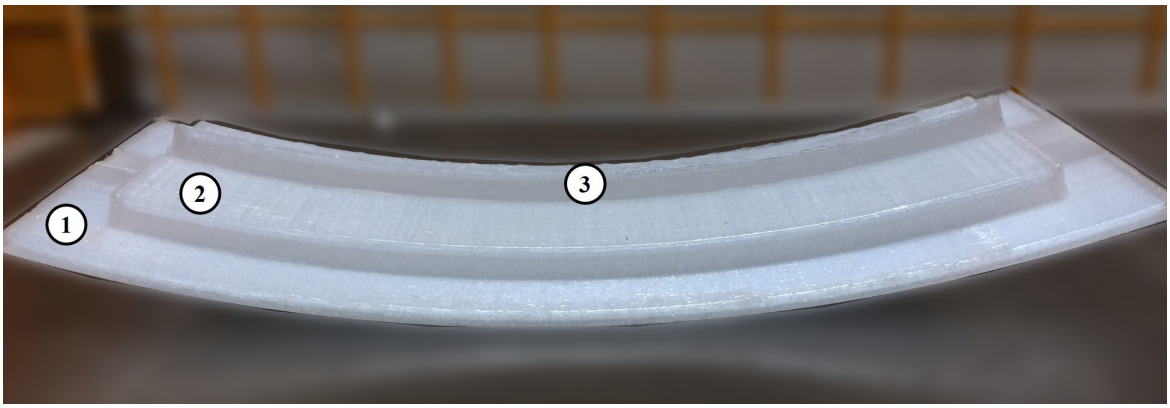


Fig. 7.1 Baffle 3-D printed from Polycarbonate

An Ultimaker 3 3-D printer was used to print the baffles. Using a fill factor of 40 %, it took approximately 5 hours per baffle to print. The printing temperature was 270 °C. A thermal enclosure had to be built around the printer to avoid warping of the material during the printing process.

7.2 Mass Flow Results

The mass flow rate was measured experimentally using the plenum system described in section 4.2. Measurements were taken at 150 RPM intervals in a rotational speed range from 150-1500 RPM. Figure 7.2 shows the relationship between total mass flow rate through the machine and the rotational speed with and without grilles covering the inlets and outlets. The mass flow rate was non-dimensionalised according to equation 5.1.

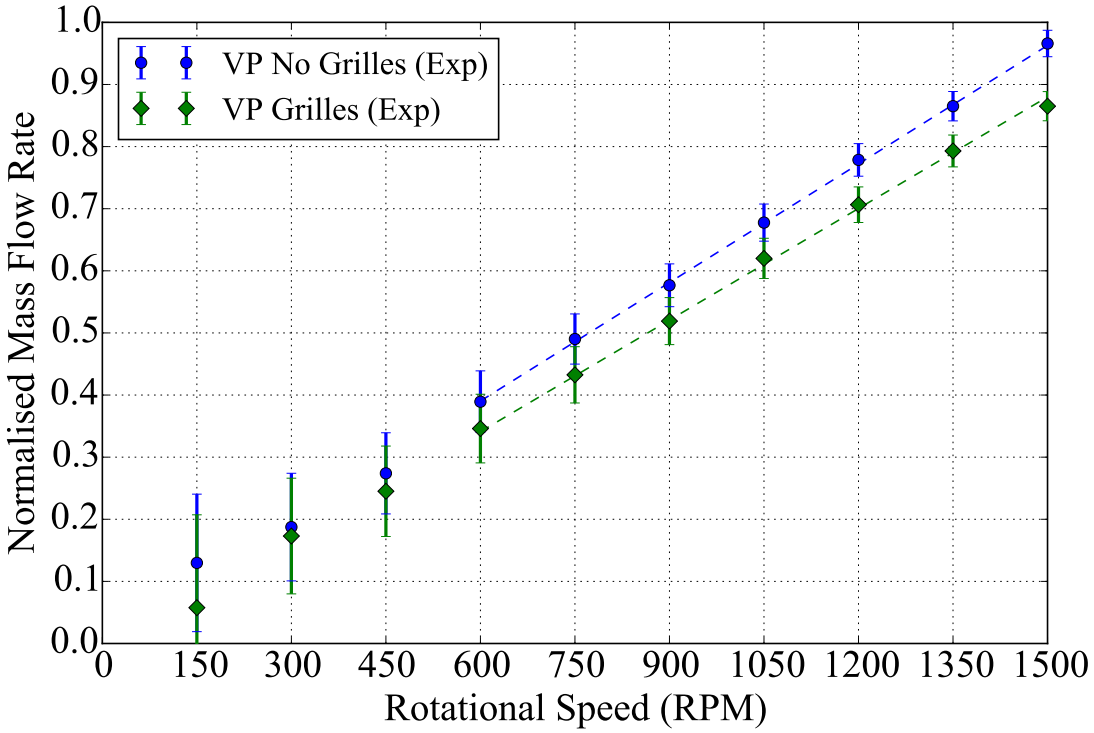


Fig. 7.2 Experimentally measured mass flow rates through the Vented Protoype with and without grilles at various rotational speeds; Mass flow rate normalised according to equation 5.1

Equivalent to the Benchmark Machine, the grilles restrict the air flowing in and out of the machine, reducing the total flow rate. The difference between the flow rate with and without the grilles is bigger in comparison to the Benchmark machine, amounting to 0.101 $\dot{m}_n$ at synchronous speed (0.064 $\dot{m}_n$ for the BM). Figure 7.2 clearly shows the linear relationship between the mass flow rate and the rotational speed for 600-1500 RPM. The trendlines were calculated using the OLS method. They show an excellent fit to the experimental data with R^2 values of 0.998 with and without the grilles.

Figure 7.3 shows a comparison of the experimentally measured mass flow rates through the Benchmark Machine and Vented Prototype without grilles covering the inlets and outlets. At synchronous speed, the total mass flow rate of the Vented Prototype is 0.034 $\dot{m}_n$ below the flow rate of the Benchmark Machine. At lower speeds, the flow rate of the Vented Prototype was measured to be slightly above the Benchmark Machine. However, this is most likely caused by the measurement uncertainty. All data points are within the measurement uncertainty of one another, as indicated by the error bars in figure 7.3. The mass flow rates are calculated from the pressure drop measured at the inlet duct according to equation 4.1. As the measurement uncertainty of the used pressure gauge is constant at 1 % full scale and the pressure drop decreases with the flow rate, the mass flow rate measurement uncertainty is higher at low flow rates.

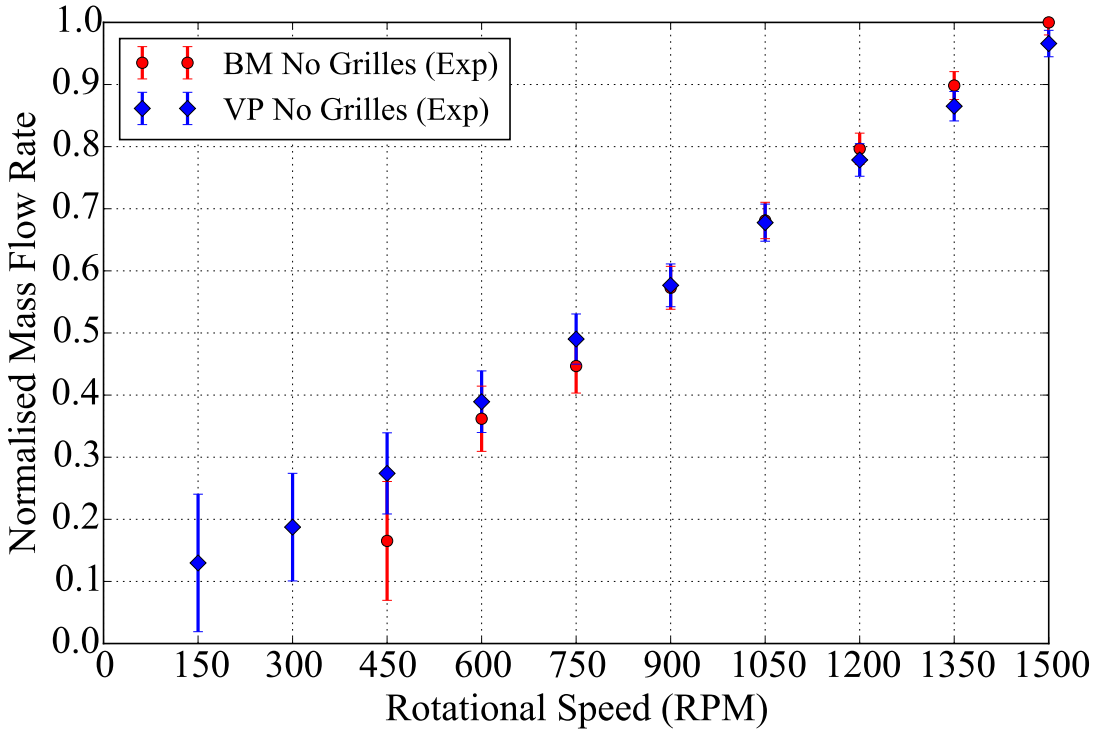


Fig. 7.3 Comparison of experimentally measured mass flow rates without grilles through the Benchmark Machine and Vented Protoype at various rotational speeds; Mass flow rate normalised according to equation 5.1

Due to the baffle in the stator-casing duct, the mass flow rate of the Vented Prototype is expected to be below the flow rate of the Benchmark Machine (view section 6.4.3). The CFD simulations predicted a 0.136 $\dot{m}_n$ reduction in total flow rate, which is significantly above

the measured reduction of $0.034\,\dot{m}_n$. This difference can be explained by the inaccurate radial length of the baffles. While they were designed to have a radial length of $0.41\,b_n$, measurements taken after the experimental tests showed they only extended $0.18\,b_n$ into the stator-casing duct. This was determined by removing the baffles from the casing, inserting Blu Tack into the stator casing-duct, inserting the baffles and measuring the depth of the imprint left by the baffles in the blue tack.

The discrepancy between designed and actual baffle length was caused by manufacturing issues. Both utilised 3-D printing materials proved to be inferior regarding printing accuracy, sensitivity to printer settings and print times in comparison to more conventional 3-D printing materials. The biggest challenge was to avoid warping of the material while the print was still in progress. That challenge was thought to have been overcome by building a thermal enclosure around the printer, keeping the temperature inside the printer well above ambient. But the measurements taken after the experimental tests showed this was not sufficient.

As a consequence of the inferior printing accuracy, the inner diameter of the outer cylindrical sector of the baffles (3) (view figure 7.1) was not equivalent to the casing outer diameter, causing a gap between the baffle body and the casing and thus reducing the radial extension of the baffle into the stator-casing duct. As discussed in section 6.4.3, the baffle length influences the mass flow rate, flow distribution and thermal performance of the machine. For the actual baffle length of $0.18\,b_n$, the reduction in total mass flow rate predicted by CFD is $0.032\,\dot{m}_n$, which is in good agreement with the experimentally measured reduction of $0.034\,\dot{m}_n$.

Figure 7.4 shows a comparison between CFD MRF, CFD SM and the experimentally measured mass flow rates at various rotational speeds. The CFD MRF simulations were run with baffle lengths of $0.41\,b_n$ and $0.18\,b_n$ for rotational speeds ranging from 150-1500 RPM at 150 RPM intervals. The SM simulation was only run at 1500 RPM for a baffle length of $0.41\,b_n$ due to its high computational expense. Equivalent to the experimental data, the CFD MRF results show a linear correlation between rotational speed and mass flow rate for 600-1500 RPM, predicting the mass flow rate trend correctly.

The CFD MRF mass flow rate for a baffle length of $0.18\,b_n$ is lower in comparison to the experimental data with a $0.123\,\dot{m}_n$ difference at synchronous speed, which is consistent with the results of the Benchmark Machine ($0.137\,\dot{m}_n$ difference). Equivalent to the Benchmark Machine, the MRF approach underpredicts the mass flow rate as the pumping effect occurring between the salient rotor and stator as well as the fan blades and the fan housing cannot be predicted accurately using a steady-state approach. This was confirmed by running a

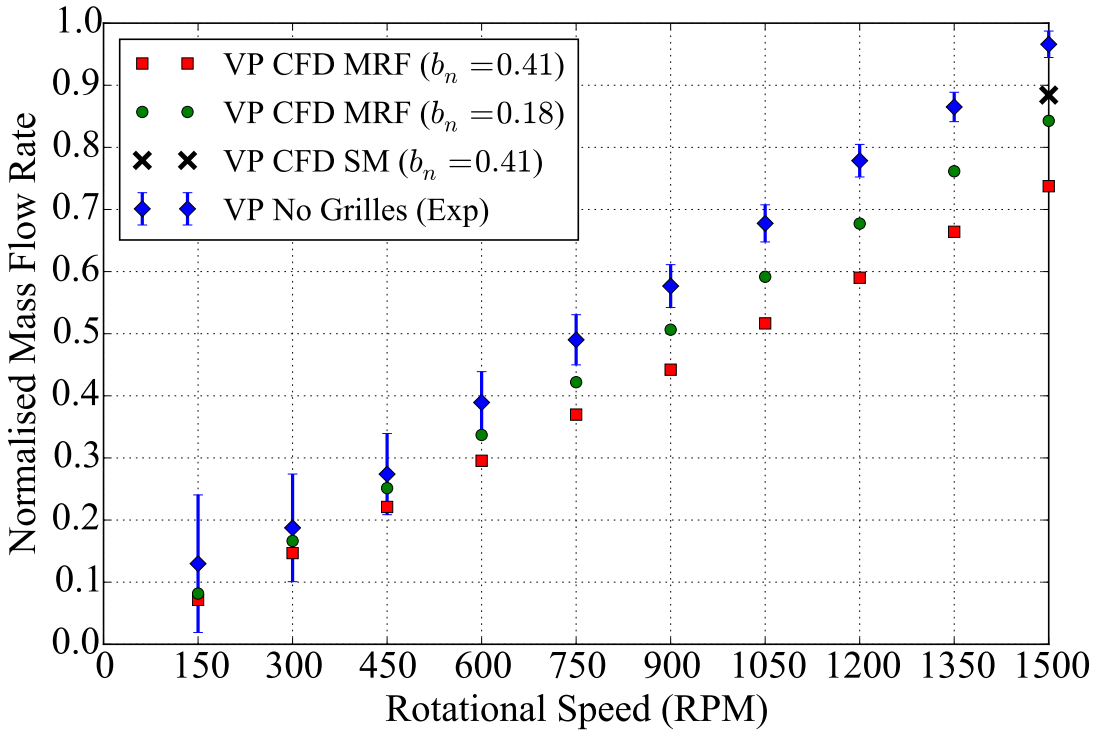


Fig. 7.4 Comparison of CFD and experimentally measured mass flow rate through the Vented Prototype at various rotational speeds; Mass flow rate normalised according to equation 5.1

transient simulation at synchronous speed for a baffle length of 0.41 b_n. The difference in mass flow rate between MRF and SM for a baffle length of 0.41 $b_n$is 0.147 $\dot{m}_n$, and hence consistent with the results of the BM model (0.135 $\dot{m}_n$ difference). Due to time constraints no SM simulation was conducted for a baffle length of 0.18 b_n, but a similar difference is expected for this case.

7.3 Torque Results

The torque measurements were taken as described in section 4.3 at 150 RPM intervals from 150-1500 RPM. Figure 7.5 shows a comparison of the experimentally measured windage and friction torque at various rotational speeds between the Benchmark Machine and the Vented Prototype. The torque M_n has been non-dimensionalised according to equation 5.3.

The torque measured for the Vented Prototype is higher than the torque of the Benchmark Machine with a maximum difference of 9.2 % at synchronous speed. Equivalent to the BM,

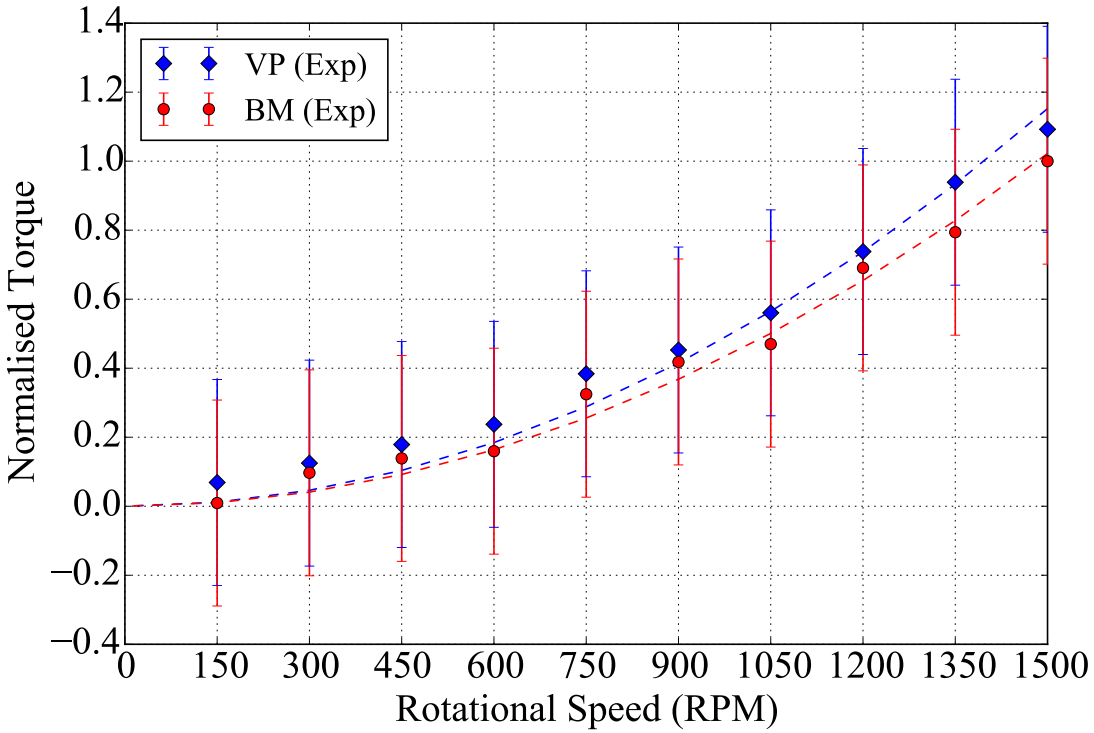


Fig. 7.5 Comparison of experimentally measured windage and friction torque between the Benchmark Machine and the Vented Prototype at various rotational speeds; Torque normalised according to equation 5.3

the torque increases quadratically with the rotational speed. The trendlines in figure 7.5 were calculated using the OLS method assuming a y-intercept of 0. They show an excellent fit to the data points with a R^2 value of 1.000 for the Benchmark Machine and a R^2 value of 0.971 for the Vented Prototype.

The CFD results predicted the windage and friction torque to be marginally lower for the Vented Prototype, as shown in figure 7.6. According to the CFD results, 90.3 % of the torque can be attributed to the fan and the fan torque increases with the total mass flow rate. But the utilised torque transducer is used for measuring torque and controlling the rig at full load, and its relative accuracy at no-load is relatively poor with a measurement uncertainty of ± 14.5 % at synchronous speed. The results of the VP and BM are within each other's measurement accuracy, as indicated by the error bars in figure 7.5. This means it is unclear if the windage and friction torque of the VP has actually increased or if it just a measurement accuracy issue. As the windage and friction losses are only a minor loss contributor in the

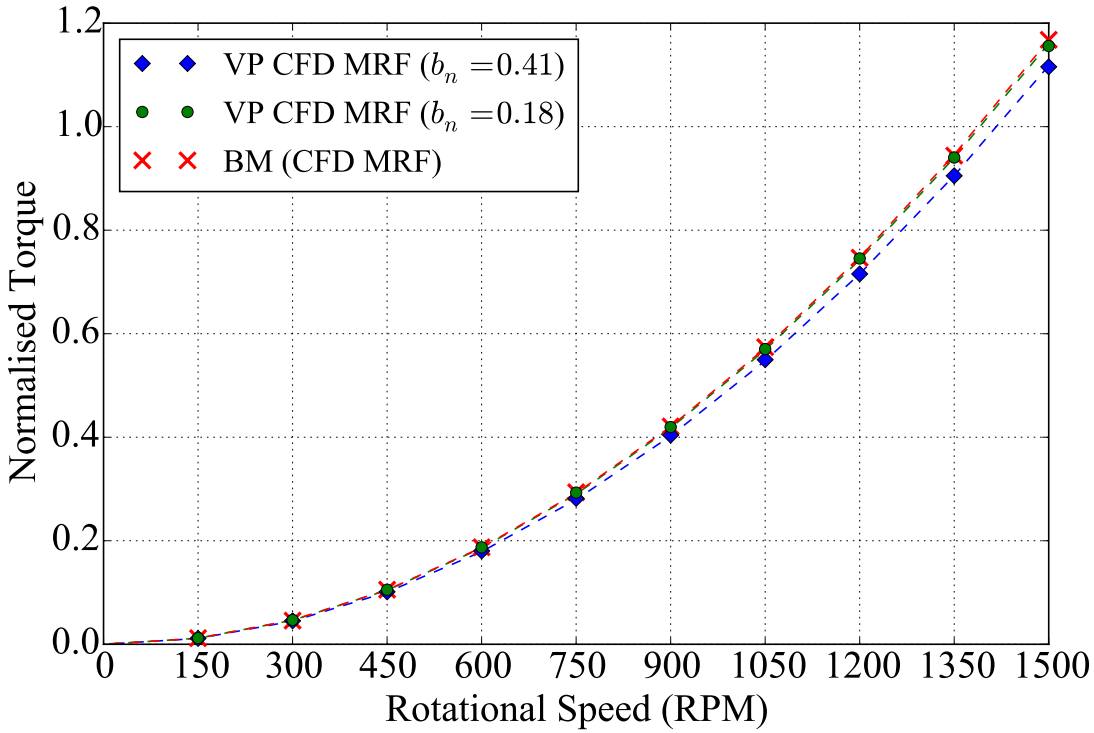


Fig. 7.6 Comparison of CFD windage and friction torque between the Benchmark Machine and the Vented Prototype at various rotational speeds; Torque normalised according to equation 5.3

investigated machine, and the agreement between CFD and experimental data was good, it was not deemed necessary to design a test rig with an improved measurement uncertainty.

Figure 7.7 shows a comparison between the CFD and the experimentally measured windage and friction torque dependent on the rotational speed. The CFD MRF torque was determined from the same simulations described in the previous section 7.2 for baffle lengths of 0.41 b_n and 0.18 b_n. It was calculated by exporting the moments of all rotating surfaces around the axis of rotation and multiplying them by 2, as a 180° periodic model was utilised.

Figure 7.7 shows good agreement between CFD and experimental results. The square relationship between rotational speed and windage and friction torque is predicted correctly by the CFD simulations. The trendlines were calculated using the OLS method assuming a y-intercept of 0. They show an excellent fit to the data points with a R^2 value of 1 for the CFD and 0.971 for the experimental data. The difference between CFD MRF and experimental data amounts to 0.063 M_n at synchronous speed for a baffle length of 0.18 b_n. As for the

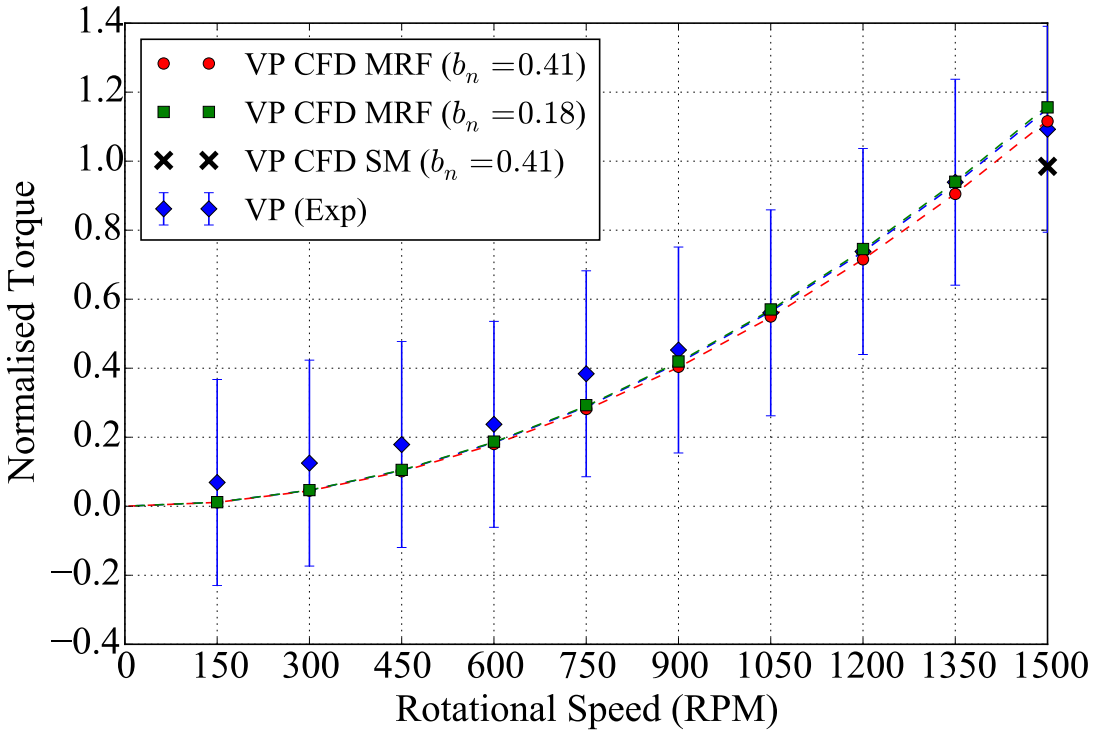


Fig. 7.7 Comparison of CFD and experimentally measured windage and friction torque of the Vented Prototype at various rotational speeds; Torque normalised according to equation 5.3

Benchmark Machine, the torque is predicted to be lower using the SM approach, with the difference between MRF and SM being 0.131 M_n for a baffle length of 0.41 b_n.

It is also important to keep in mind that a simple analytical correlation has been used for the calculation of the bearing losses, adding some additional measurement uncertainty which could not be quantified within this project. An accurate determination of the bearing losses would require disassembling the machine completely and measuring the torque of the bare shaft.

7.4 Thermal Results

For the thermal validation, the machine was run at various power factors and loads. This section focusses on the thermal results for full load and a power factor of 0.8, as this is the operating point the machine is designed for. Temperatures were measured in multiple locations in the stator and rotor windings. To enable a comparison to CFD temperatures and

test data taken on different days, the temperatures at both inlets were averaged and subtracted from the winding temperatures. The resulting temperature rise has been non-dimensionalised according to equation 5.4 throughout this chapter. The core length was non-dimensionalised according to equation 5.5. The NDE of the core is defined as the axial position corresponding to zero l_n and the core DE is defined as a core length of one l_n as shown in figure 5.6.

The stator copper losses implemented into the CFD model were calculated according to equation 4.7 based on the experimentally measured 3-phase averaged stator current and the resistance calculated based on the experimentally measured average stator winding temperature. The rotor copper losses were calculated according to equation 4.8 based on the experimentally measured rotor current and voltage. The exciter losses were assumed to be 10 % of the rotor copper losses. The rotor and stator iron losses were implemented based on Nuzzo's electromagnetic FEA results (view chapter 6.2). The stray losses were taken from the manufacturer's data sheet and distributed over the main rotor and stator iron and the exciter rotor and stator iron based on volume.

7.4.1 Impact of the Rotation Modelling Approach

There is a negative correlation between the total mass flow rate through the machine and the winding temperatures. As discussed in sections 5.1 and 7.2, the steady-state MRF approach underpredicts the total flow rate through the machine by $0.135\,\dot{m}_n$ (BM) or $0.147\,\dot{m}_n$ (VP) in comparison to the transient SM approach. The pumping effect occurring between the salient rotor and stator as well as the fan blades and the fan housing cannot be predicted correctly using a steady-state approach. This causes the CFD winding temperatures to be overpredicted. This chapter discusses the impact the reduced flow rate has on the thermal results.

A major problem of using the SM approach for modelling Conjugate Heat Transfer is the substantial difference in time scale between the fluid flow and the thermal conduction solution in the solid components. Selecting an appropriate time step is essential to achieve accurate simulation results. Small time steps in the range of 1° per time step (1.11×10^{-4} s) are required to model the fluid flow correctly, and the flow solution takes 3 360° revolutions to show converged, periodic behaviour. Experimental tests showed that the investigated machine takes 3-4 hours to reach steady thermal temperatures at full load, hence ~100 million time steps would be required for the thermal solution to converge, which would take several years on a desktop PC. This made the SM approach impractical to apply for

CHT simulations initially. In ANSYS Fluent v18.0, a new feature was introduced making it possible to choose different time step sizes for the fluid and solid parts of the domain. This enabled the investigation of the influence the rotation modelling approaches have on the thermal solution.

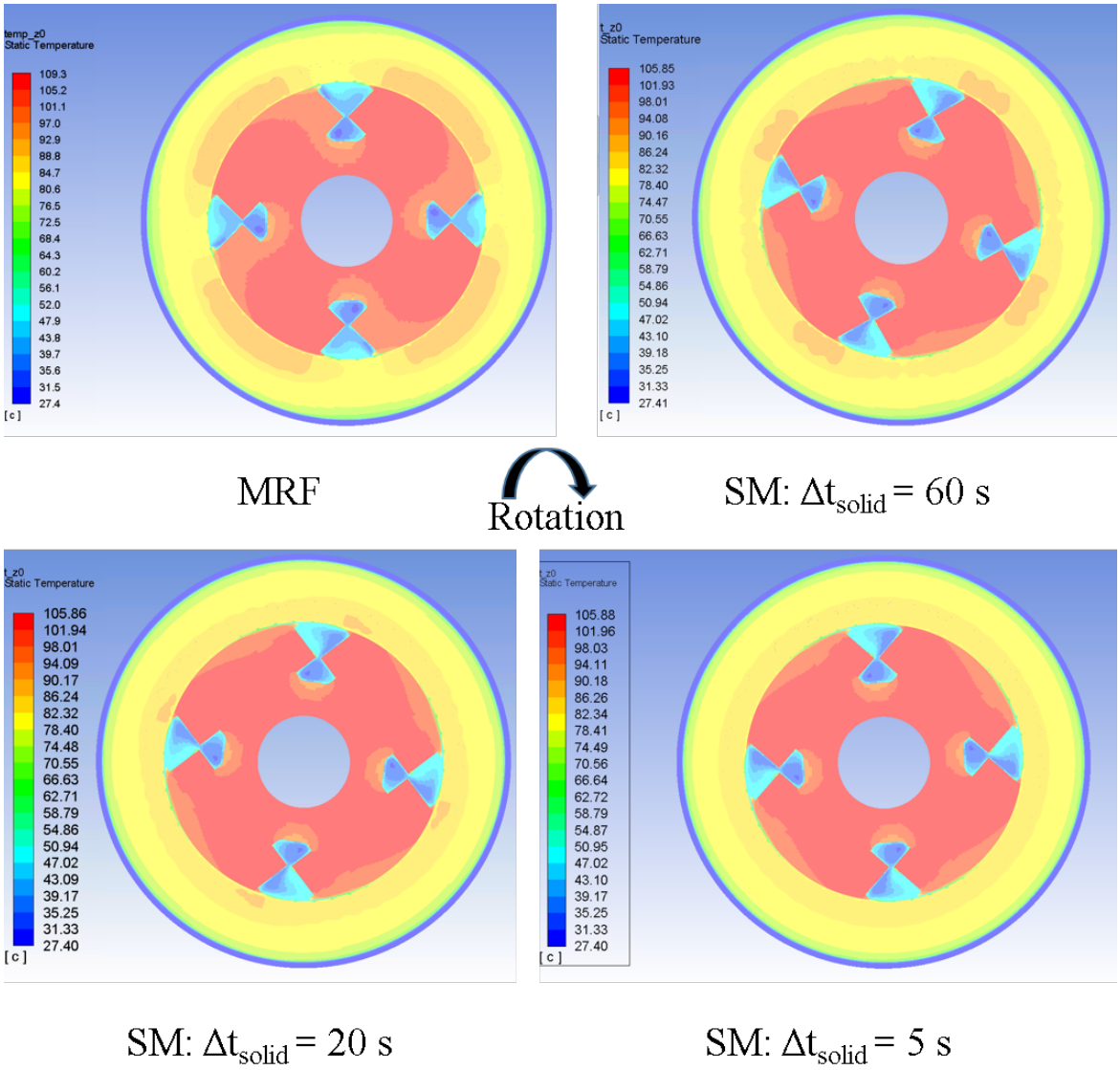


Fig. 7.8 Temperature contour comparison between MRF and SM simulations with various solid time step sizes conducted on a sub model

To investigate the influence of the solid time step size on the simulation results the sub model presented in chapter 6.1 was solved initially. In figure 7.8, the temperature contours in the centre of the core for the MRF approach are compared to the SM approach with solid time step sizes of 60, 20 and 5 s. The fluid time step size was chosen to be 2.22×10^{-4} s, corresponding

to 2° of rotation per time step. The simulations were considered to be converged when the peak and average winding temperatures were steady.

As discussed in chapter 3.4.4, one of the disadvantages of the MRF approach is that the temperature profile develops based on the frozen position of the rotor. Hot spots develop in the stator windings above the poles, as they are cooled by less and hotter air in comparison to the stator windings above the interpolar space. Figure 7.8 clearly shows the superiority of the SM approach in this regard. The stator winding hot spots above the poles become less distinguished with decreasing solid time step size until they do not visibly vary circumferentially for a 5 s solid time step. As a result, the peak stator and rotor winding temperatures decrease in comparison to the MRF approach.

Due to the high computational demand of the full VP model presented in chapter 6.3, solving it with a 5 s solid time step is not feasible. To enable a comparison to the MRF approach and quantify the impact of the reduced mass flow rate through the machine on the thermal performance, the VP model was solved using the SM approach with the following time steps: A fluid time step of 2.22×10^{-4} s, corresponding to 2° of rotation per time step, and a 5 minute time step for the solid parts. This resulted in a computation time of 5 weeks until steady temperatures were reached. The solution was initialised with the converged isothermal SM solution, which required an additional two weeks of computation time.

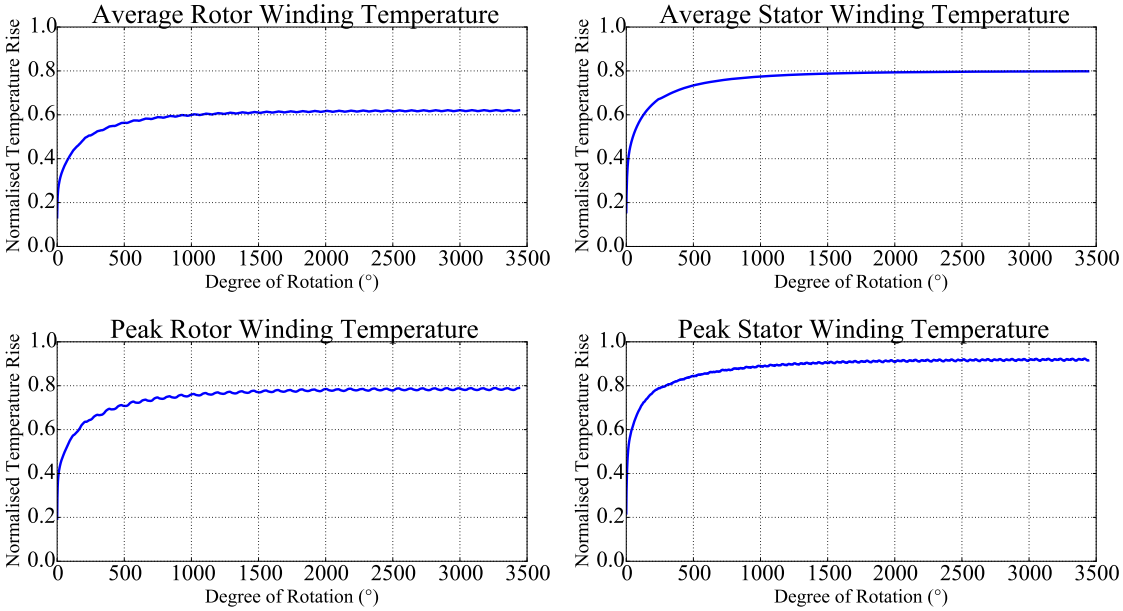


Fig. 7.9 Convergence of rotor and stator winding temperature rises during the CHT SM simulation of the Vented Prototype; Temperature rise normalised according to equation 5.4

Figure 7.9 shows the convergence of the peak and average rotor and stator winding temperature rises during this simulation. The solution was initialised with the converged isothermal SM solution, which required an additional two weeks of computation time.

Figure 7.10 shows a comparison of the temperature rise contours at an axial location of $0.70\,l_n$ between the MRF and SM approach. The peak and average temperature rises are significantly lower in the rotor and stator using the SM approach. The stator winding temperature rise was found to be reduced by 11.7 % (peak) and 8.5 % (average). The rotor winding temperature rise reduction was of a similar magnitude, with a 11.2 % (peak) and 10.9 % (average) reduction in comparison to the MRF approach. The temperature reduction can be attributed to the increased mass flow rate through the machine using the SM approach.

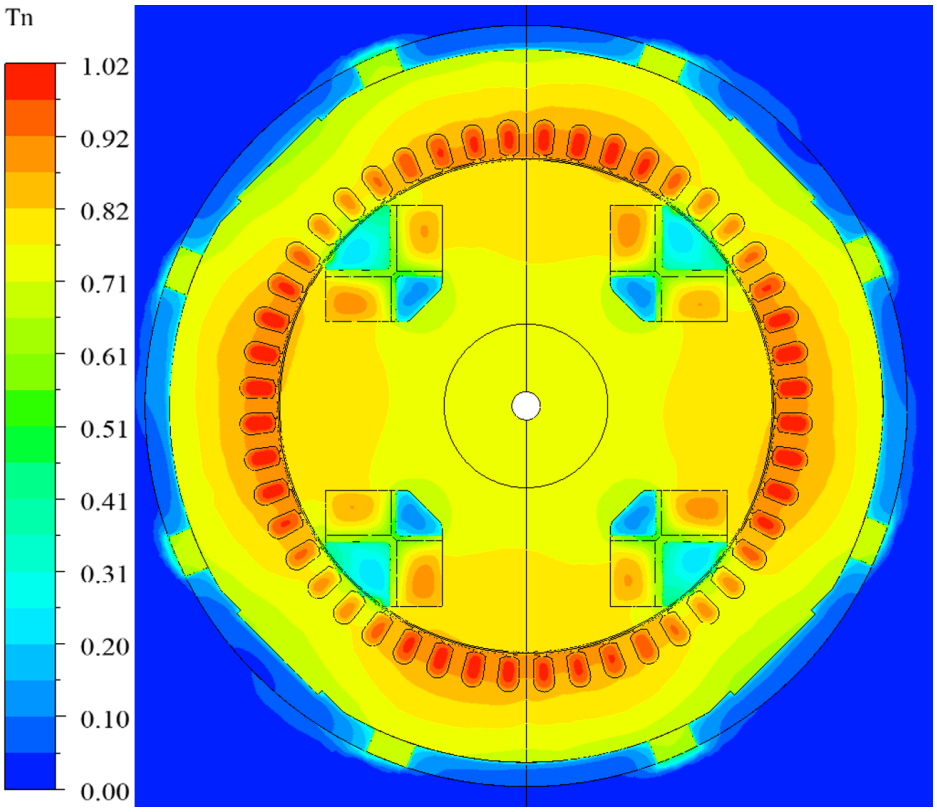
The SM circumferential temperature variation in the stator, depending on the relative position to the rotor poles, is much less distinguished in comparison to the MRF approach. Figure 7.11 illustrates this even better by showing a comparison of the temperature rise along the core length in the centre of every stator slot between the MRF and SM approach.

In addition to the reduction in temperature rise, the temperature rise variation between slots depending on their relative position to the rotor poles is considerably reduced using the SM approach. While the temperature rise varied by up to 15.0 % between slots for the MRF approach, the maximum difference is only 5.3 % for the SM approach. With a decreasing solid time step size, the SM temperature variation is expected to converge towards 0.

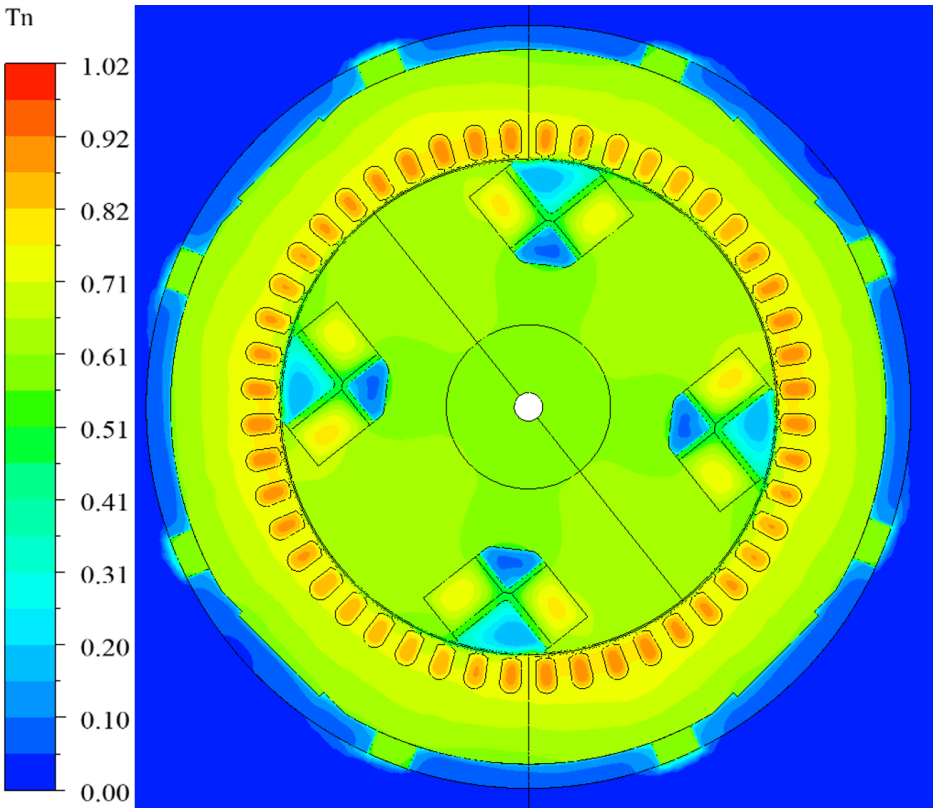
The torque is predicted to be $0.164\,M_n$ (BM) or $0.131\,M_n$ (VP) lower using the SM approach. The difference can be attributed to the fan pressure torque. As the flow through the fan and the adjacent machine outlets is highly transient and dependent on the position of the fan blades relative to the outlets, the steady-state MRF approach is not capable of capturing the flow characteristics in this area correctly.

While the SM approach is clearly superior for higher accuracy modelling of electrical machines, its high computational demand makes it unfeasible to use for the design optimisation of electrical machines. But it is important to quantify the impact using the steady-state MRF approach has on the simulation results. Hence, it is recommended to run a SM simulation of the optimal machine design to confirm its validity.

Table 7.1 summarises the result comparison between the MRF and SM modelling approaches. All properties are non-dimensionalised. Negative flow rates through the vents indicate radially inwards flow.



(a) MRF



(b) SM

Fig. 7.10 Comparison of MRF and SM temperature rise contours at an axial location of $0.70\,l_n$; Temperature rise normalised according to equation 5.4

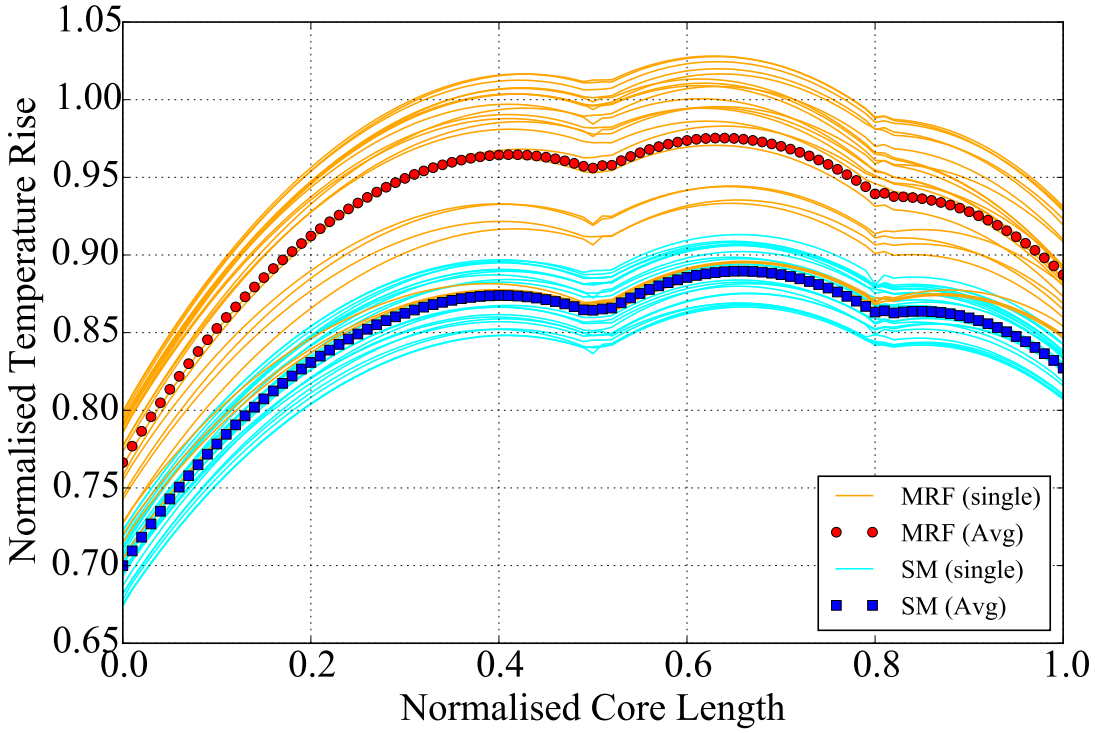


Fig. 7.11 Comparison of stator winding temperature rise variation between slots between the MRF and SM approach; Temperature rise normalised according to equation 5.4

Table 7.1 Comparison of MRF and SM simulations results; All properties normalised

	MRF	**SM**	**Difference**
Mass Flow			
Total	0.737	0.884	+0.147
Stator-Casing Duct In	0.447	0.536	+0.088
Airgap In	0.279	0.335	+0.055
Vent 1	-0.021	-0.019	-0.002
Vent 2	-0.035	-0.027	-0.002
Temperature			
Peak Stator Winding	1.032	0.915	-0.117
Average Stator Winding	0.883	0.798	-0.085
Peak Rotor Winding	0.901	0.790	-0.112
Average Rotor Winding	0.729	0.620	-0.109
Torque	1.116	0.985	-0.131

7.4.2 Stator Results

Figure 7.12 shows a comparison of the experimentally measured stator winding temperature rise in the core at full load and a power factor of 0.8 between the Benchmark Machine and the Vented Prototype.

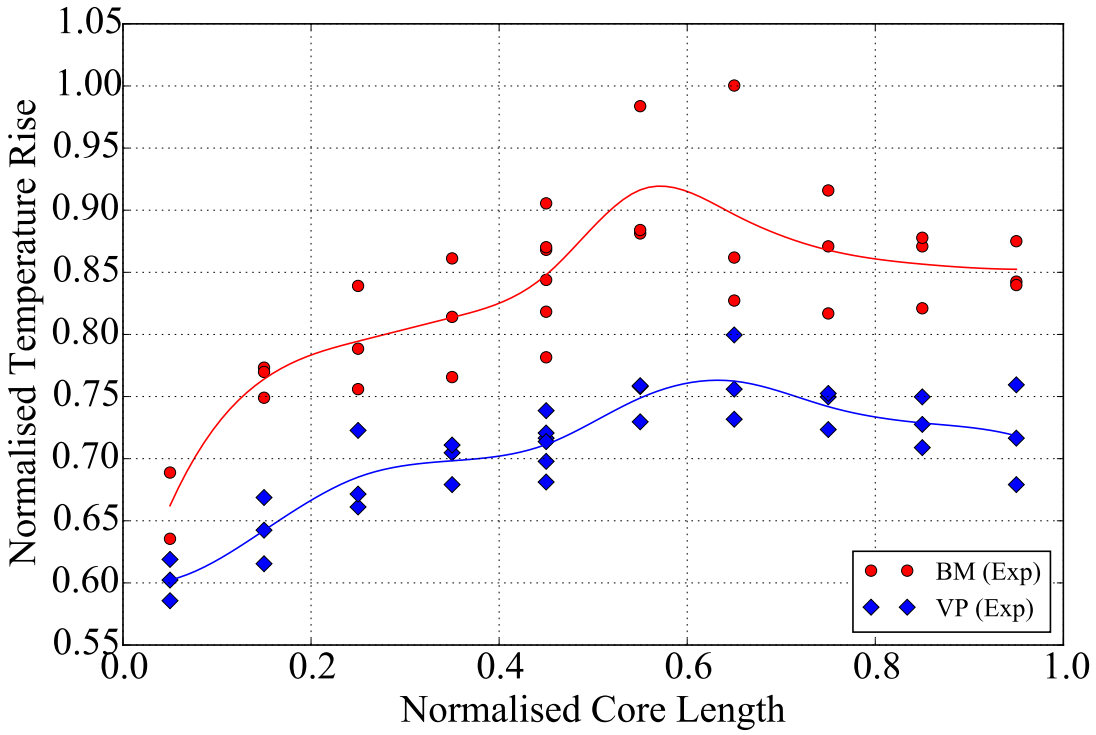


Fig. 7.12 Comparison of experimentally measured stator winding temperature rise in the core at full load and 0.8 power factor between the BM and VP; NDE at the left; Temperature rise normalised according to equation 5.4

The stator winding temperature rise of the Vented Prototype is significantly reduced all along the core length. The single-phase peak temperature rise, located at a core length of 0.65 l_n, is reduced by 20.1 %. The 3-phase peak temperature rise is reduced by 15.4 %. The average temperature rise is reduced by 12.3 %.

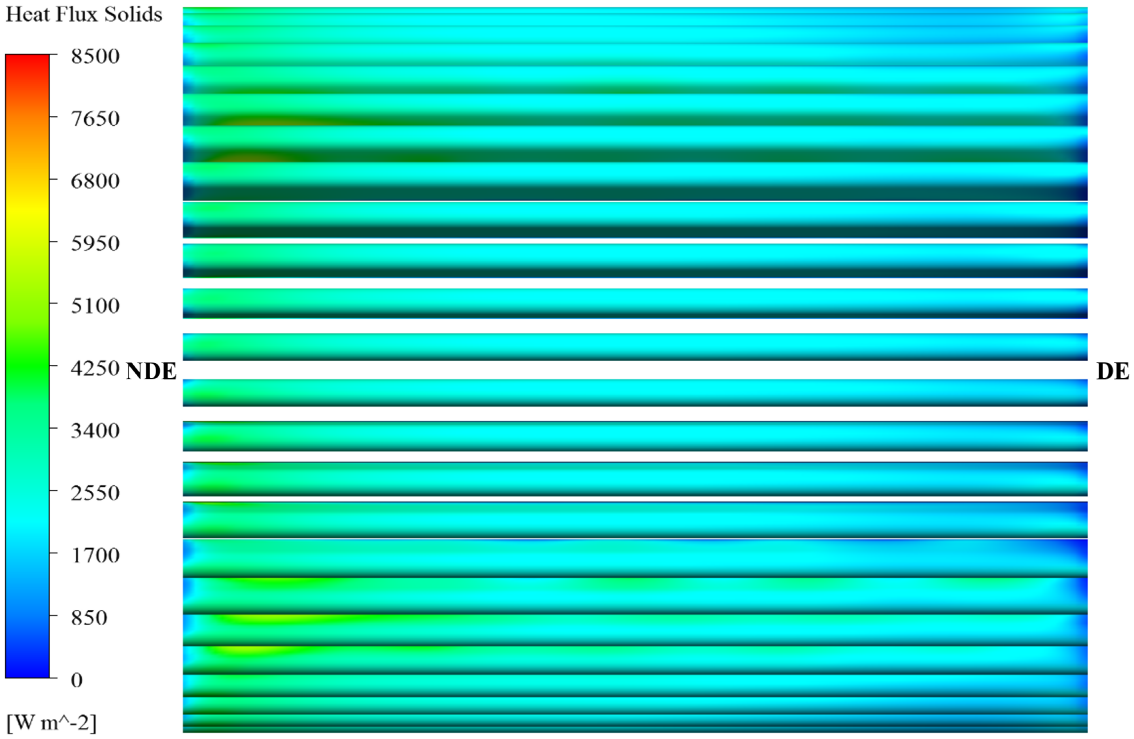
The temperature rise variation between RTDs in the same axial location is reduced for the Vented Prototype. The maximum variation amounts to 6.8 % at 0.65 l_n, which is around 40 % of the 17.3 % variation of the Benchmark Machine. The reasons causing the temperature variations between RTDs in the same axial location have been discussed in detail in section 5.3.1. The reduced temperature variation of the Vented Prototype can potentially be

attributed to a better, more regular insulation of the windings. The vents could improve the resin penetration by adding an additional path for the resin to reach the windings. Gravity pushes the resin radially inwards through the vents into the windings. Besides the reduction in temperature variation between slots in the same location, the improved insulation also reduces the winding temperatures by improving the thermal conductivity of the stator slots. Even a small increase in thermal conductivity is beneficial for the winding temperatures, as proven during the stator winding conductivity sensitivity study on the Benchmark Machine (view section 5.3.1). Future work is required to confirm this theory.

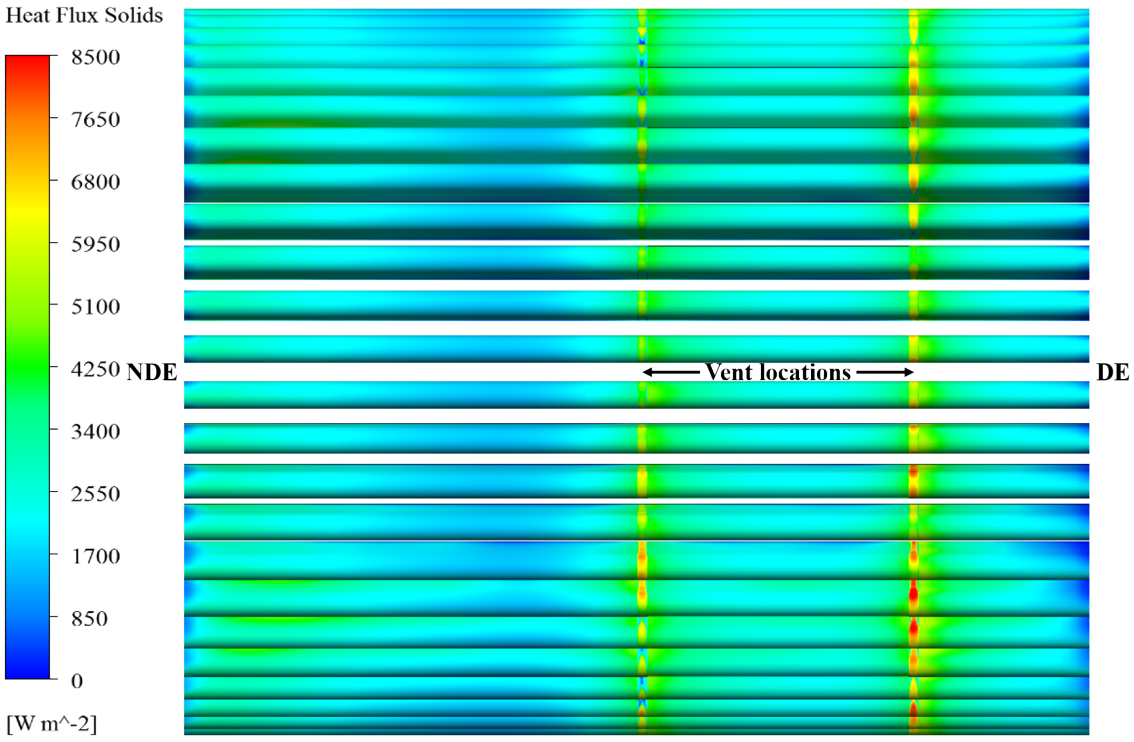
The current imbalance between the three phases, which depends on the grid demand, was of a similar magnitude for the Vented Prototype and Benchmark Machine tests. The Vented Prototype test corresponding to figure 7.14 showed a 4.2 % difference in current between the minimum and maximum phase current, which is slightly below the 6.2 % variation observed for the Benchmark Machine. Equivalent to the BM, no correlation could be found between the variation in phase current and local winding temperature rise. The difference in 3-phase average current between the BM and VP tests is only 0.01 % for the tests displayed in figure 7.12, making the test results closely comparable.

The temperature rise profile of the Vented Prototype is similar to the Benchmark Machine profile, increasing from $0.602\,T_n$ at the NDE to its peak value of $0.800\,T_n$ (single-phase) or $0.762\,T_n$ (3-phase average) at $0.65\,l_n$. From there on the temperature rise decreases to $0.718\,T_n$ at the DE. On top of the reduction in temperature rise compared to the Benchmark Machine, the temperature rise profile of the Vented Prototype is also more even. The VP difference between minimum and maximum temperature rise is 21.4 % (single-phase) or 16.0 % (3-phase), compared to 36.5 % (single-phase) or 25.4 % (3-phase) for the BM. The localised convective cooling through the vents on both sides of the machine hot spot reduces the hot spot temperature rise.

Figure 7.13 shows a comparison of the heat flux from the stator core windings to the stator iron between the Benchmark Machine and the Vented Prototype. It can clearly be seen that adding vents to the stator improves the heat removal from the stator windings. As heat is removed through convective heat transfer in the locations of the vents, the heat flux is substantially improved in comparison to the Benchmark Machine, where the heat is conducted into the stator iron. 13.2 % of the total heat generated in the stator iron and stator windings of the Vented Prototype is removed by convective heat transfer through the vents: 5.6 % through the first vent, and 7.3 % through the second vent. The circumferential



(a) Benchmark Machine



(b) Vented Prototype

Fig. 7.13 Comparison of heat flux from stator core windings to stator iron and vents between Benchmark Machine and Vented Prototype; Radially inwards view

variation in heat flux visible in figure 7.13 is caused by the MRF approach, as the rotor poles are frozen in a specific position (view section 3.4.4).

Figure 7.14 shows a comparison between the CFD and the experimentally measured stator winding temperature rise of the Vented Prototype at full load and a power factor of 0.8. The CFD temperature rise was taken in the geometric centre of the slot and averaged over all slots to make up for the circumferential temperature variation resulting from the MRF rotation modelling approach (view chapters 3.4.4 and 7.4.1).

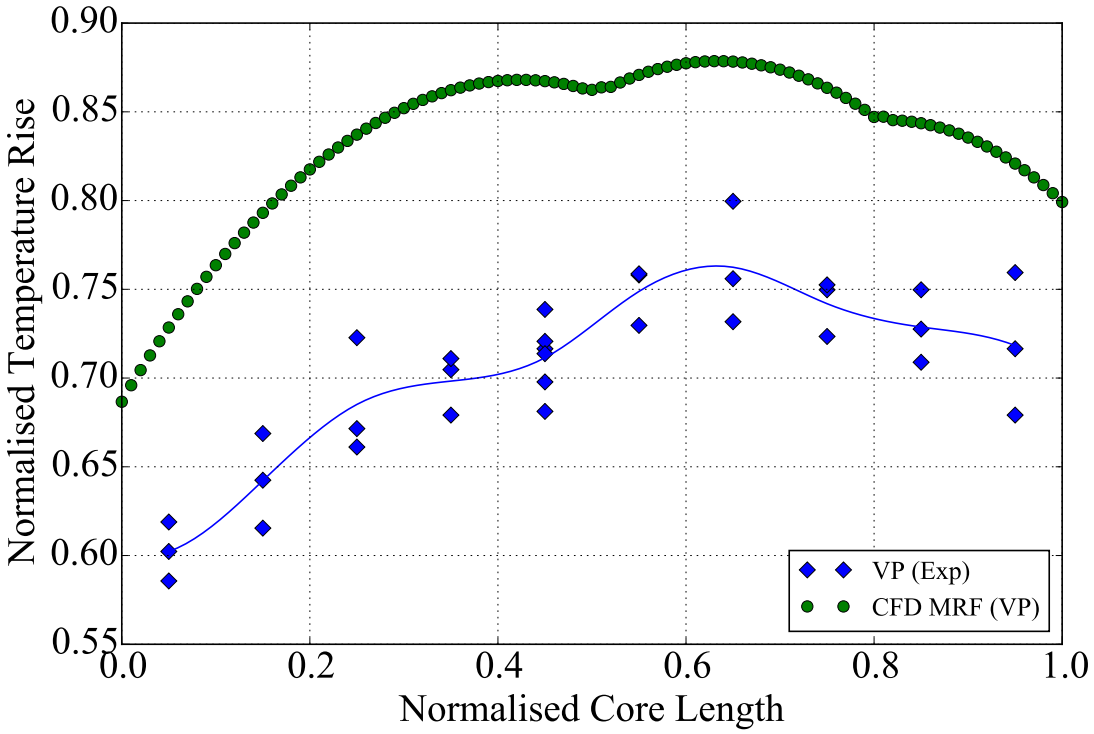


Fig. 7.14 Comparison between Vented Prototype CFD MRF and experimentally measured stator winding temperature rise in the core at full load and 0.8 power factor; NDE at the left; Temperature rise normalised according to equation 5.4

The stator winding temperature rise profile along the axial core length is predicted correctly by the CFD model. The temperature rise increases from 0.687 T_n at the NDE until it reaches its peak value of 0.879 T_n at 0.63 l_n. From there on it declines to 0.799 T_n at the DE. The stator winding temperature rise predicted by the CFD simulation is above the experimentally measured temperature rise, with a maximum difference of 15.1 % at a core length of 0.35 l_n. The average difference is 13.0 % and the difference in peak temperature rise at an axial location of 0.65 l_n amounts to 7.9 %. The reasons causing differences between CFD and

experimental data for the Benchmark Machine (view section 5.3.1), such as the uncertainty related to the exact RTD position within the slots, manufacturing uncertainties and the simplified endwinding geometry, also apply for the Vented Prototype. Additional reasons are discussed below.

The main reason causing the difference between CFD and experimental results is the chosen rotation modelling approach. As discussed in chapters 7.2 and 7.4.1, the MRF approach underpredicts the total flow rate through the machine by 0.147 $\dot{m}_n$ in comparison to the SM approach as the pumping effect occurring between the salient rotor and stator as well as the fan blades and the fan housing cannot be predicted correctly using a steady-state approach. This causes the MRF stator winding temperature rise to be overpredicted by 8.5 % on average, making up 65 % of the difference between CFD and experimental results.

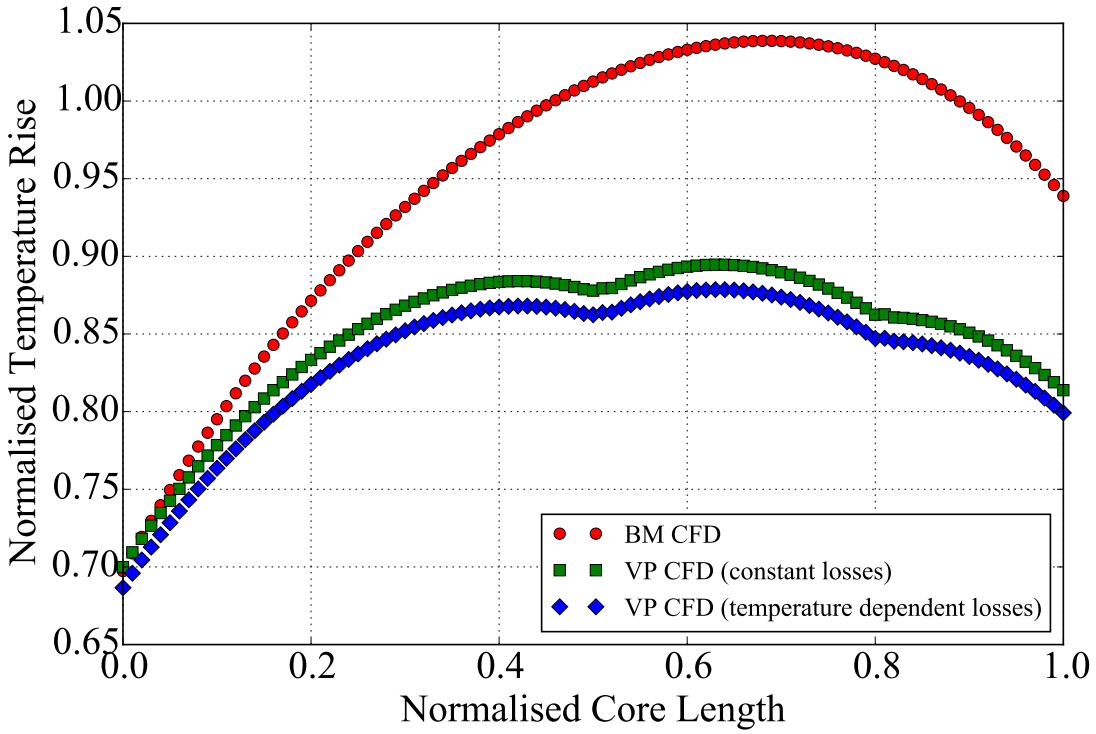


Fig. 7.15 Comparison of CFD MRF stator winding temperature rise in the core at full load and 0.8 PF between BM and VP under consideration of the reduced copper losses; NDE at the left; Temperature rise normalised according to equation 5.4

The stator winding temperature rise reduction observed during the experimental tests is above the reduction predicted by the CFD investigations. One reason for that is that the reduction in stator copper losses, as a result of the reduced stator winding temperatures, was

not considered during the optimisation procedure. The temperature dependent local loss calculation presented in chapter 3.7.3 had not been developed at the time of the optimisation run. To quantify its impact, the VP CFD model was solved again under consideration of the reduced copper losses. Figure 7.15 presents a comparison of the CFD stator winding temperature rise in the core at full load and 0.8 power factor between the Benchmark Machine and Vented Prototype under consideration of the reduced stator winding temperatures.

With the stator copper losses being adjusted for the reduced stator winding temperatures, the peak stator winding temperature rise reduction predicted by CFD is 16.0 %. The average stator winding temperature rise is predicted to decrease by 11.6 %. This is in good agreement with the experimentally measured reductions of 20.1 % peak and 12.3 % average. The remaining difference can potentially be attributed to the improved thermal conductivity of the stator slots as a result of a better resin insulation during the VPI process.

The stator iron axial conductivity sensitivity study discussed in chapter 5.3.1 was carried out for the Vented Prototype as well to determine if the impact of axial stator iron conductivity on winding temperatures is more substantial for a vented machine. Figure 7.16 shows how a variation of the thermal stator iron conductivity in axial direction influences the peak stator winding temperature rise of a machine with no, one and two stator vents. The anisotropy ratio is defined according to equation 5.7. The stator winding temperature difference is defined as the temperature difference in comparison to the isotropic case according to equation 5.8.

The vented machines show the same trend as the non-vented machine. Peak and average stator winding temperatures increase with decreasing axial stator iron conductivity. For anisotropy ratios in the range of 0.3-1.0 the peak stator winding temperature rise increase by the same amount for the non-vented and vented machines. For lower anisotropy ratios, the stator winding temperature rise of the vented machines increases more in comparison to the non-vented machine. The maximum peak stator winding temperature rise increase is 3.4 °C, occurring in the machine with two vents at an anisotropy ratio of 0.025.

Adding vents to the stator amplifies the effect a change in axial stator steel conductivity has on the peak and average stator winding temperatures for low anisotropy ratios. This observation can be explained by the increase in heat taking an axial conduction path through the stator before being removed by air if the stator is vented. For the non-vented case and isotropic steel as stator iron material, 95 % of the stator convective heat transfer happens through the airgap and stator-casing duct (radial conduction path), while only 5 % are removed from the side surfaces (axial conduction path). If two vents are added to the stator, 80 % of the stator convective heat transfer happens through the airgap and stator-casing duct. 15 % are

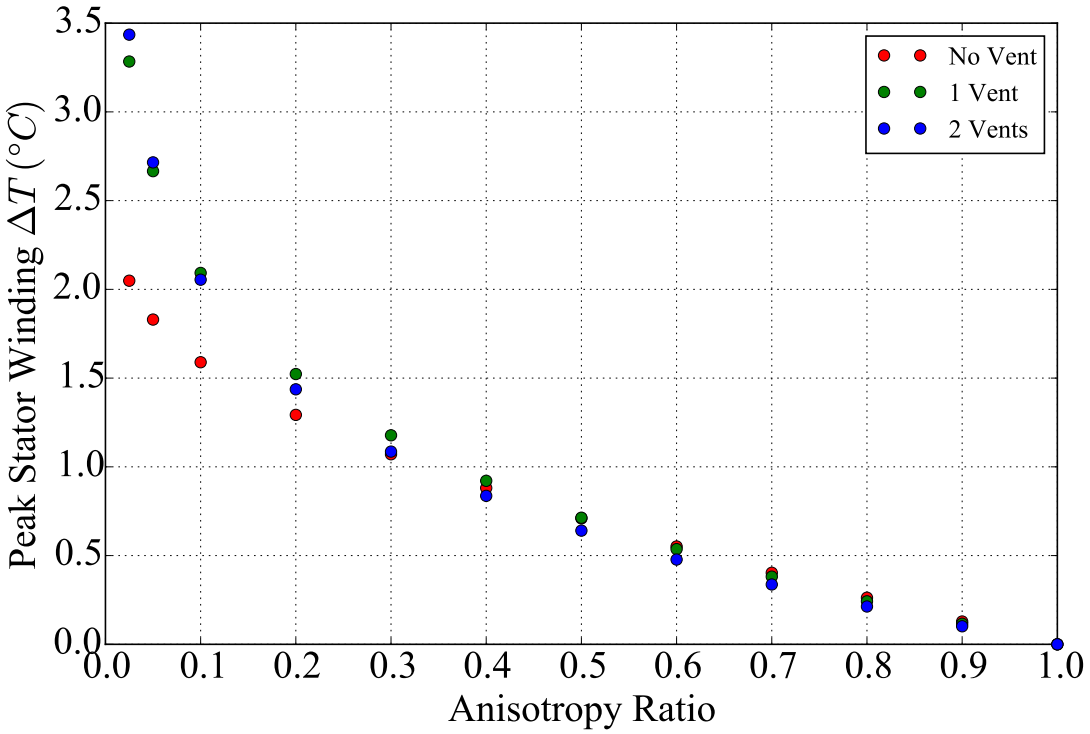
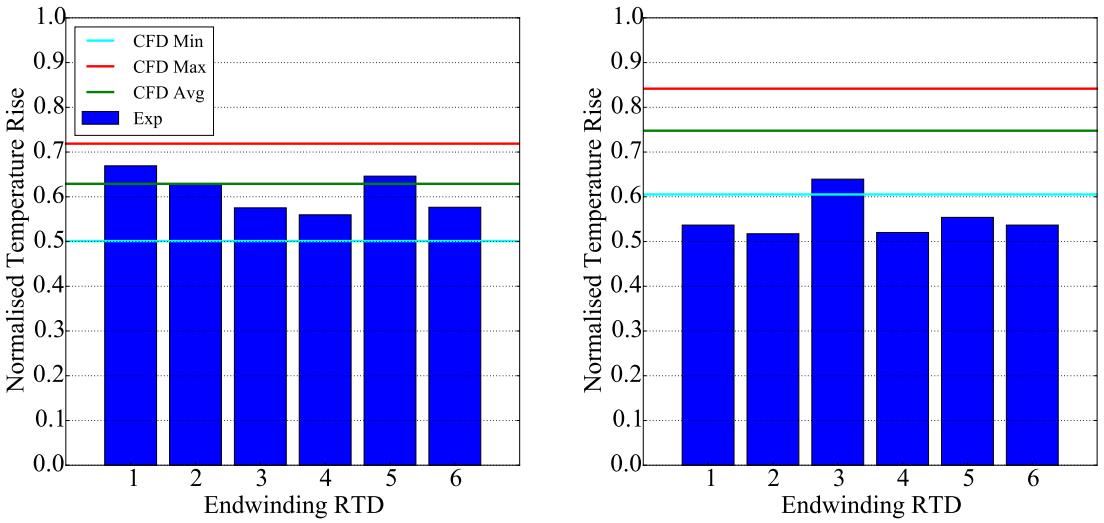


Fig. 7.16 Influence of anisotropic stator iron conductivity in axial direction on peak stator winding temperature rise difference; Comparison between machines with no, one and two stator vents; Temperature rise difference taken in relation to temperature rise of isotropic case according to equation 5.8

dissipated through the vents and 5 % through the inlet and outlet surfaces. Thus the axial conductivity plays a more important role for the stator cooling.

Equivalent to the Benchmark Machine, experimentally validating the stator endwinding temperatures proved to be difficult. 6 RTDs were distributed over the endwindings on each side during manufacturing, but the exact location of the RTDs within the endwindings was unknown and cannot be determined without destroying the machine. The local temperatures within the stator endwindings vary considerably depending on their location. Figure 7.17 shows the experimentally measured temperature rise within the NDE (left) and DE (right) stator endwindings, represented by the blue bars. They are compared to the simulation results, with the minimum CFD temperature rise represented by the light blue lines, the maximum temperature rise by the red lines and the average temperature rise by the green lines.



(a) Non-Drive End

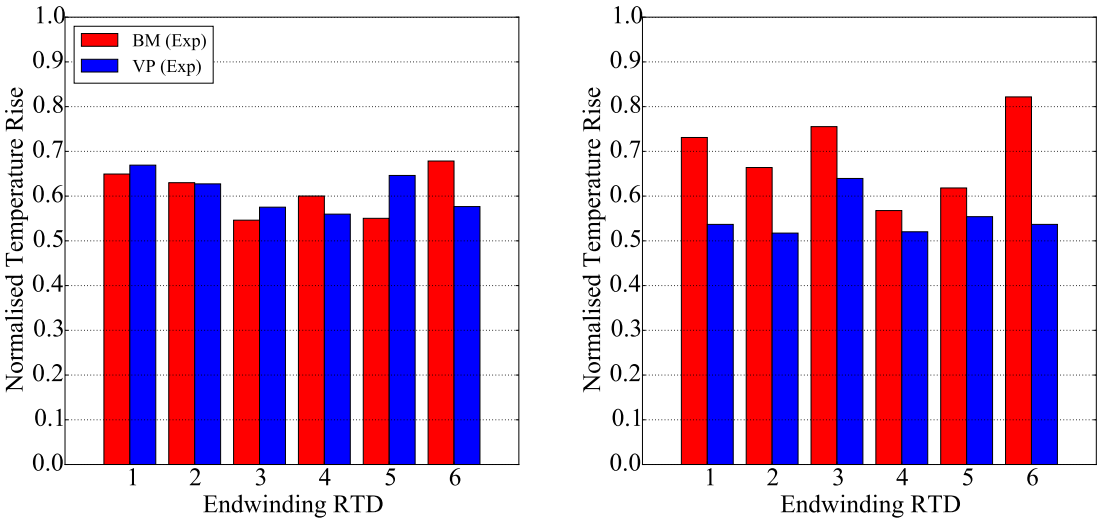
(b) Drive End

Fig. 7.17 Comparison between CFD MRF (lines) and experimentally measured (bars) VP stator winding temperature rise at full load and 0.8 PF; Temperature rise normalised according to equation 5.4

The experimentally measured temperature rises at the NDE range from 0.560 to 0.669 T_n, varying by 0.110 T_n. They show good agreement with the simulation results, staying within the range predicted by the CFD model. The agreement regarding the average temperature rise is good. The average CFD endwinding temperature rise exceeds the experimentally measured value only by 2.0 %.

The experimentally measured temperature rises at the DE range from 0.517 to 0.639 T_n varying by 0.122 T_n. The agreement between CFD and experimental data is worse in comparison to the NDE, with the simulated temperature rise being overpredicted. Only one of the six RTDs measured a temperature rise within the predicted range and the average temperature rise differs by 19.7 %. One reason for the difference between CFD and experimental results is the underpredicted endwinding heat transfer resulting from the simplified endwinding modelling approach discussed previously. Another reason is the higher complexity of the flow field around the DE endwindings. While the NDE is directly cooled by the air entering through the inlets with a known temperature, the DE endwindings are cooled by a mix of air exiting the stator-casing duct as well as the airgap and interpolar space. The flow around the DE endwindings is more restricted due to their proximity to the machine casing and the fan. This explains the worse agreement of CFD and experimental data on the Drive End.

Figure 7.18 shows a comparison of the experimentally measured stator endwinding temperature rise between the Benchmark Machine and Vented Prototype. While the NDE temperature rise is very similar, averaging at 0.609 T_n, the DE temperature rise is significantly reduced. The peak temperature rise decreased by 18.2 %. The average temperature rise was reduced by 14.2 %.



(a) Non-Drive End

(b) Drive End

Fig. 7.18 Comparison between experimentally measured stator winding temperature rise of the Benchmark Machine and Vented Prototype at full load and 0.8 PF; Temperature rise normalised according to equation 5.4

As some of the heat generated in the core windings is removed by convection through the vents, the stator winding core temperatures decrease. This results in less heat being conducted to the DE endwindings, which are on the shortest conduction path to the core stator winding hot spot, reducing their temperature. Furthermore, the stator copper losses decrease because of the temperature reduction, amplifying the effect.

According to the experimental tests, the peak and average DE temperature rise of the Vented Prototype are slightly below the NDE temperature rise. This observation disagrees with the CFD predictions (view figure 7.17) as well as the experimental stator core winding profile (view figure 7.12). Both predict higher temperatures at the DE, which is surrounded by hotter ambient air. The difference is most likely caused by the DE RTDs being placed in relatively colder locations within the endwindings. As mentioned previously, the exact locations of the stator endwinding RTDs is unknown.

Table 7.2 summarises the thermal validation of the VP stator endwindings.

Table 7.2 Comparison of VP CFD MRF & experimentally measured stator endwinding temperature rise; Temperature rise normalised according to equation 5.4

	NDE		DE	
	CFD (T_n)	**Experimental (T_n)**	**CFD (T_n)**	**Experimental (T_n)**
Min	0.501	0.560	0.605	0.517
Max	0.719	0.669	0.842	0.639
Spread	0.218	0.110	0.236	0.122
Average	0.629	0.609	0.748	0.551

7.4.3 Rotor Results

Figure 7.19 shows a comparison of the experimentally measured rotor winding temperature rise at full load and a power factor of 0.8 between the Benchmark Machine and the Vented Prototype. The endwindings are displayed in the regions of -0.2-0 l_n and 1-1.2 l_n.

The rotor winding temperature rise of the Vented Prototype has slightly increased all along the core length. The average temperature rise has increased by 2.4 %. The maximum increase was measured to be 3.2%. Temperature rises in the same axial location vary with a maximum difference of 8.0 % at 0.4 l_n, which is in good agreement with the 7.6 % variation of the Benchmark Machine. This was to be expected, because the same rotor was utilised and the difference in absolute rotor temperatures between the BM and VP is small.

The rotor winding temperature rise increases steadily from the beginning until the end of the core, approximately following a linear trend. The peak temperature rise of the Benchmark Machine was located at an axial location of 1.0 l_n. Unfortunately the RTDs located in this location broke, making it impossible to measure the new peak rotor winding temperature rise experimentally. It was calculated to be 1.036 T_n by adding the average rotor winding temperature rise increase of the VP to the experimentally measured peak rotor winding temperature rise of the BM. Considering the similarity of the temperature profiles, this is a reasonable assumption. The rotor endwindings, shown in the regions of -0.2-0 and 1-1.2 l_n in figure 7.19, are cooler than the core windings, with the outer winding layer being cooler than the inner one (view figure 4.11 for the location of the EW RTDs). Equivalent to the stator, the rotor endwindings are hotter at the Drive End as the cooling air heats up while it flows through the generator core and stator-casing duct.

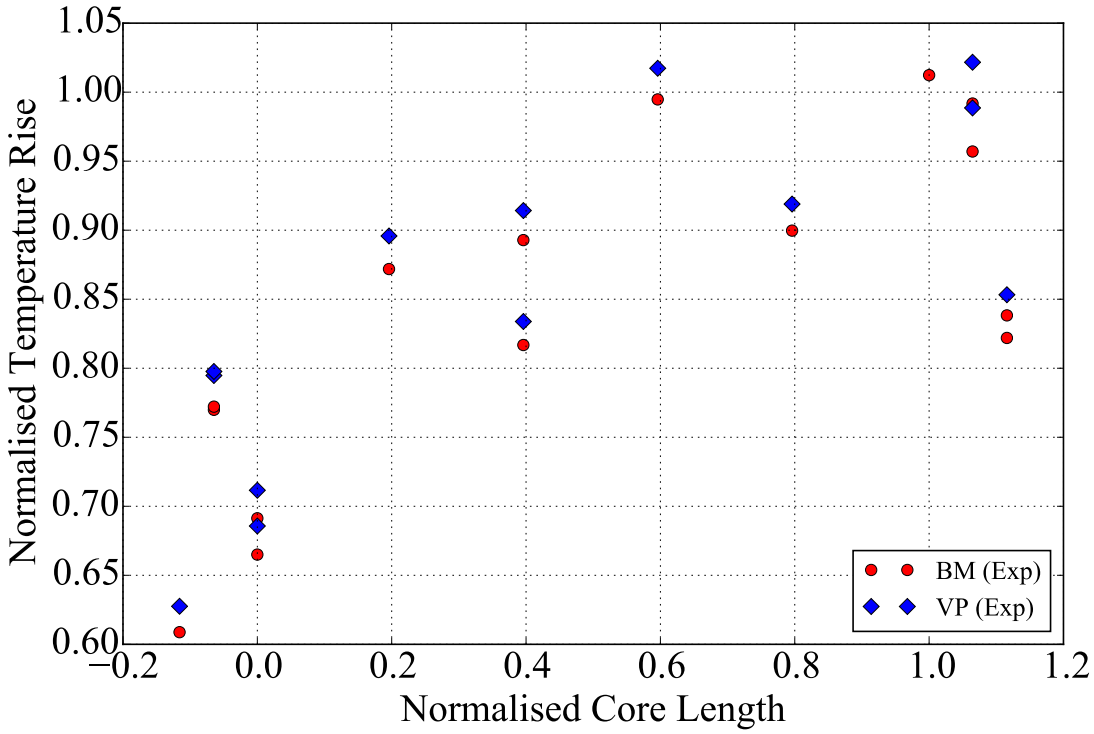


Fig. 7.19 Comparison of experimentally measured rotor winding temperature rise in the core at full load and 0.8 power factor between BM and VP; NDE at the left; Endwindings included; Temperature rise normalised according to equation 5.4

Figure 7.20 shows a comparison between the CFD and experimentally measured rotor winding temperature rise at full load and a power factor of 0.8. The CFD temperature rise was taken in the geometric centre of the winding and averaged over all windings.

CFD and experimental data show good agreement, with the CFD temperature rise being between the values measured at the two poles equipped with RTDs for the majority of the core length. The main difference between simulation and experimental results is that the CFD model predicts the rotor winding temperature rise to peak at $0.70\,l_n$, while the peak experimental temperature rise is located at $1.0\,l_n$.

Equivalent to the Benchmark Machine (view section 5.3.2), the temperature rise within the rotor windings varies considerably with the radial and circumferential position. The difference between the peak temperature rise, close to the winding centre, and the minimum temperature rise, on the inside of the interpolar space, amounts to 38 %. This means that even small misplacements of the RTDs during the insertion process can result in large discrepancies

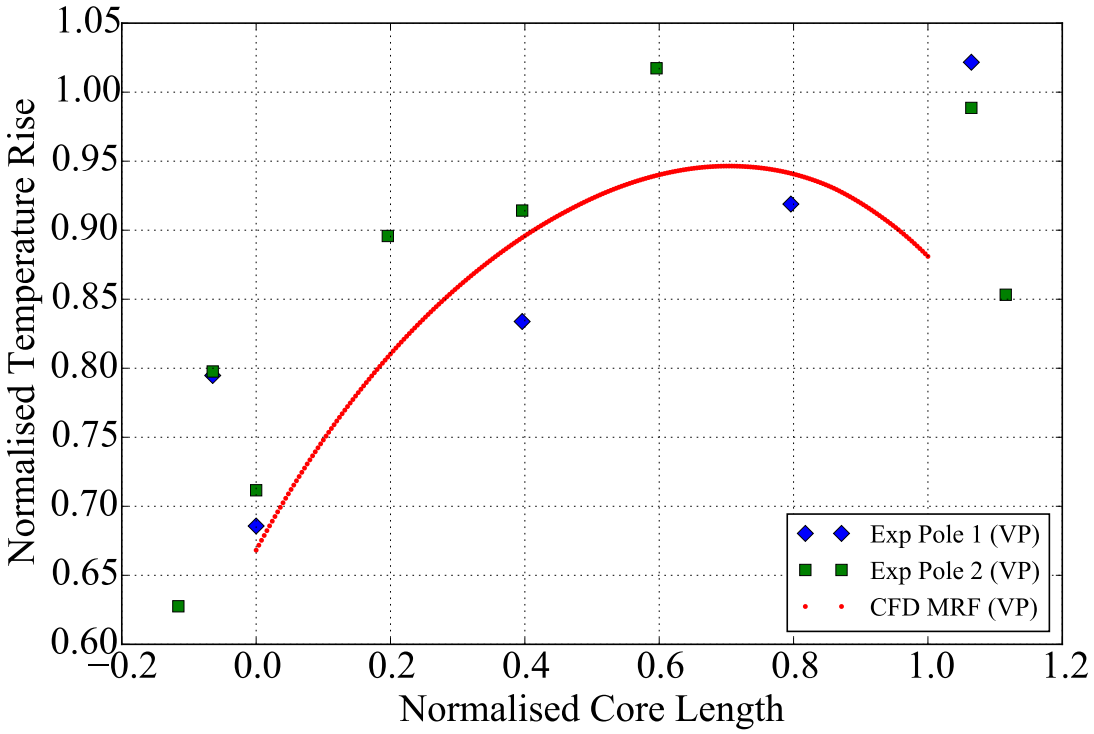


Fig. 7.20 Comparison between VP CFD MRF and experimentally measured rotor winding temperature rise at full load and 0.8 power factor; NDE at the left; Temperature rise normalised according to equation 5.4

between simulation and experimental results. There is also a difference in temperature rise between the leading and the trailing winding. The peak temperature rise of the trailing winding is 3.1 % above the leading winding according to the CFD results. As the RTDs are all located in the trailing windings, but the CFD temperature rise have been averaged over all windings, the CFD temperature rise is expected to be slightly underpredicted.

7.5 Conclusions

This chapter presented the experimental validation of the Vented Prototype CFD model. The model shows good agreement with the experimental results regarding the measured air flow and thermal properties. Reasons for differences between computational and experimental results were discussed. The utilised steady-state rotation modelling approach was identified

as the main reason for differences between CFD and experimental results. Its impact on the airflow and thermal results was discussed in detail.

Additionally, the experimental results of the Benchmark Machine and Vented Prototype were compared, highlighting the improved stator cooling of the new machine design. One of the main parameters influencing the machine lifetime is the ageing of the winding insulation material [89]. The rate of ageing of the insulation material is directly related to the electro-thermal and thermo-mechanical stresses experienced by the windings, which increase with increasing temperature. As a rule of thumb, a 10° C decrease in peak temperature will double the machine lifetime [6]. Hence the lifetime of the stator winding insulation material is expected to more than quadruple as a result of the 20.1 % reduction in peak stator winding temperature rise.

As a result of the 12.3 % reduction in average stator winding temperature, the stator copper loss of the Vented Prototype is reduced in comparison to the Benchmark Machine. The stator copper loss of an electrical machine decreases linearly with the stator winding resistance according to equation 2.1, and the stator winding resistance decreases linearly with the average stator winding temperature according to equation 2.2. The reduction in stator winding losses can be calculated from the stator winding current I_{stat}, the stator winding resistance R_{stat}, the winding temperature coefficient α and the average stator winding temperatures of the Benchmark Machine $T_{avg,stat,BM}$ and Vented Prototype $T_{avg,stat,VP}$ according to the following equation:

$$\Delta P_{Copper} = I_{stat}^2 R_{stat} \alpha (T_{avg,stat,BM} - T_{avg,stat,VP}) \tag{7.1}$$

The stator copper loss of the Vented Prototype is reduced by 6.6 % in comparison to the Benchmark Machine according to equation 7.1. Experimental measurements confirmed that the total machine efficiency of the Vented Prototype at thermal steady-state, full load and 0.8 PF is increased by 0.5 % in comparison to the Benchmark Machine.

Chapter 8

Conclusions and Outlook

Worldwide electricity generation is dominated by electrical generators, the majority of which are driven by prime movers powered by fuel combustion. Electrical motors are the main consumer of electricity in industry. Thus, improving electrical machine efficiency can significantly reduce the ecological impact of electricity generation and consumption. The copper losses occurring in the rotor and stator windings increase with temperature and are the main loss contributor in many electrical machine types. Hence, cooling improvements have the potential to improve machine efficiency.

The appropriate cooling of electrical machines is also essential to ensure safe and reliable operation. The rate of ageing of the winding insulation is directly related to its temperature, making the machine lifetime dependent on the winding temperatures. As the copper losses increase with increasing current, the power density of electrical machines is usually limited by thermal considerations.

Designing an electrical machine is highly complex as multiple physical phenomena need to be considered. Due to the interdependency of electromagnetic (EM), thermal and mechanical performance, a holistic design approach is required to ensure an optimal machine design. Within this project, the growing demand for holistic design approaches of electrical machines was addressed. This chapter summarises the work conducted during the project. The novel methodologies developed and the insight gained into the performance of the investigated machine through computational modelling and experimental testing is discussed. Recommendations for future work building on this thesis are given.

8.1 Project Summary and Conclusions

This section summarises the work conducted within this thesis and the drawn conclusions.

The stator cooling of an air-cooled synchronous generator with a power rating of several hundred kVA used for continuous industrial power generation was improved. The following steps were taken to achieve this:

1. A 180° Conjugate Heat Transfer CFD model of the investigated generator was created to identify the machine hotspots and analyse the airflow and thermal performance in detail (view chapters 3 and 5). Two different rotation modelling approaches were utilised and compared: The steady-state Multiple Reference Frame (MRF) and the transient Sliding Mesh (SM) approach (view sections 3.4.4, 7.4.1 and chapters 5 and 7).
2. The model was validated experimentally by torque, mass flow rate, rotor and stator winding temperature measurements (view chapters 4 and 5). Good agreement between CFD and experimental data was found as shown in table 8.1.

Table 8.1 Agreement between Benchmark Machine CFD and experimental results

Difference	MRF	SM
Mass Flow Rate	13.7 %	0.003 %
Torque	16.8 %	0.3 %
Peak Stator Winding Temperature Rise	4.0 %	-
Average Stator Winding Temperature Rise	12.0 %	-
Peak Rotor Winding Temperature Rise	8.5 %	-
Average Rotor Winding Temperature Rise	3.6 %	-

3. A parametric CFD model including multiple radial stator vents was created based on the validated benchmark model (view chapter 6). By creating a parametric model, and relating mesh and solver parameters to the geometric parameters to be varied, the newly developed model enabled the automated optimisation of multiple design parameters without requiring any additional user input after the initial setup. This model was utilised to investigate the impact venting the stator has on the generator airflow and thermal performance. The change in loss distribution resulting from venting the stator was considered through analytical correlations developed from an experimentally validated 2-D EM FE model (view section 6.2).
4. Initial investigations showed that the targeted reduction in stator winding temperatures could not be achieved with a single vent. Therefore it was decided to add two vents to the stator. Locating a baffle in the stator-casing duct was shown to have the potential to

reduce peak and average stator winding temperatures by influencing the mass flow and pressure distribution inside the machine. The following five design parameters were optimised with the aim of minimising the peak stator winding temperature:

- Vent locations (2 parameters, 1 for each vent)
- Vent widths (2 parameters, 1 for each vent)
- Radial baffle length (1 parameter)

The optimised machine design was predicted to have considerably reduced peak and average stator winding temperatures in comparison to the original machine design (view chapter 6).

5. A vented stator-casing arrangement was built according to the outcome of the design optimisation and tested experimentally. In comparison to the original machine design, the peak stator winding temperature rise was reduced by 20.1 %, while the average stator winding temperature rise decreased by 12.3 % (view chapter 7). As venting the stator removes active core material, the rotor current was increased to keep the generator power rating constant. This caused the peak rotor winding temperature rise to increase by 3.2 %, while the average rotor winding temperature rise increased by 2.4 %. Good agreement between CFD and experimental data was found, as shown in table 8.2, validating the design methodology.

Table 8.2 Agreement between Vented Prototype CFD and experimental results

Difference	MRF	SM
Mass Flow Rate	12.3 %	2.3 %
Torque	6.3 %	6.7 %
Peak Stator Winding Temperature Rise	7.9 %	-
Average Stator Winding Temperature Rise	13.0 %	-
Peak Rotor Winding Temperature Rise	9.0 %	-
Average Rotor Winding Temperature Rise	2.3 %	-

8.2 Novelty in this thesis

This section summarises the original contribution this thesis has made.

8.2.1 Parametric CFD Design Optimisation

The main contribution of this thesis is the development of a novel methodology for the automatic optimisation of multiple design parameters based on a 3-D Conjugate Heat Transfer

CFD model. In the past, the high complexity of the geometry, mesh and solver setup for the CFD modelling of complete electrical machines required the model setup to be updated manually when the machine design was changed. By creating a parametric model and relating mesh and solver parameters to the geometric parameters to be varied, the newly developed methodology enables the automated optimisation of multiple design parameters without requiring any additional user input after the initial model setup.

As CFD does not rely on correlations to predict air flow and heat transfer, this methodology can be implemented in the early electrical machine design stage allowing right-first-time design. The performance of complex and novel geometries, for which no correlations exist, can be investigated without having to build multiple prototypes.

The impact the design changes have on the electromagnetic performance was taken into account through analytical correlations developed from electromagnetic 2-D FEA. The FE models were not developed by the author of this thesis. By implementing these correlations into the thermal optimisation procedure, an optimal design considering the thermal as well as the electromagnetic performance can be achieved.

8.2.2 CFD Methodology Developments

To enable the development of a model capable of accurately predicting the thermal performance of the investigated synchronous generator, the following novel methodologies for CFD modelling of electrical machines were developed within this project.

Change of anisotropic conductivity orientation for endwindings
Since windings are a mixture of copper wires and various insulation materials, their thermal conductivity in wire direction is considerably higher than normal to the wire direction (view section 3.4.6). The thermal conductivity anisotropy can be implemented relatively simply in the machine core, where the windings are straight and aligned with an axis of the global coordinate system. But accurately modelling the anisotropy in the endwindings, where the wire orientation changes, is challenging.

To enable an accurate representation of the change in wire orientation in the stator endwindings, User Defined Functions (UDF) were developed and implemented into ANSYS Fluent. The thermal conductivity in the axial, radial and circumferential directions were gradually changed dependent on the axial cell coordinate. Additional UDFs were created for the rotor

endwindings, changing the thermal conductivity in X-/Y- and Z-direction depending on the cell X-/Y- and Z-coordinate (view section 3.7.2).

Gradually changing the thermal conductivity based on the actual endwinding geometry increases the model accuracy and robustness. Furthermore, the effort required for the geometry creation and separation is reduced. The developed methodology can be applied to any endwinding geometry.

Temperature dependent heat losses
Traditionally, heat losses are implemented into Conjugate Heat Transfer CFD models by defining a constant volumetric heat generation in the solid parts (view section 3.4.5). But this approach does not take the temperature dependency of the copper losses into account. Additionally, the volumetric heat generation approach assumes a constant heat generation all over the windings. In reality, the local losses vary depending on the local temperatures, which can vary considerably within the windings. Another disadvantage of this approach during the machine design stage is that the average winding temperatures are not known. They have to be estimated initially and subsequently adjusted based on the results of the CFD simulations, resulting in a time consuming iterative process.

To accurately model the heat generation within the investigated generator, UDFs were developed to calculate the heat generated in every cell dependent on the local cell temperature (view section 3.7.3). It is only required to know the winding current and resistance at one temperature to calculate localised, temperature dependent losses. This approach enables a more accurate implementation of the heat generated within the windings, resulting in a more accurate prediction of the local winding temperatures. Additionally, it is not required to iteratively adjust the copper losses during the machine design stage any more, reducing manual user input and computation time. The developed methodology can be applied to any electrical machine topology.

8.2.3 CFD Investigations

The following CFD investigations were conducted to quantify the impact of various modelling and experimental settings on the computational and experimental results. The novelty lies in quantifying their impact using a validated Conjugate Heat Transfer model of a complete synchronous generator.

Thermal conductivity sensitivity studies

A sensitivity study quantifying the impact the magnitude of the stator winding thermal conductivity normal to the wire direction has on the stator winding temperature rise was carried out using an experimentally validated CHT CFD model of a complete non-vented synchronous generator (view section 5.3.1). The impact of the winding thermal conductivity on the thermal performance of the investigated generator was found to be substantial. A decrease in thermal conductivity from $3\,\mathrm{W\,m^{-1}\,K^{-1}}$ to $0.2\,\mathrm{W\,m^{-1}\,K^{-1}}$ increases the peak stator winding temperature rise by 24.4 %.

Using the same model, a sensitivity study was conducted to quantify the impact of the magnitude of the axial stator iron thermal conductivity on the rotor and stator winding temperature rises (view section 5.3.1). The same study was conducted for a vented synchronous generator based on a validated CHT CFD model and the results were compared (view section 7.4.2). The impact of the axial stator iron conductivity on the thermal performance of the investigated generators was found to be marginally more noticeable for the vented machine, but can be considered negligible in both cases.

Comparison of steady-state and transient modelling approaches

Rotation in electrical machines is traditionally modelled using the steady-state Multiple Reference Frame approach, due to the high computational cost of the fully transient Sliding Mesh approach (view section 3.4.4). The two approaches were compared and their impact on air flow and thermal performance was analysed in detail (view section 7.4.1 and chapters 5 and 7). The SM approach was found to be superior regarding the prediction of air flow and thermal performance. The pumping effect occurring between the salient rotor and stator, as well as the fan blades and the fan housing, cannot be predicted correctly using the steady-state MRF approach.

Design of a non-intrusive mass flow measurement system

A non-intrusive mass flow measurement system was designed using an experimentally validated airflow only CFD model (view section 4.2.1). The system consists of a box, or plenum, covering the machine inlets which is connected to a calibrated conical inlet duct. The influence of the plenum dimensions and duct diameter on the total mass flow rate through the machine, the inflow conditions and the measurement uncertainty was analysed in detail. The duct diameter was identified as the most important dimension impacting the mass flow rate and measurement uncertainty. For the as optimal identified configuration, the flow rate is

predicted to decrease by 2.2 % relative to unrestricted operation. The achieved measurement uncertainty is ±2.6 % at synchronous speed.

8.2.4 Experimental Investigations

Rotor and stator winding measurements were conducted on an industrial synchronous generator with a power rating of several hundred kVA (view section 5.3). The same measurements were conducted on the newly designed prototype, which has the same power rating (view section 7.4). The thermal measurements were taken at various loads, including full load, while the machine was connected to the grid, which has not been achieved on a machine that size before. The machine was run for several hours for each load until the measured temperature rises were steady. This methodology enabled an accurate prediction of the generator's thermal performance under normal operating conditions and the impact the design changes had on the generator performance. The thermal performance has been analysed in detail.

8.3 Future Work

The following points were identified as potential future work building on this thesis:

- Due to the improvements in stator cooling achieved within this project, the hot spot of the investigated generator is now located in the rotor windings. To increase the machine's power rating, future work should focus on improving the rotor cooling.
- The developed optimisation methodology can be applied to investigate additional design changes improving the performance of the investigated generator. Especially design changes which do not influence the electromagnetic performance, such as the fan design, can be investigated with relatively little effort by editing the existing CFD models.
- The developed methodology can be applied to optimise the performance of different machine types and support machine designers in the early machine design stages.
- Advances in computing power have made High Performance Computing (HPC) clusters feasible for companies and universities to use on a regular basis. HPC clusters could be used to optimise more design parameters simultaneously considering multiple objectives or conduct optimisations using the more accurate Sliding Mesh approach.
- Due to the interdependence of electromagnetic and thermal performance, directly coupling the electromagnetic FE model with a CFD model would be beneficial to increase

the modelling accuracy and enable the optimisation of multiple design parameters for which simple analytical correlations cannot be developed.

- The thermal stator winding conductivity normal to the winding orientation was found to have a significant impact on the stator winding temperatures. Future work should focus on accurately determining the thermal conductivity, for example by conducting thermal conductivity measurements on simplified samples. Furthermore, the winding manufacture and impregnation process should be analysed to identify potential for improving the thermal conductivity, as this is highly beneficial for the thermal performance.

References

[1] Eurostat. Electricity production, consumption and market overview. https://ec.europa.eu/eurostat/statistics-explained/index.php/Electricity_production,_consumption_and_market_overview Accessed 05/2019.

[2] Hans De Keulenaer, Ronnie Belmans, Edgar Blaustein, David Chapman, and Anibal De Almeida. Energy Efficient Motor Driven Systems. *Energy and Environment*, 15(5):873–905, 2004.

[3] Official Journal of the European Union. Directive (EU) 2018/2001 of the European Parliament and of the Council of 11 December 2018 on the promotion of the use of energy from renewable sources (Text with EEA relevance.). http://data.europa.eu/eli/dir/2018/2001/oj Accessed 05/19, 2018.

[4] House of Commons - Business Energy and Industrial Strategy Committee. Electric vehicles: driving the transition - Fourteenth Report of Session 2017-19. 2018.

[5] A Boglietti, A Cavagnino, D Staton, M Shanel, M Mueller, and C Mejuto. Evolution and Modern Approaches for Thermal Analysis of Electrical Machines. *IEEE Transactions on Industrial Electronics*, 56(3):871–882, 2009.

[6] J Pyrhönen, T Jokinen, and J Hrabovcová. *Design of Rotating Electrical Machines*. Wiley, 2008.

[7] National Electrical Manufacturers Association. NEMA MG 1-2016: Motors and Generators. 2016.

[8] Yangsoo Lee, Song Yop Hahn, and S. Ken Kauh. Thermal analysis of induction motor with forced cooling channels. *IEEE Transactions on Magnetics*, 36(4):1398–1402, 2000.

[9] C Mejuto, M Mueller, M Shanel, A Mebarki, M Reekie, and D Staton. Improved Synchronous Machine Thermal Modelling. In *18th International Conference on Electrical Machines*, Vilamoura, Portugal, 2008. IEEE.

[10] Ramia Deeb. *Thermal Calculation of Permanent Magnet Motors in High Current Technology*. PhD thesis, Brno University of Technology, 2013.

[11] M Shanel. *Investigation of Rotor Cooling in Salient Pole Electrical Machines*. PhD thesis, University of Nottingham, 2002.

[12] C Micallef. *End winding cooling in Electric Machines*. PhD thesis, University of Nottingham, 2006.

[13] P H Connor. *Computational Fluid Dynamics Modelling of a Synchronous Electric Generator*. PhD thesis, University of Nottingham, 2014.

[14] L Slupik, J Smolka, and L Wrobel. Experimentally validated numerical model of coupled flow, thermal and electromagnetic problem in small power electric motor. *Computer Assisted Methods in Engineering and Science*, 20(2):133–144, 2013.

[15] J.H. Dellinger. The Temperature Coefficient of Resistance of Copper. *Bulletin of the Bureau of Standards*, 7(1):71–101, 1910.

[16] C P Steinmetz. On the Law of Hysteresis. *Transactions of the American Institute of Electrical Engineers*, 9(1):1–64, 1892.

[17] C P Steinmetz. On the Law of Hysteresis (Part II.) and Other Phenomena of the Magnetic Circuit. *Transactions of the American Institute of Electrical Engineers*, 9(1):619–758, 1892.

[18] British Standards Institution. BS EN 60034-2-1:2014 Rotating electrical machines. Standard methods for determining losses and efficiency from test (excluding machines for traction vehicles). 2014.

[19] P.H. Mellor, D. Roberts, and D.R. Turner. Lumped parameter thermal model for electrical machines of TEFC design. *IEE Proceedings B - Electric Power Applications*, 138(5):205–218, 1991.

[20] Nicolas Bracikowski, Michel Hecquet, Pascal Brochet, and Sergey V. Shirinskii. Multiphysics modeling of a permanent magnet synchronous machine by using lumped models. *IEEE Transactions on Industrial Electronics*, 59(6):2426–2437, 2012.

[21] D G Dorrel, D A Staton, J Kahout, D Hawkins, and M I McGilp. Linked Electromagnetic and Thermal Modelling of a Permanent Magnet Motor. In *3rd International Conference on Power Electronics, Machines and Drives (PEMD 2006)*, pages 536–540, Dublin, Ireland, 2006. IET.

[22] David A. Staton and Andrea Cavagnino. Convection heat transfer and flow calculations suitable for electric machines thermal models. *IEEE Transactions on Industrial Electronics*, 55(10):3509–3516, 2008.

[23] Z Xu, A La Rocca, S J Pickering, C Eastwick, C Gerada, and S Bozhko. Mechanical and Thermal Design of an Aeroengine Starter / Generator. In *2015 IEEE International Electric Machines & Drives Conference (IEMDC)*, pages 1607–1613, Coeur d'Alene, USA, 2015. IEEE.

[24] David Gerada, Abdeslam Mebarki, and Chris Gerada. Optimal design of a high speed concentrated wound PMSM. In *Proceedings - The 12th International Conference on Electrical Machines and Systems (ICEMS 2009)*, Tokyo, Japan, 2009. IEEE.

[25] G M Gilson, T Traminosoa, S J Pickering, C Gerada, and D B Hann. A Combined Electromagnetic and Thermal Optimisation of an Aerospace Electric Motor. In *XIX International Conference on Electrical Machines (ICEM 2010)*, Rome, Italy, 2010. IEEE.

[26] Aldo Boglietti, Andrea Cavagnino, and David Staton. Determination of Critical Parameters in Electrical Machine Thermal Models. *IEEE Transactions on Industry Applications*, 44(4):1150–1159, 2008.

[27] Motor Design Ltd. Motor-CAD Software. https://www.motor-design.com/motor-cad-software. Accessed 12/2018.

[28] Yujiao Zhang, Jiangjun Ruan, Tao Huang, Xiaoping Yang, Houquan Zhu, and Gao Yang. Calculation of temperature rise in air-cooled induction motors through 3-d coupled electromagnetic fluid-dynamical and thermal finite-element analysis. *IEEE Transactions on Magnetics*, 48(2):1047–1050, 2012.

[29] H K Versteeg and W Malalasekera. *An Introduction to Computational Fluid Dynamics - The Finite Volume Method*. Pearson Education Limited, 2007.

[30] S J Pickering, D Lampard, J Mugglestone, and M Shanel. Using CFD in the Design of Electric Motors and Generators. *Computational Fluid Dynamics in Practice*, 2001.

[31] B D J Maynes, R J Kee, C E Tindall, and R G Kenny. Simulation of airflow and heat transfer in small alternators using CFD. *IEE Proceedings: Electric Power Applications*, 150(2):146–152, 2003.

[32] J. Mugglestone, D. Lampard, and S. J. Pickering. Effects of end winding porosity upon the flow field and ventilation losses in the end region of TEFC induction machines. *IEE Proceedings: Electric Power Applications*, 145(5):423–428, 1998.

[33] S. Pickering, F. Thovex, P. Wheeler, and K. Bradley. Thermal Design of an Integrated Motor Drive. In *IECON 2006 - 32nd Annual Conference on IEEE Industrial Electronics*, pages 4794–4799, Paris, France, 2006. IEEE.

[34] David A Howey, Andrew S Holmes, and Keith R Pullen. Measurement and CFD prediction of Heat Transfer in Air-Cooled Disc-Type Electrical Machines. *IEEE Transactions on Industry Applications*, 47(4):1716–1723, 2011.

[35] Antonino La Rocca. *Thermal Analysis of a High Speed Electrical Machine*. PhD thesis, University of Nottingham, 2015.

[36] S Mezani, N Takorabet, and B Laporte. A combined electromagnetic and thermal analysis of induction motors. *IEEE Transactions on Magnetics*, 41(5):1572–1575, 2005.

[37] Stefano Nuzzo, Michele Degano, Michael Galea, Chris Gerada, David Gerada, and Neil Brown. Improved Damper Cage Design for Salient-Pole Synchronous Generators. *IEEE Transactions on Industrial Electronics*, 64(3):1958–1970, 2017.

[38] Jin Hwan Lee, Jun Young Song, Dae Woo Kim, Jong Wook Kim, Yong Jae Kim, and Sang Yong Jung. Particle swarm optimization algorithm with intelligent particle number control for optimal design of electric machines. *IEEE Transactions on Industrial Electronics*, 65(2):1791–1798, 2017.

[39] M. Degano, M. Di Nardo, D. Galea, M.Gerada, and C. Gerada. Global design optimization strategy of a synchronous reluctance machine for light electric vehicles. In *8th IET International Conference on Power Electronics, Machines and Drives (PEMD 2016)*, Glasgow, UK, 2016. IET.

[40] Gerd Bramersdorfer, Juan A. Tapia, Juha Pyrhönen, and Andrea Cavagnino. Modern Electrical Machine Design Optimization: Techniques, Trends, and Best Practices. *IEEE Transactions on Industrial Electronics*, 65(10):7672–7684, 2018.

[41] Andrea Cavagnino, Gerd Bramerdorfer, and Juan A. Tapia. Optimization of electric machine Designs - Part I. *IEEE Transactions on Industrial Electronics*, 64(12):9716 – 9720, 2017.

[42] Andrea Cavagnino, Gerd Bramerdorfer, and Juan A. Tapia. Optimization of electric machine Designs - Part II. *IEEE Transactions on Industrial Electronics*, 65(2):1700–1703, 2017.

[43] Xavier Jannot, Jean Claude Vannier, Claude Marchand, Mohamed Gabsi, Jacques Saint-Michel, and Daniel Sadarnac. Multiphysic modeling of a high-speed interior permanent-magnet synchronous machine for a multiobjective optimal design. *IEEE Transactions on Energy Conversion*, 26(2):457–467, 2011.

[44] Stefan Ulbrich, Jeanette Kopte, and Jens Proske. Cooling fin optimization on a TEFC electrical machine housing using a 2D conjugate heat transfer model. *IEEE Transactions on Industrial Electronics*, 65(2):1711–1718, 2017.

[45] J Buschbeck, M A Vogelsberger, A Orellano, E Schmidt, and M Bazant. Multi-Physics Optimization of High Power Density Induction Machines for Railway Traction Drives. In *2015 IEEE International Conference on Industrial Technology (ICIT)*, pages 2656–2661, Seville, Spain, 2015. IEEE.

[46] Osborne Reynolds. An experimental investigation of the circumstances which determine whether the motion of water shall be direct or sinuous, and of the law of resistance in parallel channels. *Philosophical Transactions of the Royal Society of London*, 174:935–982, 1883.

[47] M Couette. Oscillations tournantes d'un solide de révolution en contact avec un fluide visqueux. *Comptes Rendus des Séances de l'Académie des Sciences Paris*, 105:1064–1067, 1887.

[48] G.I. Taylor. Stability of a Viscous Liquid Contained between Two Rotating Cylinders. *Philosophical Transactions of the Royal Society of London A: Mathematical, Physical and Engineering Sciences*, 223:289–343, 1923.

[49] J W Daily and R E Nece. Chamber Dimension Effects on Induced Flow and Frictional Resistance of Enclosed Rotating Disks. *Journal of Basic Engineering*, 82(1):217–230, 1960.

[50] R E Nece and J W Daily. Roughness Effects on Frictional Resistance of Enclosed Rotating Disks. *Journal of Basic Engineering*, 82(3):553–560, 1960.

[51] J Tachibana and S Fukui. Heat Transfer in an Annulus with an Inner Rotating Cylinder. *Bulletin of JSME*, 3(9):119–123, 1960.

[52] K M Becker and J Kaye. Measurements of diabatic flow in an annulus with an inner rotating cylinder. *Journal of Heat Transfer*, 84(2):97–104, 1962.

[53] M. Fénot, E. Dorignac, A. Giret, and G. Lalizel. Convective heat transfer in the entry region of an annular channel with slotted rotating inner cylinder. *Applied Thermal Engineering*, 54(1):345–358, 2013.

[54] M. Fénot, Y. Bertin, E. Dorignac, and G. Lalizel. A review of heat transfer between concentric rotating cylinders with or without axial flow. *International Journal of Thermal Sciences*, 50(7):1138–1155, 2011.

[55] C J Fechheimer. An Experimental Study of Ventilation of Turbo Alternators. *Transactions of the American Institute of Electrical Engineers*, 43:476–501, 1924.

[56] C J Fechheimer. Ventilation of Revolving-Field Salient-Pole Alernators. *Transactions of the American Institute of Electrical Engineers*, 49(2):548–572, 1930.

[57] H Jamshidi, H Nilsson, and V Chernoray. Experimental and numerical investigation of hydro power generator ventilation. *IOP Conference Series: Earth and Environmental Science*, 22(1), 2014.

[58] D. A. Howey, A. S. Holmes, and K. R. Pullen. Radially resolved measurement of stator heat transfer in a rotor-stator disc system. *International Journal of Heat and Mass Transfer*, 53(1-3):491–501, 2010.

[59] S J Pickering, D Lampard, and M Shanel. Modelling Ventilation and Cooling of the Rotors of Salient Pole Machines. In *IEEE International Electric Machines and Drives Conference (IEMDC 2001)*, pages 806–808, Cambridge, USA, 2001. IEEE.

[60] N J Carew. Flow distribution and pressure drop in salient pole electrical machines. *Proceedings of the Institution of Mechanical Engineers*, 184(9):62–69, 1969.

[61] Claudinei de Moura Altea and Jurandir Itizo Yanagihara. Validation of a Numerical Method applied to the Calculation of a Hydrogenerator Ventilation System. In *15th Brazilian Congress of Thermal Sciences and Engineering (ENCIT 2014)*, Belem, Brazil, 2014.

[62] L Küng, U Bikle, O Popp, and R Jakoby. Improvement of the Cooling Performance of Symmetrically Self-Ventilated Induction Machines in the 2-15 MW Range. In *IEEE International Electric Machines and Drives Conference (IEMDC 2001)*, pages 673–680, Cambridge, USA, 2001. IEEE.

[63] M Schrittwieser, A Marn, E Farnleitner, and G Kastner. Numerical Analysis of Heat Transfer and Flow of Stator Duct Models. *IEEE Transactions on Industry Applications*, 50(1):226–233, 2014.

[64] H Jamshidi, H Nilsson, and V Chernoray. CFD-based design and analysis of the ventilation of an electric generator model, validated with experiments. *International Journal of Fluid Machinery and Systems*, 8(2):113–123, 2015.

[65] P H Connor, C N Eastwick, S J Pickering, C Gerada, and R Rolston. Stator and Rotor Vent Modelling in a MVA rated Synchronous Machine. In *22nd International Conference on Electrical Machines (ICEM 2016)*, pages 571–577, Lausanne, Switzerland, 2016. IEEE.

[66] ANSYS Inc. *ANSYS DesignModeler User's Guide Release 17.2*. 2016.

[67] ANSYS Inc. *ANSYS Meshing User's Guide Release 17.2*. 2016.

[68] ANSYS Inc. *ANSYS Fluent User's Guide Release 17.2*. 2016.

[69] ANSYS Inc. *ANSYS Fluent Theory Guide Release 17.2*. 2016.

[70] ANSYS Inc. *ANSYS CFD-Post User's Guide Release 17.2*. 2016.

[71] ANSYS Inc. *ANSYS DesignXplorer User's Guide Release 17.2*. 2016.

[72] B E Launder and D B Spalding. The Numerical Computation of Turbulent Flows. *Computer Methods in Applied Mechanics and Engineering*, 3(2):269–289, 1974.

[73] S M Salim and S C Cheah. Wall y+ Strategy for Dealing with Wall-bounded Turbulent Flows. In *Proceedings of the International MultiConference of Engineers and Computer Scientists (IMECS 2009)*, Hong Kong, 2009.

[74] Stefano Nuzzo, Michael Galea, Chris Gerada, and Neil Brown. A Fast method for Modelling Skew and its Effects in Salient-Pole Synchronous Generators. *IEEE Transactions on Industrial Electronics*, 64(10):7679–7688, 2017.

[75] K Bersch, S Nuzzo, P H Connor, C N Eastwick, M Galea, R Rolston, and G Vakil. Combined Thermofluid and Electromagnetic Optimisation of Stator Vent Cooling. In *23rd International Conference on Electrical Machines (ICEM 2018)*, pages 1116–1122, Alexandroupoli, Greece, 2018. IEEE.

[76] Z. Hashin and S. Shtrikman. A Variational Approach to the Theory of the Effective Magnetic Permeability of Multiphase Materials. *Journal of Applied Physics*, 33(10):3125–3131, 2004.

[77] Nick Simpson, Rafal Wrobel, and Phil H. Mellor. Estimation of equivalent thermal parameters of impregnated electrical windings. *IEEE Transactions on Industry Applications*, 49(6):2505–2515, 2013.

[78] Lad Idoughi, Xavier Mininger, Frédéric Bouillault, Laurent Bernard, and Emmanuel Hoang. Thermal model with winding homogenization and FIT discretization for stator slot. *IEEE Transactions on Magnetics*, 47(12):4822–4826, 2011.

[79] Mirko Javurek and Johannes Kepler. Fluent Scheme Documentation. Technical report, Johannes Kepler University Linz, Linz, 2004.

[80] British Standards Institution. BS 848-1:2007 Industrial fans - Performance testing using standardized airways. 2007.

[81] Peter H. Connor, Steve J. Pickering, Chris Gerada, Carol N. Eastwick, Chris Micallef, and Chris Tighe. Computational fluid dynamics modelling of an entire synchronous generator for improved thermal management. *IET Electric Power Applications*, 7(3):231–236, 2013.

[82] K Bersch, P H Connor, C N Eastwick, and M Galea. A CFD and experimental investigation into a non-intrusive method for measuring cooling air mass flow rate through a synchronous generator. *The Journal of Engineering*, 2019.

[83] Rafal Wrobel, Samuel J Williamson, Julian D Booker, and Phil H Mellor. Characterising the in situ Thermal Behaviour of Selected Electrical Machine Insulation and Impregnation Materials. *IEEE Transactions on Industry Applications*, 52(6):4678–4687, 2016.

[84] S La Rocca, S J Pickering, C N Eastwick, C Gerada, and K Rönnberg. Fluid flow and heat transfer analysis of TEFC machine end regions using more realistic end-winding geometry. In *9th International Conference on Power Electronics, Machines and Drives (PEMD 2018)*, Liverpool, UK, 2018. IET.

[85] Kevin Bersch, Peter H Connor, Carol N Eastwick, Michael Galea, and Rob Rolston. CFD Optimisation of the Thermal Design for a Vented Electrical Machine. In *IEEE Workshop on Electrical Machines Design, Control and Diagnosis (WEMDCD 2017)*, pages 39–44, Nottingham, UK, 2017. IEEE.

[86] ANSYS Inc. *ANSYS Workbench User's Guide Release 17.2*. 2016.

[87] Ultimaker. Technical Data Sheet Polycarbonate. https://ultimaker.com/download/74975/UM180821 TDS PC RB V11.pdf. Accessed 12/2018.

[88] Eastman. Technical Data Sheet Copolyester. https://colorfabb.com/files/AmphoraHT5300-TDS.pdf. Accessed 12/2018.

[89] Gian Carlo Montanari and Luciano Simoni. Aging Phenomenology and Modeling. *IEEE Transactions on Electrical Insulation*, 28(5):755–776, 1993.

Appendix A

Computational Fluid Dynamics Theory

A.1 Governing equations of fluid flow

For a three-dimensional, compressible Newtonian fluid in a Cartesian coordinate system, the governing equations of fluid flow are defined as the following set of partial differential equations (PDE) [29]:

$$\text{Continuity:} \quad \frac{\delta \rho}{\delta t} + \nabla \cdot (\rho \vec{v}) = 0 \tag{A.1}$$

$$\text{X-Momentum:} \quad \frac{\delta \rho u}{\delta t} + \nabla \cdot (\rho u \vec{v}) = -\frac{\delta p}{\delta x} + \nabla \cdot (\mu \nabla u) + S_{M_x} \tag{A.2}$$

$$\text{Y-Momentum:} \quad \frac{\delta \rho v}{\delta t} + \nabla \cdot (\rho v \vec{v}) = -\frac{\delta p}{\delta y} + \nabla \cdot (\mu \nabla v) + S_{M_y} \tag{A.3}$$

$$\text{Z-Momentum:} \quad \frac{\delta \rho w}{\delta t} + \nabla \cdot (\rho w \vec{v}) = -\frac{\delta p}{\delta z} + \nabla \cdot (\mu \nabla w) + S_{M_z} \tag{A.4}$$

$$\text{Energy:} \quad \frac{\delta \rho i}{\delta t} + \nabla \cdot (\rho i \vec{v}) = -p \nabla \cdot \vec{v} + \nabla \cdot (k \nabla T) + \Phi + S_i \tag{A.5}$$

The full derivation of the above set of PDE and their conversion into a set of linear algebraic equations that can be solved numerically can be found in [29]. The variables used in equations A.1-A.5 are defined as following:

- x, y, z: Cartesian coordinates
- $\vec{v}$: 3-dimensional velocity vector
- u, v, w: Velocity components in x, y, z-direction
- S_{M_x}, S_{M_y}, S_{M_z}: Momentum source terms in x, y, z-direction
- p: Pressure

- ρ: Density
- μ: Dynamic viscosity
- i: Internal energy
- T: Temperature
- k: Thermal conductivity
- t: Time
- S_i: Internal energy source term
- Φ: Source of internal energy due to deformation work on the fluid

A.2 Discretisation

Except for the most simple cases, it is not possible to solve the governing equations of fluid flow analytically. For CFD, the Finite Volume Method (FVM) is applied to convert the set of PDE into a set of algebraic equations that can be solved numerically. The investigated geometry is divided into a number of control volumes, or cells, as described in section 3.3. The governing equations are then integrated about each control volume. As the properties are conserved in every cell, they are also conserved in the whole domain. Control volume integration results in the following integral equation for any conserved property ϕ:

$$\int_V \frac{\delta \rho \phi}{\delta t} dV + \oint \rho \phi \vec{v} d\vec{A} = \oint \Gamma_\phi \nabla \phi d\vec{A} + \int_V S_\phi dV \tag{A.6}$$

with V being the cell volume, $\vec{A}$ the surface area vector and Γ_ϕ the diffusion coefficient for ϕ. Equation A.6 states that the sum of the rate of increase of any conserved property ϕ inside the control volume and the net rate of decrease of ϕ due to convection across the control volume boundaries (the two terms on the left hand side of the equation) equal the net rate of increase of ϕ due to diffusion across the control volume boundaries and the net rate of creation of ϕ inside the control volume (the two terms on the right hand side) [29]. Integration of equation A.6 on any given cell results in the following algebraic equation:

$$\frac{\delta \rho \phi}{\delta t} + \sum_f^{N_{faces}} \rho_f \vec{v}_f \phi_f \vec{A}_f = \sum_f^{N_{faces}} \Gamma_\phi \nabla \phi_f \vec{A}_f + S_\phi V \tag{A.7}$$

with N_{faces} being the number of surfaces enclosing the cell, ϕ_f the value of ϕ convected through face f, $\vec{v}_f$ the face velocity vector and $\vec{A}_f$ the face area. As the conserved properties and velocities in equation A.7 are required on the cell face, but are only known in the centre

of the cell, they need to be determined by discretisation. The discretisation schemes utilised within this thesis are listed and explained below.

For the diffusion terms, the second-order accurate central-differencing scheme is used. The diffusion coefficient at a face f between two cells P and E is calculated as following:

$$\Gamma_{\phi,f} = \frac{\Gamma_{\phi,P} + \Gamma_{\phi,E}}{2} \tag{A.8}$$

For the convective terms, the central-differencing does not produce accurate results, as convective properties are dominated by the behaviour of the flow upstream of the cell [29]. The upwind differencing scheme, which only takes the properties upstream of the current cell into account, produces much better results in this case. The second order upstream differencing scheme was used for the convective terms of all properties within this project. The value of any property ϕ at a face f is calculated as following:

$$\phi_f = \phi_u + \nabla\phi\vec{r} \tag{A.9}$$

with ϕ_u being the value of ϕ in the upstream cell, $\nabla\phi$ its gradient, and $\vec{r}$ the displacement vector from the upstream cell centroid to the face centroid. All gradients are calculated using the least squares cell based approach.

Whilst first-order discretisation schemes are generally more robust than higher-order schemes, they produce less accurate results. The numerical diffusion error is increased, particularly if the mesh is not aligned with the flow direction. Thus, second order accurate discretisation schemes have been utilised for all properties in this thesis. More details on various discretisation schemes and their advantages and disadvantages can be found in [29, 68, 69].

A.3 RANS Turbulence Modelling

The Reynolds-averaged Navier Stokes (RANS) approach is based on the Reynolds decomposition, which decomposes an instantaneous quantity ϕ into a steady mean value $\bar{\phi}$ and a fluctuating component ϕ':

$$\phi(t) = \bar{\phi} + \phi'(t) \tag{A.10}$$

Substituting equation A.10 into equations A.2-A.4 introduces 6 additional terms called Reynolds stresses which are defined as following:

$$\tau_{ij} = -\rho u_i' u_j' \tag{A.11}$$

with u_i' and u_j' being the velocity fluctuations in x/y/z-direction. Additional equations are required to predict the Reynolds stresses and solve the Navier-Stokes equations for turbulent flow. A considerable amount of research has focussed on developing turbulence models suited for different applications. Versteeg and Malalasekera [29] give an overview of different turbulence models and some of their advantages and disadvantages.

The k-ε model, which has been utilised within this project, is based on the Boussinesq hypothesis, which proposes the Reynolds stresses to be proportional to the mean rate of deformation. k is the turbulent kinetic energy per unit mass, also known as the turbulence kinetic energy, and defined as:

$$k = \frac{1}{2}(\overline{u'^2} + \overline{v'^2} + \overline{w'^2}) \tag{A.12}$$

ε is the rate of dissipation of turbulent kinetic energy per unit mass, also known as turbulence dissipation rate, and defined as:

$$\varepsilon = 2\nu\overline{s_{ij}' s_{ij}'} \tag{A.13}$$

Based on the Boussinesq hypothesis and equations A.12 and A.13, transport equations for k and ε have been developed to close the RANS equations for turbulent flow. For the standard k-ε model they are defined as following:

$$k: \quad \frac{\delta(\rho k)}{\delta t} + \nabla \cdot (\rho k \vec{v}) = \nabla \cdot (\frac{\mu_t}{\sigma_k} \nabla k) + 2\mu_t S_{ij} S_{ji} - \rho\varepsilon \tag{A.14}$$

$$\varepsilon: \quad \frac{\delta(\rho \varepsilon)}{\delta t} + \nabla \cdot (\rho \varepsilon \vec{v}) = \nabla \cdot (\frac{\mu_t}{\sigma_e} \nabla \varepsilon) + C_{1\varepsilon} \frac{\varepsilon}{k} 2\mu_t S_{ij} S_{ji} - C_{2\varepsilon} \rho \frac{\varepsilon^2}{k} \tag{A.15}$$

For the standard k-ε model, the constants in equations A.14 and A.15, are defined as: $\sigma_k = 1$, $\sigma_\varepsilon = 1.3$, $C_{1\varepsilon} = 1.44$, $C_{2\varepsilon} = 1.92$. The eddy viscosity μ_t is defined as:

$$\mu_t = \rho C_\mu \frac{k^2}{\varepsilon} \tag{A.16}$$

Appendix B

Fluent Scripts and User Defined Functions

B.1 Automatic creation of periodic boundaries

```
;Create periodic boundaries between all interfaces that start with 'str_front' and 'str_back'
(define (create-per)
        (define str_front "Interface_Back")
        (define str_back "Interface_Front")
        (define angle 180)
        (define tempfront "init")
        (define nper 2)
        (define counter -1)
        (define id1 (list))
        (define id2 (list))
        (define zone1 (list))
        (define zone2 (list))

        (define (add_id1 id)    ;add an element to list id1
                (set! id1 (cons id id1)))

        (define (add_id2 id)    ;add an element to list id2
                (set! id2 (cons id id2)))

        (define (add_zone1 zone)        ;add an element to list zone1
                (set! zone1 (cons zone zone1)))

        (for-each (lambda (name)
                ;(display-all (zone-name->id name) ": " name "\n")
                (set! tempfront (symbol->string name))
                (if (> (string-length tempfront) (string-length str_front))
                (set! tempfront (substring tempfront 0 (string-length str_front)))
                (display "")
                )
                (if (string-ci=? tempfront str_front)
                        (begin
                        (add_id1 (zone-name->id name))
                        (add_zone1 (string-tail (symbol->string name) (string-length str_front)-1 ))
                        ;(display-all (zone-name->id name) " - " id1 "\n")
                        )
                        (display "")
                )
                )
```

```
            (inquire-zone-names)
        )
        (display-all "Periodic Front Interfaces: " id1 "\n")
        (set! nper (length id1))

        (for-each (lambda (zone)
                (set! counter (+ counter 1))
                (for-each (lambda(name)
                        (if (string-ci=? (string-append str_back zone) (symbol->string name))
                                (add_id2 (zone-name->id name))
                                (display "")
                        )
                        )
                        (inquire-zone-names)
                )
                )
        zone1
        )
        (set! id2 (reverse id2))
        (display-all "Periodic Back Interfaces: " id2 "\n \n")

        (if (= (length id1) (length id2))
                (begin
                (do ((i 0 (+ i 1))) ((>= i (length id1)-1))
                        (per-bound (list-ref id2 i) (list-ref id1 i) angle (list-ref zone1 i))
                )
                (display-all " \n Following periodic BCs were created with a periodic angle of " angle " degrees: \n")
                (do ((i 0 (+ i 1))) ((>= i (length id1)-1))
                        (display-all "Per" (list-ref zone1 i) " - Coupled Surfaces: " (list-ref id2 i) " " (list-ref id1
                             ↪ i) "\n")
                )
                )
                (display-all "ERROR: Different number of front and back interfaces found!")
        )
)
```

B.2 Automatic creation of periodic repeats

```
;Create periodic repeats with names from 'int_namelist' between all interfaces in 'int_front' and 'int_back'
(define (create-repeat)
        (define int_namelist (list "rotstat_core" "rotstat_outer"))
        (define int_front (list "Interface_Rot-interface_rotstat-src-core_rot" "
             ↪ Interface_Rot-interface_rotstat-src-outer_rot"))
        (define int_back (list "Interface_Stat-interface_rotstat-trg-core_stat" "
             ↪ Interface_Stat-interface_rotstat-trg-outer_stat"))
        (define intname "")
        (define str_front "dummy")
        (define str_back "dummy")
        (define tempfront "init")
        (define temp "init")
        (define src "src")
        (define trg "trg")
        (define counter -1)
        (define counter2 -1)
        (define counter3 -1)
        (define intcount 0)
        (define id1 (list))
        (define id2 (list))
        (define zone1 (list))
        (define zone2 (list))
        (define cellID (list))
        (define cellName (list))
        (define intlist1 (list))
        (define intlist2 (list))

        (define (add_id1 id)    ;add an element to list id1
                (set! id1 (cons id id1)))
        (define (add_id2 id)    ;add an element to list id2
```

```
        (set! id2 (cons id id2)))
    (define (add_zone1 zone)        ;add an element to list zone1
        (set! zone1 (cons zone zone1)))
    (define (add_zone2 zone)        ;add an element to list zone2
        (set! zone2 (cons zone zone2)))


    ;Loop over all interfaces defined in int_back and int_front (int_back[i] must match int_front[i])
    (do ((i 0 (+ i 1))) ((>= i (length int_front)))
        (set! str_front (list-ref int_front i))
        (set! str_back (list-ref int_back i))
        (set! intname (list-ref int_namelist i))
        (set! id1 (list))
        (set! id2 (list))
        (set! zone1 (list))
        (set! zone2 (list))

        ;Add all interfaces starting with 'str-front' to list (does not check if zone is actually an interface)
        (for-each (lambda (name)
            ;(display-all (zone-name->id name) ": " name "\n")
            (set! tempfront (symbol->string name))
            (if (> (string-length tempfront) (string-length str_front))
            (set! tempfront (substring tempfront 0 (string-length str_front)))
            (display "")
            )
            (if (string-ci=? tempfront str_front)
                (begin
                (add_id1 (zone-name->id name))
                (add_zone1 (string-tail (symbol->string name) (string-length str_front)-1 ))
                ;(display-all (zone-name->id name) " - " id1 "\n")
                )
                (display "")
            )
            )
            (inquire-zone-names)
        )
        (display-all "Interface␣Zone␣1:␣" id1 "\n")

        ;Add all interfaces starting with 'str-back' to list (does not check if zone is actually an interface)
        (for-each (lambda (name)
            ;(display-all (zone-name->id name) ": " name "\n")
            (set! tempfront (symbol->string name))
            (if (> (string-length tempfront) (string-length str_back))
            (set! tempfront (substring tempfront 0 (string-length str_back)))
            (display "")
            )
            (if (string-ci=? tempfront str_back)
                (begin
                (add_id2 (zone-name->id name))
                (add_zone2 (string-tail (symbol->string name) (string-length str_back)-1 ))
                ;(display-all (zone-name->id name) " - " id1 "\n")
                )
                (display "")
            )
            )
            (inquire-zone-names)
        )
        (display-all "Interface␣Zone␣2:␣" id2 "\n␣\n")


        ;Couples all interfaces in lists
        (if (and (> (length id1) 0) (> (length id2) 0))
            (int-repeat (list-ref id1 0) (list-ref id2 0) intname)
            (display-all "No␣interfaces␣starting␣with␣" str-front "␣and/or␣" str-back "␣found!")
        )
    )
)
```

B.3 Anisotropic Conductivity Modelling in Endwindings

Stator

```
#include "udf.h"
#include <math.h>

//xxx to be replaced with numeric values according to machine specs
real k_h_stat = 400, k_l_stat = 0.43, straight_stat = xxx, r_stat = xxx, z0_stat= xxx;

real change_cond_stat(real k_1, real k_2, real r, real z)
{
        real cond_1, cond_2, cond;
        // linear relationship
        cond = (r-z)/r*k_1 + z/r*k_2;
        return cond;
}

DEFINE_PROPERTY(ew_axial,c,t)
{
real pos[ND_ND];
real z, cond, z_bend;

C_CENTROID(pos,c,t);
z = fabs(pos[2])-z0_stat;
z_bend = z-straight_stat;

if (z<=straight_stat)
{
        cond = k_h_stat;
}
else if (z_bend<r_stat)
{
        cond = change_cond_stat(k_h_stat,k_l_stat,r_stat,z_bend);
}
else
{
        cond = k_l_stat;
}

return cond;
}

DEFINE_PROPERTY(ew_tangential,c,t)
{
real pos[ND_ND];
real z, cond, z_bend;

C_CENTROID(pos,c,t);
z = fabs(pos[2])-z0_stat;
z_bend = z-straight_stat;

if (z<=straight_stat)
{
        cond = k_l_stat;
}
else if (z_bend<r_stat)
{
        cond = change_cond_stat(k_l_stat,k_h_stat,r_stat,z_bend);
}
else
{
        cond = k_h_stat;
}

return cond;
}
```

```
DEFINE_PROPERTY(ew_radial,c,t)
{
real cond;
cond = k_l_stat;
return cond;
}

DEFINE_PROPERTY(cond_high_stat,c,t)
{
        return k_h_stat;
}

DEFINE_PROPERTY(cond_low_stat,c,t)
{
        return k_l_stat;
}
```

Rotor

```
#include "udf.h"
#include <math.h>

//xxx to be replaced with numeric values according to machine specs
real k_h = 400, k_l = 1.45, z0=xxx, new_wind=xxx, straight=xxx, r=xxx, x0=xxx,y0=xxx;
real pos[ND_ND];
real z,y,x,cond,x_bend,y_bend,z_bend;

real change_cond(real k_1, real k_2, real r, real z, real x)
{
        real cond;
        // Circle relationship
        r = sqrt(pow(z,2)+pow(x,2));
        cond = sqrt(pow(k_1*x/r,2)+pow(k_2*z/r,2));

        return cond;
}

DEFINE_PROPERTY(cond_ew_rot_Z,c,t)
{
C_CENTROID(pos,c,t);
x = fabs(pos[0]);
y = fabs(pos[1]);
z = fabs(pos[2])-z0;
z_bend = z-straight;
x_bend = x-x0;
y_bend = y-y0;

if (z<=straight)
{
        cond = k_h;
}
else if ((y>new_wind) && (x_bend>0))
{
        cond = change_cond(k_h,k_l,r,z_bend,x_bend);
}
else if ((y<new_wind) && (y_bend>0))
{
        cond = change_cond(k_h,k_l,r,z_bend,y_bend);
}
else
{
        cond = k_l;
}
return cond;
}

DEFINE_PROPERTY(cond_ew_rot_X,c,t)
{
```

```
C_CENTROID(pos,c,t);
x = fabs(pos[0]);
y = fabs(pos[1]);
z = fabs(pos[2])-z0;
z_bend = z-straight;
x_bend = x-x0;
y_bend = y-y0;

if (z<=straight)
{
        cond = k_l;
}
else if ((y>new_wind) && (x_bend>0))
{
        cond = change_cond(k_l,k_h,r,z_bend,x_bend);
}
else if (y>new_wind)
{
        cond = k_h;
}
else
{
        cond = k_l;
}
return cond;
}

DEFINE_PROPERTY(cond_ew_rot_Y,c,t)
{
C_CENTROID(pos,c,t);
x = fabs(pos[0]);
y = fabs(pos[1]);
z = fabs(pos[2])-z0;
z_bend = z-straight;
x_bend = x-x0;
y_bend = y-y0;

if (z<=straight)
{
        cond = k_l;
}
else if ((y<new_wind) && (y_bend>0))
{
        cond = change_cond(k_l,k_h,r,z_bend,y_bend);
}
else if (y<new_wind)
{
        cond = k_h;
}
else
{
        cond = k_l;
}
return cond;
}

DEFINE_PROPERTY(cond_high_rot,c,t)
{
        return k_h;
}

DEFINE_PROPERTY(cond_low_rot,c,t)
{
        return k_l;
}
```

B.4 Temperature dependent heat generation

```
#include "udf.h"
//xxx to be replaced with numeric values according to machine specs
real T_0 = xxx, T_ref xxx, z_core=xxx;
real R_0_stat = xxx, I_stat = xxx, V_core_stat = xxx, V_EW_stat = xxx;
real R_0_rot = xxx, I_rot = xxx, V_core_rot = xxx, V_EW_rot = xxx;
real pos[ND_ND];

DEFINE_SOURCE(Copper_Losses_Stator,c,t,dS,eqn)
{
        real losses;

        C_CENTROID(pos,c,t);
        if (fabs(pos[2]) <= z_core)
                losses = I_stat*I_stat*R_0_stat*(T_ref+C_T(c,t))/(T_ref+T_0)*1.5/V_core_stat;
        else
                losses = I_stat*I_stat*R_0_stat*(T_ref+C_T(c,t))/(T_ref+T_0)*1.5/V_EW_stat;

        return losses;
}

DEFINE_SOURCE(Copper_Losses_Rotor,c,t,dS,eqn)
{
        real losses;

        C_CENTROID(pos,c,t);
        if (fabs(pos[2]) <= z_core)
                losses = I_rot*I_rot*R_0_rot*(T_ref+C_T(c,t))/(T_ref+T_0)/V_core;
        else
                losses = I_rot*I_rot*R_0_rot*(T_ref+C_T(c,t))/(T_ref+T_0)/V_EW;

        return losses;
}
```